SEASONALITY FROM SPELEOTHEMS:

HIGH-RESOLUTION ION MICROPROBE STUDIES AT SOREQ CAVE, ISRAEL

By

Ian James Orland

A dissertation submitted in partial fulfillment of

the requirements for the degree of

Doctor of Philosophy

(Geoscience)

at the

UNIVERSITY OF WISCONSIN-MADISON

2012

Date of final oral examination: 11/2/12

The dissertation is approved by the following members of the Final Oral Committee:

John W. Valley, Professor, Geoscience (primary advisor)
Clark M. Johnson, Professor, Geoscience
Anders E. Carlson, Associate Professor, Geoscience
Stephen R. Meyers, Assistant Professor, Geoscience
John W. Williams, Professor, Geography
Miryam Bar-Matthews, Senior Research Scientist, Geological Survey of Israel

Dedicated to Kate, to my family, and to my many teachers

Table of Contents

Acknowledgements

Great thanks are due to my primary advisor, Prof. John Valley, who provided an enormous amount of energy, encouragement, and enthusiasm for this project. Prof. Valley introduced me not only to the power of SIMS analysis, but also to collaborators integral to the success of this study. Dr. Mira Bar-Matthews (Geological Survey of Israel; GSI), Prof. Alan Matthews (Hebrew University in Jerusalem), Dr. Avner Ayalon (GSI), and Yuval Burstyn who have studied Soreq Cave cumulatively for 60+ years, provided all of the Soreq samples referenced in this thesis, help with sample analysis, generous room and board in their home for my visit to Israel, and illuminating discussions about caves and climate.

Drs. Noriko Kita, Takayuki Ushikubo, and Reinhard Kozdon are responsible for the state-of-the-art isotope measurements made at the WiscSIMS laboratory at UW-Madison. The skill with which they align and tune the ion microprobe and critically evaluate the results is unequaled in the earth sciences; I greatly appreciate the time and care they put into both helping me understand the ion microprobe as well as ensuring that my analysis sessions ran smoothly.

Thanks are also in order for the UW-Madison members of my dissertation committee – Profs. Anders E. Carlson, Clark M. Johnson, Stephen R. Meyers, and John (Jack) W. Williams (Dept. of Geography) – for their guidance and insight. I received great support and inspiration from faculty, staff, librarians, fellow graduate students, and WiscSIMS group members throughout the entirety of my time in the Department of Geoscience. I have shared an office with three wonderful scientists that were kind (and patient) enough to entertain all types of discussion, productive or otherwise – Penny Lancaster, Dayi Ortiz, and Anthony Pollington.

More specific thanks go to Profs. Jay Quade (University of Arizona) and Jim McManus (Oregon State University) as well as six peer-reviewers for comments that greatly improved the

first two chapters of this dissertation; Dr. Bin Fu and Andrew Trzaskus for help with ion microprobe analysis; Brian Hess and Jim Kern for assistance with sample preparation; Mike Spicuzza, Prof. Zhengyu Liu, Prof. John Kutzbach, and Drs. Zeb Page, Philipp Heck, Andy Czaja, Ken Williford, and Brian Beard for helpful discussions; Lance Rodenkirch for guidance at the W. M. Keck Laboratory for Biological Imaging at UW-Madison; Dr. John Fournelle, Dayi Ortiz, Phillip Gopon, and Chloe Bonamici for help with the SEM; Dr. Omri Dvir for guidance on the HUJI LA-ICP-MS; Anthony Pollington and Dr. Ellen Syracuse for MATLAB tips and tricks; Dr. Tom Helser, Beth Matta, Prof. Bryan Black, and Craig Kastelle for their initiative, expertise, and collaboration on multiple fascinating otolith projects; and the Israel Nature and Parks Authority for access to Soreq Cave.

Funding came from NSF (AGS-1003487, EAR-0440343), DOE (93ER14389), Israel Science Foundation (grant 910/05), the Comer Science and Education Foundation, the United States-Israel Binational Science Foundation (2010316), and the Sigma Xi Scientific Research Society. The Department of Geology & Geophysics at UW-Madison provided financial assistance and a Weeks Research Assistantship. Wisc-SIMS is partly supported by the NSF (EAR-0319230, EAR-0744079, EAR 1053466).

Certainly, the completion of this thesis is due in large part to the seemingly endless support and encouragement of my wonderful friends, my family, and my wife, Kate.

Publication References

Portions of this dissertation have been published in peer-reviewed scientific journals. Ultimately, the goal is to publish the entire body of work. For reference, the citation information for the chapters that have been published (1&2) as well as the chapter that is currently under peer-review (5) is listed below.

Chapter 1:

Orland, I. J., Bar-Matthews, M., Kita, N. T., Ayalon, A., Matthews, A., and Valley, J. W. (2009) Climate deterioration in the eastern Mediterranean as revealed by ion microprobe analysis of a speleothem that grew from 2.2 to 0.9 ka in Soreq Cave, Israel. *Quaternary Research* **71**, 27-35.

Chapter 2:

Orland I. J., Bar-Matthews M., Ayalon A., Matthews A., Kozdon R., Ushikubo T., and Valley J. W. (2012) Seasonal resolution of Eastern Mediterranean climate change since 34 ka from a Soreq Cave speleothem. *Geochimica et Cosmochimica Acta* **89**, 240-255.

Chapter 5 (collaborative manuscript):

Matta M. E., Orland I. J., Ushikubo T., Helser T. E., Black B. A., and Valley J. W. *in review*. Otolith oxygen isotopes measured by high-precision secondary ion mass spectrometry reflect life history of a yellowfin sole (*Limanda aspera*).

Sample Index and UW Catalog Numbers

All of the samples examined in this dissertation were acquired from collaborators unattached to the University of Wisconsin. Soreq Cave samples are from Dr. M. Bar-Matthews at the Geological Survey of Israel, otolith samples are from Dr. T. Helser at the Alaska Fisheries Science Center (NOAA), and Spring Valley Cavern samples are from Dr. R. L. Edwards at the University of Minnesota. Since data from these samples are discussed in published literature, the original sample names are preserved in this work to avoid confusion. All specimens referenced in this thesis are in the collections of the Department of Geoscience, University of Wisconsin-Madison, under file numbers UW 1993 and 2008 as defined in the table below. Serial numbers with the 1993 prefix are also described in Orland (2008; UW MS thesis).

UW catalog number	Published sample name	Sample type	Description	Locality*	Described In
1993/1	2-6	Whole slab (minus chips)	calcite stalagmite	SC	Chapter 1**
1993/1.1	2-6 (chip A)	1 cm^3 chip in epoxy round			
1993/1.1B	2-6 (back of A)	Cut-off back of epoxy round			
1993/1.2	2-6 (chip B)	1 cm^3 chip in epoxy round			
1993/1.2B	2-6 (back of B)	Cut-off back of epoxy round			
1993/1.3	2-6 (chip C)	1 cm^3 chip in epoxy round			
1993/1.3B	2-6 (back of C)	Cut-off back of epoxy round			
1993/1.4	2-6 (chip D)	1 cm^3 chip in epoxy round			
1993/1.4B	2-6 (back of D)	Cut-off back of epoxy round			
1993/1.5	2-6 (chip E)	1 cm^3 chip in epoxy round			
1993/1.5B	2-6 (back of E)	Cut-off back of epoxy round			
1993/2	12-1-54	1 cm^3 chip in epoxy round	calcite stalagmite	SC	**
1993/2B	back of 12-1-54	Cut-off back of epoxy round			
1993/3	2N	Whole slab (minus chips)	calcite stalactite	SC	Chapters 2, 4; Supplements C, E**
1993/3.0	2N	Portion of slab removed to make single cut edge			
1993/3.1	2N (chip A)	1 cm^3 chip in epoxy round			
1993/3.1B	2N (back of A)	Cut-off back of epoxy round			
1993/3.2	2N (chip B)	1 cm^3 chip in epoxy round			
1993/3.2B	2N (back of B)	Cut-off back of epoxy round			
1993/3.3	2N (chip C)	1 cm^3 chip in epoxy round			
1993/3.3B	2N (back of C)	Cut-off back of epoxy round			
1993/3.4	2N (chip D)	1 cm^3 chip in epoxy round			
1993/3.4B	2N (back of D)	Cut-off back of epoxy round			
1993/3.5	2N (chip E)	1 cm^3 chip in epoxy round			
1993/3.5B	2N (back of E)	Cut-off back of epoxy round			
1993/3.6	2N (chip F)	1 cm^3 chip in epoxy round			
1993/3.6B	2N (back of F)	Cut-off back of epoxy round			
1993/3.7	2N (chip G)	1 cm^3 chip in epoxy round			
1993/3.7B	2N (back of G)	Cut-off back of epoxy round			
1993/3.8	2N (chip H)	1 cm^3 chip in epoxy round			
1993/3.8B	2N (back of H)	Cut-off back of epoxy round			
1993/3.9	2N (chip I)	1 cm^3 chip in epoxy round			
1993/3.9B	2N (back of I)	Cut-off back of epoxy round			
1993/3.10	2N (chip J)	1 cm^3 chip in epoxy round			

UW catalog number	Published sample name	Sample type	Description	Locality*	Described In
1993/3.10B	2N (back of J)	Cut-off back of epoxy round			
1993/3.11	2N (chip K)	1 cm^3 chip in epoxy round			
1993/3.11B	2N (back of K)	Cut-off back of epoxy round			
1993/3.12	2N (chip L)	1 cm^3 chip in epoxy round			
1993/3.12B	2N (back of L)	Cut-off back of epoxy round			
1993/3.13	2N (chip M)	1 cm^3 chip in epoxy round			
1993/3.13B	2N (back of M)	Cut-off back of epoxy round			
1993/3.14	2N (chip N)	1 cm^3 chip in epoxy round			
1993/3.14B	2N (back of N)	Cut-off back of epoxy round			
1993/3.15	2N (chip O)	1 cm^3 chip in epoxy round			
1993/3.15B	2N (back of O)	Cut-off back of epoxy round			
1993/3.16	2N (chip P)	1 cm^3 chip in epoxy round			
1993/3.16B	2N (back of P)	Cut-off back of epoxy round			
1993/4	–	Slab of wood	Mediterranean Pine	above SC	**
1993/5	SVC-982	Whole slab (minus chips), glued to glass plate	calcite stalagmite	SVC	Supplement D**
1993/5.1	SVC-982 (chip 1)	1 cm^2 chip in epoxy round			
1993/5.2	SVC-982 (chip 2)	1 cm^2 chip in epoxy round			
1993/5.3	SVC-982 (chip 3)	1 cm^2 chip in epoxy round			
1993/5.4	SVC-982 (chip 4)	1 cm^2 chip in epoxy round			
1993/5.5	SVC-982 (chip 5)	1 cm^2 chip in epoxy round			
1993/5.6	SVC-982 (chip 6)	1 cm^2 chip in epoxy round			
1993/5.7	SVC-982 (chip 7)	1 cm^2 chip in epoxy round			
1993/5.8	SVC-982 (chip 8)	1 cm^2 chip in epoxy round			
1993/5.9	SVC-982 (roasted chip 1)	roasted chip in epoxy round			
1993/5.10	SVC-982 (roasted chip 2)	roasted chip in epoxy round			
2008/1	5-3b	Vertical slice of stalagmite mounted in epoxy round	calcite stalagmite	SC	Chapter 3
2008/2.1	18-O specimen 1 (unroasted half)	Half of right-hand Yellowfin Sole otolith in epoxy round	aragonite otolith	BS	Chapter 5
2008/2.2	18-O specimen 1 (roasted half)	Half of right-hand Yellowfin Sole otolith in epoxy round	aragonite/calcite otolith		
2008/3.1	6501	Bottle of crushed powder (unsorted)	aragonite	Cumberland	Supplement A
2008/3.2	6501	Bottle of crushed powder (500-1000 μm)			
2008/3.3	6501	Bottle of crushed powder (250-500 μm)			
2008/3.4	6501	Bottle of crushed powder (<250 μm)			
2008/4	UWArg-4	Hand sample	aragonite	Morocco	Supplement A
2008/4.1	UWArg-4.1	Bottle of crushed powder (500-1000 μm)			
2008/4.2	UWArg-4.1	Bottle of crushed powder (250-500 μm)			
2008/4.3	UWArg-4.1	Bottle of crushed powder (<250 μm)			
2008/5	UWArg-5	Bottle with chip of sample	aragonite	Czech Rep.	Supplement A
2008/5.1	UWArg-5	Bottle of crushed powder (500-1000 μm)			
2008/5.2	UWArg-5	Bottle of crushed powder (250-500 μm)			
2008/5.3	UWArg-5	Bottle of crushed powder (<250 μm)			
2008/6.1	6505	Bottle of crushed powder (500-1000 μm)	aragonite (not homogeneous)	Livermore, CA	Supplement A
2008/6.2	6505	Bottle of crushed powder (250-500 μm)			
2008/6.3	6505	Bottle of crushed powder (<250 μm)			
2008/7.1	6515	Bottle of crushed powder (500-1000 μm)	aragonite (not homogeneous)	Chester Co., PA	Supplement A

UW catalog number	Published sample name	Sample type	Description	Locality*	Described In
2008/7.2	6515	Bottle of crushed powder (250-500 μm)			
2008/7.3	6515	Bottle of crushed powder (<250 μm)			
2008/8.1	6540	Bottle of crushed powder (500-1000 μm)	aragonite (not homogeneous)	Tucson, AZ	Supplement A
2008/8.2	6540	Bottle of crushed powder (250-500 μm)			
2008/8.3	6540	Bottle of crushed powder (<250 μm)			
2008/9	UWArg-3	Bottle with chip of sample	calcite	Argentina	Supplement A
2008/9.1	UWArg-3	Bottle of crushed powder (500-1000 μm)			
2008/9.2	UWArg-3	Bottle of crushed powder (250-500 μm)			
2008/9.3	UWArg-3	Bottle of crushed powder (<250 μm)			
2008/10.1	UWArg-6	Bottle of crushed powder (500-1000 μm)	prehnite	Argentina	Supplement A
2008/10.2	UWArg-6	Bottle of crushed powder (250-500 μm)			
2008/10.3	UWArg-6	Bottle of crushed powder (<250 μm)			

*: Locality abbreviations include:
SC (Soreq Cave, Israel: 31°45.35'N, 35°1.35'E)
SVC (Spring Valley Cavern, MN, USA: 43°44'N, 92°24'W)
BS (Bering Sea: 56°42'N, 163°24'W)
**: These samples are also described in Orland (2008: UW MS thesis)

Optical images of the speleothem and otolith samples listed above are included at the end of this document (**page 298**).

Data Repository Index

Large data tables and figures for each chapter are included in the supplementary files available with the online version of this dissertation.

Chapter 1:

DR1.1

Ion microprobe raw and corrected oxygen isotope values, analytical notes, model ages, and fluorescence and banding classifications of analyses from Soreq Cave sample 2-6.

DR1.2

Reflected light and CLFM images of sample 2-6 with ion microprobe analysis spots indicated.

Chapter 2:

DR2.1

Ion microprobe raw and corrected oxygen isotope ratios from 1,223 analyses of sample 2N from Soreq Cave.

DR2.2

Composite maps of the ion microprobe analytical traverse of sample 2N.

DR2.3

SEM images of ion microprobe pits from $\delta^{18}O$ analyses in sample 2N.

Chapter 3:

DR3.1

Ion microprobe raw and corrected oxygen isotope ratios from 231 analyses of sample 5-3b from Soreq Cave.

DR3.2

High-resolution map of trace element and $\delta^{18}O$ ion microprobe analyses in sample 5-3b.

DR3.3

Correlation results (including Pearson's *r*- and p-values, as well as Spearman's ρ-value) of trace element concentrations measured by both ion microprobe and LA-ICP-MS analysis in two regions of sample 5-3b (the inner and outer portions shown in Figure 3.3).

DR3.4

Rainfall amount and $\delta^{18}O$ values measured above Soreq Cave from 1990-2008. Monthly tabulation of rainfall data began in 1995.

DR3.5

SEM images of ion microprobe pits from trace element and $\delta^{18}O$ analyses in sample 5-3b.

Chapter 4:

DR4.1

Fluorescent images of sample 2N showing the tie-lines (yellow) used to generate fluorescence intensity profiles of each sample chip (A-I, M-P).

DR4.2

Fluorescence intensity values measured across each chip.

DR4.3

MATLAB code (.m file) for `peakfinder_window`.

DR4.4

SEM images of ion microprobe pits from trace element analyses in sample 2N.

Chapter 5:

DR5.1

Ion microprobe raw and corrected oxygen isotope ratios from 203 analyses of an otolith "18-O specimen 2" from a yellowfin sole.

DR5.2

Single-crystal XRD results measured in the unroasted and roasted halves of the (right-hand) yellowfin sole otolith that mirrors the (left-hand) specimen investigated in this study.

Supplemental Appendices:

DRSupp.1

Ion microprobe raw and corrected oxygen isotope ratios from 89 analyses of a roasted portion of sample SVC-982 from Spring Valley Caverns, MN.

DRSupp.2

Reflected light and CLFM images from the roasted portion of sample SVC-982 (two chips) with ion microprobe analysis spots indicated.

Introduction

Speleothems are carbonate cave deposits that can preserve a geochemical record of local climate as they grow. In particular, oxygen isotope ratios and trace element concentrations in speleothem calcite provide important proxies of past climate change. Most speleothem paleoclimate studies, however, have been performed at a sampling resolution that corresponds to several decades or centuries, so seasonal or decadal climate signals are averaged and information is lost. This dissertation describes the development of a high-resolution analytical approach to measuring seasonal-resolution climate patterns in speleothem calcite. The high-resolution, high-precision analysis capabilities of the WiscSIMS ion microprobe at the University of Wisconsin-Madison enable us to unlock this information in both pre-historic and modern samples from the Soreq Cave (Israel) natural laboratory.

This dissertation consists of five chapters formatted for journal publication. Each chapter is an independent study that includes various levels of contribution from the co-authors listed on its title page. I am the lead investigator and author on the first four chapters; the fifth chapter is a collaborative project where I am second author. Chapters 1 and 2 are published in peer-reviewed journals, while chapters 3–5 are in various stages of submission for peer-revision. Chapter 1 is my MS thesis, completed at the University of Wisconsin in 2008, which established the methodology used in the remaining chapters. Chapters 2–4 expand on the findings of Chapter 1 by examining a wider suite of geochemical records in cave samples of particular paleoclimate interest. Chapter 5 is a departure from the focus on cave formations, but nonetheless relies on similar analytical techniques; this chapter reports a collaborative study of sub-annual-resolution environmental signals recorded in a fish otolith (ear-stone).

Extensive prior work on Soreq Cave speleothems suggests that rapid climate change events are recorded together with insight into seasonal changes in moisture availability. Chapters 1 and 2 describe a combination of ion microprobe $\delta^{18}O$ analyses with confocal laser fluorescent microscope (CLFM) imaging of annual growth bands in Soreq Cave speleothems that grew between 34 and 1 ka. This high-resolution methodology reveals seasonal climate patterns in the Eastern Mediterranean (EM) region over broad windows of time as well as across rapid climate events such as the termination of the Younger Dryas cold event (11.6 ka).

Chapter 3 reports a similar investigation of a modern Soreq speleothem, which grew from 1990-2008 on a sampling device in the cave. Results show correlations between $\delta^{18}O$ values, Mg concentrations (measured by both ion microprobe and laser ablation inductively coupled mass spectrometry; LA-ICP-MS) and annual rainfall amount measured above the cave. Using the fluorescent bands imaged by CLFM as annual markers, the geochemical data show that Soreq speleothems record seasonal climate as well as extreme wet or dry events. Furthermore, the data serve to validate our interpretation of $\delta^{18}O$ values and fluorescent banding in pre-historic samples. The novel analytical/imaging approach applied in this work will greatly enhance the seasonal resolution of $\delta^{18}O$- and trace element-based paleoclimate records derived from cave deposits.

Chapter 4 returns to the ancient (34–4 ka) sample analyzed in Chapter 2 to explore quantitative characterization of fluorescent annual banding patterns in that speleothem. Similar to studies of sediment cores that assess the grayscale index of digitized core images, this chapter examines the intensity of fluorescence across a radial traverse of the speleothem. The banding information is paired with trace element results from both a continuous LA-ICP-MS transect and seasonal-resolution ion microprobe spots to construct a

unique multi-proxy record of paleoclimate. Geochemical results from the modern speleothem in Chapter 3 are then used to calibrate the resulting climate interpretations.

The analytical methodology developed in this dissertation can be repurposed to examine high-resolution geochemical variability in other types of carbonate samples. The WiscSIMS lab has facilitated studies of nautilus shells, mollusk shells, coral skeletons, foraminifera tests, and fish otolith, which each contain geochemical proxy records of environmental change. Analysis of fish otoliths has been a particular focus as a result of collaboration with colleagues at the National Oceanic and Atmospheric Administration. The final chapter of this dissertation is a collaborative manuscript that, along with associated appendices, records the significant effort spent to develop the method for ion microprobe analysis of fish otoliths. These efforts include the identification and characterization of an appropriate analytical standard for aragonite, implementation of appropriate sample preparation techniques, and the development of guidelines for environmental interpretations.

CHAPTER I

Climate deterioration in the Eastern Mediterranean as revealed by ion microprobe analysis of a speleothem that grew from 2.2 to 0.9 ka in Soreq Cave, Israel

Ian J Orland[1], Miryam Bar-Matthews[2], Noriko T Kita[1], Avner Ayalon[2],

Alan Matthews[3], John W Valley[1]

[1]*Dept. of Geology and Geophysics, University of Wisconsin, 1215 W Dayton St., Madison, WI, 53706, USA*

[2]*Geological Survey of Israel, 30 Malchei Israel St., Jerusalem, 95501, Israel*

[3]*The Institute of Earth Sciences, The Hebrew University, Givat Ram, Jerusalem, 91904, Israel*

Orland I. J., Bar-Matthews M., Kita N. T., Ayalon A., Matthews A., and Valley J. W. (2009) Climate deterioration in the Eastern Mediterranean as revealed by ion microprobe analysis of a speleothem that grew from 2.2 to 0.9 ka in Soreq Cave, Israel. *Quat. Res.* **71**, 27-35.

Abstract

Analysis of oxygen isotope ratios ($\delta^{18}O$) by ion microprobe resolves a sub-annual climate record for the eastern Mediterranean from a Soreq Cave stalagmite that grew between 2.2 and 0.9 ka. In contrast to conventional drill-sampling methods that yield a total variation of 1.0‰ in $\delta^{18}O_{calcite}$ values across our sample, the methods described here reveal up to 2.15‰ variation within single annual growth bands. Values of $\delta^{18}O$ measured by ion microprobe vary in a regular saw-tooth pattern that correlates with annual, graded fluorescent growth banding. Modern records of precipitation and of cave dripwater indicate that variable $\delta^{18}O_{calcite}$ values record regular seasonal differences in $\delta^{18}O_{rainfall}$ modified by mixing in the vadose zone. Large differences in $\delta^{18}O$ values measured across a single band ($\Delta^{18}O_{dark\ calcite\ -\ light\ calcite}$) are interpreted to indicate wetter years, while smaller differences represent drier years. Oxygen isotopes record: (1) month-scale growth increments, (2) changes in $\Delta^{18}O_{dark\ calcite\ -\ light\ calcite}$ that represent seasonality, (3) a systematic, long-term decrease in maximum $\Delta^{18}O_{dark\ calcite\ -\ light\ calcite}$ values, and (4) an overall increase in average $\delta^{18}O_{calcite}$ values through time. These results suggest a drying of regional climate that coincides with the decline of the Roman and Byzantine Empires in the Levant region.

Introduction

Soreq Cave, Israel, contains a record of continuous cave-deposit (speleothem) growth from 185 ka to the present, and these speleothems are the focus of many paleoclimate investigations (Bar-Matthews et al., 1996, 1997, 2003; Ayalon et al., 1999; Matthews et al., 2000; Kolodny et al., 2003; McGarry et al., 2004). Speleothems in Soreq Cave preserve geochemical signals of local climate as they grow. If calcite is precipitated in isotopic equilibrium, oxygen isotopes in speleothem calcite can provide a geochemical measure of past climate change (Hendy, 1971). At decadal to century scales, fluctuations in the $\delta^{18}O$ values preserved in Soreq Cave speleothems reflect changes in rainfall amount, the rainfall source, and cave-air temperature. It follows that on annual or sub-annual time scales $\delta^{18}O_{calcite}$ measurements may reveal records of seasonality as well as paleoclimate. Hence, the goal of this study is to improve the temporal resolution of the Soreq Cave oxygen isotope record by using an ion microprobe to acquire high-spatial resolution $\delta^{18}O$ analyses.

Crucial for this study is the body of previous work that characterizes modern Soreq Cave conditions, local climate patterns, and cave hydrology (Ayalon et al., 1998, 2004; Kaufman et al., 2003). These studies chronicle multiple climatic and geochemical variables, including surface and cave-air temperature, rainfall amount and isotopic composition, dripwater chemistry, and cave atmosphere composition. Significantly, there is a regular pattern of seasonal variation in regional climate; on average, 95% of the annual precipitation falls during the winter "wet-season" between November and April, with January being the wettest month (Fig. 1.1; Ayalon et al., 2004; Mitchell and Jones, 2005). These records also show that the $\delta^{18}O$ values of averaged monthly rainfall are highest at the beginning and end of each wet-season, and lowest during the periods of increased precipitation (Fig. 1.1). Barring substantial mixing of seasonal groundwaters

in this semi-arid environment, it follows that a seasonal signal will be preserved in the $\delta^{18}O_{calcite}$ values of Soreq Cave speleothems.

The oxygen isotope data for previous Soreq Cave paleoclimate studies (Bar-Matthews et al., 1997, 2003) were acquired by acid-digestion of calcite powder drilled from speleothem samples using a 0.5-1.0 mm-diameter dental drill. Each drill-spot represents a finite period of time determined by the growth rate of the speleothem. In Soreq Cave, stalagmite growth rates are generally between ~0.01 and 0.1 mm yr^{-1}. This typically corresponds to a temporal resolution of 10-100 yr for each drill analysis, and where there are discontinuations in growth individual analyses can integrate over a century of calcite precipitation. The current study explores the paleoclimate record by combining imaging with high-spatial resolution and high-precision ion microprobe analysis in order to determine if an oxygen isotope record exists in sub-annual detail. Although high-spatial resolution measurement of $\delta^{18}O_{calcite}$ values has been previously accomplished in speleothems using ion microprobes (Kolodny et al., 2003; Treble et al., 2005, 2007), these studies all report experimental difficulties affecting accuracy and no studies of the pre-instrumental climate record have documented sub-annual growth as a record of seasonality. If such a record is found in Soreq Cave, will it indicate seasonal variations, and will such variations provide a more accurate long-term record of drought, or of annual precipitation?

Modern cave setting and climate

Soreq Cave is situated in the carbonate-dominated western flank of the Judean Hills in central Israel (31°45.35'N, 35°1.35'E; Fig. 1.2). The cave formed in Cenomanian Weradim Formation dolomite and is currently ~400 m above sea level and 40 km inland from the Mediterranean Sea. The cave roof varies in thickness from <10 to >40 m and some 50% of the

hillslope above the cave has a shallow soil cover, 5-40 cm thick. Mediterranean C3-type vegetation predominates (Danin, 1988). Mean annual air temperature above Soreq Cave is 20.3°C. When the cave was discovered in 1968 as a result of quarrying, average measured air temperature was constant (annually) at 20.0°C in the cave and temperatures varied seasonally from 19.5-20.5°C (Asaf, 1975). There is no known pre-1968 opening to the cave.

Rainfall and dripwater patterns

The Eastern Mediterranean Sea is the dominant source of precipitation in central Israel today (Gat and Carmi, 1987; Bar-Matthews et al., 2003; Bar-Matthews and Ayalon, 2004). Ayalon et al. (1998) show that $\delta^{18}O$ and δD values in modern rainwater follow the Mediterranean Meteoric Water Line (MMWL). McGarry et al. (2004) conclude that the eastern Mediterranean has consistently been the moisture source for central Israel for at least the last 140 ka.

As shown in Figure 1.1, there is a seasonal pattern to the amount and $\delta^{18}O$ value of modern rainfall above Soreq Cave (Ayalon et al., 2004). Ayalon et al. (1998) showed that this pattern was reflected in Soreq Cave dripwaters. For their study, Ayalon et al. collected two categories of dripwaters: "slow drip" and "fast drip". Slow dripwaters dripped at rates <2 ml/day, while fast dripwaters – occurring only during the wet-season – dripped at >6 ml/min and started immediately following heavy rainfall events. The sample in this study was located in an area of the cave where fast dripwaters are common during the winter months.

The slow dripwaters are interpreted to approach the "baseline" composition of water in the unsaturated zone above the cave (Ayalon et al., 1998). Kaufman et al. (2003) used tritium observations to find that the oldest age of dripwaters in Soreq Cave is ~30 yr and all dripwaters contain a component of younger water. The two major hydrological components that supply the

slow dripwater reservoir are: (1) rains at the beginning and end of each rainy season that have relatively high $\delta^{18}O$ values and saturate the finer pores in the upper vadose zone, and (2) more intense rainfall, which has relatively low $\delta^{18}O$ values, that occurs during the wet-season. Fast dripwaters are fed by intense wet-season rains, and are more directly connected to the surface by high-permeability and fractured bedrock conduits. Infiltration of low-$\delta^{18}O$, wet-season rains into the vadose zone is incomplete as some rainwater with very low-$\delta^{18}O$ values from heavy storms is lost as runoff. The $\delta^{18}O$ value of infiltration is also increased due to evapotranspiration at the surface.

Between 1991 and 1996, slow dripwaters collected in Soreq Cave show a typical seasonal variation in $\delta^{18}O$ values of ~1‰ (Fig. 1.3). Fast dripwaters had $\delta^{18}O$ values that were ~0.2-0.6‰ lower than concomitant slow dripwaters, ~1.0-1.5‰ higher than the average $\delta^{18}O$ values of intensive rainstorms, and ~0.3-1.0‰ higher than the average of all rainfall events (Ayalon et al., 1998).

Effect of rainfall amount on $\delta^{18}O_{rain}$

The eastern Mediterranean region today shows a strong seasonal contrast of winter and summer weather. Precipitation data collected between 1990 and 2007 from above Soreq Cave indicate that average annual rainfall is between 500 and 600 mm (Table A1.1). In general, 95% of the rainfall in this region occurs during the winter wet season, which extends from November until April. These rainfall records also show that values of $\delta^{18}O$ in precipitation are inversely correlated ($r^2 = 0.70$, $p < 0.0001$) to annual rainfall amount by the equation:

$$\delta^{18}O_{rain}\ (‰, \text{VSMOW}) = -0.0036(\textit{annual ppt, mm}) - 3.9 \qquad (1)$$

Thus, an increase of $\delta^{18}O_{rainfall}$ values by 1‰ corresponds to ~280 mm less rain per year (Ayalon et al., 1998, 2004).

Surface, cave, and dripwater temperatures

The modern local climate at Soreq Cave is representative of eastern Mediterranean semi-arid conditions. Average annual air temperature is 20.3°C; the wet-season average temperature is 14°C, while the dry season average is 26°C. Within Soreq Cave, air temperature varies by a maximum of ~2° (20-22°C). Measurements of dripwater temperature within the cave also vary annually by a maximum of ~2° (18-20°C) (Ayalon et al., 1998). Although special care, such as installing a double door, has been taken to maintain natural cave atmosphere conditions, these measured temperature fluctuations have likely been amplified by the presence of humans since the cave became a Nature Reserve in 1975. Therefore, it is reasonable to assume that 2°C is an upper bound on the annual temperature gradient of both the cave air and dripwater.

Also of note, Ayalon et al. (1998) observed a weak correlation ($r^2 = 0.42$, $p < 0.0001$) between surface temperature and the $\delta^{18}O$ values of individual rain events in the vicinity of Soreq Cave. This relationship, which shows that increased surface temperatures correspond with increased $\delta^{18}O_{rainfall}$ values, reflects the seasonal variability shown in Figure 1.1.

With regard to the observed $\delta^{18}O_{rain}$-$T_{surface}$ relationship, it is important to evaluate the extent to which temperature, and specifically long-term temperature change, plays a role in controlling the isotope values measured in our speleothem sample. The empirical relationship of $\delta^{18}O_{rain}$ values and $T_{surface}$, which has a slope of ~1‰/2°C (see Fig. 4 in Ayalon et al., 1998), suggests a significant increase in average $T_{surface}$ is needed to affect a large change in annually averaged $\delta^{18}O_{dripwater}$ values. Moreover, the temperature dependence of calcite-water equilibrium

would work to diminish such an effect; a 2°C increase in cave and dripwater temperatures from 18 to 20°C will reduce the equilibrium $\delta^{18}O_{calcite}$ value by 0.45‰ (O'Neil et al., 1969). The combination of these two effects means that a hypothetical increase of 2°C in average $T_{surface}$ might only increase the $\delta^{18}O_{calcite}$ value of speleothem growth by ~0.5‰. McGarry et al. (2004) calculated dripwater temperatures from $\delta^{18}O$ values of fluid inclusions in Soreq Cave speleothems and concluded that temperatures are constant over the last 1.3 ka. Although we have no direct, long-term record of surface temperatures in this region, it seems unlikely that average annual temperatures would have increased by 2°C (or more) on a centennial time scale in the late Holocene. Thus, for this study of a 2.2-ky-old speleothem we attribute changes in $\delta^{18}O_{calcite}$ values to the effect of rainfall amount.

Conditions of isotopic equilibrium

In order for $\delta^{18}O_{calcite}$ values of speleothems to be a reliable record of paleoprecipitation, the calcite needs to form under conditions of isotopic equilibrium in the cave. For this study, there are two processes that might confound interpretation of $\delta^{18}O_{calcite}$: (1) evaporation of groundwater in the vadose zone, and (2) rapid degassing of CO_2 from dripwaters. First, the evaporation of vadose zone water has been evaluated at Soreq Cave by analysis of oxygen and hydrogen isotopes (Ayalon et al., 1998). Significant vadose zone evaporation would increase both D/H and $^{18}O/^{16}O$ in groundwater, and would shift the dripwater compositions away from and below the MMWL. Values of $\delta^{18}O$ and δD from dripwater samples throughout the cave, however, plot along the MMWL indicating no significant (>1‰ in $\delta^{18}O$) evaporation. These results verify that the annual fluctuation of $\delta^{18}O_{dripwater}$ values in Soreq Cave is primarily due to the seasonal mixing of rainwater and water in the vadose seepage zone.

Second, some workers suggest that rapid outgassing of CO_2 from dripwater – a process that can cause non-equilibrium, kinetic fractionation of oxygen (and carbon) isotopes – is an important, and often overlooked, element of speleothem formation (Mickler et al., 2006). One way to test for disequilibrium processes is by comparing contemporaneous $\delta^{18}O$ records of multiple speleothems from the same cave. Dorale et al. (2002) called this the "replication test" and concluded that a positive correlation between such records strongly suggested that vadose zone and kinetic disequilibrium processes were not significant in that cave. Dorale et al. argued that by passing a replication test, a speleothem $\delta^{18}O$ record could be considered a primary environmental record. For this study, the inference of equilibrium conditions is based on the consistency of the composite $\delta^{18}O$ record of Soreq Cave speleothems (Bar-Matthews et al., 1997) and their correlation with foraminiferal $\delta^{18}O$ records from the adjacent Eastern Mediterranean Sea (Bar-Matthews et al., 2003).

Materials and methods

U-Th dating

This study examines Soreq Cave speleothem sample 2-6, a drip-formed stalagmite that is composed of low-magnesium calcite. The portion of the sample we examine here was cut perpendicular to the growth axis and has a radius of 5.5 cm. Eight U-series ages, obtained from MC-ICP-MS analyses at the Geological Survey of Israel (GSI), range from 2183±170 to 1025±110 yr (Table 1.1). Linear extrapolation of the average observed growth rate to the core and outer rim of the sample indicates that the speleothem grew from ~2.2-0.9 ka.

For each of the eight age measurements ~0.3 g of calcite powder was dissolved in 7 N HNO_3 and a ^{236}U-^{229}Th Harwell spike was added prior to U and Th purification. Each sample

was loaded into mini-columns that contained 2 ml Bio-Rad AG 1x8 200-400 mesh resin. The U was eluted by 1 N HBr and Th with 6 N HCl. Afterwards, the U and Th solutions were dried and redissolved in 2 ml and 5 ml of 0.1 N HNO_3, respectively.

Measurement of Th and U isotope ratios was performed at the GSI using a Nu Instruments Ltd MC-ICP-MS equipped with 12 Faraday counters and 3 ion counters. The sample was loaded into the MC-ICP-MS through an Aridus® micro-concentric desolvating nebulizer sample introduction system. Instrumental mass bias was amended using an exponential equation by correcting the measured $^{238}U/^{235}U$ ratio to the known natural value. Calibration of ion-counters relative to the Faraday cups was attained by cycling measurements through different collector configurations. The reproducibility of each measured $^{234}U/^{238}U$ ratio was 0.11% (2σ) (Vaks et al., 2007).

Ages obtained from the U/Th ratios measured in Soreq Cave speleothems are corrected for detrital ^{232}Th (Table 1.1); the correction is based on an isochron method and is determined specifically for Soreq Cave speleothems (Kaufman et al., 1998). Kaufman et al. determine that the detrital components within Soreq Cave speleothems have a $^{232}Th/^{238}U$ ratio of ~1.8.

Sample preparation, confocal laser fluorescent microscopy

After analysis for geochronology, a radial portion of sample 2-6 was cut into five ~1 cm chips and mounted, along with 4-6 grains of UWC-3 (calcite standard; $\delta^{18}O$ = 12.49‰, VSMOW; Kozdon et al., 2008), in three polished 1-inch-diameter epoxy rounds. At the University of Wisconsin-Madison (UW-Madison), we employed a number of analytical methods including secondary electron microscopy, backscatter electron microscopy, electron backscatter

diffraction, and optical microscopy to determine that the sample was free of aragonite and any detrital material that might interfere with high-spatial resolution analysis.

Confocal laser fluorescent microscopy (CLFM) was subsequently completed at the Keck Bioimaging Laboratory at UW-Madison using a Bio-Rad MRC-1024 scanning confocal microscope operated with a 40 mW, 488 nm laser line. Images of speleothem fluorescence were collected using an emission filter that allows light with wavelengths between 505 and 539 nm (visible, green). Linear image adjustment was applied in order to increase the contrast and brightness of published images.

Ion microprobe analysis of $\delta^{18}O$

Ion microprobe oxygen isotope data were acquired at UW-Madison using a CAMECA ims-1280 large radius multicollector ion microprobe. A total of 719 oxygen analyses were made from ~10 μm-diameter spots along a 5.5 cm traverse of sample 2-6. Spot sizes varied from 7-12 μm in diameter between the different analysis sessions depending on the primary beam condition. Throughout the experiment, 4-5 consecutive measurements of UWC-3 calcite standard were performed before and after every set of 10-15 sample analyses (recorded in the data repository, DR1.1). The ion microprobe instrumental mass fractionation factor ($IMF = \delta^{18}O_{measured} - \delta^{18}O_{VSMOW}$) in calcite is calculated from each bracketing set of eight or more measurements of UWC-3 and was typically -3.22‰. The precision of a set of bracketing standard analyses, on average 0.34‰ (2 standard deviation, s.d.; DR1.1), is used to estimate the spot-to-spot reproducibility of a block of sample analyses; this value of reproducibility is the best estimate of the analytical uncertainty of individual sample analyses.

For each oxygen isotope analysis, we utilized a ~2.5 nA primary beam of $^{133}Cs^{+}$ ions,

focused to ~10 μm in diameter at the sample surface, to sputter a 1 μm-deep pit in calcite. Charging of the sample surface was compensated by (1) an electron flood gun, and (2) a gold coat on the epoxy mount, which was applied following cleaning in deionized water and ethyl alcohol. Each epoxy round was prepared such that all analytical spots were within 5 mm of the center of the mount and the UWC-3 standard. For the procedures used in the UW-Madison lab, this setup prevents instrument bias related to sample position such as reported by Treble et al. (2007).

A typical secondary $^{16}O^-$ ion intensity was $3x10^9$ cps. The mass resolving power was 2,200 and $^{18}O^-$ and $^{16}O^-$ ions were simultaneously collected by two Faraday Cup detectors in the multicollection system. Individual analyses took about 4 min each, which included pre-sputtering to burn through the Au-coat (10 s), followed by automatic recentering of secondary ions in the field aperture (~60 s), and finally, integration of oxygen ions for isotopic measurements (80 s; 20 cycles of 4 s integrations). More detailed analytical conditions are described by previous workers (Kelly et al., 2007; Kita et al., 2007; Page et al., 2007).

Results

Fluorescent banding

Confocal laser fluorescent microscopy (CLFM) of sample 2-6 reveals concentric banding (<1 μm to >100 μm in width) that occurs in a distinct cyclical pattern; the fluorescence of each band progresses gradually with time from “light” to “dark” with a sharp boundary to the next light fluorescent zone occurring at the end of each darkening gradient (Fig. 1.4). This sequence of fluorescence is observed across the entirety of the prepared sample. We use the terms light and dark to refer to fluorescent and non-fluorescent material, respectively, and not to isotope

ratio, for the remainder of this manuscript.

As shown by Figures 1.4 and 1.5 the width and gradient of the fluorescent pattern is different from one band to the next. Furthermore, there are a number of unconformities that truncate the bladed tips of older crystal growth; these truncations generally occur as straight bands of light calcite cutting across the dark portion of a bladed growth band. Truncations always "face" in the same direction (Fig. 1.5A). We count 182 bands thicker than 10 μm, and a further ~176 thinner than 10μm, across this sample (growth spans ~1.3 ka). There are also "island" features where a single fluorescent band forms a continuous loop <200 μm in diameter (Fig. 1.5B); islands, which are uncommon in the radial section that we imaged, are probably the result of a calcite crystal growing with a different orientation on the outer surface of the speleothem.

$\delta^{18}O$ analyses

Variations of $\delta^{18}O$. The investigation of ion microprobe oxygen isotope compositions from sample 2-6 (DR1.1 and DR1.2) reveals a strong correlation between $\delta^{18}O$ values and the repeated pattern of light/dark fluorescent banding imaged by CLFM. Within single couplets that contain between 2 and 6 analyses we observe consistently smooth increases of $\delta^{18}O$ values by as much as 2.15‰ from the light to the dark calcite (older to younger growth). Figure 1.4 illustrates this distinctive saw-tooth pattern through several cycles. Similar isotopic sequences are correlated to CLFM imaging throughout the sample.

On a broader scale, the 6-point running average of $\delta^{18}O_{\text{light calcite}}$ values (solid line in Fig. 1.6A) increases by ~1‰ between the oldest and youngest calcite in sample 2-6. The sharpest increase in this running average occurs ca. 1.9 ka. We note that conventional drill-sample

analysis across the entire sample 2-6 reveals a total variation in $\delta^{18}O_{calcite}$ values of 1.0‰; again, with the ion microprobe we observe variation of up to 2.15‰ in $\delta^{18}O$ values within a single growth band.

Variations of $\Delta^{18}O_{dark\text{-}light}$. The difference in $\delta^{18}O$ values, $\Delta^{18}O_{dark\text{-}light}$, between light and dark calcite of the same couplet (i.e., $\delta^{18}O_{dark\ calcite} - \delta^{18}O_{light\ calcite}$) varies across the sample. Furthermore, the maximum values of $\Delta^{18}O_{dark\text{-}light}$ decrease from >2.1‰ to <1.0‰ between ~2.0 and 1.3 ka. This decrease in the isotopic contrast of individual growth bands is coincident with the increase in the running average of $\delta^{18}O_{light\ calcite}$ values (Fig. 1.6). Out of 75 bands analyzed across the sample no dark calcite has a lower $\delta^{18}O$ value than its coupled light calcite (Fig. 1.6A).

Discussion

Annual fluorescent banding

There is contention surrounding the identification and utility of speleothem banding, annual or otherwise, in recent literature (Polyak and Asmerom, 2001; Betancourt et al., 2002; Baker and Genty, 2003; Asmerom and Polyak, 2004; Tan et al., 2006). The study of speleothem banding is still under development.

As described above, we used CLFM to detect and examine the regular, fluorescent banding pattern. The combination of excitation and emission wavelengths (488 nm and 505-539 nm, respectively) employed to generate the fluorescence observed in sample 2-6 suggests that organic acids were present in dripwaters during calcite precipitation (Senesi et al., 1991; McGarry and Baker, 2000; Shopov, 2004). Tan et al. (2006) pointed to other studies in English and Chinese caves (Baker et al., 1993, 1999; Ban et al., 2005) that attribute similar patterns of fluorescence and banding caves to seasonal, climate-driven changes in the input of organic

substances into cave dripwaters. Tan et al. conclude that climate regimes with distinct wet/dry seasons may produce an annual flush of organic acids from the soil column that is recorded in the light fluorescent growth banding of underlying speleothems; such a pattern, if observed in an appropriate climatic setting, likely represents annual banding.

Soreq Cave is ideally situated to record annual fluorescent bands. Not only are there distinct wet and dry seasons, but also, the signal of annual climate variation is observed in the $\delta^{18}O$ values of dripwaters in the cave (Ayalon et al., 1998). Since groundwater mixing does not homogenize $\delta^{18}O_{dripwater}$ values in Soreq Cave, it follows that the signal of an annual flush of organic acids would be preserved. Thus, we suggest that in sample 2-6, the sharp onset of a fluorescent band is caused by increased rainfall at the beginning of the wet-season. During the dry season, we hypothesize that decomposition of plant matter supplies organic acid to the upper soil column. Then, as rainfall returns to the region, organic acids are again flushed into the cave.

We should note that neither the intensity nor the persistence of the fluorescent signal within a band should be used as an indicator of a sub-annual timescale. Rather, we interpret these bands as delineating only the beginning/end of each annual wet/dry season cycle. The correlation of observed patterns of growth banding with sub-annual isotope measurements provides a test of the interpretation that the fluorescent bands in our sample record an annual cycle.

It should also be discussed that the total number of fluorescent bands counted (~358) is less than the number of years indicated by U-series geochronology (~1300). The record of some years is undoubtedly removed by truncations (Fig. 1.5A) or by periods of non-deposition. It is further uncertain whether some of the subtle changes in fluorescence represent discrete storm events or single years.

Oxygen isotope patterns and annual banding

The pattern of $\delta^{18}O$ variation described above and illustrated in Figure 1.4 bears a strong resemblance to the modern seasonal variation of $\delta^{18}O_{dripwater}$ values in Soreq Cave (Fig. 1.3) (Ayalon et al., 1998, 2004). Using this seasonal dripwater variation as a guide, we interpret the correlated patterns of $\delta^{18}O_{calcite}$ values and fluorescent banding as the annual cycle of wet and dry seasons prevalent in the region. The $\delta^{18}O$ values of light fluorescent portions reflect the low $\delta^{18}O$ values of mid-winter, wet-season rainfall. The gradual increase of $\delta^{18}O$ values across each band reflects an increased proportion of high-$\delta^{18}O$ vadose zone water, which we refer to here as "baseline" dripwater, contributing to dripwaters during warmer, drier months. Just as with the fluorescent banding, a sharp boundary occurs at the end of each gradient of increasing $\delta^{18}O$ values; the beginning of the following year's wet-season, also marked by the flush of fluorescent organics, coincides with an abrupt drop of $\delta^{18}O_{calcite}$ values.

The $\delta^{18}O$ value of calcite at the beginning and end of each annual band is representative of dripwater from discrete periods of the seasonal cycle, the beginning of the winter wet-season in November and spring/summer vadose zone water, respectively. Thus, $\Delta^{18}O_{dark\text{-}light}$ is a measure of "seasonality" and is obtained by analyzing the light and dark extremities of each resolvable band.

Prolonged wet periods are recorded by low $\delta^{18}O$ values, as seen ca. 2.0 ka in Figure 1.6A, and correlate with larger values of $\Delta^{18}O_{dark\text{-}light}$ in Figure 1.6B. Conversely, relatively dry periods, marked by higher $\delta^{18}O$ values after 1.9 ka, are characterized by decreasing maximum $\Delta^{18}O_{dark\text{-}light}$ values. Hence, the climatic transition that is inferred from the shift in $\delta^{18}O$ values is reflected in our measure of seasonality as the maximum value of $\Delta^{18}O_{dark\text{-}light}$ dropped from >2.1‰ to <1.0‰

between ~2.0 and 1.3 ka.

Environmental interpretation of sub-annual isotope record from sample 2-6

Given our understanding of the modern hydrologic system above Soreq Cave, we propose a model that explains the empirical correlation between decreasing $\Delta^{18}O_{dark\text{-}light}$ values, the general drying of climate, and an increase in seasonal contrast (i.e. drier summers or shorter wet seasons). In our model, $\Delta^{18}O_{dark\text{-}light}$ values are driven by the proportionally larger contribution of wet-season rains to the low $\delta^{18}O$ values of light calcite. Figure 1.7 provides a test of this model; it illustrates that the $\delta^{18}O$ values of dark calcite, representative of the baseline vadose zone water, remain generally constant across the full range of $\Delta^{18}O_{dark\text{-}light}$ values observed in the sample. Although Figure 1.6A shows that the $\delta^{18}O$ values of dark calcite do shift across the sample, this change may reflect a response of the baseline vadose zone water to varying climate. Thus, the isotope composition of baseline vadose zone water remains relatively unchanged and $\Delta^{18}O_{dark\text{-}light}$ is determined by the amount that wet-season rains (that form light fluorescent calcite) depress the $\delta^{18}O$ value of groundwater supplied to the cave.

The model proposed above is consistent with the suggestion of Ayalon et al. (1998) that much of the precipitation at the beginning and end of each wet-season must be sequestered in the porous upper vadose zone. By not immediately incorporating these short-lived, high-$\delta^{18}O$-value rains directly into cave dripwaters, the sinusoidal pattern of $\delta^{18}O_{rain}$ variance (Fig. 1.1) is truncated into the saw-tooth pattern of $\delta^{18}O_{calcite}$ values observed in Figure 1.4. Similarly, Ayalon et al. (1998) observed that drip rates throughout the cave slow significantly during dry months; if too little water remains in the vadose zone to allow speleothems to grow during dry summers, the

$\Delta^{18}O_{dark\text{-}light}$ signal would be correspondingly smaller.

Implications of a high-resolution speleothem record

The development of sub-annual resolution isotopic records in speleothems using *in situ* analysis by ion microprobe presents a number of avenues for additional paleoclimate and geochemical interpretations. First, by analyzing only the wet-season calcite – the light fluorescent portion of each band – it is possible to more accurately track significant changes in $\delta^{18}O_{calcite}$. As shown in Figure 1.7, the $\delta^{18}O$ values of light calcite in sample 2-6 are more representative of changing seasonality than the relatively constant $\delta^{18}O$ values of dark calcite. Furthermore, if the light portion of each growth band represents wet-season rainfall with a lesser component of baseline vadose zone water, then mixing of >30-year-old (Ayalon et al., 1998; Kaufman et al., 2003) vadose zone water is avoided.

Second, by calculating $\delta^{18}O_{groundwater}$ values from the measured values of $\delta^{18}O$ in wet-season calcite (O'Neil et al., 1969), we can estimate paleorainfall amounts based on modern empirical data. Past studies (Ayalon et al., 1998; Bar-Matthews and Ayalon, 2004; Ayalon et al., 2004) show that at Soreq Cave: (1) $\delta^{18}O_{average\ fast\ dripwater} - \delta^{18}O_{average\ rain} = \sim 1‰$, and (2) there is a linear correlation between annual precipitation, in mm, and annual average $\delta^{18}O_{rain}$ given by Eq. (1). Using these relations, we suggest that the measured variation of $\delta^{18}O_{calcite}$ between 1.9 and 1.3 ka represents a decrease in average annual precipitation by as much as 300-400 mm (Fig. 1.6C). The record of paleorainfall in Figure 1.6C contrasts with previous studies from other Soreq Cave speleothems that could not resolve sub-annual variation (Bar-Matthews et al., 1998; Bar-Matthews and Ayalon, 2004). The calculated changes in paleorainfall estimates of earlier studies were smoothed because their isotope sampling methods mixed together both winter and

summer calcite deposition from multiple years. With the ion microprobe we are able to measure $\delta^{18}O$ values of calcite deposited during single months or weeks of the wet-season, thus resolving $\delta^{18}O$ values that are representative of the dominant rainwater compositions (light fluorescence, winter, fast dripwater) versus $\delta^{18}O$ that is influenced by vadose zone waters (dark fluorescence, spring/summer, slow dripwater).

It should be emphasized that these estimates of paleorainfall are based on three assumptions: (1) that the amount vs. $\delta^{18}O_{rain}$ relationship held over the time period during which the sample 2-6 grew, (2) that average annual temperature change was negligible across this time period, and 3) that average fast dripwater, represented by light fluorescent calcite, is consistently offset by 1‰ from the average $\delta^{18}O$ value of average annual rainfall. We think that all three assumptions are reasonable. With regard to the first assumption, the moisture source for this region has been the Mediterranean Sea for at least the last 140 ka (McGarry et al., 2004). Furthermore, the $\delta^{18}O$ value of the Mediterranean has been almost constant over the past 2.0 ka (Schilman et al., 2001). Thus, it is reasonable to think that the amount vs. $\delta^{18}O_{rain}$ relationship (Eq. (1)) held for the time interval represented by sample 2-6. The second assumption, that average annual temperature was constant across the period of growth, is supported by cave air temperatures calculated from fluid inclusions (McGarry et al., 2004) and sea surface temperatures of the Eastern Mediterranean Sea (Emeis et al., 1998, 2000). The third assumption, that $\delta^{18}O_{average\ fast\ dripwater} - \delta^{18}O_{average\ rain} = \sim 1‰$, is based on empirical observations made by Bar-Matthews and Ayalon (2004).

The third implication of high-resolution isotopic studies of speleothems is the possibility for better understanding equilibrium and kinetic deposition processes. It is clear from the irregular banding pattern and the range of $\delta^{18}O$ values measured within single growth bands of

sample 2-6 that one of the conventional tests of equilibrium deposition, the Hendy (1971) test, would return erroneous results with dental drill sampling. For sample 2-6, and probably many others, such a test would have to be carried out with an ion microprobe targeted with detailed imaging to ensure that the required isotope measurements do not represent a bulk average of multiple growth zones. Although we did not examine carbon isotopes for this report, an in-depth study of $\delta^{13}C$ values in sample 2-6 may reveal information about overlying vegetation, cave ventilation, and the process of equilibrium deposition.

Climate deterioration from 1.9-1.3 ka (AD 100-700)

The discussion above presents new data that suggests decreasing rainfall and thus climate deterioration from AD 100-700 in the Levant region. Other important independent evidence for changes in rainfall comes from lake levels in the Dead Sea (Neev and Emery, 1995). Enzel et al. (2003) established a quantitative link between modern precipitation and Dead Sea levels and confirmed the direct influence of regional climate on the hydrology of the Dead Sea basin. Radiocarbon ages of organic remains in the adjacent Mount Sedom salt caves (Frumkin et al., 1991, 2001) and exposed sedimentary sequences (Bookman et al., 2004) suggest that Dead Sea levels dropped by at least 10-15 m between ~100 BC and AD 700 (Fig. 1.6D). These studies agree with the oxygen isotope record presented here that indicates desiccation of regional climate from AD 100-700.

Finally, we note that the changes we detect in seasonality from Soreq Cave correspond to a time period where historical records exist. Issar and Zohar (2004) outlined the history of the Roman and Byzantine Empires in the eastern Mediterranean, and concluded that climate change contributed to the decline of their rule in the Levant. Beginning in the 3rd century AD, the

coupled effects of attacks on the eastern and northern borders of the Roman Empire, anarchy in Rome, and the suggested climate change weakened the economic system. Eventually, Byzantine rule in the Levant succumbed to the rapidly growing Islamic empire at the Battle of Yarmouk in AD 636, perhaps pressured by the inability of the agricultural economy to fully adjust to the drier climate (Issar and Zohar, 2004).

Our data support the hypothesis that climate change played a role in the decline of Roman rule in the Levant by showing a gradual decrease in annual rainfall punctuated by steep drops at AD ~100 and 400 (Fig. 1.6C). Furthermore, the decline in $\Delta^{18}O_{dark\text{-}light}$ values (Fig. 1.6B) suggests that there were always dry years, but the number of wet periods that might have aided high crop yields decreased.

Conclusions

The combination of laser confocal microscopy with high-resolution and high-precision oxygen isotope analysis of a Soreq Cave speleothem reveals a sub-annual record of paleoclimate in the eastern Mediterranean region. High-precision ion microprobe analyses (average 2 s.d. = ±0.34‰, ~10 μm-diameter spot) show regular fluctuations in $\delta^{18}O$ values that correlate to fluorescent banding; this pattern is interpreted to be an annual record of seasonal variation in rainfall. This is the first report of seasonality in speleothems dating from before the instrumental record of climate. Using these data, we document changes in both seasonality and annual precipitation in the region from 2.2-0.9 ka. Our estimates of steep drops in precipitation coincide with both a drop of water levels in the Dead Sea and the decline of Roman rule in this region. The combination of confocal laser fluorescent imaging and high-resolution ion microprobe oxygen isotope analysis is a viable method for evaluating paleoclimate at sub-annual resolution

in Soreq Cave and should prove useful in other cave localities.

Acknowledgments

We thank J. Quade and two anonymous reviewers for comments that greatly improved this manuscript; T. Ushikubo and B. Fu for help with ion microprobe analysis; B. Hess and J. Kern for assistance with sample preparation; M. Spicuzza, Z. Liu, A. Carlson, and J. Kutzbach for helpful discussions; L. Rodenkirch for guidance at the Keck Bioimaging Lab at UW-Madison; J. Fournelle for help with the SEM; and the Israel Nature and Parks Authority for access to Soreq Cave. Funding came from NSF (EAR04-40343), DOE (93ER14389), Israel Science Foundation (grant 910/05), the Comer Science and Education Foundation, as well as Sigma Xi and the Department of Geology and Geophysics at UW-Madison. Wisc-SIMS is partly supported by the NSF (EAR03-19230, EAR07-44079).

References

Asaf, M., 1975. Karstic features in Soreq Cave. Unpublished MSc thesis, Tel Aviv University, 66 p.

Asmerom Y., and Polyak V. J. (2004) Comment on "A test of annual resolution in stalagmites using tree rings." *Quaternary Research* **61**, 119-121.

Ayalon, A., Bar-Matthews, M., and Sass, E., 1998. Rainfall-recharge relationships within a karstic terrain in the Eastern Mediterranean semi-arid region, Israel: $\delta^{18}O$ and δD characteristics. Journal of Hydrology 207, 18-31.

Ayalon, A., Bar-Matthews, M., and Kaufman, A., 1999. Petrography, strontium, barium and uranium concentrations, and strontium and uranium isotope ratios in speleothems as palaeoclimatic proxies: Soreq Cave, Israel. The Holocene 9, 715-722.

Ayalon, A., Bar-Matthews, M., and Schilman, B., 2004. Rainfall isotopic characteristics at various sites in Israel and the relationships with unsaturated zone water. In: Geological Survey of Israel Reports, GSI/16/04, The Ministry of National Infrastructures, Jerusalem.

Baker, A., Smart, P. L., Edwards, R. L., and Richards, D. A., 1993. Annual growth banding in a cave stalagmite. Nature 364, 518-520.

Baker, A., Proctor, C. J., and Barnes, W. L., 1999. Variations in stalagmite luminescence laminae structure at Poole's Cavern, England, AD 1910 to AD 1996: Calibration of a paleoprecipitation proxy. The Holocene 9, 683-688.

Baker, A., and Genty, D., 2003. Comment on "A test of annual resolution in stalagmites using tree rings." Quaternary Research 59, 476-478.

Ban, F., Pan, G., and Wang, X., 2005. Timing and possible mechanism of organic substance formation in stalagmite laminae from Beijing Shihua Cave. Quaternary Sciences 25, 265-268.

Bar-Matthews, M., Ayalon, A., Matthews, A., Sass, E., and Halicz, L., 1996. Carbon and oxygen isotope study of the active water-carbonate system in a karstic Mediterranean cave: Implications for paleoclimate research in semiarid regions. Geochimica et Cosmochimica Acta 60, 337-347.

Bar-Matthews, M., Ayalon, A., and Kaufman, A., 1997. Late Quaternary paleoclimate in the Eastern Mediterranean region from stable isotope analysis of speleothems at Soreq Cave, Israel. Quaternary Research 47, 155-168.

Bar-Matthews, M., Ayalon, A., and Kaufman, A., 1998. Middle to Late Holocene (6500 years period) paleoclimate in the Eastern Mediterranean region from stable isotopic composition of speleothems from Soreq Cave, Israel. In: Issar, A. S., and Brown, N. (Eds.), Water, Environment and Society in times of Climate Change. Kluwer Academic Publishers, Boston, pp. 203-214.

Bar-Matthews, M., Ayalon, A., Gilmour, M., Matthews, A., and Hawkesworth, C. J., 2003. Sea-land oxygen isotopic relationships from planktonic foraminifera and speleothems in the Eastern Mediterranean region and their implication for paleorainfall during interglacial intervals. Geochimica et Cosmochimica Acta 67, 3181-3199.

Bar-Matthews, M., and Ayalon, A., 2004. Speleothems as paleoclimate indicators, a case study from Soreq Cave located in the eastern Mediterranean region, Israel. In: Battarbee, R. W., Gasse, F., and Stickley, C. E. (Eds.), Past Climate Variability through Europe and Africa. Springer, Dordrecht, The Netherlands, pp. 363-391.

Betancourt, J. L., Grissino-Mayer, H. D., Salzer, M. W., and Swetnam, T. W., 2002. A test of "annual resolution" in stalagmites using tree rings. Quaternary Research 58, 197-199.

Bookman, R., Enzel, Y., Agnon, A., and Stein, M., 2004. Late Holocene lake-levels of the Dead Sea. Bulletin of the Geological Society of America 116, 555-571.

Danin, A., 1988. Flora and vegetation of Israel and adjacent areas. In: Tom-Tov, Y., and Tchernov, E. (Eds.), The Zoogeography of Israel. Dr. W. Junk Publishers, Dordrecht, The Netherlands.

Dorale, J. A., Edwards, R. L., and Onac, B. F., 2002. Stable isotopes as environmental indicators in speleothems. In: Daoxian, Y., and Cheng, Z. (Eds.), Karst processes and the carbon cycle: Final report of IGCP379. Geologic Publishing House, Beijing, China, pp. 107-120.

Emeis, K. C., Schulz, H. M., Struck, U., Sakamoto, T., Doose, H., Erlenkeuser, H., Howell, M., Kroon, D., and Paterne, M., 1998. Stable isotope and alkenone temperature records of sapropels from sites 964 and 967: Constraining the physical environment of sapropel formation in the eastern Mediterranean Sea. In: Robertson, A. H. F., Emeis, K. C., Richter, C., and Camerlenghi, A. (Eds.), Proceedings of the Ocean Drilling Program, Scientific Results 160. Ocean Drilling Program, College Station, pp. 309-331.

Emeis, K. C., Struck, U., Schulz, H. M., Rosenberg, R., Bernasconi, S., Erlenkeuser, H., Sakamoto, T., and Martinez-Ruiz, F., 2000. Temperature and salinity variations of Mediterranean Sea surface waters over the last 16,000 years from records of planktonic stable oxygen isotopes and alkenone unsaturation ratios. Palaeogeography, Palaeoclimatology, Palaeoecology 158, 259-280.

Enzel, Y., Bookman, R., Sharon, D., Gvirtzman, H., Dayan, U., Baruch, Z., and Stein, M., 2003. Late Holocene climates of the Near East deduced from Dead Sea level variations and modern regional winter rainfall. Quaternary Research 60, 263-273.

Frumkin, A., Magaritz, M., Carmi, I., and Zak, I., 1991. The Holocene climatic record of the salt caves of Mount Sedom, Israel. The Holocene 1, 191-200.

Frumkin, A., Kadan, G., Enzel, Y., and Eyal, Y., 2001. Radiocarbon chronology of the Holocene Dead Sea: Attempting a regional correlation. Radiocarbon 43, 1179-1189.

Gat, J. R., and Carmi, I., 1987. Effect of climate changes on the precipitation and isotopic composition of water in a climate transition zone: Case of the Eastern Mediterranean Sea area. International Association of Hydrological Sciences Publication 168, 513-523.

Hendy, C. H., 1971. The isotopic geochemistry of speleothems – I. The calculation of the effects of different modes of formation on the isotopic composition of speleothems and their applicability as paleoclimate indicators. Geochimica et Cosmochimica Acta 35, 801-824.

Issar, A. S., and Zohar, M., 2004. Climate change: Environment and civilization in the Middle East. Springer-Verlag, Berlin.

Kaufman, A., Wasserburg, G. J., Porcelli, D., Bar-Matthews, M., Ayalon, A., and Halicz, L., 1998. U-Th isotope systematics from the Soreq Cave, Israel and climatic correlations. Earth and Planetary Science Letters 156, 141-155.

Kaufman, A., Bar-Matthews, M., Ayalon, A., and Carmi, I., 2003. The vadose flow above Soreq Cave, Israel: A tritium study of the cave waters. Journal of Hydrology 273, 155-163.

Kelly, J. L., Fu, B., Kita, N. T., and Valley, J. W., 2007. Optically continuous silcrete quartz cements of the St. Peter Sandstone: High precision oxygen isotope analysis by ion microprobe. Geochimica et Cosmochimica Acta 71, 3812-3832.

Kita, N. T., Ushikubo, T., Fu, B., Spicuzza, M. J., and Valley, J. W., 2007. Analytical developments on oxygen three isotope analyses using a new generation ion microprobe IMS-1280. Lunar Planetary Science Conference Abstracts 38, #1981.

Kolodny, Y., Bar-Matthews, M., Ayalon, A., and McKeegan, K. D., 2003. A high spatial resolution $\delta^{18}O$ profile of a speleothem using an ion-microprobe. Chemical Geology 197, 21–28.

Kozdon, R., Ushikubo, T., Kita, N. T., Spicuzza, M. J., and Valley, J. W., 2008. Intratest oxygen isotope variability in planktonic foraminifera: Real vs. apparent vital effects by ion microprobe. Chemical Geology 258, 327-337.

Matthews, A., Ayalon, A., and Bar-Matthews, M., 2000. D/H ratios of fluid inclusions of Soreq cave Israel speleothems as a guide to the Eastern Mediterranean Meteoric Line relationships in the last 120 ky. Chemical Geology 166, 183-191.

McGarry, S. F., and Baker, A., 2000. Organic acid fluorescence: Applications to speleothem palaeoenvironmental reconstruction. Quaternary Science Reviews 19, 1087-1101.

McGarry, S., Bar-Matthews, M., Matthews, A., Vaks, A., Schilman, B., and Ayalon, A., 2004. Constraints on hydrological and paleotemperature variations in the Eastern Mediterranean region in the last 140ka given by the δD values of speleothem fluid inclusions. Quaternary Science Reviews 23, 919-934.

Mickler, P. J., Stern, L. A., and Banner, J. A., 2006. Large kinetic isotope effects in modern speleothems. Geological Society of America Bulletin 118, 65-81.

Mitchell, T. D., and Jones, P. D., 2005. An improved method of constructing a database of monthly climate observations and associated high-resolution grids. International Journal of Climatology 25, 693-712.

Neev, D., and Emery, K. O., 1995. The destruction of Sodom, Gomorrah, and Jericho: Geological, climatological, and archaeological background. Oxford University Press, New York.

O'Neil, J. R., Clayton, R. N., and Mayeda, T. K., 1969. Oxygen fractionation in divalent metal carbonates. Journal of Chemical Physics 51, 5547–5558.

Page, F. Z., Ushikubo, T., Kita, N. T., Riciputi, L. R., and Valley, J. W., 2007. High-precision oxygen isotope analysis of picogram samples reveals 2-μm gradients and slow diffusion in zircon. American Mineralogist 92, 1772-1775.

Polyak, V. J., and Asmerom, Y., 2001. Late Holocene climate and cultural changes in the southwest United States. Science 294, 148-151.

Schilman, B., Bar-Matthews, M., Almogi-Labin, A., and Luz, B., 2001. Global climate instability reflected by Eastern Mediterranean marine records during the late Holocene. Palaeogeography, Palaeoclimatology, Palaeoecology 176, 157-176.

Senesi, N., Miano, T. M., Provenzano, M. R., and Brunetti, G., 1991. Characterisation, differentiation and classification of humic substances by fluorescence spectroscopy. Soil Science 152, 259-271.

Shopov, Y. Y., 2004. Activators of luminescence in speleothems as source of major mistakes in interpretation of luminescent paleoclimatic records. International Journal of Speleology 33, 25-33.

Tan, M., Baker, A., Genty, D., Smith, C., Esper, J., and Cai, B., 2006. Applications of stalagmite laminae to paleoclimate reconstructions: Comparison with dendrochronology/ climatology. Quaternary Science Reviews 25, 2103-2117.

Treble, P. C., Chappell, J., Gagan, M. K., McKeegan, K. D., and Harrison, T. M., 2005. In situ measurement of seasonal $\delta^{18}O$ variations and analysis of isotopic trends in a modern speleothem from southwest Australia. Earth and Planetary Science Letters 233, 17-32.

Treble, P. C., Schmitt, A. K., Edwards, R. L., McKeegan, K. D., Harrison, T. M., Grove, M., Chen, H., and Wang, Y. J., 2007. High resolution SIMS $\delta^{18}O$ analyses of Hulu Cave speleothem at the time of Heinrich event 1. Chemical Geology 238, 197-212.

Vaks, A., Bar-Matthews, M., Ayalon, A., Matthews, A., Halicz, L., and Frumkin, A., 2007. Desert speleothems reveal climatic window for African exodus of early modern humans. Geology 35, 831-834.

Figures

Figure 1.1: Modern rainfall data from the eastern Mediterranean region. Open circles and triangles show the average percentage of total annual rainfall per month (left axis) from Ayalon et al. (2004) and Mitchell and Jones (2005), respectively. Data from Ayalon et al. (2004) were collected from above Soreq Cave. Data from Mitchell and Jones (2005) were acquired from the CRU TS 2.1 database and represent interpolated rainfall within ~500 km of Soreq Cave from 1901 to 2002. The filled squares illustrate the monthly average of rainfall $\delta^{18}O$ values (right axis) collected above Soreq Cave from 1995-2008.

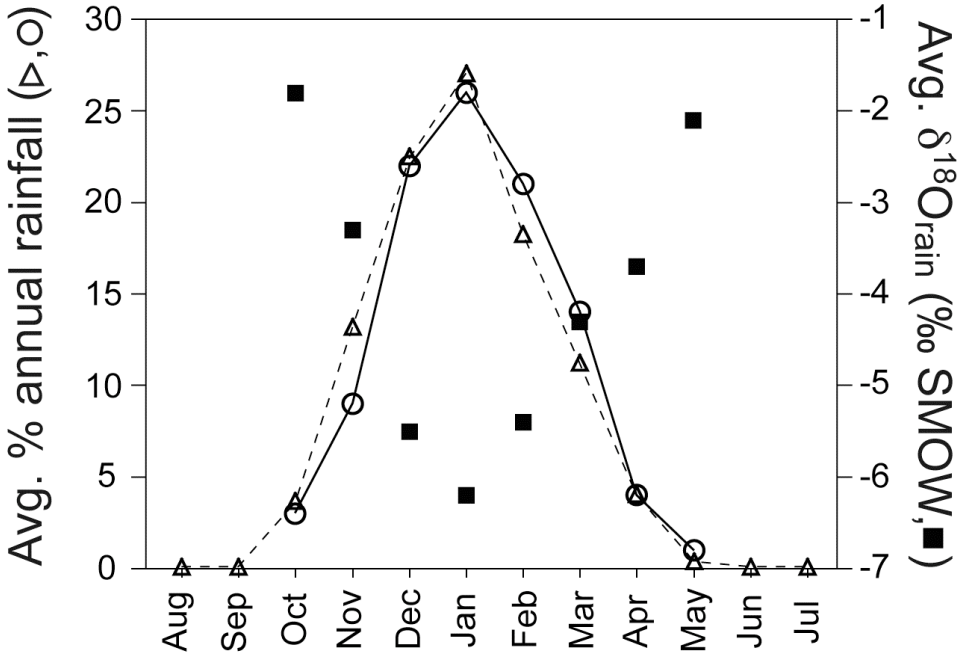

Figure 1.2: Map of Israel showing the location of Soreq Cave (adapted from Bar-Matthews et al., 2003).

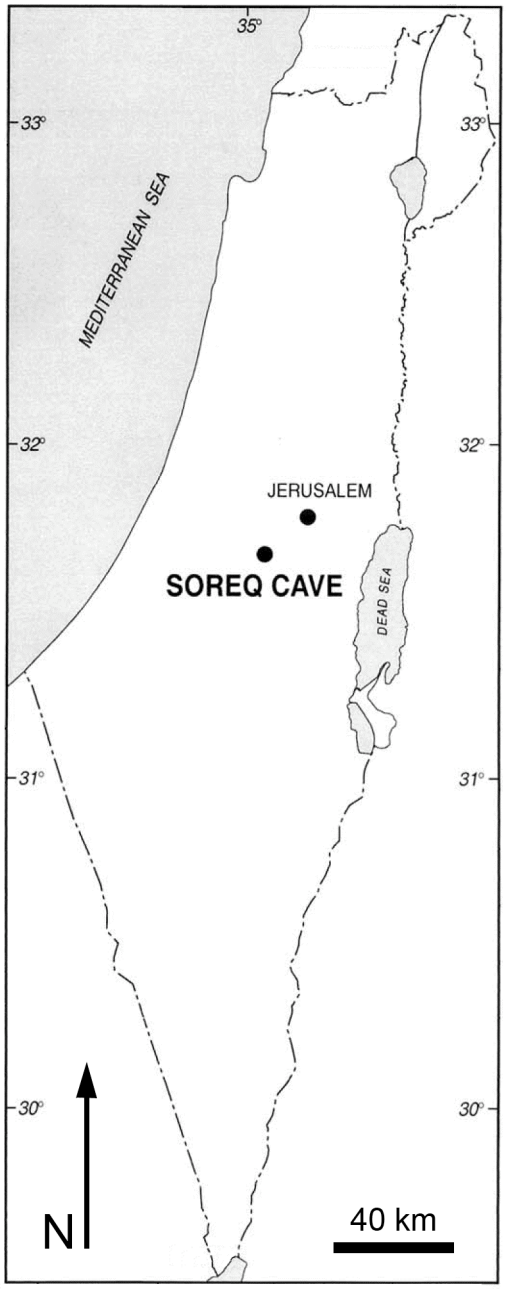

Figure 1.3: Values of $\delta^{18}O$ (SMOW) of modern dripwater from 1991-1996 in Soreq Cave. Values of "slow dripwater" are shown by open boxes, averaging 3-4 month intervals, and data from multiple drips show low variability. The annual variation in $\delta^{18}O$ values is typically ~1‰. "Fast dripwaters" (dashed lines) could only be collected during the peak of the wet-season, and have consistently lower $\delta^{18}O$ values than concurrent slow dripwaters. The annual average $\delta^{18}O$ value of precipitation above the cave is shown by the heavy lines; the precipitation isotope value has a regular offset of ~1‰ from the $\delta^{18}O_{average\ fast\ dripwater}$ values of that year. Cumulative measurements of annually averaged $\delta^{18}O_{rain}$ values before 1994 excluded some minor rainfall events and are not included here (adapted from Ayalon et al., 1998).

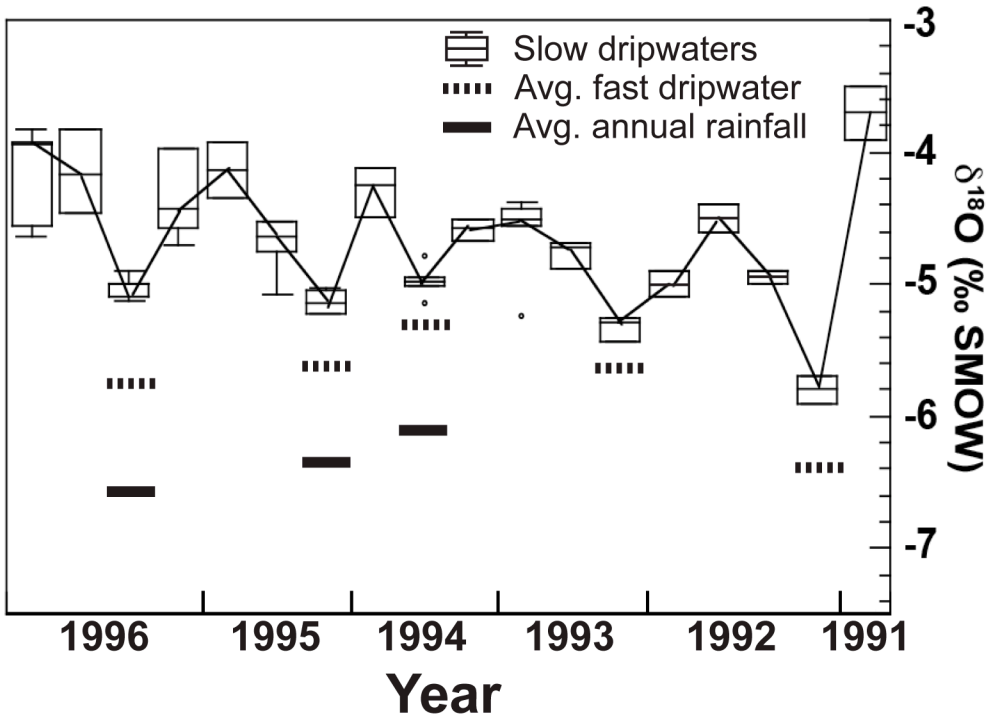

Figure 1.4 (next page): A fluorescent green image (true color) of sample 2-6 produced by confocal laser fluorescent microscopy for several annual light-dark couplets dated ca. 1.65 ka. Ion microprobe analysis spots, 10 μm in diameter, are highlighted with white ovals. The horizontal axes of the two graphs are scaled to the fluorescent image in order to highlight the correlation of $\delta^{18}O$ (PDB) variation and growth bands. As a reference, the average spot-to-spot precision of these analyses (2 s.d. = ±0.32‰) is plotted in the lower left of the upper graph. Values of $\delta^{18}O$ are lowest during the winter rainy season (bright fluorescence at the beginning of each band, marked by solid vertical lines) and gradually increase during the dry season as fluorescence darkens from right to left. The lower traverse was completed months after the upper traverse as a check of pattern reproducibility; the newer data may suggest the presence of an additional band, marked by the dashed vertical line in the graphs. Note that in the lower traverse, (1) a surface scratch compromised one analysis, and (2) the four highlighted analyses are in sequence with the saw-tooth pattern if their placement within the growth band is considered.

Figure 1.4:

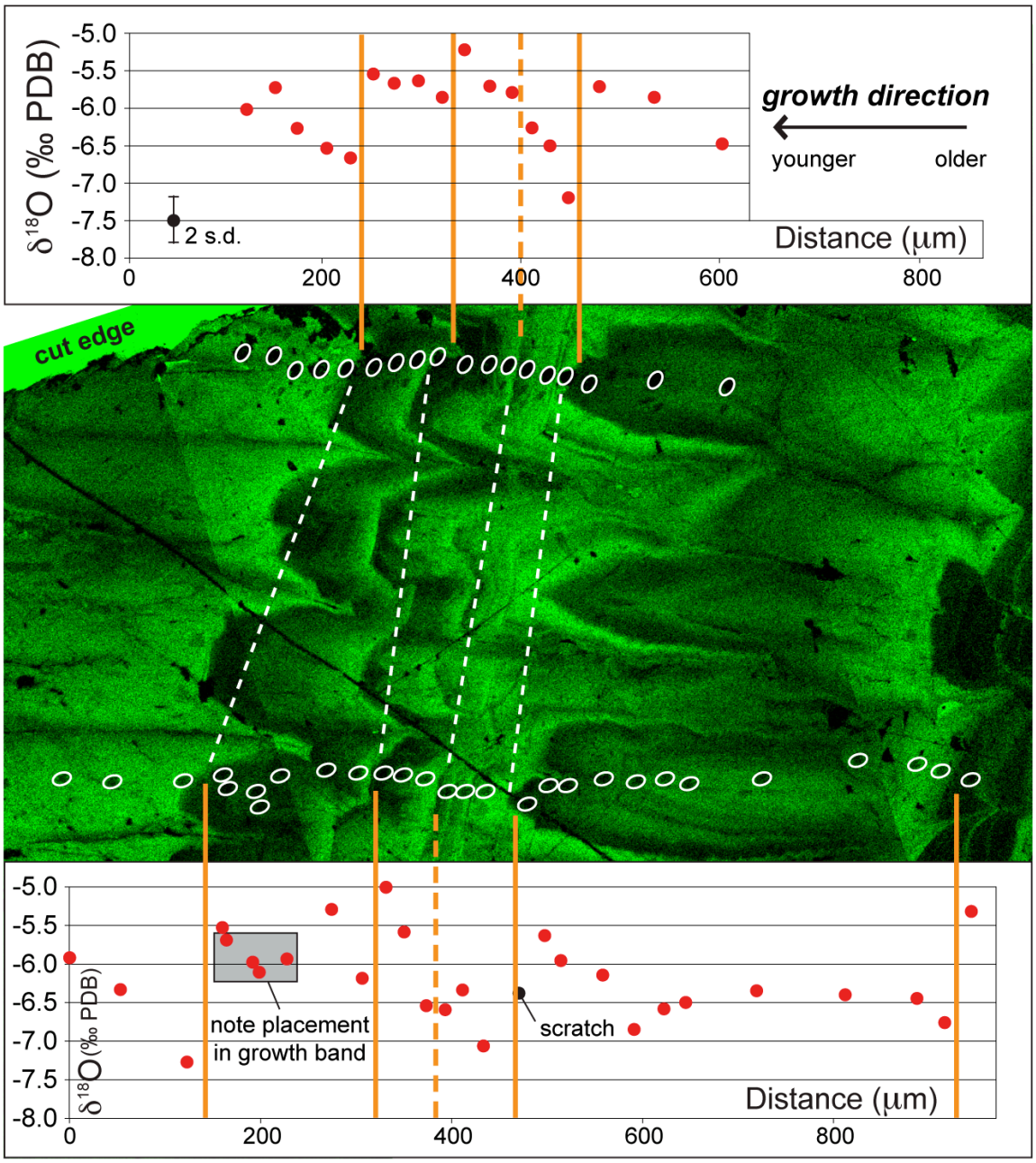
δ18O (‰ PDB)
-5.0
-5.5
-6.0
-6.5
-7.0
-7.5
-8.0
2 s.d.
0
200
400
600
800
growth direction
younger
older
Distance (μm)
cut edge
δ18O (‰ PDB)
note placement
in growth band
scratch
Distance (μm)

Figure 1.5: Confocal laser fluorescent microscopy images of interesting banding features in sample 2-6. Panel A shows a "truncation" feature that cuts across the regular, chevron banding pattern. The irregular fluorescent spot in panel A results from epoxy infilling porous space. Panel B highlights an "island" feature, uncommon in our sample, where a growth band appears to wrap around on itself; this feature is probably the result of a calcite crystal growing with a different orientation. The arrows in both panels indicate growth direction.

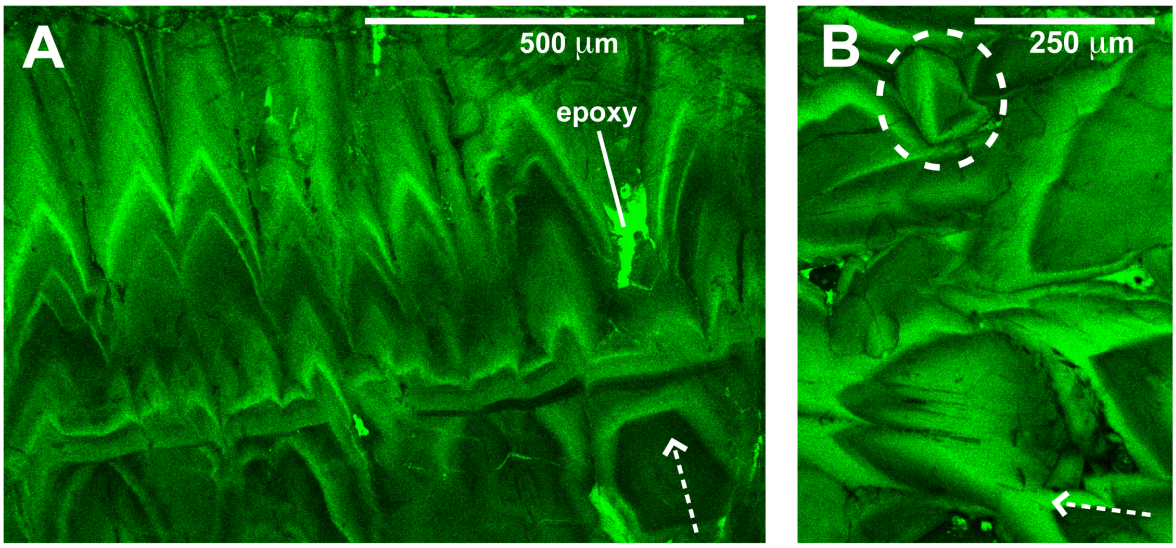

Figure 1.6 (next page): Panel A shows the measured $\delta^{18}O$ (PDB) values for ion microprobe analysis of light and dark fluorescent calcite bands across Soreq Cave sample 2-6. Analytical precision (2 s.d. = ±0.34‰) is illustrated in the lower left of panel A. For all 75 bands analyzed in this sample, the dark fluorescent calcite always has a higher $\delta^{18}O$ value than its coupled light fluorescent calcite. In general, for light fluorescent calcite, higher $\delta^{18}O$ values represent drier climates while lower $\delta^{18}O$ values are characteristic of wetter climates (see text for explanation). The heavy line, a 6-point running average, shows the general variability of $\delta^{18}O_{\text{light calcite}}$ values from 2.2-0.9 ka. Panel B shows values of $\Delta^{18}O_{\text{dark-light}}$ ($\delta^{18}O_{\text{dark calcite}} - \delta^{18}O_{\text{light calcite}}$) of individual annual bands. The heavy dashed line emphasizes the decrease in maximum $\Delta^{18}O_{\text{dark-light}}$ values from 2.0-1.3 ka. Panel C plots estimates of annual precipitation amounts (mm) calculated from the $\delta^{18}O$ values of wet-season calcite (light fluorescence) assuming a dripwater temperature of 19°C and Eq. (1); the dashed arrows highlight sharp decreases in annual rainfall amounts at ~1.9 and 1.6 ka. The shaded region represents the range of rainfall estimates calculated for dripwater temperature between 18 and 20°C. The average deviation of modern rainfall data from Eq. (1) is shown in the lower left of panel C. The mean and 1 s.d. range of annual rainfall in Jerusalem for the last 150 years, as collected by the Israel Meteorological Survey, is plotted on the left axis. Panel D illustrates concurrent changes in another paleorainfall proxy for the Levant region, the Dead Sea level (mbsl; Bookman et al., 2004). The circles along the age-axis represent the eight U-series dates (ka) acquired by MC-ICP-MS (Table 1.1).

Figure 1.6:

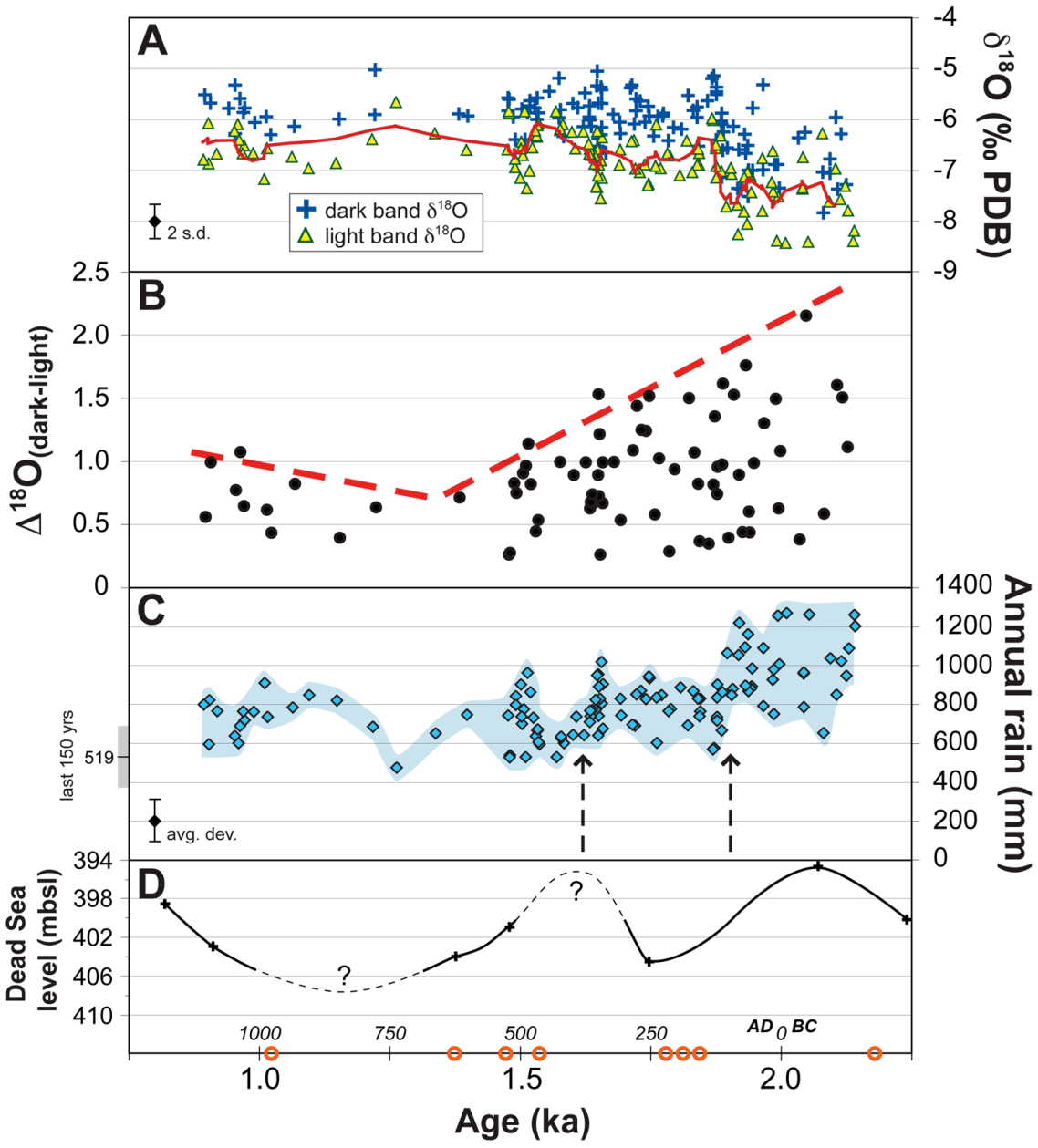
A
B
C
D
dark band δ18O
light band δ18O
2 s.d.
δ18O (‰ PDB)
-4
-5
-6
-7
-8
-9
Δ18O(dark-light)
2.5
2.0
1.5
1.0
0.5
0
last 150 yrs
519
avg. dev.
Annual rain (mm)
1400
1200
1000
800
600
400
200
0
Dead Sea level (mbsl)
394
398
402
406
410
?
?
1000
750
500
250
AD 0 BC
1.0
1.5
2.0
Age (ka)

Figure 1.7: Measured $\delta^{18}O$ (PDB) values versus the $\Delta^{18}O_{dark\text{-}light}$ of each analyzed band in Soreq Cave sample 2-6. Dark fluorescent calcite $\delta^{18}O$ values (crosses) are relatively constant across the full range of observed $\Delta^{18}O_{dark\text{-}light}$ values, suggesting that the $\delta^{18}O$ of water in the vadose zone remained similar through time. Conversely, the $\delta^{18}O$ values of light fluorescent calcite (triangles) become more negative as $\Delta^{18}O_{dark\text{-}light}$ values increase. This trend is interpreted to reflect an increasing contribution of winter rains (see text for explanation).

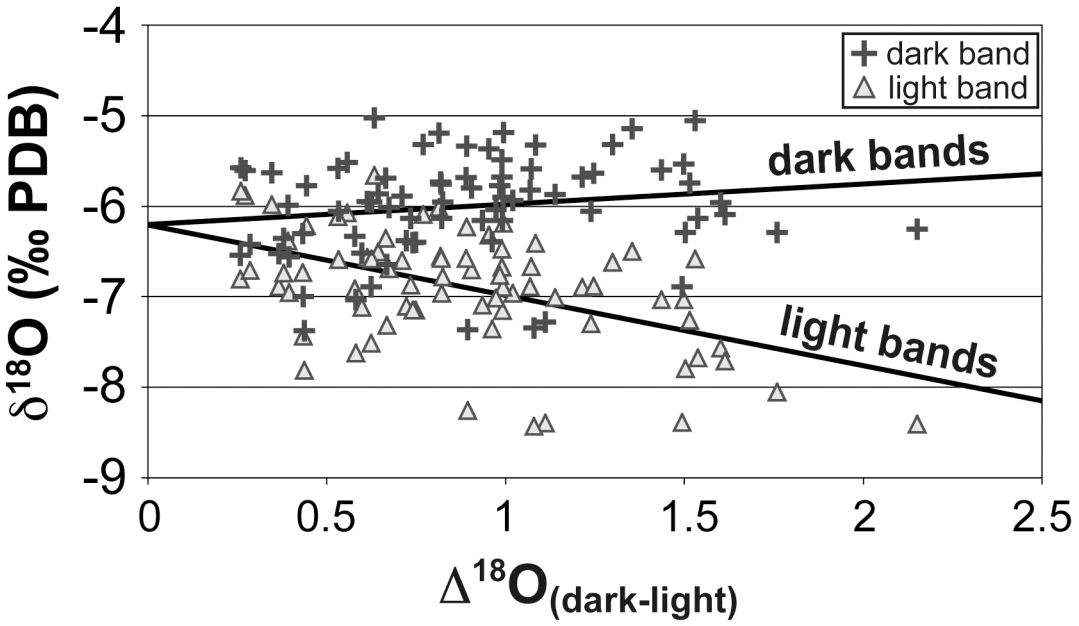

Tables

Table 1.1. U/Th age data from MC-ICP-MS analysis of Soreq Cave sample 2-6. The positions of age analyses in sample 2-6 are shown in Figure 1.6.

Sample	U conc. (ppm)	$^{234}U/^{238}U$	$^{230}Th/^{234}U$	$^{230}Th/^{232}Th$	Age (yr BP) uncorrected	Age (yr BP) corrected
2.6.1	0.5540 ± 0.0004	1.02931 ± 0.00145	0.01445 ± 0.00036	7.15 ± 0.18	1583 ± 80	1025 ± 110
2.6.2	0.5310 ± 0.0003	1.02859 ± 0.00099	0.01440 ± 0.00059	19.70 ± 0.81	1578 ± 130	1376 ± 150
2.6.3	0.5110 ± 0.0002	1.03124 ± 0.00081	0.01510 ± 0.00040	23.51 ± 0.62	1655 ± 90	1475 ± 105
2.6.4	0.5620 ± 0.0003	1.03288 ± 0.00087	0.01559 ± 0.00039	22.86 ± 0.47	1709 ± 90	1538 ± 105
2.6.5	0.4550 ± 0.0002	1.03359 ± 0.00120	0.01895 ± 0.00120	16.83 ± 1.08	2080 ± 260	1782 ± 310
2.6.6	0.4860 ± 0.0002	1.02976 ± 0.00249	0.01894 ± 0.00056	18.93 ± 0.56	2080 ± 120	1814 ± 145
2.6.7	0.4850 ± 0.0003	1.02791 ± 0.00165	0.01929 ± 0.00065	18.80 ± 0.63	2118 ± 140	1846 ± 170
2.6.8	0.5580 ± 0.0002	1.03047 ± 0.00134	0.02174 ± 0.00067	24.94 ± 0.78	2390 ± 150	2183 ± 170

All errors are listed at the 2σ confidence level

Appendices

Table A1.1: Annual rainfall data collected above Soreq Cave from 1990-2007. These data are used to construct the amount effect shown in equation [1]. The positions of age analyses in sample 2-6 are shown in Figure 1.6.

Year (wet-season spans 2 years)	Rainfall amount (mm)	Annually averaged $\delta^{18}O$ (‰, VSMOW)
1990-91	415	-5.0*
91-92	1020	-8.0*
92-93	660	-7.1*
93-94	500	-6.10
94-95	603	-6.35
95-96	617	-6.56
96-97	679	-5.82
97-98	527	-5.27
98-99	199	-4.42
99-00	376	-6.00
2000-01	412	-5.53
01-02	636	-6.15
02-03	777	-5.95
03-04	301	-5.47
04-05	442	-5.10
05-06	434	-5.40
06-07	392	-5.23
Average	**529**	**-5.85**

* Measurements of cumulative $\delta^{18}O$ values before 1993-94 excluded some minor rainfall events.

Data Repository Index

Large data tables and figures for each chapter are included in the supplementary files available with the online version of this dissertation.

DR1.1: Ion microprobe raw and corrected oxygen isotope values, analytical notes, model ages, and fluorescence and banding classifications of analyses from Soreq Cave sample 2-6.

DR1.2: Reflected light and CLFM images of sample 2-6 with ion microprobe analysis spots indicated.

CHAPTER II

Seasonal resolution of Eastern Mediterranean climate change since 34 ka from a Soreq Cave speleothem

Ian J Orland[1], Miryam Bar-Matthews[2], Avner Ayalon[2], Alan Matthews[3], Reinhard Kozdon[1], Takayuki Ushikubo[1], John W Valley[1]

[1]*WiscSIMS, Department of Geoscience, University of Wisconsin, 1215 W Dayton St., Madison, WI, 53706, USA*

[2]*Geological Survey of Israel, 30 Malchei Israel St., Jerusalem, 95501, Israel*

[3]*The Institute of Earth Sciences, The Hebrew University, Givat Ram, Jerusalem, 91904, Israel*

Orland I. J. Bar-Matthews M., Ayalon A., Matthews A., Kozdon R., Ushikubo T., and Valley J. W. (2012) Seasonal resolution of Eastern Mediterranean climate change since 34 ka from a Soreq Cave speleothem. *Geochim. Cosmochim. Acta* **89**, 240-255.

Abstract

The combination of ion microprobe analysis of $\delta^{18}O$ and confocal laser fluorescent microscope imaging of annual growth bands in a Soreq Cave speleothem provides sub-annual-scale climate information between 34 and 4 ka. This high-resolution methodology is ideal both for comparing seasonal climate patterns across broad windows of time and examining rapid climate events, such as the Younger Dryas termination, in detail. The sub-annual $\delta^{18}O$ gradients we report represent a combination of seasonal variability in rainfall amount and air temperature. A distinct change in both the pattern of fluorescent banding and the gradient of $\delta^{18}O$ measured *in situ* across single, annual growth bands indicates a change in seasonal climate patterns of the Eastern Mediterranean region following Heinrich event 1 and again after the Younger Dryas. Throughout the Holocene, wet winters and dry summers characterized regional climate. During the Younger Dryas, we find that regional climate may have been more arid than in the Holocene, but the fluorescent banding pattern indicates that the supply of dripwater to the cave was more consistent year-round. We suggest that a reduced gradient of seasonal precipitation, occasional snowfall, and vegetation differences may have all contributed to the isotope and fluorescent banding patterns observed during Heinrich event 1 and the last glacial stadial. Detailed investigation of the Younger Dryas termination reveals a rapid onset of regional environmental change. Fluorescent band counting indicates that the Younger Dryas termination, as recorded by rainfall in the Eastern Mediterranean, spanned a minimum of 12 years.

1. INTRODUCTION

1.1. Background

Model predictions of climate change over the next century are in broad agreement with respect to globally averaged surface temperatures, showing an increase of ~2-4 °C given projected greenhouse gas emissions, but key details remain uncertain (IPCC, 2007). Likewise, models predict a climate response that varies by both region and rate. It follows that high-resolution proxy records of past climate events are essential for calibrating model forecasts of seasonal and abrupt climate change on both regional and global scales. In this paper, we present a high-resolution geochemical climate proxy from a cave deposit in the Eastern Mediterranean (EM) region that is a record of seasonal precipitation from 34 to 4 ka. Combined with data presented in Orland et al. (2009), we build a regional record of seasonal climate from 34 to 1 ka.

Cave deposits (speleothems) are valuable records of multiple paleoclimate variables in numerous locations around the globe (e.g., Baker at al., 1993; Wang et al., 2001; McDermott, 2004; Fairchild et al., 2006; Baldini et al., 2008; Cheng et al., 2009; Lachniet, 2009; Wong et al., 2011). In many cases, geochemical tracers in speleothems are used to identify changes in global and regional climate trends on a decadal to millennial scale. Given conventional drill-sampling techniques (mm-scale spatial resolution) and typical speleothem growth rates, however, most speleothem-based proxy studies from semi-arid climates are unable to resolve seasonal or sub-annual information. Following the methodology established by Orland et al. (2009), this study examines the utility of *in situ* micron-scale (sub-annual temporal resolution) ion microprobe oxygen isotope ($\delta^{18}O$) analysis for interpreting seasonal climate patterns in a Soreq Cave (Israel) stalactite ("sample 2N", Fig. 2.1) that grew during the last glacial period, deglaciation and Holocene.

1.2. Related environmental proxy records

The record of seasonal climate from this study represents new information for interpreting mid-latitude climate dynamics during Northern Hemisphere deglaciation. Speleothem sample 2N provides a relevant record of both regional- and hemisphere-scale climate responses to deglaciation (Bar-Matthews et al., 1999, 2000, 2003). The existing $\delta^{18}O$ record from Soreq Cave generally agrees with that of other speleothems in the region (Frumkin et al., 2000; Verheyden et al., 2008). Soreq Cave is located such that it is influenced by the eastward advection of complex climatic variability in the North Atlantic. Further, the Soreq Cave isotope record may respond indirectly to an enhanced African Monsoonal System (Almogi-Labin et al., 2004, 2009) and movement of the Intertropical Convergence Zone, a major climate teleconnection mechanism examined and invoked by many paleoclimate workers (Wang et al., 2006; Anderson et al., 2009; Cheng et al., 2009; Waldmann et al., 2010; Denton et al., 2010).

Nearby regional paleoclimate records include lake level, marine sediment, and pollen environmental proxies. Shoreline sediments from the Dead Sea, which is in a terminal basin ~45 km east of Soreq Cave, are used to reconstruct paleo-Dead Sea levels and regional water balance (Enzel et al., 2003; Bartov et al., 2003; Bookman et al., 2004; Lisker et al., 2009; Torfstein et al., 2009; Stein et al., 2010; Waldmann et al., 2010). Understanding the contributions of both precipitation and evaporation is imperative for interpreting Dead Sea levels; since this is ambiguous in Dead Sea shoreline records, the interpretation of past regional rainfall amount is uncertain. Curiously, however, Dead Sea level is highest during the last ice age when high $\delta^{18}O$ values in Soreq Cave speleothems are interpreted by Bar-Matthews et al. (1997, 2003) to indicate a drier EM climate. In order to reconcile this dispute, workers have turned to marine and lacustrine sediment records.

Kolodny et al. (2005) use marine and terrestrial sediments to suggest that the long-term $\delta^{18}O$ trends observed in Soreq Cave speleothems are a result of changes in $\delta^{18}O$ of the Mediterranean Sea. Based on foraminiferal geochemistry, however, Almogi-Labin et al. (2009) argue that the $\delta^{18}O$ values observed in Soreq Cave cannot be explained solely by Mediterranean Sea surface $\delta^{18}O$, and that sea-land distance and relative elevation change due to lower sea levels must be accounted for as water vapor is transported from the EM to Soreq Cave.

Studies of pollen records near Soreq Cave (Baruch and Bottema, 1991, 1999; Bottema, 1995; Rossignol-Strick, 1995; Hajar et al., 2008; Langgut et al., 2011) show an increase in the abundance of temperate vegetation from the last glacial maximum (LGM) into the Holocene, indicating wetter climate in the Holocene. Rossignol-Strick (1995) concludes that oxygen isotope and pollen records from the EM and Arabian seas show two distinct climate regimes during the last deglaciation: a cold, arid Younger Dryas, and a temperate early Holocene with warm winters and wet summers.

The implication by Rossignol-Strick (1995) that seasonal climate differed between the Younger Dryas, the early Holocene, and the modern is a major motivation for the work presented here. Although some studies (Atkinson et al., 1987; Denton et al., 2005) have reported significant changes in Northern Hemisphere seasonality associated with millennial-scale warming (Bølling-Allerød) and cooling (Younger Dryas) events, few proxy records are capable of resolving seasonal climate across the Northern Hemisphere deglaciation. Denton et al. (2005) suggest that winter Arctic sea ice extended much further south in the Atlantic during the Younger Dryas, resulting in relatively frigid winters but mild summers. Tierney et al. (2011) introduce the pairing of paleoclimate proxy data with an isotope-enabled climate model in order to identify seasonal climate changes as the cause for the East African Humid Period, 11-5 ka.

The main goal of this study is to determine if Soreq Cave speleothems show the $\delta^{18}O$ signal of any significant seasonality changes during Northern Hemisphere deglaciation that can inform us about EM climate dynamics since the LGM.

Speleothem sample 2N preserves a record of calcite deposition across the last deglaciation. Although there are hiatuses in the growth record along the analytical traverse, we are able to interpret seasonality information from areas of consistent growth. The micro-imaging techniques used in this study allow us to recognize growth hiatuses, areas of irregular crystal growth, and non-calcite inclusions in a speleothem; we can then target ion microprobe analyses accordingly. Hence, this study utilizes the unparalleled spatial resolution of micro-analytical methodology to: (1) examine seasonality data over long time spans, and (2) reconstruct hemisphere-scale climate events that took place over short time spans. Prior studies from Soreq Cave, described in the following section, are integral to our climate interpretations.

1.3. Prior work at Soreq Cave

This investigation builds on prior characterization of Soreq Cave hydrology (Ayalon et al., 1998, 2004), the conventionally sampled 185 ka record of $\delta^{18}O$ from Soreq Cave speleothems (Bar-Matthews et al., 2003; Almogi-Labin et al., 2009), and analyses of both fluid inclusions (McGarry et al., 2004) and mass-47 CO_2 isotopologue anomalies (Δ_{47}) in Soreq speleothem calcite (Affek et al., 2008). These studies make Soreq an ideal natural laboratory to apply new procedures for high-precision analysis of $\delta^{18}O$ in 10 μm spots by ion microprobe and imaging of annual growth bands by confocal laser fluorescence microscopy (CLFM). Orland et al. (2009) developed the high-resolution methodology as part of a detailed study of $\delta^{18}O$ in a Soreq Cave stalagmite that grew from 2.2 to 0.9 ka. This study applies the high-resolution methodology to a

stalactite that formed between 33.8 and 4.4 ka.

The geological and hydrological setting of Soreq Cave, located in the Judean Hills 20 km west of Jerusalem, is well described by numerous studies of Soreq speleothems and hydrology (Bar-Matthews et al., 1996, 1997, 2003; Ayalon et al., 1998, 1999, 2004; Matthews et al., 2000; Kolodny et al., 2003; McGarry et al., 2004; Orland et al., 2009; Bar-Matthews and Ayalon, 2011). In the modern EM, ~95% of the annual rainfall occurs during the winter "wet season," which extends from November until April. Over the past 15 years, average annual rainfall above the cave is ~500 mm. Furthermore, modern precipitation demonstrates an "amount effect," a negative linear correlation of the amount and $\delta^{18}O$ value of annual rainfall (Ayalon et al., 1998, 2004; Orland et al., 2009).

Critical for this study is the work of Ayalon et al. (1998, 2004) to examine rainfall and dripwater $\delta^{18}O$ values in and above Soreq Cave on a sub-annual timescale. They find that rainfall $\delta^{18}O$ values vary seasonally above Soreq Cave, with the lowest $\delta^{18}O$ values occurring during the peak of the winter wet season. Furthermore, Ayalon et al. (1998) and Orland et al. (2009) show that the modern pattern of seasonal $\delta^{18}O$ variability in rainfall is transmitted to dripwaters in the cave. We assume that seasonal $\delta^{18}O$ variability in paleorainfall was likewise transmitted to dripwaters. Next, we assert that the seasonal dripwater $\delta^{18}O$ signal is reliably recorded in Soreq speleothems.

Prior work in Soreq Cave indicates that it is reasonable to assume that $\delta^{18}O$ values in sample 2N reflect isotopic equilibrium with dripwater. Although Affek et al. (2008) find evidence for kinetic isotope effects in their measurements of Δ_{47} in Soreq Cave speleothems, they determine the corresponding effect on $\delta^{18}O$ to be negligible and ultimately conclude that their samples precipitated at near-equilibrium conditions for $\delta^{18}O$. Moreover, Bar-Matthews et al.

(1996, 1997) established that sample 2N both passes the Hendy test for equilibrium precipitation (Hendy, 1971) and replicates the $\delta^{18}O$ variability of other samples from Soreq. Work in other caves (Mickler et al., 2006; Banner et al., 2007; Baldini et al., 2008) highlights the potential influence of seasonal pCO_2variability in a cave atmosphere on both isotopic equilibrium and seasonal growth rates. Since Soreq Cave had no natural entrance before it was discovered during a quarrying operation in 1968, seasonal ventilation of the cave atmosphere is presumed to have been insignificant. Additionally, Orland et al. (2009) demonstrate that the spatial resolution of our micro-analytical technique will allow us to account for changes in seasonal growth rates and avoid seasonally biasing the $\delta^{18}O$ record in sample 2N. Given these observations, we suggest that sample 2N precipitated in isotopic equilibrium and the $\delta^{18}O$ measurements we present here faithfully record a seasonal paleorainfall signal.

Orland et al. (2009) established guidelines to interpret combined $\delta^{18}O$ and CLFM data from the analysis of a late Holocene Soreq Cave calcite stalagmite (sample 2-6). CLFM imaging along the analytical traverse from the Holocene sample reveals a consistent sawtooth pattern of fluorescence intensity across concentric growth bands. The beginning of each growth band is marked by a sharp onset of bright-fluorescent calcite ("bright calcite"), followed by a gradual reduction in fluorescence intensity to dark-fluorescent calcite ("dark calcite") (Fig. 2.2A). The end of each growth band is marked by the sharp change to bright calcite in the next band. Ion microprobe analysis of the same analytical traverse shows that $\delta^{18}O$ values vary in a similar sawtooth pattern; the lowest $\delta^{18}O$ values occur at the sharp onset of bright calcite and then gradually increase as fluorescence gradually decreases.

Orland et al. (2009) interpret that these cycles represent annual banding and attribute the covarying patterns of fluorescence and $\delta^{18}O$ to a strongly seasonal rainfall pattern similar to the

modern EM rainfall regime. They suggest that the onset of intense, low-$\delta^{18}O$ precipitation in the wet season flushes organic acids that accumulate in the upper soil column during the dry summer into the cave, causing the sharp onset of bright fluorescent, low-$\delta^{18}O$ calcite. Fluorescence intensity decreases and $\delta^{18}O$ values increase in the speleothem following the wet season flush, and the cycle repeats itself at the beginning of the following wet season.

In order to quantify seasonality, Orland et al. (2009) defined the variable $\Delta^{18}O$. Within a single annual growth band, $\Delta^{18}O$(dark-bright) = $\delta^{18}O$(dark calcite) – $\delta^{18}O$(bright calcite) (Fig. 2.2A). In sample 2-6, higher values of $\Delta^{18}O$(dark-bright) indicate more rain during the wet season, and thus a wetter year, while lower $\Delta^{18}O$(dark-bright) values indicate generally dryer conditions. This proxy of seasonality relies on the assumption that the modern pattern of distinct wet and dry seasons is consistent with the climate regime of the last 2.2 ka. In support of this assumption, Orland et al. (2009) observed that $\delta^{18}O$ values in dark-fluorescent calcite are relatively constant compared to $\delta^{18}O$ values of bright calcite (see their Supplementary Material). Thus, dark calcite reflects dry season dripwater from a mixed vadose zone reservoir and provides a "baseline" $\delta^{18}O$ value that changes slowly on a decadal scale. Therefore, in sample 2-6, it is the $\delta^{18}O$ value of bright calcite that varies from year to year, creating differences in $\Delta^{18}O$(dark-bright). This model of fluorescence and $\delta^{18}O$ values previously established in sample 2-6 will be evaluated with data from the past 34 kyr in sample 2N.

2. MATERIALS AND METHODS

2.1. U-Th dating

New U-Th disequilibrium ages of sample 2N, a stalactite composed of low-magnesium

calcite (Bar-Matthews et al., 2000), were acquired by multi-collector inductively coupled plasma mass spectrometer analysis at the Geological Survey of Israel. The analytical method is described in Bar-Matthews et al. (2010). Twenty-four calcite aliquots were collected along a radial traverse of a 1 cm-thick slab of the speleothem, sawed orthogonally to the vertical growth axis. Calculated ages range from 4.5 ± 0.2 ka to 31.0 ± 0.9, and are corrected for excess ^{232}Th. The assumed initial ^{230}Th/^{232}Th activity ratio is 1.69, established in the detailed isochron study of Soreq Cave speleothems by Kaufman et al. (1998).

We define an "age model" for sample 2N based on linear interpolation between 11 selected U-Th dates. Of the 24 total ages measured, this simplified age model excludes: five measurements that incorporated irregular calcite growth (see Section 4.1.1 for further discussion) and eight ages that were bracketed by adjacent spots with overlapping error bars. The electronic annex Figure A2.1 illustrates the overlap between the linear interpolation age model and a more complex Bayesian age model (Scholz and Hoffman, 2011) that includes all 24 ages. Given the excellent agreement between model types as well as our focus on the comparison of extended time periods, we think the linear interpolation model is suitable. Linear extrapolation of observed growth rates to the core and outer rim indicate that the δ^{18}O analyses presented here span from 33.8 to 4.4 ka. Table 2.1 lists the measured isotope ratios, uncorrected and corrected U-Th disequilibrium ages of all 24 measurements.

2.2. Sample preparation

A second 1-cm thick slab of stalactite 2N was cut adjacent to the piece dated at the Geological Survey of Israel and sent to the University of Wisconsin-Madison (UW-Madison) for ion microprobe analysis. At UW-Madison this slab was cut along its longest radius (13.8 cm)

into 13 ~1 cm^3 cubes using a thin-kerf jeweler's saw. Figure 2.1 shows where the 13 cubes (A-I, M-P) were cut from the slab of sample 2N and indicates the "working traverse" (white dashes) along which ion microprobe analysis was completed. The 13 cubes were mounted in pairs in seven 1-inch-diameter epoxy rounds (Fig. 2.1, inset). In each epoxy mount, 3-4 grains of UWC-3 (calcite standard; $\delta^{18}O$ = 12.49‰, VSMOW; Kozdon et al., 2009) and the working traverse were placed within ~5 mm of the center of each mount to prevent instrument bias during ion microprobe analysis related to sample position (Valley and Kita, 2005, 2009; Treble et al., 2007; Kita et al., 2009). Each round was polished using diamond paste in a progression from 6 to 1 μm grits and a final polish was applied using a colloidal alumina (0.05 μm) solution. Warm tap water and a soft toothbrush were used to remove any colloidal alumina residue. The polishing method was previously verified with sample 2-6 when imaging by reflected light profilometer confirmed a surface relief of less than 3 μm in the analytical portion of three epoxy rounds.

2.3. Confocal laser fluorescent microscopy

Imaging of the fluorescent growth bands in sample 2N was performed in the Keck Bioimaging Lab at UW-Madison with a Bio-Rad MRC-1024 scanning confocal microscope. A 40 mW laser with a wavelength of 488 nm coupled with an emission filter, which allows the transmission of fluorescent light with wavelengths between 505 and 539 nm, produced images of green growth bands. As we are unaware of a suitable method for fluorescence standardization, the focal plane depth, laser power, and signal gain were held constant in order to normalize image intensity. A series of 10-14 overlapping images (959 x 1199 μm) were collected with a 10x objective lens (100x total magnification) along the working traverse of each 1 cm-long sample chip. Stitched together, the fluorescence images – combined with reflected light image

maps from an optical microscope – were used to select domains for ion microprobe $\delta^{18}O$ analyses.

2.4. Ion microprobe analysis of $\delta^{18}O$

High spatial resolution analyses of oxygen isotope ratios were completed on the CAMECA ims-1280 large radius multicollector ion microprobe at UW-Madison. Before insertion in the ion microprobe, each polished epoxy round was: (1) cleaned in a sonicator with both distilled water and ethanol; (2) gold coated with a coating thickness of ~60 nm; and (3) imaged with a reflected-light microscope for mapping purposes. The $\delta^{18}O$ analysis spots are oval with an approximate length of 10 μm in the long dimension; the sample was oriented so that the shorter dimension of the analysis spots was parallel to the working traverse. Using the standard-sample-standard bracketing technique outlined by prior workers (Kita et al., 2009; Kozdon et al., 2009; Orland et al., 2009; Valley and Kita, 2009), each block of sample analyses is assigned the precision of the bracketing standards. Thus, the spot-to-spot reproducibility of the 8 standard analyses bracketing each block of 10-15 sample analyses is assigned as the precision for those analyses. The average precision for the $\delta^{18}O$ spots on sample 2N is ±0.30‰ (2 standard deviations, s.d.).

Each $\delta^{18}O$ analysis spot is sputtered with a ~1.7 nA primary beam of $^{133}Cs^{+}$ ions, focused to ~10 μm diameter at the sample surface. Over the course of each 4 min analysis, the beam ablates a ~1 μm deep pit in the calcite (~2 ng). Both the gold coating applied to the sample surface as well as a normal-incidence electron flood gun provide charge compensation. The secondary ion intensity for $^{16}O^{-}$ was generally 2.5 x 10^{9} cps, depending on the primary beam intensity. The mass resolving power for the measurement of $\delta^{18}O$ is 2200; $^{16}O^{-}$ and $^{18}O^{-}$ ions are

counted simultaneously on two Faraday cup collectors in multicollection mode. Further discussion of WiscSIMS analytical methods is presented elsewhere (Kita et al., 2009; Orland et al., 2009; Valley and Kita, 2009; Kozdon et al., 2011). Data are reported in the data repository, DR2.1.

The first analytical pass along the working traverse of each sample cube includes widely-spaced analyses that help define the general pattern of $\delta^{18}O$ variability across each sample section and to explore areas of interest. A more detailed analytical pass followed, with paired $\delta^{18}O$ analyses in the brightest and darkest fluorescent portion of 165 bands. Domains with visible surface pitting were avoided, except as discussed below. In the growth bands with paired analyses, analysis spots were placed in the widest, clearest portion of the fluorescent banding pattern.

After ion microprobe analysis, the gold coating was removed from each sample mount by lightly abrading the surface using a medium-nap pad wetted with 0.25 μm diamond suspension. Each sample mount was then reimaged by CLFM to classify the fluorescence (dark, bright, intermediate or mixed) of each analysis spot.

2.5. Post ion microprobe investigation

Following ion microprobe analysis, secondary electron and backscatter electron imaging by scanning electron microscopy was used to examine representative spots measured by ion microprobe. For analysis spots with imperfect pit-bottoms (e.g., cracks in calcite, microporosity) we used the respective ion yield values to check analytical validity. Analyses that are unimpeded by excessive porosity, irregular surface conditions, inclusions of other minerals, or primary beam aberrations have an expected range of ion yield values. As discussed below, we defined this

range statistically for sample 2N and use it as the final test of validity for each spot.

A standard-sample-standard bracketing technique was used to determine the "percent yield" of each analysis relative to the average yield of the bracketing standards (DR2.1). On average, analysis spots in sample 2N had yields that were 96.7% of the bracketing standard analyses. The Tukey definition of a suspected outlier (Tukey, 1977) limits the accepted range of "percent yield" values to between 93.2% and 100.4%. The 73 suspected outliers (<6% of 1223 sample analyses, highlighted in DR2.1) are omitted from the plots and interpretations presented here.

As discussed further in Section 3.2, microporosity exists in some portions of sample 2N. Although some ion yield values from the most porous areas are classified as outliers by the Tukey definition, most fall within the accepted range and are included in the interpretations below.

3. RESULTS

3.1. CLFM imaging

CLFM reveals concentric fluorescent bands across the majority of the ~13 cm working traverse of sample 2N. Fluorescent bands are only absent in portions of the sample with "irregular crystal growth," discussed below. Each fluorescent band is defined by a single gradational transition between bright fluorescent calcite ("bright calcite") and dark, non-fluorescent calcite ("dark calcite"). Band widths vary from ~2 μm (2 pixels resolved by digital CLFM images) to 100 μm. Smaller bands may be common, but are not resolved by this technique.

Qualitative observation of the fluorescent banding across the working traverse of sample

2N reveals that there is significant variability in the banding pattern that is not seen in younger samples from Soreq cave (Fig. A2.2). Figure 2.2 illustrates, in cartoon form, the four types of fluorescent banding pattern observed across the working traverse of 2N. From 10.5 ka to present in speleothem 2N, the fluorescence banding pattern is similar to that observed (Fig. 2.2A) throughout Holocene sample 2-6 (Orland et al., 2009). Specifically, each band has an abrupt onset of bright calcite followed by a gradient to dark calcite through time; the pattern repeats itself with an abrupt return to bright calcite at the beginning of the next band. Normal to the axis of elongation, the growth bands are concentric and crenulated; the growth fronts have a regular, chevron pattern. The chevron pattern reflects the radial c-axis orientation of calcite rhombohedra that precipitated on the outer surface of the stalactite. Linear truncations of the chevron pattern by a sharp fluorescent band, which occur in several intervals with irregular periodicity throughout sample 2N, are interpreted to represent dissolution of the outer surface of sample 2N and a time hiatus (see Fig. 1.5A).

Markedly different fluorescent banding patterns exist, however, in growth prior to 10.5 ka. From ~13.5 to 11 ka, the abrupt onset of fluorescence at the beginning of each band is commonly smoothed so that the majority of bands have a gradual gradient from bright to dark calcite as well as from dark to bright in the subsequent fluorescent band (Fig. 2.2B). This sinusoidal fluorescence intensity describes the majority of bands during this period.

Before 15 ka sinusoidal fluorescence is also common, but the fluorescence pattern observed within some annual bands is reversed with respect to Holocene growth described above. As a result, two more banding categories are observed. A number of the annual growth bands during this time period have a reversed sawtooth fluorescence pattern (Fig. 2.2C). Rather than the bright-to-dark progression of Holocene bands, a sharp dark boundary indicates the

beginning of these bands. A gradient to bright fluorescence then lasts until the end of the band, where the next sharp dark boundary occurs. The fourth banding category (Fig. 2.2D) is identical in fluorescence pattern to the gradational transitions in Figure 2.2B, but ion microprobe analysis indicates that the oxygen isotope gradient is reversed as discussed below. All four of the fluorescence patterns described above are present before 22 ka.

These banding pattern classifications are first made by visual examination of the CLFM images and then interrogated by ion microprobe analysis of $\delta^{18}O$. The difference between the banding patterns described in Figures 2.2B and D is determined by whether the bright calcite has a lower $\delta^{18}O$ value than the adjacent dark calcite (2.2B) or vice versa (2.2D).

There are three areas of the working traverse where calcite crystals have an irregular habit and do not contain concentric fluorescent bands (arrows in Fig. 2.1). There are no calculated values of $\Delta^{18}O$ in these areas. This irregular calcite is identified by CLFM and indicated as "irregular crystal growth" in Figure 2.3A (hashed vertical rectangles), calcite crystals form a cross-hatched pattern with a much higher porosity relative to the rest of the sample. The irregular crystal growth, discernable to the naked eye on a polished surface, is clearly identified in both reflected-light (Fig. 2.1) and CLFM imaging (Fig. A2.2). Further discussion of this material is in Section 4.1.1.

3.2. Ion microprobe analysis of $\delta^{18}O$

Results of the 1223 $\delta^{18}O$ sample analyses and 589 standard measurements are recorded in chronological order of analysis in DR2.1. The $\delta^{18}O$ values measured in sample 2N range from -9.1 to -2.5‰ (VPDB). Figure A2.3 plots the $\delta^{18}O$ value and the fluorescence classification of each ion microprobe spot. In Figure 2.3A, which shows analyses with either dark or bright

fluorescence classifications, an 11-point running average is plotted for only dark calcite spots between 14 and 0 ka. The running average illustrates the high $\delta^{18}O$ "baseline" of this dataset since 14 ka.

Imaging of ion microprobe pits by backscatter electron imaging reveals that some dark fluorescent calcite in older portions of sample 2N contains microporosity (Fig. A2.4). Void spaces in the microporous regions tend to have elongated shapes with long axes parallel to the radial growth direction of calcite crystals. Inspection of backscatter electron images from areas with microporosity indicates that most void spaces have a maximum dimension less than 1 μm in length, do not appear to be interconnected, and amount to at most ~7% of the total area in a single pit-bottom. To ensure that the microporosity, which varied in its distribution along single bands, did not affect ion microprobe analyses, we made a total of 63 $\delta^{18}O$ measurements along seven 0.5-2 mm traverses parallel to bands displaying microporosity (Table A2.5). The mean value of two standard deviations of the seven groups of $\delta^{18}O$ analyses along individual bands is 0.71‰, approximately two times the average spot-to-spot precision (2 s.d.) of the bracketing UWC-3 calcite standard analyses obtained during these analyses (0.31‰).

Some excess in variability of the along-band analyses as compared to standard analyses is expected. Orland et al. (2009) showed that $\delta^{18}O$ within annual growth bands is zoned, thus, slight variability in the positions of analysis spots along the strike of an annual band results in greater heterogeneity than the homogeneous calcite standard. Furthermore, the greatest intra-band $\delta^{18}O$ variability is observed along bands that have the highest degree of microporosity in sample 2N (as inferred from optical microscopy and anomalously low ion yield values). These are bands that would otherwise be avoided by the analyst. Thus, we are confident in measurements of $\delta^{18}O$ within bands that display lesser degrees of microporosity.

3.3 Calculating $\Delta^{18}O$(dark-bright)

Orland et al. (2009) proposed that the difference in $\delta^{18}O$ values between the bright and dark fluorescent calcite of a single annual band [$\Delta^{18}O$(dark-bright) = $\delta^{18}O$(dark)–$\delta^{18}O$(bright)] represents a quantitative measure of seasonality. While all values of $\Delta^{18}O$(dark-bright) are positive in sample 2-6, fluorescent banding patterns are occasionally reversed (i.e., dark-to-bright, Figs. 2.2C and D) in sample 2N such that $\Delta^{18}O$(dark-bright) values are negative in 52 (32%) of the 165 analyzed bands. Where the fluorescent banding pattern is reversed, $\delta^{18}O$ values in bright calcite are higher than $\delta^{18}O$ values in dark calcite. Note, however, that the sawtooth pattern of $\delta^{18}O$ variability remains the same across each band, irrespective of fluorescence; lower $\delta^{18}O$ values always precede higher $\delta^{18}O$ values.

We simplify visual comparison of $\Delta^{18}O$ across sample 2N by plotting $|\Delta^{18}O|$(dark-bright), the magnitude of the $\delta^{18}O$ gradient within single annual bands, in Figure 2.3B. Figure 2.2 illustrates how $|\Delta^{18}O|$ values are calculated from different fluorescent banding patterns. The calculated values of $|\Delta^{18}O|$ range from 0.0‰ to 2.5‰. No relationship is evident between $|\Delta^{18}O|$ values and band widths.

4. DISCUSSION

Coupled changes in $|\Delta^{18}O|$ and fluorescent banding in sample 2N indicate multiple significant environmental changes above Soreq Cave in the last 34 kyr. Given the complexities of the ocean-atmosphere-soil-cave system and the lack of similar seasonal records in the literature, the interpretations we outline below are ripe for further interrogation. We examine the results from the perspective of, first, only the fluorescent banding data, and second, after

incorporating the oxygen isotope data.

4.1. Interpretation of fluorescent banding

The occurrence of fluorescence at the excitation and emission wavelengths used in CLFM imaging of sample 2N indicates that the fluorescent bands we observe are likely a result of seasonal variability of organic acids in cave dripwaters (Senesi et al., 1991; Baker et al., 1996; McGarry and Baker, 2000; Tan et al., 2006). The combination of the hydrologic setting of Soreq Cave with distinct seasonal rainfall further supports the idea that fluorescent banding in Soreq speleothems is caused by annually variable organic acid infiltration (Orland et al., 2009). For much of sample 2N, fluorescent bands are easily discernable and many have widths of 10-50 μm. Two features of the fluorescent banding are discussed in more detail below: (1) areas of irregular banding where calcite crystal growth is atypical, and (2) variability in the pattern of fluorescent banding (as in Fig. 2.2).

4.1.1. Irregular banding pattern

There are portions of sample 2N, highlighted by three hashed rectangles between 22 and 14 ka in Figure 2.3A, where the crystal habit of speleothem calcite takes on an irregular, lattice-type structure (Figs. 2.1, A2.2). Figure 2.1 shows that these domains are lenses that pinch out. Thus, while any continuous-growth age model would assign long periods to these zones, their growth duration is uncertain, especially before Heinrich event 1 (H1). There are three likely explanations for the irregular crystal growth habit. First, Bar-Matthews et al. (2003) find that speleothems with regular growth during these time periods have consistent isotopic profiles. Hence, the most likely explanation for the irregular crystal growth habit is a change in the local

hydrologic character of the cave-groundwater system (i.e. drip supply) where sample 2N was growing.

Second, a change in environmental factors within the cave (i.e. cave humidity, pCO_2 of the cave atmosphere) may have resulted in a different physical or chemical mechanism of calcite precipitation. Interestingly, these irregular portions are coincident with periods of time, the LGM (~20 ka) and Bølling-Allerød (~14 ka), which other Northern Hemisphere proxies (McGarry et al., 2004; Affek et al., 2008; Almogi-Labin et al., 2009) identify as having vastly different environmental conditions: the LGM was cold and dry, while the Bølling-Allerød was warm and wet. Perhaps the resumption of concentric banding at the onset of Heinrich 1 (H1) and Younger Dryas (YD) climate events (Fig. 2.3) is a clue for the cause of banding variability.

Third, it is possible that the irregular crystals formed as a result of calcite recrystallization in the speleothem. U-Th ages determined from irregular calcite crystals are within error of the ages in adjacent, "regular" crystal growth, suggesting that if this material was recrystallized, either the U/Th ratio was preserved or calcite replacement happened soon after primary precipitation of the speleothem calcite. Furthermore, the irregular calcite does not cut across adjacent banding patterns, suggesting that it accumulated on the outer surface of the speleothem and was later covered by regular calcite growth. Since the cause of the irregular crystal growth may be a change in the local hydrological environment and/or regional climate, we avoid interpreting the $\delta^{18}O$ data analyzed in these zones. Notably, $\delta^{18}O$ values that were measured in the irregular calcite (included in Figs. 2.3, A2.3) do not change the interpretations that follow.

4.1.2. Fluorescent pattern variability

This section outlines hypothetical climatic interpretations of the fluorescent banding

patterns that are characteristic of different portions of sample 2N (Fig. 2.2). Discussion in subsequent sections will include oxygen isotope data.

Throughout the portion of sample 2N that grew after 10.5 ka, annual growth bands are characterized by a sharp onset of bright fluorescence followed by a gradual return to dark fluorescence (Fig. 2.2A). Here we adopt the fluorescence-climate interpretation of Orland et al. (2009). Specifically, the onset of heavy rain events at the beginning of the winter wet season transports organic acids, which accumulated in the upper soil column during the dry season, into the cave where they are trapped in speleothem calcite. Based on the consistency of speleothem fluorescent banding, we suggest that the modern, annual pattern of distinct wet and dry seasons was the dominant climate regime in the EM for at least the last 10.5 ka.

Before 10.5 ka, sample 2N records two additional patterns of fluorescent banding: fluorescence intensity that varies sinusoidally across bands (Figs. 2.2B and D) and dark-to-bright fluorescence patterns (Figs. 2.2C and D) that are reversed relative to the bright-to-dark Holocene pattern. Gradual sinusoidal transitions between bright and dark calcite suggest that rainfall was more consistent during the onset and termination of organic acid production in the soil, perhaps due to a reduced gradient in seasonal rainfall or a change in organic acid production. During the YD, when pollen records (Rossignol-Strick, 1995; Langgut et al., 2011) indicate that semi-arid species dominate EM vegetation, a different plant population may have caused distinct fluorescent patterns by altering the timing, type or amount of organic acid delivery into the cave.

The reversed fluorescence patterns suggest multiple possible changes in the manner that organic acids are delivered into Soreq Cave. We present four potential explanations for the intermittent reversals in the order of fluorescence banding before 15 ka. (1) A change in the timing or rate of organic acid production in the soil column relative to wet season rainfall events.

(2) Reduced seasonality of rainfall (i.e. less distinct wet and dry seasons). (3) Snowfall or frozen ground during the winters of H1 and YD. (4) A change in the dominant type or amount of vegetation. Hypotheses for both reversed and sinusoidal fluorescence patterns are evaluated in the following section by considering $\delta^{18}O$ and $\Delta^{18}O$ values within annual bands.

4.2. Interpretation of $\delta^{18}O$ and $\Delta^{18}O$ values

Almogi-Labin et al. (2009) examined conventionally measured $\delta^{18}O$ values in sample 2N and found that they agree with the (inverse) NGRIP Greenland ice core $\delta^{18}O$ record. Thus, the $\delta^{18}O$ data reported in Figure 2.3A, which include all ion microprobe measurements in bright and dark fluorescent calcite from samples 2N and 2-6, are used to help guide the identification of the major climatic periods. Following the LGM, Figure 2.3A illustrates that $\delta^{18}O$ values record: (1) the end of the LGM, H1; (2) the onset, duration, and termination of the YD; and (3) the Holocene up to ~0.9 ka.

By themselves, $\delta^{18}O$ values from the late Holocene can be used to interpret a regional history of seasonal climate based on the modern "amount effect". But what about before the Holocene, when the climate modes in the North Atlantic and EM were significantly different? Can we apply the present-day amount effect as suggested by Bar-Matthews et al. (2003)? Recent studies suggest caution (Vaks et al., 2006; Almogi-Labin et al., 2009). They note that lower sea levels during the LGM effectively moved Soreq Cave inland and to a higher elevation relative to its Holocene position. This would increase Rayleigh fractionation of water vapor during transport to the cave and decrease local rainfall $\delta^{18}O$ values by ~1-1.5‰ during the LGM, independent of rainfall amount (Vaks et al., 2006; Almogi-Labin et al., 2009).

The advantage of the micro-analytical approach presented here is that we are able to

consider two features in addition to $\delta^{18}O$ values: the fluorescent pattern of annual growth bands discussed above and calculated values of $|\Delta^{18}O|$(dark-bright). We consider all three factors in parallel for the climate interpretations below.

4.2.1. The Holocene

Orland et al. (2009) found that $\delta^{18}O$ and $\Delta^{18}O$(dark-bright) values could be used together to examine hydrological characteristics of Soreq Cave. A plot of $\delta^{18}O$ vs. $\Delta^{18}O$(dark-bright) using data from late Holocene sample 2-6 (Fig. 2.7 in Orland et al., 2009) illustrates that the $\delta^{18}O$ of dark calcite is relatively consistent while the $\delta^{18}O$ of bright calcite is more variable and, thus, dictates $\Delta^{18}O$ values. Orland et al. (2009) describe dark calcite as representing "baseline" dripwater that entered the cave from a vadose zone reservoir during the dry season and bright calcite reflects infiltration of wet-season precipitation. It is clear that the distinct wet/dry seasonal climate of the late Holocene is reflected in $\Delta^{18}O$ data.

For sample 2N, a similar plot of $\delta^{18}O$ vs. $|\Delta^{18}O|$(dark-bright) for analyses dated between 10.5 and 4 ka (Fig. 2.4) shows a nearly identical pattern to the late Holocene sample examined by Orland et al. (2009). Namely, the $\delta^{18}O$ values of dark calcite in 2N after 10.5 ka are relatively consistent, while the $\delta^{18}O$ values of bright calcite are more variable and dictate $|\Delta^{18}O|$ values. Thus, the isotope data confirm the fluorescent banding interpretation described above: the climate regime of distinct wet and dry seasons persists throughout the Holocene in the EM. This conclusion does not point to a persistence of wet summers in the early Holocene as proposed by Rossignol-Strick (1995).

We note two additional features of Holocene $\delta^{18}O$ and $|\Delta^{18}O|$ values. First, the running

average of baseline (dark) $\delta^{18}O$ values increases ~1‰ from 10.5 to 5 ka (Fig. 2.3A). Lower $\delta^{18}O$ values in the early Holocene likely reflect contributions of meteoric water (low $\delta^{18}O$) from a combination of enhanced westerlies that cause rainfall over the entire Mediterranean (Kallel et al., 1997) and increased freshwater runoff from the Nile into the EM as a result of the orbitally driven African Monsoon (Marino et al., 2008).

Second, there is an interesting isotopic change across Sapropel event 1 (S1, 8.5-7.0 ka; Bar-Matthews et al., 2000), which is identified in other Soreq speleothems (Bar-Matthews et al., 1999, 2000) and highlighted in Figures 2.3 and 2.5A. S1 is defined stratigraphically by anoxic marine sediments that form as a result of Nile runoff and increased EM density stratification (Rossignol-Strick et al., 1982; De Lange et al., 2008). Hence, lower $\delta^{18}O$ values are expected in Soreq speleothems. Indeed, there is an excursion of $\delta^{18}O$ analyses in bright calcite to lower values, but $\delta^{18}O$ values of dark "baseline" calcite remain relatively unchanged. As a result, $|\Delta^{18}O|$ values are larger during S1 with a peak at 8.3 ka. Although the increase in $|\Delta^{18}O|$ values across this time period agrees with the interpretation that S1 is a wet period at Soreq (Bar-Matthews et al., 2000), it is curious that the dark baseline $\delta^{18}O$ values do not change. The consistent $\delta^{18}O$ values in dark domains suggest that either: (1) the residence time of baseline vadose groundwater is long enough that deluge events during S1 winters do not perturb $\delta^{18}O$ values of summer dripwater; (2) Rayleigh distillation increases the $\delta^{18}O$ of summer rainfall to balance the $\delta^{18}O$ decrease of EM source water; (3) the $\delta^{18}O$ value of source water did not decrease significantly due to freshwater input from the Nile; or (4) sample 2N does not fully record S1. The number and length of growth hiatuses in this section of the sample are unknown; although the pattern of $\delta^{18}O$ values across this section of the speleothem may be representative of the entire S1 event, it

is possible that sample 2N only records a portion of the S1 event. We can pin the location of S1 in sample 2N if future ion probe analysis of $\delta^{13}C$ identifies the large, positive $\delta^{13}C$ excursion that is reported in other Soreq speleothems (Bar-Matthews et al., 2000).

4.2.2. The Younger Dryas

Prior to 10.5 ka, both the fluorescent banding patterns and $|\Delta^{18}O|$ values in sample 2N are consistently different than in the Holocene. Qualitative observation of CLFM imaging from the YD, the duration of which is inferred from $\delta^{18}O$ values shown in Figure 2.5B, indicates that the majority of bands have sinusoidal fluorescence intensity. Notably, the scarcity of measurable $|\Delta^{18}O|$ values from the height of the YD is due to narrow banding; reliable paired analyses of $\delta^{18}O$ within individual bands during the YD are rare in sample 2N. The onset and termination of the YD event are characterized in sample 2N with wider fluorescent banding, and thus, reliable $|\Delta^{18}O|$ analyses.

The onset of the YD is marked by a decrease in $|\Delta^{18}O|$ values (Fig. 2.5B). Although there are few $|\Delta^{18}O|$ measurements from the height of the YD, the convergence of the running averages of bright and dark $\delta^{18}O$ analyses (dotted line, Fig. 2.5B) suggests $|\Delta^{18}O|$ is low during this period. In combination with the sinusoidal fluorescence pattern of the YD, the transition to low $|\Delta^{18}O|$ values may indicate a decrease in seasonality and reduced annual rainfall. Colder conditions year-round during the YD (Denton et al., 2005; Almogi-Labin et al., 2009) could reduce evaporation-induced fractionation of rainwater and shallow groundwater, thus lowering $|\Delta^{18}O|$. Furthermore, since cooler conditions would reduce organic decomposition rates in the soil (Davidson and Janssens, 2006) and widen the temporal window of organic acid production in the

overlying soil, the sinusoidal fluorescent banding pattern is likely caused by a more consistent year-round supply of dripwater to the cave. While the narrow bands and reduced $|\Delta^{18}O|$ values in sample 2N point to lower annual rainfall totals during the YD, we cannot make a quantitative estimate of annual rainfall for this period.

The pollen records that were briefly discussed in the introduction indicate that YD vegetation in the EM is not only different from that in the Holocene, but also suggest a more arid regional climate. This agrees with our hypothetical explanation of YD seasonal climate and provides another potential cause for the sinusoidal fluorescent banding pattern. Perhaps decomposition of the herbaceous vegetation of the YD (Hajar et al., 2008) produces different types or amounts of organic acids in a different seasonal time window. For now, however, we prefer the reduced seasonality explanation for sinusoidal fluorescent banding since it better explains the combined fluorescence and isotopic results.

Figure 2.5B illustrates that sample 2N records the YD termination in two stages. First, there is a period ("bright termination") where the $\delta^{18}O$ values of bright calcite decrease ~2‰ while dark calcite $\delta^{18}O$ is relatively unchanged. This first stage causes a steady increase in maximum $|\Delta^{18}O|$ values, mirroring the gradual decrease at the YD onset (see dashed line, Fig. 2.5B). In the second stage ("dark delay"), dark calcite $\delta^{18}O$ values remain high while bright calcite $\delta^{18}O$ values remain low. Near the end of the second stage, the $\delta^{18}O$ value of dark calcite abruptly reduces by ~1.5‰ so that both bright and dark calcite $\delta^{18}O$ have approached their approximate Holocene values. The delayed response of dark band $\delta^{18}O$ values fits with the interpretation of Soreq Cave hydrology (Orland et al., 2009). The integrated "baseline" $\delta^{18}O$ value of vadose groundwater is represented by dark calcite growth and lags the surface-driven signal recorded in bright calcite. We interpret that a combination of rapid reduction of EM

surface water $\delta^{18}O$ values and increased seasonal rainfall drives the large drop in bright $\delta^{18}O$ values, and the residence time of the vadose zone prevents an immediate response of dark $\delta^{18}O$ values. It is unclear why a similar delay is not observed at the onset of the YD.

We highlight two further observations from the CLFM imaging in Figure 2.5B: (1) the pattern of banding across the YD termination, and (2) the number of bands across the termination. Following the duration of the YD, where fluorescent bands are closely spaced with subtle fluorescence gradients, bands become wider and brighter at the termination. This suggests that the termination was a period of significant, rapid climatic change and that the coincident shift in $\delta^{18}O$ values does not just reflect a shift in the $\delta^{18}O$ value of the rainwater source (i.e., EM surface waters).

We estimate a minimum duration of the YD termination in the EM by counting the number of fluorescent bands across the $\delta^{18}O$ gradients identified by ion microprobe analysis. Across the first stage, "bright termination", there are 12 fluorescent bright-dark couplets following an apparent discontinuity. Thus, at a minimum (assuming no hiatuses or years of little growth during this stage), the full passage of the YD termination as reflected in EM rainfall took place over 12 years. This time span is consistent with other climate proxies that constrain environmental responses to the YD termination to a decadal scale (Taylor et al., 1997; Severinghaus et al., 1998; Steffensen et al., 2008). Across the second stage, "dark delay", there are 10 more fluorescent bright-dark couplets that represent the extra time required to complete the isotopic shift in dripwaters that reached sample 2N.

4.2.3. Heinrich event 1 and last glacial period.

Prior to 15 ka, $\Delta^{18}O$ values are different from those in the Holocene and YD in two

important ways: first, the mean of $|\Delta^{18}O|$ values is higher, and second, "reversal" of the fluorescent banding pattern is common and results in negative values of $\Delta^{18}O$ (open circles and open triangles in Fig. 2.3B). These differences in $|\Delta^{18}O|$ and fluorescent banding must be due to environmental changes, which are hypothesized below.

Before 15 ka, the mean value of $|\Delta^{18}O|$ is 1.0 with a standard deviation of 0.6; after the YD event, the mean value of $|\Delta^{18}O|$ decreases to 0.7 with a standard deviation of 0.4. A student t-test suggests that we can reject the null hypothesis (that populations have equivalent mean values) with >99% confidence. Further, a Kolmogorov-Smirnov test indicates that the cumulative distributions of each population differ significantly, with >98% confidence.

One possible cause of higher mean $|\Delta^{18}O|$ values before 15 ka is a more intense seasonal rainfall gradient; wetter wet seasons (with lower $\delta^{18}O$ values) would cause larger $|\Delta^{18}O|$ values. Similarly, a pulse of spring meltwater in periods with winter snowfall would introduce lower $\delta^{18}O$ values to the cave, resulting in increased $|\Delta^{18}O|$ values. Consider another scenario however, where rainfall persists year-round and there is no discernable dry season or baseline dripwater $\delta^{18}O$ value. Increased rainfall during warm months, when $\delta^{18}O$(rain) is higher than in winter months, would cause a wider annual range of dripwater $\delta^{18}O$ and thus, larger $|\Delta^{18}O|$ values. Therefore, in order to identify the most likely climatic interpretation of higher $|\Delta^{18}O|$ values, we must consider the reversal in fluorescent banding pattern.

Here, we examine four hypothetical environmental causes for the "reversed" fluorescent banding patterns (Figs. 2.2C and D) before 15 ka. (1) A change in the relative timing of the wet season and the production of organic acids above the cave might cause the organic acids to appear in a different location in the growth band. (2) A reduced gradient of annual rainfall

amount (i.e. less distinct wet and dry seasons) could change the timing of organic acid delivery into the cave. (3) Snowfall during H1 and YD winters might delay delivery of organic-poor dripwaters each year until spring melt, causing a sharp onset of dark calcite. (4) A change in the dominant type or amount of vegetation could alter the type and timing of organic acid production and the resultant fluorescent banding.

The first suggestion (hypothesis #1) is that given bimodal wet and dry seasons, a change in the timing of wet season rainfall events relative to the production of organic acids would change the pattern of fluorescence relative to the $\delta^{18}O$ value of calcite. Although such a scenario seems possible, it is unrealistic since the wet season determines the timing of the growing season. As long as low-$\delta^{18}O$ rainfall is coincident with wet seasons that flush accumulated organic acids into the cave, then low $\delta^{18}O$ calcite will have bright fluorescence.

The second suggestion (hypothesis #2) is that a reduced gradient of annual rainfall may contribute to the shift in the timing of fluorescence delivery relative to the observed $\delta^{18}O$ gradient. Even with lower annual rainfall totals than in the Holocene, it is conceivable that relatively consistent year-round rainfall would result in organic acids being delivered to the cave as they are produced rather than after accumulating during a dry season (as in the Holocene). Although year-round rainfall would probably not cause sharp fluorescent boundaries (as in Fig. 2.2C), such a scenario could result in the "reversed" sinusoidal pattern of fluorescence intensity illustrated in Fig. 2.2D. Furthermore, given consistent year-round rainfall, we would anticipate a plot of $\delta^{18}O$ vs. $\Delta^{18}O$ to show no evidence of the consistent baseline $\delta^{18}O$ values observed in Holocene growth (Fig. 2.4). Indeed, for "reversed sinusoidal" (Fig. 2.2D) bands between 34 and 15 ka there is not a consistent $\delta^{18}O$ baseline (Fig. A2.6D). Therefore, a reduced gradient of seasonal rainfall may cause the "reversed sinusoidal" bands. But what about the "reversed

sawtooth" (Fig. 2.2C) bands, which exhibit a $\delta^{18}O$ baseline in bright calcite (Fig. A2.6C)?

If snow cover and frozen ground persisted through the winter above Soreq Cave (hypothesis #3) this would reduce or stop both water flow and organic decomposition above the cave during the season that presently has the highest drip rates and forms bright calcite. The melting of snow in spring would then contribute a large amount of low-$\delta^{18}O$ water to the cave. If late fall rains removed organic acids from overlying groundwaters, then the snowmelt would contain few organic acids. This scenario would account for the sharp onset of dark calcite. Bands with a sharp onset of dark fluorescence occur during the cold glacial period and H1 event, when snowfall was possible.

A change in vegetation (#4) is another hypothesized cause of the fluorescence reversal. Perhaps different plant species delivered a distinct suite of organics to the soil before 15 ka, or perhaps the same organics were delivered on an alternate schedule. At present, $\delta^{13}C$ values provide the only record of vegetation changes measured in Soreq speleothems; given the assumption of isotopic equilibrium in Soreq samples, there would be a notable signal in $\delta^{13}C$ values if a shift in the ratio of C3- and C4-type plants occurred. Conventional analyses of $\delta^{13}C$ in Soreq speleothems (Bar-Matthews et al., 1997) show that vegetation changes gradually from a mix of C3 and C4 plants during glacial periods to C3-dominated interglacial periods. This gradual change does not fit the discreet difference in banding patterns before and after 15 ka. If the plant population were to change abruptly without altering the C3/C4 ratio, however, isotopic data alone would not distinguish the shifting ecosystem. Langgut et al. (2011) offer the most reliable regional pollen record across the deglaciation. Interestingly, they document a more rapid change to temperate vegetation than indicated by Soreq $\delta^{13}C$ measurements. Going forward, one way to resolve this discrepancy – albeit at low resolution – might be by direct analysis of lipid

compounds in sample 2N (e.g., Rushdi et al., 2011).

It is evident that, independent of other regional paleoclimate records, the fluorescence reversal represents a regional climatic response. We suggest that "reversed sinusoidal" fluorescent bands (Fig. 2.2D) during H1 may indicate a year-round supply of dripwater to the upper soil column and cave. Furthermore, bands with "reversed sawtooth" fluorescence (Fig. 2.2C), most common during the H1 event, may indicate spring snowmelt. Future work will determine if vegetation changes play a role in the fluorescent banding reversals. For now, we look to test our interpretations with evidence from other regional and global environmental proxies.

Denton et al. (2010) compile prior work (including Crowley, 1992; Broecker, 1998; Clark et al., 2004; Wang et al., 2006; Toggweiler et al., 2006; Anderson et al., 2009; Cheng et al., 2009) and present an intriguing global-scale model of the last deglaciation from which we can infer seasonality in the EM. In this model, glacial meltwater input to the North Atlantic slows Atlantic Meridional Overturning Circulation, causes the H1 and YD stadials, and induces the spread of winter sea ice in the North Atlantic and severe winters in the Northern Hemisphere. Reduced heat transport to the Northern Hemisphere, a result of the bipolar seesaw (Broecker, 1998), causes the Intertropical Convergence Zone to shift south, which in turn moves atmospheric circulation cells, including the westerlies in both hemispheres, to the south. In the Afro-Asian monsoon region, these changes result in widespread drought during H1 (Stager et al., 2011). In the EM, shifting the Northern Hemisphere westerlies to the south during the H1 and YD events could move these winds and their characteristic weather systems over Soreq Cave and bring moisture to the region on a year-round basis. The sinusoidal fluorescence in sample 2N during both the H1 and YD may indicate year-round rainfall, but it is important to note that this

scenario could still result in less total annual rainfall than during the Bølling-Allerød or Holocene. Our snowmelt explanation for bands with "reversed sawtooth" fluorescence (Fig. 2.2C) also fits the Denton et al. model, although the increased occurrence of this band pattern before 15 ka suggests H1 winters above Soreq had more snowfall than YD winters.

Although it is instructive to test our climate hypotheses against a simplified explanation of the Denton et al. (2010) model, we acknowledge the need for more rigorous tests. Other regional paleoclimate proxies, including both Dead Sea level and pollen records, can potentially contribute to these tests. Drawbacks with these alternative proxies, however, confound any strong conclusions at this time. Ongoing analysis of trace elements in sample 2N will provide more information to evaluate on both millennial and sub-annual timescales, and may further explain hydrologic and vegetation changes. Finally, examining isotope-enabled climate simulations (Schmidt et al., 2007; LeGrande and Schmidt, 2008; Tierney et al., 2011) of the last deglaciation at seasonal resolution may provide additional constraints for our seasonal climate hypotheses, the interpretation of EM climate proxies, and the mechanisms that drive EM climate change.

5. CONCLUSIONS

This study presents the first detailed record of seasonal-scale environmental information from a speleothem that grew during the last deglaciation. The combination of 10 μm-diameter spot analyses of $\delta^{18}O$ by ion microprobe and CLFM imaging allows for the study of sub-domains of individual annual growth bands. The large data set provides new constraints for interpreting climate change at the sub-annual scale. This high-resolution analytical method is ideal for examining both rapid climate change events (e.g., Younger Dryas termination) as well as

seasonal climate differences between broad time slices (e.g., Younger Dryas vs. Holocene).

High-precision ion microprobe analyses of $\delta^{18}O$ (0.3‰, 2 s.d., 10 μm-diameter spot) in samples 2N (34-4 ka) and 2-6 (2.2-0.9 ka) show regular fluctuations across fluorescent bands that record seasonal rainfall variability. Calculated values of $|\Delta^{18}O|$, the magnitude of the $\delta^{18}O$ difference within individual annual growth bands, indicate the seasonal character of rainfall. The fluorescent patterns of individual growth bands contribute further to paleoclimate interpretations:

(1) In the Holocene, the ubiquitous sawtooth pattern of both $\delta^{18}O$ and fluorescence variability (Fig. 2.2A) indicates that the modern seasonal regime of wet winters and dry summers has been consistent since 10.5 ka. Smaller $|\Delta^{18}O|$ values indicate dryer years.

(2) Small values of $|\Delta^{18}O|$ and narrow banding indicate that climate during the Younger Dryas may have been drier than during the Holocene. Sinusoidal intensity of fluorescent banding, however, suggests that dripwater supply from the overlying soil column was more consistent throughout the year than in the Holocene.

(3) The isotope record of the YD termination in sample 2N occurs in multiple stages, which supports the interpretation of cave hydrology presented by Orland et al. (2009). Band-counting across the Younger Dryas termination, constrained by the *in situ* $\delta^{18}O$ data, gives a minimum estimate of 12 years for the isotope shift associated with the hemisphere-wide rapid warming event.

(4) The Heinrich 1 event is characterized by a regular reversal in the fluorescent banding pattern (i.e. dark-before-bright banding) relative to that in the Holocene. Furthermore, the mean $|\Delta^{18}O|$ value during this period is higher than during the YD and Holocene. Decreased seasonal rainfall gradients, regular snow cover, and different overlying vegetation are proposed as possible causes for these observations. The banding patterns

and $|\Delta^{18}O|$ values indicate that the modern amount effect – an empirical relationship of annual rainfall $\delta^{18}O$ value to rainfall amount – is unreliable when applied to Soreq Cave speleothems during either Heinrich 1 or the last glacial period.

(5) The fluorescent banding and $|\Delta^{18}O|$ values during the last glacial stadial are most similar to that during Heinrich 1, suggesting comparable climate.

Acknowledgments

We thank N. Kita for help with ion microprobe set-up and operation; F. He, A. Carlson, S. Meyers, J. Williams, and C. Johnson for fruitful conversation and guidance; A. Trzaskus for help with an ion microprobe analysis session; B. Hess, J. Kern, and M. Spicuzza for assistance with sample preparation; L. Rodenkirch for guidance at the Keck Bioimaging Lab at UW-Madison; J. Fournelle and D. Ortiz for guidance at the UW-Madison SEM lab. V. Ersek and two anonymous reviewers provided helpful comments that improved this manuscript. Funding support came from Comer Science and Education Foundation, NSF (AGS-1003487, EAR-0838058), DOE (93ER14389), and the United States-Israel Binational Science Foundation (2010316). WiscSIMS is partially supported by NSF-EAR (0319230, 0744079, 1053466).

References

Affek H. P., Bar-Matthews M., Ayalon A., Matthews A. and Eiler J. M., (2008) Glacial/interglacial temperature variations in Soreq cave speleothems as recorded by 'clumped isotope' thermometry. *Geochim. Cosmochim. Acta* **72**, 5351-5360.

Almogi-Labin A., Bar-Matthews M., and Ayalon A. (2004) Climate variability in the Levant and northeast Africa during the Late Quaternary based on marine and land records. In *Human Paleoecology in the Levantine Corridor* (eds. N. Goren-Inbar and J. D. Speth). Oxbow Press, Oxford. pp. 117-134.

Almogi-Labin A., Bar-Matthews M., Shriki D., Kolosovsky E., Paterne M., Schilman B., Ayalon A., Aizenshtat Z. and Matthews A. (2009) Climatic variability during the last ~90 ka of the southern and northern Levantine basin as evident from marine records and speleothems. *Quat. Sci. Rev.* **28**, 2882-2896.

Anderson R. F., Ali A., Bradtmiller L. I., Nielsen S. H. H., Fleisher M. Q., Anderson B. E. and Burckle L. H. (2009) Wind-driven Upwelling in the Southern Ocean and the Deglacial Rise in Atmospheric CO_2. *Science* **323**, 1443-1448.

Atkinson T. C., Briffa K. R. and Coope G. R. (1987) Seasonal temperatures in Britain during the past 22,000 years, reconstructed using beetle remains. *Nature* **325**, 587-592.

Ayalon A., Bar-Matthews M. and Sass E. (1998) Rainfall-recharge relationships within a karstic terrain in the Eastern Mediterranean semi-arid region, Israel: $\delta^{18}O$ and δD characteristics. *J. Hydro.* **207,** 18-31.

Ayalon A., Bar-Matthews M. and Kaufman A. (1999) Petrography, strontium, barium and uranium concentrations, and strontium and uranium isotope ratios in speleothems as palaeoclimatic proxies: Soreq Cave, Israel. *The Holocene* **9,** 715-722.

Ayalon A., Bar-Matthews M. and Schilman B. (2004) Rainfall Isotopic Characteristics at Various Sites In Israel and the Relationships with Unsaturated Zone Water. In *Geological Survey of Israel Reports, GSI/16/04*. The Ministry of National Infrastructures, Jerusalem.

Baker A., Smart P. L., Edwards R. L. and Richards D. A. (1993) Annual growth banding in a cave stalagmite. *Nature* **364,** 518-520.

Baker A., Barnes W. L. and Smart P. L. (1996) Speleothem luminescence intensity and spectral characteristics: Signal calibration and a record of palaeovegetation change. *Chem. Geol.* **130**, 65-76.

Baldini J. U. L., McDermott F., Hoffman D. L., Richards D. A. and Clipson N. (2008) Very high-frequency and seasonal cave atmosphere PCO_2 variability: Implications for stalagmite growth and oxygen isotope-based paleoclimate records. *Earth Planet. Sci. Lett.* **272**, 118-129.

Bard E., Rostek F., Turon J.-L. and Gendreau S. (2000) Hydrological impact of Heinrich Events in the subtropical northeast Atlantic. *Science* **289**, 1321-1324.

Bar-Matthews M., Ayalon A., Matthews A., Sass E. and Halicz L. (1996). Carbon and oxygen isotope study of the active water-carbonate system in a karstic Mediterranean cave: Implications for paleoclimate research in semiarid regions. *Geochim. Cosmochim. Acta* **60,** 337-347.

Bar-Matthews M., Ayalon A. and Kaufman A. (1997) Late Quaternary paleoclimate in the eastern Mediterranean region from stable isotope analysis of speleothems at Soreq Cave, Israel. *Quat. Res.* **47,** 155-168.

Bar-Matthews M., Ayalon A., Kaufman A. and Wasserburg G. J. (1999) The Eastern Mediterranean paleoclimate as a reflection of regional events: Soreq Cave, Israel. *Earth Planet. Sci. Lett.* **166**, 85-95.

Bar-Matthews M., Ayalon A. and Kaufman A. (2000) Timing and hydrological conditions of sapropel events in the Eastern Mediterranean, as evident from speleothems, Soreq cave, Israel. *Chem. Geol.* **169**, 145-156.

Bar-Matthews M., Ayalon A., Gilmour M., Matthews A. and Hawkesworth C. J. (2003) Sea-land oxygen isotopic relationships from planktonic foraminifera and speleothems in the Eastern Mediterranean region and their implication for paleorainfall during interglacial intervals. *Geochim Cosmochim. Acta* **67,** 3181-3199.

Bar-Matthews M., Marean C. W., Jacobs Z., Karkanas P., Fisher E. C., Herries A. I. R., Brown K., Williams H. M., Bernatchez J., Ayalon A. and Nielssen P. J. (2010) A high resolution and continuous isotopic speleothem record of paleoclimate and paleoenvironment from 90-53 ka from Pinnacle Point on the south coast of South Africa. *Quat. Sci. Rev.* **29**, *2131-2145.*

Bar-Matthews M. and Ayalon A. (2011) Mid-Holocene climate variations revealed by high-resolution speleothem records from Soreq Cave, Israel and their correlation with cultural changes. *The Holocene* **21**, 163-171.

Baldini J. U. L., McDermott F., Hoffmann D. L., Richards D. A. and Clipson N. (2008) Very high-frequency and seasonal cave atmosphere PCO_2 variability: Implications for stalagmite growth and oxygen isotope-based paleoclimate records. *Earth Planet. Sci. Lett.* **272**, 118-129.

Banner J. L., Guilfoyle A., James E. W., Stern L. A. and Musgrove M. (2007). Seasonal variations in modern speleothem calcite growth in central Texas, USA. *J. Sed. Res.* **77**, 615-622.

Bartov Y., Goldstein S. L., Stein M. and Enzel Y. (2003) Catastrophic arid episodes in the Eastern Mediterranean linked with the North Atlantic Heinrich events. *Geology* **31**, 439-442.

Baruch U. and Bottema S. (1991) Palynological evidence for climatic changes in the Levant ca. 17,000-9,000 B. P. In *The Natufian Culture in the Levant. International Monographs in Prehistory, Archaeological Series 1* (eds. O. Bar-Yosef and F. R. Valla), Ann Arbor/Michigan, pp. 11-20.

Baruch U. and Bottema S. (1999) A new pollen diagram from Lake Hula: vegetational, climatic, and anthropogenic implications. In *Ancient lakes: Their cultural and biological diversity* (eds. H. Kawanabe, G. W. Coulter and A. C. Roosevelt), Ghent: Kenobi Productions , pp. 75-86.

Bookman R., Enzel Y., Agnon A. and Stein M. (2004) Late Holocene lake-levels of the Dead Sea. *GSA Bull.* **116,** 555-571.

Bottema S. (1995) The Younger Dryas in the eastern Mediterranean. *Quat. Sci. Rev.* **14**, 883-891.

Broecker W. S. (1998) Paleocean circulation during the last deglaciation: A bipolar seesaw? *Paleocean.* **13**, 119-121.

Cheng H., Edwards R. L., Broecker W. S., Denton G. H., Kong X., Wang Y., Zhang R. and Wang X. (2009) Ice Age Terminations. *Science* **326**, 248-252.

Clark P. U., McCabe A. M., Mix A. C. and Weaver A. J. (2004) Rapid rise of sea level 19,000 years ago and its global implications. *Science* **304**, 1141-1144.

Crowley T. J. (1992) North Atlantic deep water cools the Southern Hemisphere. *Paleocean.* **7**, 489-497.

Davidson E. A. and Janssens I. A. (2006) Temperature sensitivity of soil carbon decomposition and feedbacks to climate change. *Nature* **440**, 165-173.

De Lange G. J., Thomson J., Reitz A., Slomp C. P., Principato M. S., Erba E. and Corselli C. (2008) Synchronous basin-wide formation and redox-controlled preservation of a Mediterranean sapropel. *Nature Geo.* **1**, 606-610.

Denton G. H., Alley R. B., Comer G. C. and Broecker W. S. (2005) The role of seasonality in abrupt climate change. *Quat. Sci. Rev.* **24**, 1159-1182.

Denton G. H., Anderson R. F., Toggweiler J. R., Edwards R. L., Schaefer J.M and Putnam A. E. (2010) The Last Glacial Termination. *Science* **328**, 1652-1656.

Enzel Y., Bookman R., Sharon D., Gvirtzman H., Dayan U., Baruch Z. and Stein, M. (2003) Late Holocene climates of the Near East deduced from Dead Sea level variations and modern regional winter rainfall. *Quat. Res.* **60**, 263-273.

Fairchild I. J., Smith C. L., Baker A., Fuller L., Spötl C., Mattey D., McDermott F. and E.I.M.F. (2006) Modification and preservation of environmental signals in speleothems. *Earth Sci. Rev.* **75**, 105-153.

Frumkin A., Ford D. C. and Schwarcz H. P. (2000) Paleoclimate and vegetation of the last glacial cycles in Jerusalem from a speleothem record. *Glob. Biogeochem. Cycl.* **14**, 863-870.

Hajar L., Khater C. and Cheddadi R. (2008) Vegetation changes during the late Pleistocene and Holocene in Lebanon: a pollen record from the Bekaa Valley. *The Holocene* **18**, 1089-1099.

Hendy C. H. (1971) The isotopic geochemistry of speleothems – I. The calculation of the effects of different modes of formation on the isotopic composition of speleothems and their applicability as paleoclimate indicators. *Geochim. Cosmochim. Acta* **35**, 801-824.

IPCC (2007) Climate Change 2007: The physical science basis. Summary for policymakers. Contribution of working group I to the fourth assessment report. The Intergovernmental Panel on Climate Change.

Kallel N., Paterne M., Duplessy J.-C., Vergnaud-Grazzini C., Pujol C., Labeyrie L., Arnold M., Fontugne M. and Pierre C. (1997) Enhanced rainfall in the Mediterranean region during the last sapropel event. *Ocean. Acta* **20**, 697-712.

Kaufman A., Wasserburg G. J., Porcelli D., Bar-Matthews M., Ayalon A. and Halicz L. (1998) U-Th isotope systematics from the Soreq cave, Israel and climatic correlations. *Earth Planet. Sci. Lett.* **156,** 141-155.

Kita N. T., Ushikubo T., Fu B. and Valley J. W. (2009) High Precision SIMS Oxygen Isotope Analyses and the Effect of Sample Topography, *Chem. Geol.* **264**, 43-57.

Kolodny Y., Bar-Matthews M., Ayalon A. and McKeegan K. D. (2003). A high spatial resolution $\delta^{18}O$ profile of a speleothem using an ion microprobe. *Chem. Geol.* **197**, 21-28.

Kolodny Y., Stein M. and Machlus M. (2005) Sea-rain-lake relation in the Last Glacial East Mediterranean revealed by $\delta^{18}O$-$\delta^{13}C$ in Lake Lisan aragonites. *Geochim. Cosmochim. Acta* **69**, 4045-4060.

Kozdon R., Ushikubo T., Kita N. T., Spicuzza M. and Valley J. W. (2009) Intratest oxygen isotope variability in the planktonic foraminifer *N. pachyderma:* Real vs. apparent vital effects by ion microprobe. *Chem. Geol.* **258**, 327-337.

Kozdon R., Kelly D. C., Kita N. T., Fournelle J. H. and Valley J. W. (2011) Planktonic foraminiferal oxygen isotope analysis by ion microprobe technique suggests warm tropical sea surface temperatures during the Early Paleogene. *Paleocean.* **26**, PA3206.

Lachniet M. S. (2009) Climatic and environmental controls on speleothem oxygen-isotope values. *Quat. Sci. Rev.* **28**, 412-432.

Langgut D., Almogi-Labin A., Bar-Matthews M. and Weinstein-Evron M. (2011) Vegetation and climate changes in the South Eastern Mediterranean during the Last Glacial-Interglacial cycle (86 ka): new marine pollen record. *Quat. Sci. Rev.* **30**, 3960-3972.

LeGrande A. N. and Schmidt G. A., (2008) Ensemble, water isotope-enabled, coupled general circulation modeling insights into the 8.2 ka event. *Paleocean.* **23**, PA3207.

Lisker S., Vaks A., Bar-Matthews M., Porat R. and Frumkin A. (2009) Stromatolites in caves of the Dead Sea Fault Escarpment: implications to latest Pleistocene lake levels and tectonic subsidence. *Quat. Sci. Rev.* **28**, 80-92.

Marino G., Rohling E. J., Sangiorgi F., Hayes A., Casford J. L., Lotter A. F., Kucera M. and Brinkhuis H. (2008) Early and middle Holocene in the Aegean Sea: interplay between high and low latitude climate variability. *Quat. Sci. Rev.* **28**, 3246-3262.

Matthews A., Ayalon A. and Bar-Matthews M. (2000) D/H ratios of fluid inclusions of Soreq Cave Israel speleothems as a guide to the Eastern Mediterranean Meteoric Line relationships in the last 120 ky. *Chem. Geol.* **166,** 183-191.

McDermott F. (2004) Palaeo-climate reconstruction from stable isotope variations in speleothems: a review. *Quat. Sci. Rev.* **23**, 901-918.

McGarry S. F. and Baker A. (2000) Organic acid fluorescence: applications to speleothem palaeoenvironmental reconstruction. *Quat. Sci. Rev.* **19**, 1087-1101.

McGarry S. F., Bar-Matthews M., Matthews A., Vaks A., Schilman B. and Ayalon A. (2004) Constraints on hydrological and paleotemperature variations in the eastern Mediterranean region in the last 140ka given by the δD values of speleothem fluid inclusions. *Quat. Sci. Rev.* **23,** 919-934.

Mickler P. J., Stern L. A. and Banner J. L. (2006) Large kinetic isotope effects in modern speleothems. *GSA Bull.* **118**, 65-81.

Orland I. J., Bar-Matthews M., Kita N. T., Ayalon A., Matthews A. and Valley J. W. (2009) Climate deterioration in the eastern Mediterranean as revealed by ion microprobe analysis of a speleothem that grew from 2.2 to 0.9 ka in Soreq Cave, Israel. *Quat. Res.* **71**, 27-35.

Rossignol-Strick M., Nesteroff W., Olive P. and Vergnaud-Grazzini C. (1982) After the deluge: Mediterranean stagnation and sapropel formation. *Nature* **295**, 105-110.

Rossignol-Strick M. (1995) Sea-land correlation of pollen records in the Eastern Mediterranean for the glacial-interglacial transition: biostratigraphy versus radiometric time-scale. *Quat. Sci. Rev.* **14**, 893-915.

Rushdi A. I., Clark P. U., Mix A. C., Ersek V., Simoneit B. R. T., Cheng H. and Edwards R. L. (2011) Composition and sources of lipid compounds in speleothem calcite from southwestern Oregon and their paleoenvironmental implications. *Environ. Earth Sci.* **62**, 1245-1261.

Schmidt G. A., LeGrande A. N. and Hoffman G. (2007) Water isotope expressions of intrinsic and forced variability in a coupled ocean-atmosphere model. *J. Geophys. Res.* **112**, D10103.

Scholz D. and Hoffman D. L. (2011) StalAge – An algorithm designed for construction of speleothem age models. *Quat. Geochron.* **6**, 369-382.

Senesi N., Miano T. M., Provenzano M. R. and Brunetti G. (1991) Characterisation, differentiation and classification of humic substances by fluorescence spectroscopy. *Soil Science* **152**, 259-271.

Severinghaus J. P., Sowers T., Brook E. J., Alley R. B. and Bender M. L. (1998) Timing of abrupt climate change at the end of the Younger Dryas interval from thermally fractionated gases in polar ice. *Nature* **391**, 141-146.

Stager J. C., Ryves D. B., Chase B. M. and Pausata F. S. R. (2011) Catastrophic Drought in the Afro-Asian Monsoon Region During Heinrich Event 1. *Science* **331**, 1299-1302.

Steffensen J. P., Andersen K. K., Bigler M., Clausen H. B., Dahl-Jensen D., Fischer H., Goto-Azuma K., Hansson M., Johnsen S. J., Jouzel J., Masson-Delmotte V., Popp T., Rasmussen S. O., Rothlisberger R., Ruth U., Stauffer B., Siggaard-Andersen M.-L., Sveinbjornsdottir A. E., Svensson A. and White J. W. C. (2008) High-resolution Greenland ice core data show abrupt climate change happens in few years. *Science* **321**, 680-684.

Stein M., Torfstein A., Gavrieli I. and Yechieli Y. (2010) Abrupt aridities and salt deposition in the post-glacial Dead Sea and their North Atlantic connection. *Quat. Sci. Rev.* **29**, 567-575.

Tan M., Baker A., Genty D., Smith C., Esper J. and Cai B. (2006) Applications of stalagmite laminae to paleoclimate reconstructions: Comparison with dendrochronology/ climatology. *Quat. Sci. Rev.* **25**, 2103-2117.

Taylor K. C., Mayewski P. A., Alley R. B., Brook E. J., Gow A. J., Grootes P. M., Meese D. A., Saltzman E. S., Severinghaus J. P., Twickler M. S., White J. W. C., Whitlow S. and Zielinski G. A. (1997) The Holocene-Younger Dryas Transition Recorded at Summit, Greenland. *Science* **278**, 825-827.

Tierney J. E., Lewis S. C., Cook B. I., LeGrande A. N. and Schmidt G. A. (2011). Model, proxy and isotopic perspectives on the East African Humid Period. *Earth Planet. Sci. Lett.* **307**, 103-112.

Toggweiler J. R., Russell J. L. and Carson S. R. (2006) Midlatitude westerlies, atmospheric CO_2, and climate change during the ice ages. *Paleocean.* **21**, PA2005.

Torfstein A., Haase-Schramm A., Waldmann N., Kolodny Y. and Stein M. (2009) U-series and oxygen isotope chronology of the mid=Pleistocene Lake Amora (Dead Sea basin). *Geochim. Cosmochim. Acta* **73**, 2603-2630.

Treble P. C., Schmitt A. K., Edwards R. L., McKeegan K. D., Harrison T. M., Grove M., Chen H. and Wang Y. J. (2007) High resolution SIMS $\delta^{18}O$ analyses of Hulu Cave speleothem at the time of Heinrich event 1. *Chem. Geol.* **238,** 197-212.

Tukey J. W. (1977) *Exploratory Data Analysis*. Addison-Wesley Publishing Co., Reading.

Valley J. W. and Kita N. T. (2005) First Results from the UW CAMECA IMS-1280. Fourth Biennial Geochemical SIMS Workshop.

Valley J. W. and Kita N. T. (2009) *In situ* Oxygen Isotope Geochemistry by Ion Microprobe. In *MAC Short Course: Secondary Ion Mass Spectrometry in the Earth Sciences*, vol. 41 (ed. M. Fayek). Mineralogical Association of Canada, Toronto. pp. 19-63.

Vaks A., Bar-Matthews M., Ayalon A., Matthews A., Frumkin A., Dayan U., Halicz L., Almogi-Labin A. and Schilman B. (2006) Paleoclimate and location of the border between Mediterranean climate region and the Saharo-Arabian Desert as revealed by speleothems from the northern Negev Desert, Israel. *Earth Planet. Sci. Lett.* **249**, 384-399.

Verheyden S., Nader F. H., Cheng H., Edwards L. R. and Swennen R. (2008) Paleoclimate reconstruction in the Levant region from the geochemistry of a Holocene stalagmite from the Jeita cave, Lebanon. *Quat. Res.* **70**, 368-381.

Waldmann N., Torfstein A. and Stein M. (2010) Northward intrusions of low- and mid-latitude storms across the Saharo-Arabian belt during past interglacials. *Geology* **38**, 567-570.

Wang Y. J., Cheng H., Edwards R. L., An Z. S., Wu J. Y., Shen C.-C. and Dorale J. (2001) A High-Resolution Absolute-Dated Late Pleistocene Monsoon Record from Hulu Cave, China. *Science* **294**, 2345-2348.

Wang X., Auler A. S., Edwards R. L., Cheng H., Ito E. and Solheid M. (2006) Interhemispheric anti-phasing of rainfall during the last glacial period. *Quat. Sci. Rev.* **25**, 3391-3403.

Wong C. I., Banner J. L. and Musgrove M. (2011) Seasonal dripwater Mg/Ca and Sr/Ca variations driven by cave ventilation: Implications for and modeling of speleothem paleoclimate records. *Geochim. Cosmochim. Acta* **75**, 3514-3529.

Figures

Figure 2.1: Stalactite sample 2N from Soreq cave, Israel, cut in horizontal cross-section. Samples from the matching face were drilled for geochronology (Table 2.1). The "working traverse" for ion microprobe analysis of $\delta^{18}O$ is highlighted with a white dashed line and the location of the 1 cm cubes (A-P) cut for ion microprobe mounts are outlined in black. Areas of irregular calcite crystal growth, indicated by white arrows, are visible in cubes M, N, and O. Inset, left: picture of a 25 mm round epoxy mount for ion microprobe analysis with cubes E and F positioned with the working traverse centered and UWC-3 calcite standard grains in the middle. Inset, right: map of Israel showing the location of Soreq Cave (SC), Jerusalem (J), the Eastern Mediterranean Sea (EM) and the Dead Sea (DS).

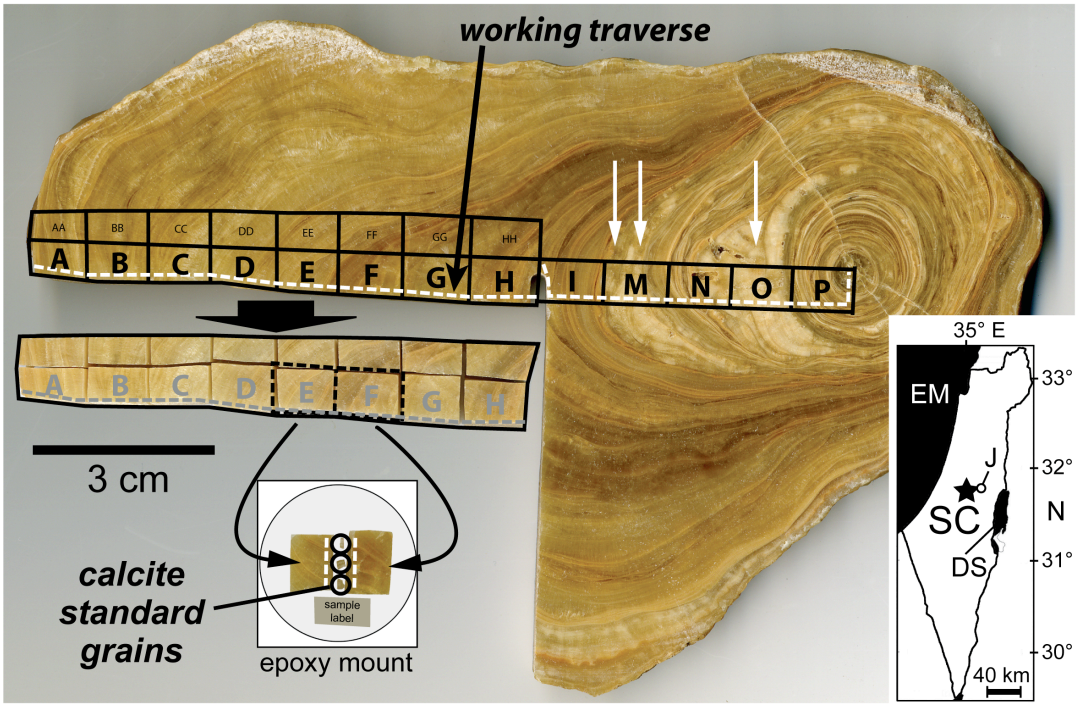

Figure 2.2: Four patterns (A-D) of fluorescence and $\delta^{18}O$ variability within annual growth bands; each pattern is assigned a symbol for use in Figures 2.3B and 2.5. A schematic illustration of each pattern is shown above an example from sample 2N. In each plot of $\delta^{18}O$, blue crosses and green triangles represent dark and bright fluorescent calcite, respectively. Error bars indicate 2 s.d. of each actual $\delta^{18}O$ analysis. Red spots in CLFM images show the location of ion microprobe analyses (~10 μm diameter). Note the definition of $|\Delta^{18}O|$ illustrated by the vertical bars.

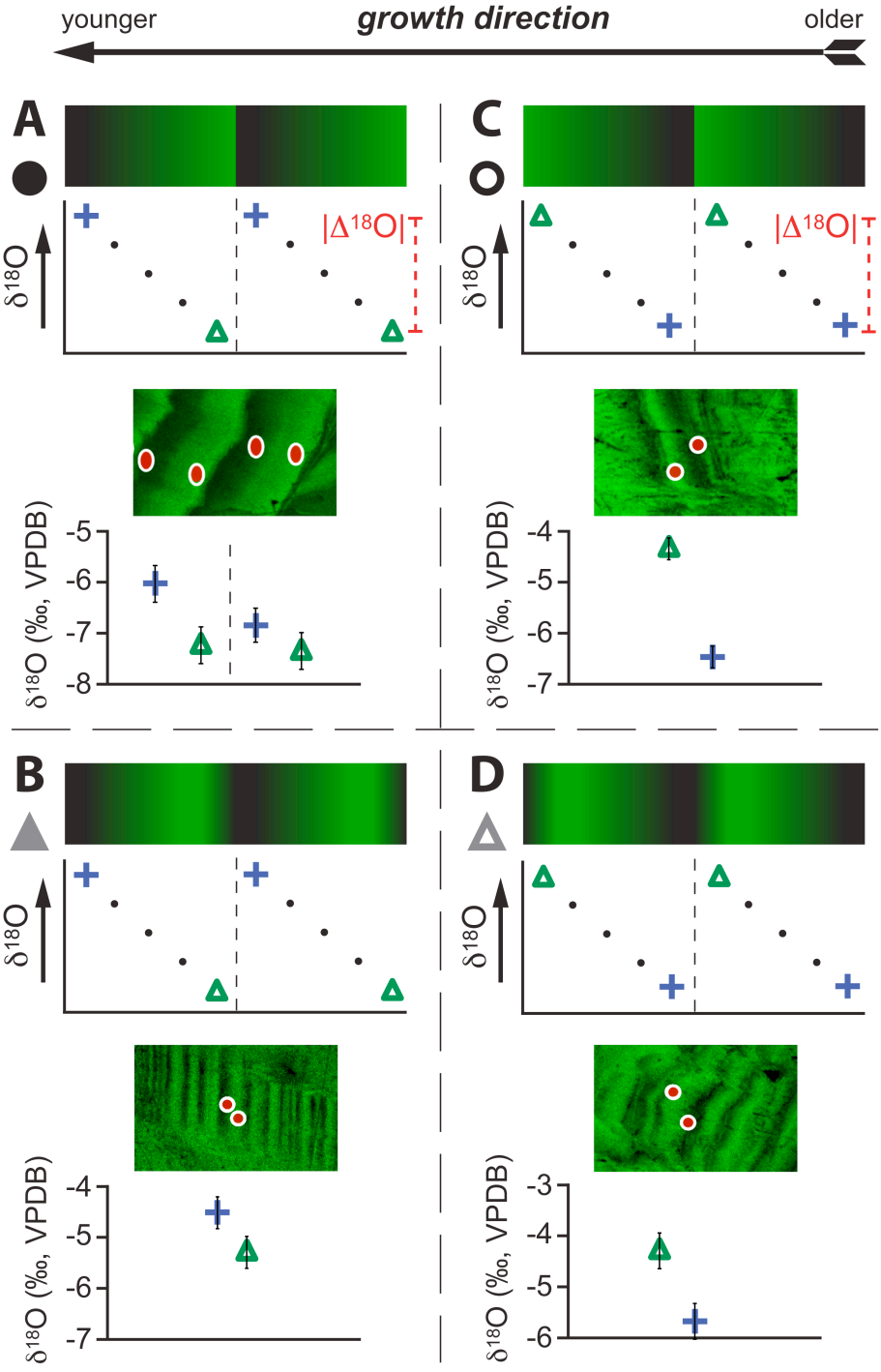

Figure 2.3 (next page): A shows the measured $\delta^{18}O$ (‰, VPDB) values for ion microprobe analysis of the brightest (green triangles) and darkest (blue crosses) fluorescent calcite within each band across sample 2N (34-4 ka). Data from sample 2-6 (Orland et al., 2009) is included from 2.2-0.9 ka to illustrate the continuity of $\delta^{18}O$ and fluorescence patterns in different samples during the Holocene. During the Holocene, higher $\delta^{18}O$ values represent drier climates while lower $\delta^{18}O$ values are characteristic of wetter climates. The heavy black line, an 11-point running average of dark calcite from ~14-4 ka, shows the general trend of "baseline" $\delta^{18}O$ values during periods of time when dark calcite has consistently higher $\delta^{18}O$ values. Zones of irregular calcite growth are outlined by the hashed rectangles between 22 and 14 ka. U-Th ages with 2σ errors and the average 2 s.d. for $\delta^{18}O$ measurements (0.30‰) are shown at the top. Panel **B** shows values of $|\Delta^{18}O|$ [where $\Delta^{18}O = \delta^{18}O(\text{dark calcite}) - \delta^{18}O(\text{bright calcite})$] of individual bands. See Figure 2.2 for the explanation of the symbols used to plot $|\Delta^{18}O|$. The Younger Dryas (YD), Heinrich 1 (H1), and Sapropel 1 (S1) events are highlighted with yellow shaded bars. Dates for H1 are from Bard et al. (2000), and dates for S1 are from Bar-Matthews et al. (2000).

Figure 2.3:

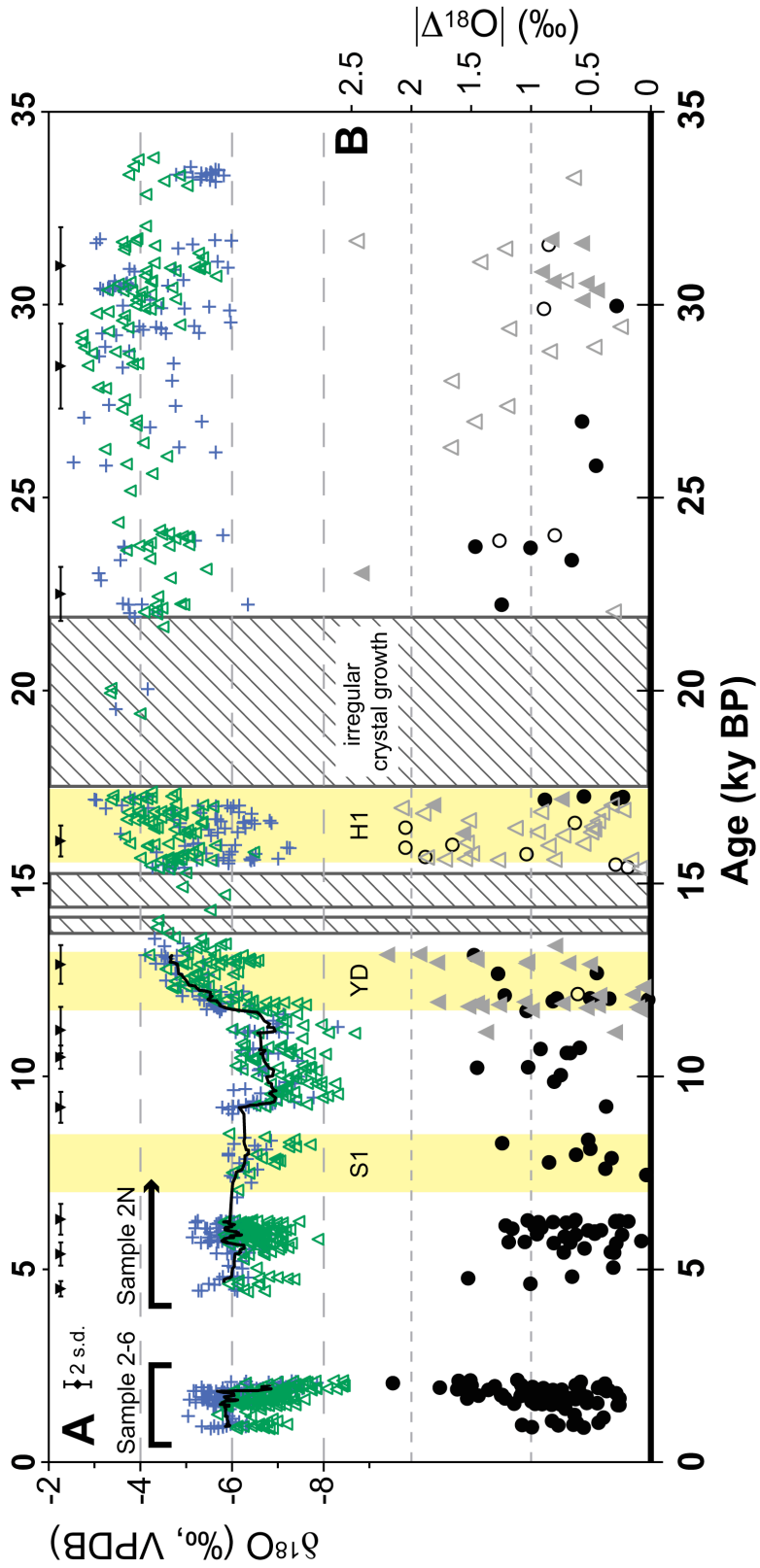
|Δ18O| (‰)
2.5
2
1.5
1
0.5
0
B
irregular
crystal growth
H1
YD
S1
Age (ky BP)
0
5
10
15
20
25
30
35
A
2 s.d.
Sample 2N
Sample 2-6
-2
-4
-6
-8
δ18O (‰, VPDB)

Figure 2.4: Plot of $\delta^{18}O$(calcite) vs. $|\Delta^{18}O|$(dark-bright) for every pair of analyses within a single annual band between 10.5 and 4 ka (n = 49). As in Figure 2.3, green triangles represent $\delta^{18}O$ measurements made in bright calcite and blue crosses represent $\delta^{18}O$ measurements made in dark calcite. Linear best-fit regressions of each population illustrate trends discussed in the text. The dashed line is fit to measurements in bright fluorescent calcite (R^2 = 0.33) and the solid line (mean = -6.08‰, s.d. = 0.42‰) is fit to measurements in dark calcite.

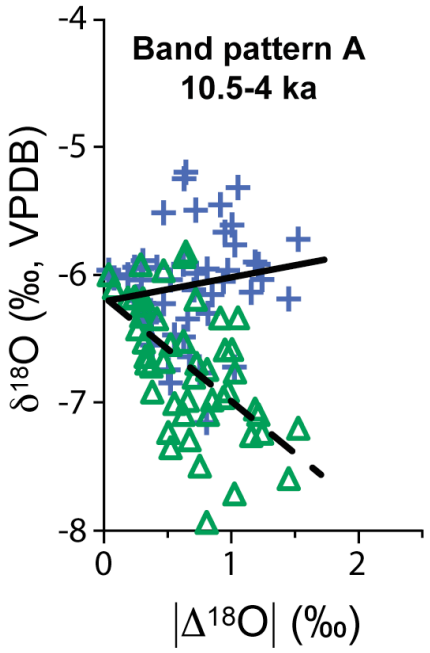

Figure 2.5 (next page): Oxygen isotope data and CLFM imaging of sample 2N across the Sapropel 1 (panel A) and Younger Dryas (panel B) events. In both panels A and B, the upper portion of the graph shows $\delta^{18}O$(calcite) values across the climate event as recorded in sample 2N. The solid lines indicate running averages of the $\delta^{18}O$ data values with dark and bright fluorescent classifications. The lower portion of each graph plots $|\Delta^{18}O|$(dark-bright) across the same time period. The red dotted lines indicate the difference between the running averages of dark and bright $\delta^{18}O$ analyses. In panel B, the heavy dashed line illustrates an interesting pattern of $|\Delta^{18}O|$ variability at the onset and termination of the Younger Dryas (see text for discussion). The corresponding CLFM images from sample 2N are stitched together above the graphs and the shaded boxes indicate corresponding portions of the $\delta^{18}O$ record. The white arrows in the CLFM images show the location of banding discontinuities.

Figure 2.5:

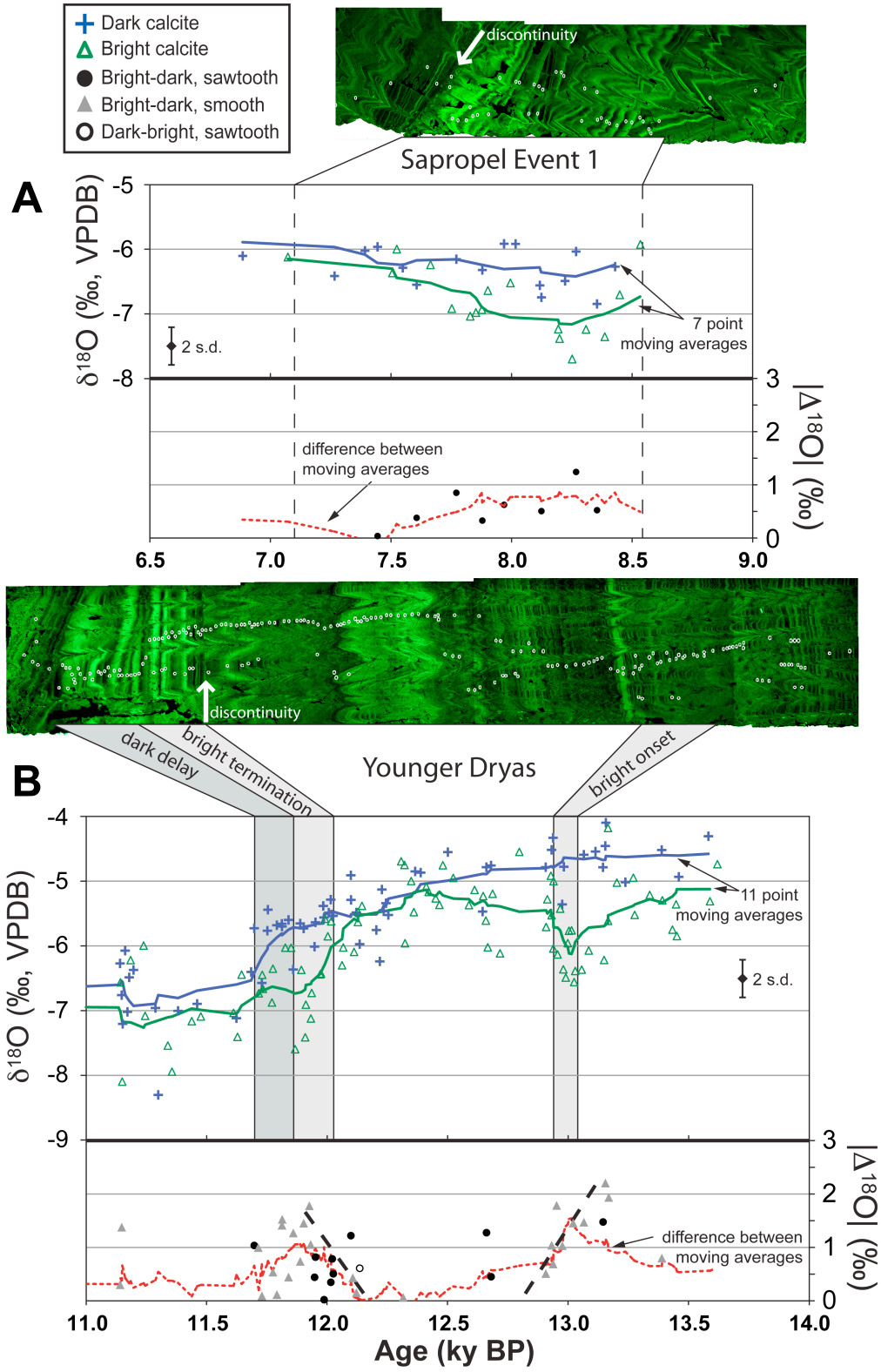
Dark calcite
Bright calcite
Bright-dark, sawtooth
Bright-dark, smooth
Dark-bright, sawtooth
discontinuity
Sapropel Event 1
A
δ18O (‰, VPDB)
2 s.d.
7 point
moving averages
difference between
moving averages
|Δ18O| (‰)
6.5
7.0
7.5
8.0
8.5
9.0
discontinuity
dark delay
bright termination
Younger Dryas
bright onset
B
11 point
moving averages
2 s.d.
difference between
moving averages
11.0
11.5
12.0
12.5
13.0
13.5
14.0
Age (ky BP)

Table 2.1: U/Th age data from multi-collector inductively coupled plasma mass spectrometry analysis of sample 2N

Sample name	Distance from edge (mm)	U conc. (ppm)	$^{234}U/^{238}U$	$^{230}Th/^{234}U$	$^{230}Th/^{232}Th$	Age (yr) uncorrected	Age (yr) corrected
2N-1	**4.6**	**0.4200 ± 0.0003**	**1.02401 ± 0.00120**	**0.04735 ± 0.00070**	**13.10 ± 0.20**	**5300 ± 300**	**4500 ± 200**
2N-3B	**13.7**	**0.3898 ± 0.0003**	**1.01753 ± 0.00113**	**0.05845 ± 0.00094**	**10.29 ± 0.17**	**6500 ± 200**	**5400 ± 300**
2N-4C	17.0	0.3785 ± 0.0003	1.01523 ± 0.00130	0.05800 ± 0.00074	11.63 ± 0.15	6500 ± 200	5500 ± 300
2N-5B	18.9	0.3687 ± 0.0004	1.01733 ± 0.00135	0.06283 ± 0.00081	12.21 ± 0.16	7100 ± 200	6000 ± 300
2N-6	23.1	0.3682 ± 0.0002	1.01920 ± 0.00131	0.06597 ± 0.00117	13.71 ± 0.24	7400 ± 300	6000 ± 400
2N-7+8	27.2	0.5841 ± 0.0004	1.01891 ± 0.00120	0.05557 ± 0.00062	19.81 ± 0.22	600 ± 140	5600 ± 200
2N-11	36.3	0.3516 ± 0.0002	1.01923 ± 0.00152	0.06140 ± 0.00068	10.44 ± 0.12	6900 ± 180	5700 ± 300
2N-12	**40.8**	**0.3536 ± 0.0004**	**1.04713 ± 0.00150**	**0.08501 ± 0.00121**	**5.05 ± 0.08**	**9700 ± 280**	**6300 ± 400**
2N-13	**45.3**	**0.3219 ± 0.0002**	**1.03091 ± 0.00070**	**0.11127 ± 0.00094**	**6.05 ± 0.05**	**12900 ± 260**	**9200 ± 400**
2N-15	65.7	0.3757 ± 0.0002	1.05584 ± 0.00184	0.11004 ± 0.00129	7.01 ± 0.08	12700 ± 300	9600 ± 400
2N-16	**73.9**	**0.3898 ± 0.0003**	**1.03186 ± 0.00124**	**0.10284 ± 0.00074**	**16.40 ± 0.12**	**11800 ± 180**	**10600 ± 300**
2N-16+17	75.7	0.4195 ± 0.0002	1.03399 ± 0.00092	0.09253 ± 0.00062	19.65 ± 0.13	10600 ± 150	9600 ± 300
2N-17	77.6	0.3898 ± 0.0003	1.03454 ± 0.00136	0.14110 ± 0.00167	4.77 ± 0.06	16500 ± 420	10600 ± 500
2N-17B	**82.7**	**0.3611 ± 0.0004**	**1.02960 ± 0.00124**	**0.15299 ± 0.00172**	**4.40 ± 0.05**	**18000 ± 470**	**11200 ± 600**
2N-18	**88.2**	**0.3826 ± 0.0003**	**1.04747 ± 0.00163**	**0.14812 ± 0.00164**	**6.41 ± 0.07**	**17400 ± 500**	**12900 ± 500**
2N-20*	97.1	0.5672 ± 0.0004	1.05566 ± 0.00129	0.14313 ± 0.00123	18.46 ± 0.16	16800 ± 300	15300 ± 400
2N-20+21*	99.8	0.6384 ± 0.0007	1.05845 ± 0.00208	0.17045 ± 0.00184	7.50 ± 0.08	20300 ± 480	15800 ± 600
2N-21	**103.9**	**0.7739 ± 0.0006**	**1.05889 ± 0.00111**	**0.14585 ± 0.00094**	**27.70 ± 0.19**	**17100 ± 240**	**16100 ± 400**
2N-22*	108.5	0.5413 ± 0.0003	1.05795 ± 0.00107	0.20533 ± 0.00115	4.29 ± 0.03	24900 ± 350	15400 ± 600
2N-23*	113.9	0.3824 ± 0.0002	1.07316 ± 0.00118	0.20665 ± 0.00109	5.95 ± 0.03	21000 ± 300	18200 ± 400
2N-24*	121.3	0.4034 ± 0.0003	1.07005 ± 0.00199	0.18878 ± 0.00104	7.45 ± 0.04	22700 ± 300	17700 ± 400
2N-25	**124.7**	**0.5966 ± 0.0005**	**1.07111 ± 0.00147**	**0.19409 ± 0.00217**	**41.63 ± 0.49**	**23400 ± 600**	**22500 ± 700**
2N-26	**127.4**	**0.6305 ± 0.0004**	**1.06448 ± 0.00114**	**0.24987 ± 0.00330**	**17.45 ± 0.24**	**31200 ± 1000**	**28400 ± 1100**
2N-27	**129.8**	**0.5113 ± 0.0005**	**1.06262 ± 0.00089**	**0.25501 ± 0.00291**	**53.26 ± 0.67**	**32000 ± 840**	**31000 ± 1000**

All errors are listed at the 2σ confidence level. Ages used in the age model are in bold (see text for explanation, also Fig. A2.1). Ages from areas of irregular crystal growth are asterisked. The positions of age analyses in sample 2N are indicated in Fig. A2.3.

Appendices

Figure A2.1: Comparison of the linear interpolation age model used in this study (blue dashed line) to a more complex Bayesian age model generated by StalAge (green line, red 95% confidence envelope; Scholz and Hoffmann, 2011). The age models show consistent overlap throughout the sample, only diverging where the linear interpolation model has excluded ages measured in areas of the sample with "irregular crystal growth" (indicated by the vertical gray bars, see text). The yellow horizontal bar outlines the duration of the Younger Dryas event and shows that the timing of the YD onset and termination events do not change with the Bayesian age model. Thus, for this study, which examines the climate regimes of discrete intervals as well as abrupt events easily recognized in the isotope record, the linear interpretation age model is preferable.

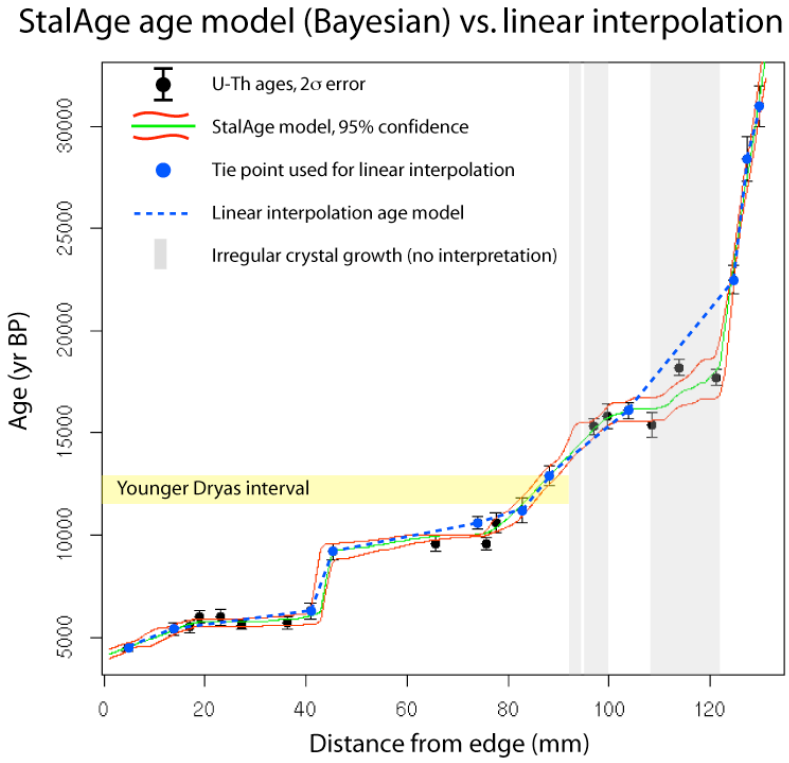

Figure A2.2: Fluorescence patterns for representative portions of sample 2N. Each panel shows a ~1x4 mm view of stitched CLFM images from the analytical traverse. Note the lattice-type crystal structure in panel D that is shown as a zone of irregular calcite growth in Figure 2.3.

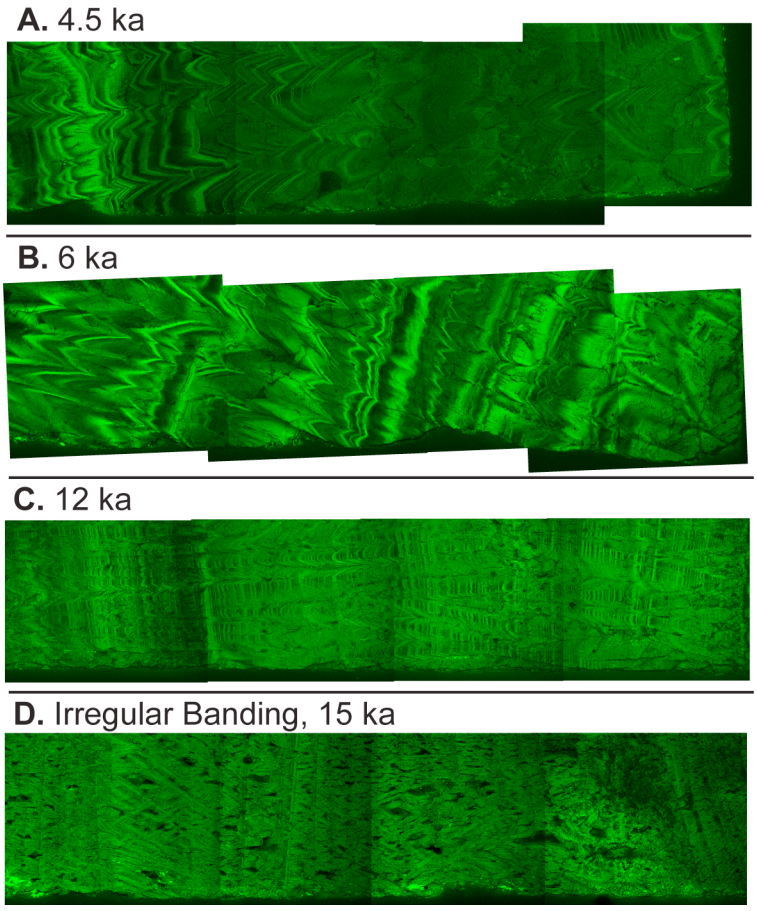

Figure A2.3 (next page): Panel A shows the U-Th ages calculated from multi-collector inductively coupled plasma mass spectrometry analysis of calcite drilled from sample 2N; ages shown in black are used in the age model and ages shown in gray are excluded from the age model (see text). Each gray triangle (excluded age) is linked horizontally to an orange symbol that indicates the position of the drill pit of that excluded age relative to the drill pits of the two adjacent model ages (black). Thus, the orange symbols identify age analyses that are not in chronostratigraphic order. **Panel B** illustrates the growth rates of sample 2N calculated from the U-Th ages used in the age model. **Panel C** is a plot of $\delta^{18}O$ (‰, VPDB) data from each point analyzed in sample 2N (34-4 ka) and sample 2-6 (2.2-0.9 ka). The solid green and blue lines are 11-point running averages of the bright and dark analyses, respectively. See the figure legend for symbol definitions. Zones of irregular crystal growth are indicated by gray rectangles. Vertical dashed red lines illustrate the boundaries of each sample chip, which are labeled along the horizontal axis.

Figure A2.3:

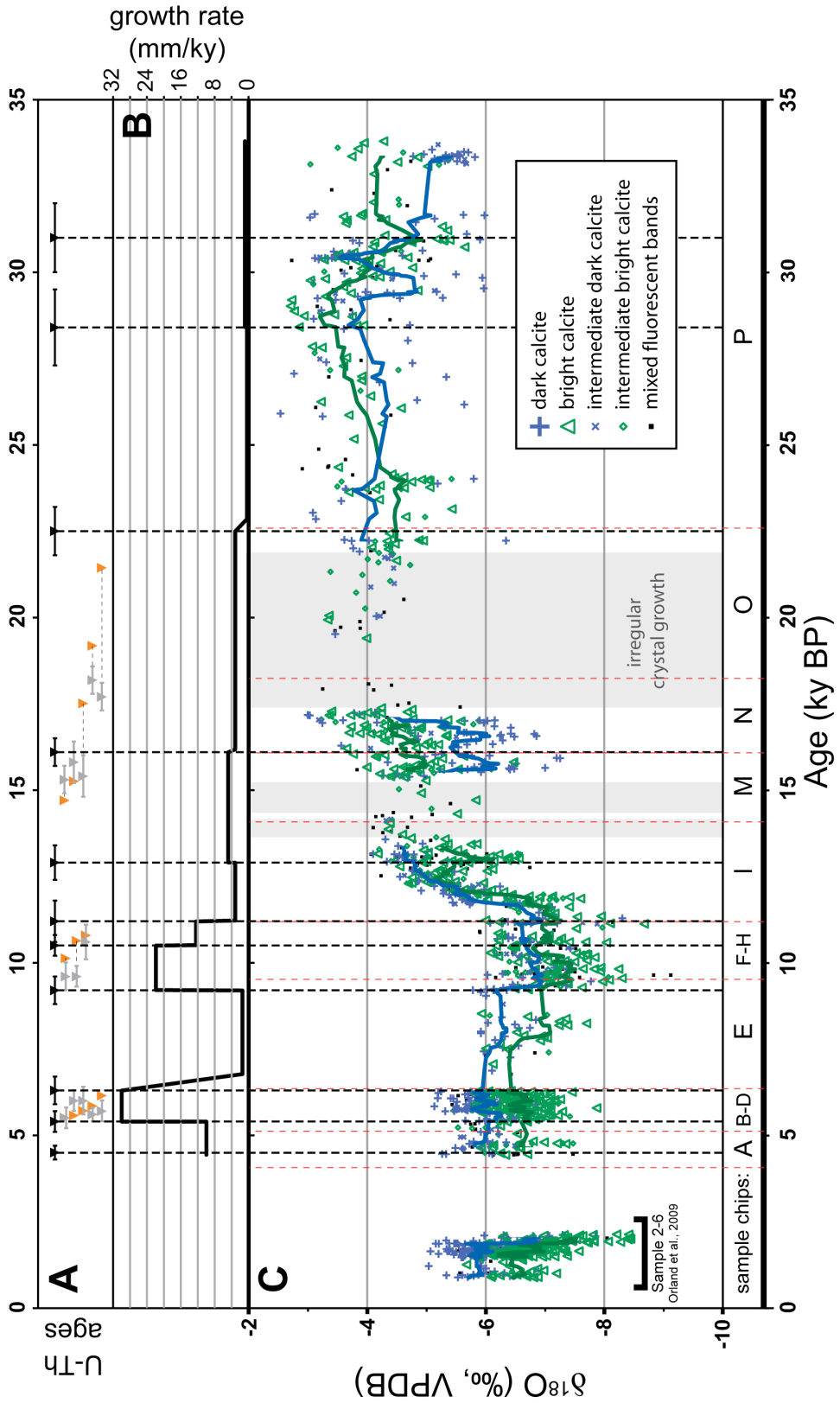
growth rate
(mm/ky)
32
24
16
8
0
A
B
C
U-Th
ages
δ18O (‰, VPDB)
-2
-4
-6
-8
-10
dark calcite
bright calcite
intermediate dark calcite
intermediate bright calcite
mixed fluorescent bands
irregular
crystal growth
Sample 2-6
Orland et al., 2009
sample chips:
A
B-D
E
F-H
I
M
N
O
P
0
5
10
15
20
25
30
35
Age (ky BP)

Figure A2.4: Backscatter electron image of spots P-61, 62, 63. Note the microporosity in the bottom of the middle pit (P-62); porous areas make up 7% of the pit area. Ion yield from spot P-62 was 98.4% of that in nine bracketing standard analyses, which is within the accepted range defined in section 2.5.

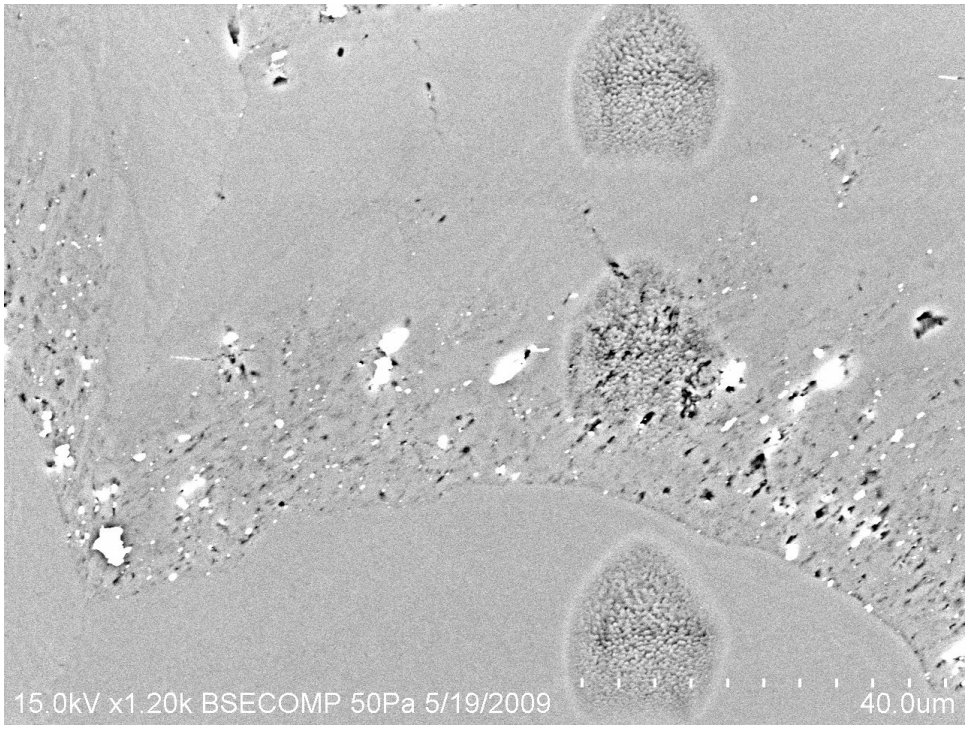

Table A2.5: Values of $\delta^{18}O$ from ion microprobe measurements along a number of individual fluorescent growth bands in sample 2N.

	$\delta^{18}O$ (‰, VSMOW)	2 s.d. assigned by bracketing UWC3	% yield of bracketing UWC3	$\delta^{18}O$ (‰, VSMOW), if accepted	elimination justification
Band 1 (20090731): dark fluorescent band, has microporosity, wide					
2N-OP_P-186	25.32	0.24	95.5	25.32	
2N-OP_P-187	25.30	0.24	94.5	25.30	
2N-OP_P-188	25.20	0.24	92.6		bad yield, Tukey
2N-OP_P-189	25.03	0.24	95.0	25.03	
2N-OP_P-190	25.21	0.24	94.6	25.21	
2N-OP_P-191	25.66	0.24	92.9		bad yield, Tukey
2N-OP_P-192	25.11	0.24	95.1	25.11	
band average	25.26			25.19	
band 2 s.d.	**0.41**			**0.25**	
Band 2 (20090731): dark fluorescent band, has microporosity, wide					
2N-OP_P-193	25.80	0.24	95.0	25.80	
2N-OP_P-194	25.42	0.24	95.2	25.42	
2N-OP_P-195	25.41	0.24	97.0	25.41	
2N-OP_P-196	25.44	0.24	96.1	25.44	
2N-OP_P-197	25.23	0.40	96.9	25.23	
2N-OP_P-198	25.99	0.40	95.3		poor placement
2N-OP_P-199	25.18	0.40	96.3	25.18	
band average	25.50			25.41	
band 2 s.d.	**0.59**			**0.44**	
Band 3 (20090731): dark fluorescent band, severe microporosity					
2N-OP_P-200	26.98	0.40	95.5	26.98	
2N-OP_P-201	28.10	0.40	78.4		bad yield
2N-OP_P-202	25.72	0.40	89.0		bad yield
2N-OP_P-203	25.89	0.40	94.8	25.89	
2N-OP_P-204	25.69	0.40	92.6		bad yield, Tukey
2N-OP_P-205	27.34	0.40	82.0		bad yield
2N-OP_P-206	26.08	0.40	95.3	26.08	
2N-OP_P-207	26.18	0.21	94.8	26.18	
2N-OP_P-208	27.23	0.21	89.1		bad yield
band average	26.58			26.28	
band 2 s.d.	**1.72**			**0.97**	
Band 4 (20090731): dark fluorescent band, has microporosity, narrow					
2N-OP_P-209	27.12	0.21	92.9		bad yield, Tukey
2N-OP_P-210	27.36	0.21	94.7	27.36	
2N-OP_P-211	27.28	0.21	94.7	27.28	
2N-OP_P-212	27.61	0.21	94.7	27.61	
2N-OP_P-213	27.52	0.21	94.2	27.52	
2N-OP_P-214	27.70	0.21	92.1		bad yield, Tukey
2N-OP_P-215	27.23	0.21	94.2	27.23	
2N-OP_P-216	27.48	0.21	94.9	27.48	
band average	27.41			27.41	
band 2 s.d.	**0.40**			**0.30**	

Table A2.5 (ctd):

	$\delta^{18}O$ (‰, VSMOW)	2 s.d. assigned by bracketing UWC3	% yield of bracketing UWC3	$\delta^{18}O$ (‰, VSMOW), if accepted	elimination justification
Band 5 (20090731): dark and smeared fluorescent band, severe microporosity					
2N-OP_P-217	27.34	0.21	94.0		poor placement
2N-OP_P-218	27.65	0.21	92.6		bad yield, Tukey
2N-OP_P-219	25.45	0.29	93.2	25.45	
2N-OP_P-220	26.20	0.29	95.0	26.20	
2N-OP_P-221	26.93	0.29	93.3	26.93	
2N-OP_P-222	26.30	0.29	94.1	26.30	
2N-OP_P-223	26.71	0.29	94.7	26.71	
2N-OP_P-224	25.56	0.29	94.0	25.56	
2N-OP_P-225	25.60	0.29	94.6	25.60	
2N-OP_P-226	24.74	0.29	95.0	24.74	
2N-OP_P-227	27.36	0.29	94.8		poor placement
2N-OP_P-228	26.42	0.29	93.5	26.42	
band average	26.35			25.99	
band 2 s.d.	**1.79**			**1.40**	
Band 6 (20090731): bright fluorescence with sinusoidal intensity across band, no microporosity, narrow					
2N-OP_P-229	27.09	0.29	94.3	27.09	
2N-OP_P-230	26.62	0.29	97.5	26.62	
2N-OP_P-231	26.83	0.39	94.5	26.83	
2N-OP_P-232	26.57	0.39	95.5	26.57	
2N-OP_P-233	26.02	0.39	95.5	26.02	
2N-OP_P-234	25.70	0.39	95.1		poor placement
2N-OP_P-235	26.31	0.39	95.8	26.31	
2N-OP_P-236	26.16	0.39	95.7	26.16	
2N-OP_P-237	26.36	0.39	96.5	26.36	
2N-OP_P-238	25.85	0.39	95.3	25.85	
2N-OP_P-239	25.32	0.39	94.9		poor placement
2N-OP_P-240	27.23	0.39	96.5		poor placement
band average	26.34			26.42	
band 2 s.d.	**1.14**			**0.79**	
Band 7 (20090801): dark fluorescent band, has microporosity					
2N-MN_N-60	25.24	0.47	95.8	25.24	
2N-MN_N-61	24.23	0.47	94.9		poor placement
2N-MN_N-56	23.84	0.47	92.2		bad yield, Tukey
2N-MN_N-55	24.48	0.15	92.2		bad yield, Tukey
2N-MN_N-54	24.46	0.15	96.5	24.46	
2N-MN_N-57	24.98	0.47	95.4	24.98	
2N-MN_N-58	24.29	0.47	96.5	24.29	
2N-MN_N-59	25.11	0.47	96.3	25.11	
band average	24.58			24.82	
band 2 s.d.	**0.97**			**0.83**	
Average spot-to-spot precision (2 s.d.) of all spots:	**0.31**		Average band 2 s.d.:	**0.71**	

Legend:
bad yield, Tukey: yield outlier by Tukey definition (see DR2.1; accepted range from 93.2-100.4%)
poor placement: poor spot placement within band
bad yield: yield outlier of 3 s.d. range from 91.1-102.2%

Figure A2.6: Plot of $\delta^{18}O$ vs. $|\Delta^{18}O|$ for all analysis pairs measured between 34-15 ka in sample 2N. Each panel (A-D) corresponds with a banding pattern identified in Figure 2; symbols as in Figure 2. Linear best-fit regressions of each population (dashed lines = bright fluorescent calcite, solid lines = dark calcite) show trends discussed in the text. The mean and standard deviation of each sub-horizontal population are listed in place of R^2 values.

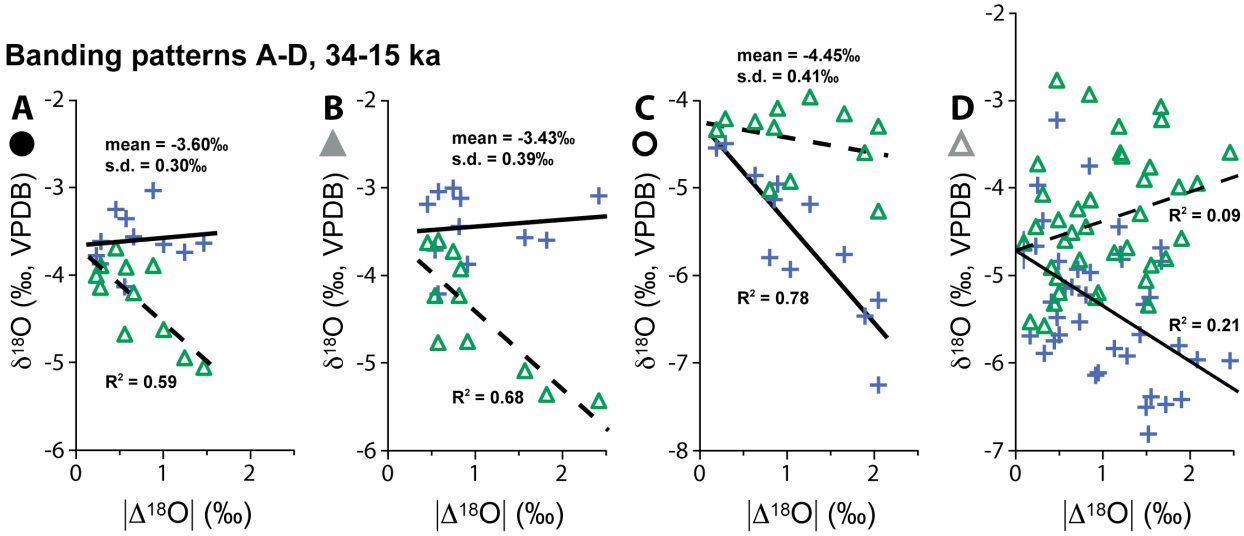

Data Repository Index

Large data tables and figures for each chapter are included in the supplementary files available with the online version of this dissertation.

DR2.1: Ion microprobe raw and corrected oxygen isotope ratios from 1,223 analyses of sample 2N from Soreq Cave.

DR2.2-A through DR2.2-I, DR2.2-M through DR2.2-P: Composite maps of samples 2N-A through 2N-I and 2N-M through 2N-P. Each map includes both reflected-light microscopy of a gold-coated sample and CLFM imaging of the polished sample. The location of each ion microprobe analysis is marked by a white ~10 μm oval.

DR2.3: SEM images of ion microprobe pits from $\delta^{18}O$ analyses in sample 2N.

CHAPTER III

Seasonal climate signal in a modern Soreq Cave stalagmite (1990-2008) revealed by high-resolution geochemical analysis

Ian J. Orland[1], Yuval Bursytn[2], Miryam Bar-Matthews[3], Reinhard Kozdon[1], Avner Ayalon[3], Alan Matthews[2], John W. Valley[1]

[1]*WiscSIMS, Department of Geoscience, University of Wisconsin, 1215 W Dayton St., Madison, WI, 53706, USA*

[2]*The Institute of Earth Sciences, The Hebrew University, Givat Ram, Jerusalem, 91904, Israel*

[3]*Geological Survey of Israel, 30 Malchei Israel St., Jerusalem, 95501, Israel*

Abstract

High-resolution isotopic and geochemical analyses in a modern (1990–2008) Soreq Cave stalagmite are compared to instrumental records of rainfall and dripwater from the cave, with the aim of determining how seasonal-resolution climate information is transmitted to speleothem geochemistry. *In situ*, micron-scale analysis of oxygen isotope ratios ($\delta^{18}O$) and trace elements by ion microprobe in combination with a continuous, linear traverse of trace element concentrations by laser-ablation ICP-MS (LA-ICP-MS) allow definition of geochemical pathways within the cave. Records of rainfall amount and rainfall $\delta^{18}O$ collected above the cave verify the chronology of the analytical traverse. Fluorescent banding, imaged by confocal laser fluorescent microscopy (CLFM), and trace element variations are used to define 18 annual growth increments. Reduced intensity of fluorescent banding and a change in trace element variability reflect the decrease in average rainfall from 628 mm/yr (1990–1998) to 433 mm/yr (1999–2008). During the wetter period before 1998, Pearson (*r*-value) and Spearman (ρ-value) correlation coefficients are >0.5 for ion microprobe analyses of the element pairings Sr-Y, Y-P, and Mn-Si. After the transition to the drier period in 1999, a different set of element pairings have *r*- and ρ-values >0.5, including Mg-$\delta^{18}O$, Mg-Sr, and Sr-Ba. Principal component analysis of data from the adjacent LA-ICP-MS traverse identifies two primary underlying modes of trace element variability. Based on the ion microprobe correlations and principal component analyses, we suggest that a greater seasonal influx of colloidal material into the cave during the wetter period (1990-1998) brought about greater P, Cu, Sr, Na, and U variability in the stalagmite. The co-variability of $\delta^{18}O$, Mg, Sr, and Ba is characteristic of the trace element pattern from the drier period (1999-2008) of growth when colloidal transport is reduced. These findings support a two-reservoir model of Soreq Cave dripwaters. One reservoir displays a well-mixed “baseline” with a

decadal residence time that supplies water to the cave year-round, probably from fine pores or grain-boundary films in the vadose zone. The second reservoir is seasonal rainwater that is enriched in colloidal material and rapidly transmitted to the cave. Finally, the similar patterns of fluorescence intensity, P, and Cu concentrations support the hypothesis that fluorescent bands in Soreq Cave speleothems are caused by the influx of organic colloids.

1. INTRODUCTION

Cave deposits (speleothems) often preserve climate information in their geochemistry. Measurements of oxygen and carbon isotope ratios ($\delta^{18}O$, $\delta^{13}C$) as well as trace element concentrations in carbonate speleothems are used to decipher both paleoclimate and paleoenvironmental conditions (Fairchild et al., 2000, 2006; Richards and Dorale, 2003; McDermott, 2004; Baldini et al., 2008; Cheng et al., 2009, 2012; Lachniet et al, 2009). The need to improve the continental paleoclimate record, combined with innovations in high spatial-resolution geochemical analyses, has resulted in development of seasonal-resolution climate records from speleothems. Multiple *in situ* analytical techniques permit seasonal-resolution analyses: laser-ablation inductively-coupled-plasma mass-spectrometry (LA-ICP-MS) and synchrotron radiation micro X-ray fluorescence for trace element analyses; ion microprobe for $\delta^{18}O$ and trace element analyses (Fairchild et al., 2001; Finch et al., 2001; Huang et al., 2001; Kuczumow et al., 2001; Treble et al., 2003, 2005; Borsato et al., 2007; Orland et al. 2009). High spatial-resolution records of trace elements in speleothems reflect seasonal changes in both cave atmosphere and hydrology that respond to regional climate (Treble et al., 2003; Borsato et al., 2007; Mattey et al., 2010; Wong et al., 2011). Likewise, high spatial-resolution analyses of $\delta^{18}O$ add seasonal rainfall information (Johnson et al., 2006; Orland et al., 2009, 2012).

Studies that combine seasonal-resolution analyses of trace elements and $\delta^{18}O$ (Johnson et al., 2006) are uncommon because conventional drill-sampling techniques for $\delta^{18}O$ analyses are typically incapable of sampling at the required spatial resolution. Recent advances in the accuracy and precision of $\delta^{18}O$ analyses by the ion microprobe at the WiscSIMS Laboratory, University of Wisconsin-Madison (UW-Madison), allow users to resolve subtle $\delta^{18}O$ variability in carbonate paleoclimate proxy records on a 10 μm scale (Weidel et al., 2007; Valley and Kita,

2009; Orland et al., 2009, 2012; Kozdon et al., 2011). With this technique, it is now possible to measure the variability of $\delta^{18}O$ in speleothems at a finer spatial resolution than trace element measurements by LA-ICP-MS; seasonal-scale climate interpretations that integrate analyses of $\delta^{18}O$ and trace elements are now viable in many more speleothems.

This study combines high-resolution data from several techniques in order to examine the coupled behavior of $\delta^{18}O$ and trace elements in a modern speleothem (sample "5-3b") from the semi-arid Soreq Cave locality in Israel (Figure 3.1). Measurements by LA-ICP-MS (continuous trace element traverse) and WiscSIMS ion microprobe (trace element and $\delta^{18}O$ spot analyses) are paired with imaging by confocal laser fluorescent microscopy (CLFM). The results will provide a basis for paleoclimate interpretations of both $\delta^{18}O$ and trace element records from Soreq Cave, which is a well-studied site in the Judean Hills 40 km inland from the Mediterranean Sea, and other caves in semi-arid regions. (Bar-Matthews et al., 1997, 1999, 2003, 2011; Ayalon et al., 1998, 1999, 2002; Matthews et al., 2000; Kaufman et al., 2003; Kolodny et al., 2003; McGarry et al., 2004; Affek et al., 2008).

Prior work on Soreq Cave speleothems at WiscSIMS used CLFM imaging of fluorescent bands to guide sub-annual-resolution ion microprobe analyses of $\delta^{18}O$ (Orland et al., 2009, 2012). Coupled variability of fluorescence and $\delta^{18}O$ values was first identified across what were interpreted as annual growth bands in a Late Holocene speleothem (Orland et al., 2009). In that study, it was proposed that fluorescent bands were caused by organic compounds like humic and fulvic acids that were flushed into the cave during an annual winter wet-season. Orland et al. (2009) show that the sharp onset of each fluorescent band coincides with a drop in speleothem $\delta^{18}O$ that resembles the modern seasonal variability in dripwater and rainfall $\delta^{18}O$ values; modern values of rainfall $\delta^{18}O$ and dripwater $\delta^{18}O$ values are lowest from November to April

when >95% of annual rainfall occurs (Figure 3.2). Cave monitoring at Soreq shows that as the winter wet-season ends, the source of dripwater gradually shifts to a high-$\delta^{18}O$ "baseline" vadose-zone reservoir (Ayalon et al., 1998) that is suggested to have fewer organic colloids in suspension (Orland et al., 2009). Based on this evidence, Orland et al. (2009) suggested that regular, sawtooth variability of $\delta^{18}O$ and fluorescence observed in Holocene Soreq speleothems mark annual growth bands; the gradual increase of $\delta^{18}O$ across each band accompanies a decrease in fluorescence and ends with an abrupt return to low $\delta^{18}O$ values at the onset of the next winter wet-season and bright fluorescent band.

Here we seek to further test the hypothesis that coupled variability of fluorescence and $\delta^{18}O$ delineate annual growth bands and rainfall amounts in a detailed analysis of modern stalagmite 5-3b. The age of sample 5-3b is constrained by its growth on a man-made object placed in Soreq Cave in 1990; the sample was collected in 2008. Because the maximum age of sample 5-3b is known, we can: (1) test the hypothesis that the fluorescent bands are annual markers, and subsequently (2) compare speleothem geochemistry to instrumental records of both rainfall amount and isotope chemistry measured above Soreq. In addition, we use correlation statistics and principal component analysis to assess the co-variability of $\delta^{18}O$, trace elements, and fluorescence measured in sample 5-3b (e.g. Borsato et al., 2007; Wassenburg et al., 2012). These comparisons allow us to evaluate the response of the geochemistry of 5-3b to changes in annual rainfall amount and test whether organic colloids are the cause of fluorescent banding in the sample.

2. MATERIALS AND METHODS

Sample 5-3b is a calcite stalagmite that grew on the base of a stationary drip-collecting apparatus placed in Soreq Cave in July 1990. It was removed from Soreq in August 2008, and then cut in half along its vertical growth axis. The cross section of 5-3b prepared for analysis measures 5.4 mm along the vertical axis and 10.0 mm across the base. Figure A3.1 in the Appendices shows optical imagery of 5-3b before and after being sectioned for casting in a 25 mm-diameter epoxy mount. The 25 mm epoxy round, which includes 3 grains of UWC-3 (calcite standard, $\delta^{18}O$=12.49‰ VSMOW; Kozdon et al., 2009), was ground and polished at UW-Madison using diamond paste in a progression from 6 to 1 μm grits. The final polish was attained with a colloidal alumina (0.05 μm) solution. Further sample preparation details are described in Orland et al. (2012).

2.1. Confocal laser fluorescent microscopy

Following polishing, 5-3b was imaged by confocal laser fluorescent microscopy (CLFM) at the UW-Madison Keck Bioimaging Lab with a Bio-Rad MRC-1024 scanning confocal microscope. Fluorescence was stimulated with a 40 mW laser (488 nm wavelength), and a filter isolated the emitted wavelengths between 505 and 539 nm – the green portion of the visible spectrum. A series of overlapping images were collected with a 10x objective lens (100x total magnification, 959 x 1199 μm field of view) in order to generate a stitched map of the entire sample surface. Because we are unaware of a method to standardize fluorescence intensity during CLFM imaging, the focal-plane depth, laser power, and signal gain were held constant in order to normalize intensity measurements; for this reason, interpretation of fluorescence variability is limited to relative – not absolute – intensity values from the CLFM images. Along

with reflected-light images at the same scale, the CLFM map was used to identify growth bands and target spots for $\delta^{18}O$ and trace element analysis by ion microprobe.

2.2. Ion microprobe analysis

Ion microprobe analysis of $\delta^{18}O$ in 5-3b followed the methodology established in earlier work using the CAMECA ims-1280 at the WiscSIMS lab, UW-Madison (Orland et al., 2009, 2012). Before analysis, the epoxy mount was cleaned in two successive 30 s sonication sessions, the first in ethanol and the second in distilled water. Next, a gold coat of ~60 nm thickness was applied to the polished surface to alleviate sample charging during ion microprobe analysis. A focused primary beam of $^{133}Cs^{+}$ ions was used to sputter each analysis pit *in situ*. The $\delta^{18}O$ analysis pits were 1 μm deep and oval-shaped, with the long dimension varying for different sessions from 10 to 15 μm depending on both primary-beam tuning and Cs-source conditions. Both $^{18}O^{-}$ and $^{16}O^{-}$ ions were collected by Faraday cups in multicollection mode. Using the standard-sample-standard bracketing technique outlined by prior workers (Kita et al., 2009; Valley and Kita 2009; Kozdon et al., 2009), the average spot-to-spot reproducibility for the $\delta^{18}O$ analyses of UWC-3 calcite standard run with sample 5-3b was ±0.30‰ (2 standard deviations, s.d.; see the data repository, DR3.1).

This study is the first to report a suite of trace element concentrations in a carbonate from the WiscSIMS ion microprobe. We report elemental concentrations of Mg, Si, P, Mn, Fe, Zn, Sr, Y, and Ba (Table A3.2). A 1.0 nA primary beam of O^{-} ions with an accelerating voltage of 13 kV was generated from a duoplasmatron source and focused onto the sample surface. Sputtered secondary ions with a positive charge were accelerated across a 10 kV potential into the double-focusing mass spectrometer. Each spot analysis took 10 minutes and included: pre-sputtering to

ablate the Au coating and stabilize secondary-ion emission (60 s), automatic beam centering (60 s), and five 90 s cycles of the magnet scanning through a range of masses (6.5-138). Non-peak positions were included in each analytical cycle at masses 6.5, 6.8, and 131 in order to allow the magnet to stabilize either after completing a cycle (6.5, 6.8) or when jumping a large gap in mass (131). Each analyzed mass was measured for either 2.0 s (Si) or 2.96 s (all others) followed by a 2.0 s waiting period. Ions of each mass were counted by the center-axis electron multiplier except for $^{40}Ca^{+}$ ions, which were directed into a center-axis Faraday cup to avoid saturating the electron multiplier. The count rate measured for each element during a cycle was normalized to the count rate of ^{40}Ca measured in that same cycle. For ^{24}Mg, ^{31}P, ^{55}Mn, ^{57}Fe, ^{88}Sr, ^{89}Y, and ^{137}Ba, the average of ^{40}Ca-normalized count rates from all five cycles was used to calculate elemental concentrations. Decreasing count rates observed in the first 3 cycles of ^{28}Si and ^{64}Zn measurements, perhaps due to surface contamination, are removed from consideration so that for these elements only the final two cycles with stable count rates were averaged for the concentration calculations.

To avoid variability in matrix effects that would stem from using NIST glass as a standard, we used the UWC-3 calcite standard to calibrate ion microprobe measurements of trace elements in 5-3b. We established the trace element profile of UWC-3 from a combination of electron microprobe analyses at UW-Madison (see supplemental material in Kozdon et al., 2009), LA-ICP-MS analyses at The Hebrew University-Jerusalem (HUJI; Table A3.3), and acid-digestion ICP-atomic emission spectroscopy (AES) and ICP-MS analyses by a commercial laboratory (Table A3.3). We report concentrations of nine elements in UWC-3: three from electron microprobe (Mg, Mn, Fe) and six from LA-ICP-MS (Si, P, Zn, Sr, Y, Ba). Results from the commercial laboratory show excellent agreement with these concentrations (Table A3.4).

Relative sensitivity factors (RSF) for WiscSIMS analyses of these nine trace elements in calcite were calculated using the average of five UWC-3 analyses at the beginning of the ion microprobe session (Table A3.4). The RSF values are used to convert elemental count rates measured in 5-3b into elemental concentrations.

Following the analytical sessions, a thin gold coat was added to the sample surface to allow imaging of the pit-bottoms by scanning electron microscope (SEM). Ion microprobe pits from both trace element and $\delta^{18}O$ analyses were examined at high magnification (>2500 x) for irregularities like inclusions, cracks, or epoxy. Each pit-bottom was classified as "regular," "intermediate," or "irregular" (Table A3.2). For trace element analyses, the irregular pits (n=3) do not appear to have systematic offsets for any element. Therefore, all trace element analyses are included in our interpretations.

Oxygen isotope analyses are screened in two different ways. First, analyses with anomalous secondary-ion yields are excluded (Kozdon et al., 2009, 2011; Orland et al., 2012). As with the determination of spot-to-spot reproducibility, a standard-sample-standard technique is used to calculate the "percent yield" of each $\delta^{18}O$ analysis relative to the bracketing standard measurements. Analyses with anomalous ion yield values relative to other pits measured in the same session are assumed to reflect a sample abnormality (e.g. a non-carbonate inclusion). Because the range of "percent yield" values for each analysis session is dependent on the primary beam condition, an accepted range of percent yield is defined for each session using the Tukey outlier definition (Tukey, 1977). The accepted range of percent yield in the first analytical session was 94.3 – 99.3% and 91.1 – 101.5% in the second analytical session. A total of 12 $\delta^{18}O$ analyses fall outside of the secondary yield cut-off values (DR3.1). These analyses, which represent less than 6% of the 231 sample analyses, are excluded from further consideration.

Oxygen isotope analyses are then screened by SEM imaging. Of the 14 $\delta^{18}O$ pits classified as irregular (DR3.1), one was already eliminated as an ion yield outlier and a second is eliminated because of its anomalously poor internal precision. The remaining irregular pits show no systematic $\delta^{18}O$ offset and are included in the plots and discussion presented below.

2.3. LA-ICP-MS analysis

LA-ICP-MS analysis of 5-3b was completed at HUJI using a New Wave UP-193 nm laser ablation system with a custom-built, He-purged "super-cell." (Dvir and Kessel, *in prep*) The HUJI laser-ablation set-up is coupled with an Agilent Technologies 7500 series ICP quadrupole mass spectrometer for high-precision measurements of elemental concentration. The analytical traverse is comprised of two co-axial laser passes, the first with a low-power (50% laser power, 30 Hz, 10 μm/sec stage speed) 100 μm-diameter beam that removed ~5 μm of sample to "preclean" the surface. The second pass, for trace element analysis, used a higher power (65% power, 10 Hz, 4 μm/sec stage speed) 55 μm-diameter beam that removed a further 10 μm of sample (Figure A3.5). Elemental counts in the ICP-MS were totaled 3 times/second so that each data point represents an integration of elemental counts from the 55 μm laser spot as it advanced ~1.3 μm. Imaging of an abruptly-terminated laser traverse by reflected-light profilometer (Figure A3.6) indicates that laser ablation rate is relatively consistent across the target such that material at the trailing edge of the laser is ablated at approximately the same rate as the leading edge. Thus, the resulting traverses can be likened to 55 μm moving-averages.

Concentrations of 11 elements (Na, Mg, Si, P, Mn, Cu, Zn, Sr, Ba, Pb, and U) were calculated in sample 5-3b using five bracketing analyses – two before and three after the traverse – of a chip of NIST-610 glass standard mounted adjacent to the sample in the super-cell. Each

NIST-610 analysis is comprised of a ~30 s (120 μm-long) traverse using the same analytical settings (no pre-clean) as described above. Data reduction was completed with the Iolite software package using ^{43}Ca as an internal standard (Hellstrom et al., 2008; Paton et al., 2011). Since a characterized carbonate standard did not exist, no matrix correction was made to the concentration values measured by LA-ICP-MS (Figure A3.7). Table A3.3 suggests that no matrix correction is needed, because glass-standardized LA-ICP-MS measurements of UWC-3 show excellent agreement with acid-digestion ICP-AES/MS results.

Since the environmental interpretations presented in this study are primarily based on patterns of trace element variability, it is important to show that relative concentration values measured by LA-ICP-MS across sample 5-3b are robust. In order to do this, we demonstrate analytical reproducibility by calculating the 2 s.d. of elemental concentrations measured in the five bracketing NIST-610 analyses. Using ^{29}Si as an internal standard, the 2 s.d. of Na, Mg, P, Mn, Cu, Zn, Sr, Ba, Pb, and U concentration variability measured during the five NIST-610 analyses are <1% of the respective average concentrations (Table A3.8).

2.4. Principal component analysis

The trace element results from the continuous laser traverse are well-suited for principal component analysis (PCA; Mix et al., 1986; von Storch and Zwiers, 1999). PCA evaluates the time-series components of empirical orthogonal functions, which reveal common variability in multiple, concurrent datasets. PCA was performed with MATLAB (2010) software using the built-in `princomp` function. We applied the PCA technique to z-score normalizations (data normalized to have mean = 0, s.d. = 1) of trace element transects and a profile of fluorescence intensity that was measured parallel to the laser trench.

The fluorescence intensity data used in the PCA was obtained from a group of stitched CLFM images that follow the LA-ICP-MS traverse. The fluorescence profile was generated in ImageJ, an open-source image processing software (Rasband, 2012), by averaging the pixel brightness intensity (on a grayscale from 0-255) of a 5-pixel-wide traverse that is offset 75 μm from the laser trench. We used the AnalySeries software (Paillard et al., 1996) to re-sample the fluorescence profile by linear interpolation in order to match the sampling resolution of the LA-ICP-MS data, a requirement for PCA.

3. RESULTS

3.1. Fluorescent banding

Figure 3.3 shows CLFM imaging of the entire polished surface of stalagmite 5-3b. Concentric fluorescent banding is evident along the entire analytical traverse (Figure 3.4), which is aligned with the vertical growth axis. There is a striking transition from distinct, bright fluorescent banding in the older ("inner") portion of the sample to subtle fluorescent banding in the more porous younger ("outer") portion. A discontinuity is highlighted by a dashed line in Figure 3.3 and appears to be a healed fracture likely caused by inadvertent disturbance of the drip collector. Non-fluorescent calcite crystals that are interspersed with voids (~100 μm in diameter) act as infill above the dashed fracture. Laterally continuous growth bands cap the infill and mark the transition to subtle fluorescent banding in the outer portion. The white bracket in Figure 3.3 shows an area of "turbulent" banding where it is difficult to trace continuous fluorescent bands. The turbulent banding occurs immediately before the abrupt transition to the subtle fluorescent banding regime.

3.2. $\delta^{18}O$ analyses

Values of $\delta^{18}O$ measured by ion microprobe span a range of 5.1‰, from 22.5-27.6‰ (VSMOW). The average spot-to-spot precision measured for UWC-3 bracketing standards is ±0.30‰. Figure 3.4A illustrates the location of 213 $\delta^{18}O$ analyses made on sample 5-3b (white circles). Figure 3.4B shows the $\delta^{18}O$ values of each measurement plotted against distance (projected on the LA-ICP-MS traverse). Tabulated results of each ion microprobe $\delta^{18}O$ analysis are reported in the data repository, DR3.1. Figure DR3.2 is a high-resolution map of the analytical traverse with each ion microprobe analysis labeled.

Seven analysis pits were targeted along a single fluorescent band (Figure 3.3) in order to confirm the consistency of $\delta^{18}O$ values measured along a single band. As in Orland et al. (2012), along-band analyses are used to assess the influence of variable porosity on the reproducibility of $\delta^{18}O$ measurements. We chose to target a distinctive fluorescent band (Figure 3.3) in the outer portion of the sample. The seven $\delta^{18}O$ measurements along the targeted band in 5-3b have a 2 s.d. of 0.31‰, nearly identical to the 2 s.d. of the bracketing UWC-3 standard (0.30‰). Furthermore, their secondary ion yields vary from 96-98% of the bracketing standards, well within the yield-cutoff values of 94.3 and 99.3% for that analytical session. These results demonstrate the along-band continuity of $\delta^{18}O$ values and alleviate concerns that porosity in the outer portion of the sample may cause inaccurate measurements.

3.3. Trace element analyses

Trace element concentrations from both ion microprobe and LA-ICP-MS analyses are shown in Figure 3.4 for four elements: Mg, Sr, Si, and P. Figure A3.7 includes trace element

profiles for all 11 elements measured by LA-ICP-MS. Concentration data from the 42 ion microprobe analyses of trace elements are reported in Table A3.2.

Notably, the mass used to measure Mn concentration by LA-ICP-MS (^{55}Mn) has a common isobaric interference in ICP mass spectrometers (the argide $^{38}Ar^{16}O^{1}H$ is formed in the Ar plasma). LA-ICP-MS measurements of Mn in sample 5-3b are validated by comparable ion microprobe results. Since the calibration of ion microprobe measurements of Mn in 5-3b is based on electron microprobe analysis of Mn in UWC-3 (Kozdon et al., 2009), the ion microprobe measurements of Mn in sample 5-3b provide independent confirmation of the LA-ICP-MS transect.

3.4. Principal component analysis and correlation results

The PCA results illustrated in Figure 3.5 and discussed below incorporate 12 variables. They are: (1) a record of fluorescence intensity across 5-3b as measured by CLFM and (2) 11 LA-ICP-MS elemental transects with signals discernable above background noise (Na, Mg, Si, P, Mn, Cu, Zn, Sr, Ba, Pb, U).

PCA results are displayed in Figure 3.5 in three manners: the "percentage of total variance" explained by each principal component, the sample "scores", and the variable "loadings." We briefly outline their meaning here. PCA redistributes the variance observed in our 12 variables (11 trace element and one fluorescence transect) into 12 orthogonal axes called "principal components" (PC) that are oriented according to patterns of co-variation in the original data (Davis, 2002). In concept, the principal components reflect underlying forcing mechanisms.

Each of the PCs describes a "percentage of the total variance" observed in the original data, and they are ranked according to this value (i.e. the first principal component, PC1, explains the highest percentage of total variance). Each PC is described by a time-series of normalized "scores" that define a pattern of variability that is unique to that principal component. For every PC, all 12 of the input variables are assigned a "loading" on a scale from -1 to 1 that indicates how well each variable correlates to the PC. A loading value of one denotes perfect positive correlation to a PC, while a negative loading value signifies an inverse correlation. In Figure 3.5D-F, the loadings are plotted for each element relative to the first three PCs. Different classes of elements with shared geochemical properties are outlined in color to ease visual comparison. Alkaline earth metals are highlighted in blue (Mg) and red (Sr, Ba), while colloid- and silicate-borne elements are highlighted in green (P, Cu) and yellow (Si, Mn), respectively.

The percentage of total variance explained by the first three PCs are 26%, 24%, and 14%. Together, they yield a cumulative percentage of 64% of the total variance explained by all of the PCs. For each of the nine remaining PCs, the percentage of total variance is <8% and as such, these PCs are not discussed below as significant components of the LA-ICP-MS dataset.

In addition to PCA, a combination of three statistical conditions is used to identify significant correlations among geochemical variables in sample 5-3b: (1) Pearson *r*-value >0.5, (2) respective p-value <0.02, and (3) Spearman rank correlation ρ-value >0.5. Both Pearson *r*-values and Spearman ρ-values are measured on a scale from 0–1 with higher values indicating increased correlation. The p-value indicates the probability on a scale from 0–1 that a higher value of Pearson's *r*-value could be obtained from a non-correlating dataset. Thus, low p-values indicate more significant *r*-values.

Pearson correlation coefficients (*r*-values; Johnson and Bhattacharyya, 2009) for the inner 16 and outer 22 trace element pits are tabulated in Table 3.1; correlations that meet all three conditions from above are given in bold. The dataset was subdivided into three portions (inner, turbulent, outer) based on the fluorescent banding in Figure 3.3. The four pits analyzed within the turbulent banding layer are excluded from the correlations in Table 3.1; these four pits only served to mask correlation coefficients of the inner and outer datasets. In order to assess the correlation of each trace element to $\delta^{18}O$, we identified the $\delta^{18}O$ pit closest to the location of each trace element analysis. Although Fe and Zn concentrations were measured by ion microprobe, their respective correlation values are not included in Table 3.1 because they never meet the three significance conditions. All three statistical results for both ion microprobe and LA-ICP-MS analyses of sample 5-3b are available in DR3.3.

4. DISCUSSION

Earlier work compared $\delta^{18}O$ values measured by ion microprobe to fluorescence imaging by CLFM in two Soreq speleothems (34–4 ka and 2.2–0.9 ka) and proposed that: (1) fluorescent bands in the speleothems represent annual growth bands, and (2) fluorescence and $\delta^{18}O$ values observed in single annual growth bands record seasonal rainfall patterns like the distinct wet and dry seasons of the modern climate regime (Orland et al., 2009, 2012). The suite of fluorescence, $\delta^{18}O$, and trace element results from modern sample 5-3b test these hypotheses and add to our understanding of micro-scale trace element variability within Soreq speleothems. This information will help to calibrate paired micro-analyses of $\delta^{18}O$ and trace elements in future investigations of speleothems from semi-arid environments.

4.1. Chronology of sample 5-3b

4.1.1. Fluorescent banding

The first step towards determining if fluorescent bands (Figure 3.3) are annual is to count the number of fluorescent bands. Since the sample substrate was placed in the cave in July 1990 and sample 5-3b was collected in August 2008, we expect to see 18 annual bands assuming that all years are recorded.

In Figure 3.3, we mark 18 bands apparent by visual inspection. Twelve of the bands (longer hashes) are clearly identified by laterally-continuous layers of bright fluorescence, while six others (shorter hashes) are distinguished by more subtle fluorescent layers. Although one could argue over the validity of some bands or the apparent grouping or splitting of others, it is nonetheless evident that there is a small range of probable counts around the expected total of 18.

The composite CLFM image in Figure 3.3 also shows that fluorescent bands in the inner portion of sample 5-3b are characteristically more intense than bands in the outer portion. Two interpretations are possible for the change in fluorescence. First, it is conceivable that whatever disturbance caused the discontinuity (dashed line in Figure 3.3) also repositioned the man-made substrate so that sample 5-3b was directly beneath a new drip-point that inhibited fluorescence. Such changes are unlikely, especially since the vertical growth axis appears unchanged. Instead, we prefer a second hypothesis that the intense fluorescent bands indicate a wetter period when dripwaters above 5-3b carried an increased load of fluorescent material into the cave from the overlying soil. Correspondingly, the subtle banding in the outer portion indicates a drier period when either the supply or delivery of fluorescent material into the cave was suppressed. Geochemical analyses of both sample 5-3b and rainwater collected above the cave allow us to

scrutinize the suggested annual bands and test our explanation for the reduction in fluorescence intensity.

4.1.2. Anchor points from the $\delta^{18}O$ record

Interpretations of speleothem $\delta^{18}O$ records generally rely on the premise that rainfall $\delta^{18}O$ values are reliably transmitted to speleothem calcite. At Soreq, Ayalon et al. (1998) show that the seasonal $\delta^{18}O$ signal in rainfall above the cave is imparted to dripwaters. This section further describes how the local rainfall $\delta^{18}O$ signal between 1990 and 2008 (Figure 3.6; DR3.4) is conveyed to Soreq speleothems and identifies prominent features in the rainfall record that can be used to anchor the chronology of 5-3b.

Figure 3.2 illustrates the strong seasonal gradient of both rainfall amount and $\delta^{18}O$ values measured above Soreq Cave from 1995-2008; $\delta^{18}O$ values are lowest in the winter wet-season and highest in the fall and late spring. Since >95% of rainfall occurs between November and April, we use the notation "water year" to delineate wet seasons; a water year extends from October of one year through September of the next and is designated by the calendar year in which it ends. Figure 3.6B shows how the cumulative $\delta^{18}O$ of rain from each water year tracks the $\delta^{18}O$ of rainfall from that wet season. Thus, to simplify the presentation of rainfall data in both the tables and figures of this discussion, we reference values of rainfall amount and $\delta^{18}O$ integrated over entire water years.

Figure 3.6 also includes $\delta^{18}O$ values measured in dripwaters collected near sample 5-3b between 1991 and 1997 and starting again in 2001. These data (tabulated in Table A3.9) have two important features that demonstrate how the rainfall $\delta^{18}O$ signal is transmitted into the cave.

First, dripwater $\delta^{18}O$ is lowest during the wet season, as observed in rainwater above the cave. Second, the minimum dripwater $\delta^{18}O$ values from each year track with annual rainwater $\delta^{18}O$. In a cave-wide dripwater survey, Ayalon et al. (1998) found that minimum dripwater $\delta^{18}O$ values each year were consistently ~1‰ higher than the annual rainfall $\delta^{18}O$ value. Figure 3.6C indicates a similar offset for dripwaters collected after the 1998 study.

Critical for this study is the assumption that $\delta^{18}O$ values measured in sample 5-3b reflect near-equilibrium of $\delta^{18}O$ between calcite and dripwater. Recent modeling (Deininger et al., 2012) and experimental (Gabitov et al., 2012) studies of isotope disequilibrium in speleothems suggest that seasonal variability of drip- and growth-rates could act to amplify the seasonal gradient of speleothem $\delta^{18}O$ relative to Soreq dripwater. Given the semi-arid setting of Soreq, however, these effects would impart <1‰ to the seasonal gradient – not enough to explain the observed variability. Furthermore, measurements of mass-47 CO_2 isotopologue anomalies (Δ_{47}) in modern Soreq speleothems indicate that modern calcite precipitated in near-equilibrium conditions for $\delta^{18}O$ (Affek et al., 2008). This accords with an earlier study of calcite precipitation in modern cave pools (Bar-Matthews et al., 1996).

With the knowledge that rainwater $\delta^{18}O$ variability is reliably transmitted to Soreq speleothems, two water years in the rainfall record stand out as being useful for correlating with the 5-3b $\delta^{18}O$ record (Figure 3.6). The first is 1992, which had the highest annual rainfall total over the period of interest (1020 mm) and the lowest $\delta^{18}O$ value of cumulative annual rainfall (-8.0‰, VSMOW). The second notable year is 1999, which had the lowest rainfall total of 215 mm and the highest cumulative $\delta^{18}O$ value, -4.5‰. Figure 3.7 plots the rainfall totals and cumulative rainfall $\delta^{18}O$ values from 1991-2008 as well as all $\delta^{18}O$ values measured in 5-3b by

ion microprobe. As in Figure 3.4, the horizontal axis of Figure 3.7 is scaled to match linear distance along the LA-ICP-MS traverse. We use the 1992 and 1999 water years (indicated with thick vertical dashed lines in Figures 3.4 and 3.7) to match the rainfall data to bands in 5-3b with extreme $\delta^{18}O$ values.

In order to identify other years in the chronology, we look for the pattern of sawtooth $\delta^{18}O$ variability that earlier studies characterized in annual growth bands from Holocene Soreq speleothems (Orland et al., 2009, 2012). Using this approach, wet-season markers are assigned to the outer three growth bands (2006-08) as well as the four bands (1993-1996) that follow the particularly wet 1992 water year (Figure 3.4). In the turbulent banding layer after 1996 and following the 1999 anchor point, sawtooth patterns of $\delta^{18}O$ are apparent but fluorescent bands are less clear. Therefore, trace element results are examined for evidence of annual growth bands where fluorescent banding is muted.

4.1.3. Trace element variability and chronology

Many studies have identified records of annual trace element variability in speleothems (Fairchild et al., 2001; Treble et al., 2003, 2005; Johnson et al. 2006; Borsato et al., 2007; Fairchild and Treble, 2009). Together they provide valuable insight on the source and pathways of trace elements analyzed in sample 5-3b. For example, Borsato et al. (2007) suggest that P, Cu, Zn, Y, and Pb are commonly carried into the cave as adsorbed species on colloids, which likely includes organic particles from the overlying soil. The trace elements most commonly measured at sub-annual resolution in speleothem studies are the alkaline earth metals, Mg and Sr. They form divalent cations in solution, substitute for Ca^{2+} in calcite, and are particularly useful

geochemical indicators in caves – like Soreq – that formed within dolomite bedrock (nominally $MgCa(CO_3)_2$).

Variability of Mg and Sr in dripwater is often attributed to changes in the amount of either groundwater-bedrock interaction or prior calcite precipitation (Fairchild and Treble, 2009; Wong et al. 2011). In drier conditions, the concentration of Mg and Sr in groundwater can be increased relative to Ca because: 1) longer periods of groundwater-bedrock interaction add higher proportions of Sr and Mg to the groundwater, or 2) calcite precipitation in rocks above the cave preferentially removes Ca from groundwaters. However, rather than attributing Mg and Sr variability in sample 5-3b to the seasonal influence of either or both of these mechanisms, we adopt the hydrological routing model that Fairchild et al. (2006) use to explain trace element variability. They suggest that Mg and Sr concentrations in dripwater represent a mixture of groundwaters that have experienced different residence times or flow pathways within the vadose zone. This is the same model used to explain $\delta^{18}O$ variability in Soreq Cave dripwaters and speleothems (Ayalon et al., 1998; Kaufman et al., 2003; Orland et al., 2009).

Figure 3.6C shows that Mg concentrations in Soreq dripwaters (tabulated in Table A3.9) adhere to the suggested model, with generally increasing concentrations following each wet season. Before using both Mg and Sr concentrations to identify annual bands in 5-3b, however, we take into account that: (1) Sr can be susceptible to factors like speleothem growth rate (Boch et al., 2011), and (2) Sr and Mg variability do not match in the inner portion of 5-3b (Figure 3.4). Therefore, we focus on Mg variability to guide identification of the remaining annual bands in 5-3b.

Much like with $\delta^{18}O$, we interpret a sharp decrease in Mg concentration to indicate the onset of annual wet seasons; following the sharp decrease, a gradual increase in Mg

concentration is expected as the relative contribution of longer-residence time groundwater grows. This interpretation corroborates the delineation of the 2006-08 growth bands identified by $\delta^{18}O$ variability. Furthermore, sawtooth variability of Mg is evident (although smoothed by the continuous laser traverse) in growth bands from 2000-05 where fluorescent bands were less conclusive. The remaining annual bands, 1997-1999, are assigned to the turbulent banding layer by sawtooth $\delta^{18}O$ patterns that coincide with subtle Mg and fluorescence variability (Figure 3.4).

4.2. Comparison of rainfall and speleothem $\delta^{18}O$ records

According to the model of annual $\delta^{18}O$ variability described in Section 4.1.2, the minimum $\delta^{18}O$ value of calcite in each annual band should closely reflect the cumulative $\delta^{18}O$ of rainfall from the respective water year. In Figure 3.7C we use the isotopic fractionation factor of Tremaine et al. (2011), which is based on data from 15 modern speleothem studies, to predict $\delta^{18}O$ values of calcite in 5-3b during each wet-season between 1991 and 2008. Each predicted calcite $\delta^{18}O$ value assumes: (1) a cave-air temperature of 22.0°C (Affek et al., 2008), and (2) a dripwater $\delta^{18}O$ value that is 1‰ higher than the cumulative $\delta^{18}O$ value of annual rainfall above Soreq Cave (Ayalon et al., 1998, 2004). The similarity of the predicted $\delta^{18}O$ values to the $\delta^{18}O$ values at the onset of annual bands in sample 5-3b reinforces two points: (1) low $\delta^{18}O$ values near the beginning of a growth band reflect cumulative wet season rainfall, and (2) the assigned chronology is accurate.

The chronology is further tested by measuring the range of $\delta^{18}O$ in each proposed annual band. Orland et al. (2009) hypothesize that the range of $\delta^{18}O$ in each band of a Late Holocene speleothem is a proxy for rainfall amount. They define a variable, $\Delta^{18}O = \delta^{18}O(\text{dark calcite}) –$

$\delta^{18}O$(bright calcite), to describe the $\delta^{18}O$ range in individual bands. Here, since annual bands are not defined solely on the basis of fluorescence, $\Delta^{18}O$ values are calculated as the difference between the maximum and minimum values in the $\delta^{18}O$ sawtooth for each band. Figure 3.7D plots the $\Delta^{18}O$ value calculated for each band in 5-3b. Figure 3.8 illustrates a remarkable correlation between $\Delta^{18}O$ values measured in 5-3b and annual rainfall totals from above the cave (r^2 = 0.88). This correlation adds support to the suggested chronology of 5-3b as well as the hypothesis that $\Delta^{18}O$ values indicate the amount of wet-season rainfall and are hence a proxy for annual rainfall amount.

4.3. Climate control of seasonal trace element variability

With the chronology of 5-3b established above, this study aims to identify signatures of seasonal climate within sub-annual trace element variability. Annual rainfall totals measured between 1991 and 2008 provide a benchmark against which to compare the geochemical data from sample 5-3b. In addition to the extreme wet and dry events used to anchor the chronology, the average amount of rainfall during a water year drops 195 mm from 628 to 433 mm between 1991–1998 and 1999–2008. Ideally, the patterns of sub-annual geochemical variability reflect the shift from a wetter to a drier decade. One encouraging observation is the change in the character of fluorescent banding from the younger to older portion of sample 5-3b (Section 3.1); the distinctive fluorescence regimes likely reflect a change in dripwater chemistry that we can quantify with trace element analyses.

There is excellent agreement between ion microprobe and LA-ICP-MS analyses of Mg, Sr, Si, and P concentrations in sample 5-3b (Figure 3.4). Similar plots for Ba, Mn, and Zn (Figure A3.7) also show good agreement between concentration values measured by the two

methods. Even before statistical analysis, common patterns of variability are clear within different classes of trace elements; one class is comprised of Mg, Sr, and Ba, another includes Si, Fe, and Mn.

4.3.1. Correlation of ion microprobe data

In their study of trace elements in speleothems, Wassenburg et al. (2012) emphasize elemental correlations with *r*-values > 0.5. Our study uses an additional condition to identify the significant elemental correlations that are highlighted in Table 3.1; the Spearman rank correlation coefficient (ρ-value; Johnson and Bhattacharyya, 2009) must also be > 0.5. By including the ρ-value requirement, we eliminate correlations whose *r*-values are skewed by single extreme measurements (e.g. Mn vs. Fe).

The highlighted correlations in Table 3.1 are markedly different in the inner and outer portions of sample 5-3b. In the inner portion, the noted correlations include elements that are likely carried into the cave during relatively wet periods as either: (1) species adsorbed to organic colloids (P, Y) that may also cause fluorescence, or (2) detrital silicates, possibly including windblown dust (Sr, Mn, Si). In the outer portion, the notable correlations include elements that reflect the residence time of groundwater in the vadose zone before it reaches the cave (Mg, Sr, Ba, $\delta^{18}O$). The only correlation common to both inner and outer portions of the sample is between Sr and Ba, a logical result considering the similar ionic radii and valence states of these two species.

The switch in significant elemental correlations matches the change in rainfall measured above the cave and inferred from the shift to subtle fluorescent banding. During the relatively wetter conditions of 1991–1998, both the distinct fluorescent banding along with P-Y-Sr and

Mn-Si correlations indicate that wet-season dripwater included material washed into the cave from the near-surface. In contrast, when the rainfall record shows relatively dry conditions, subtle fluorescent banding and Mg-Sr-Ba-$\delta^{18}O$ correlations indicate that dripwaters had both a longer residence time in the vadose zone as well as a less-direct connection with the near-surface. The difference between the geochemical response recorded in the inner and outer portions of 5-3b is likely caused by the amount of suspended load carried in groundwater; trace elements that are preferentially transported by colloidal particles or organic acids are emphasized during periods of increased rainfall.

4.3.2. Principal components of LA-ICP-MS data

The panels on the left of Figure 3.5 show the time series scores of the first three PCs and their respective percentages of total variance explained. The high percentage of variance explained by PC1 and PC2 relative to each of the remaining principal components suggests that PC1 and PC2 reflect the dominant modes of trace element variability in sample 5-3b. The panels on the right of Figure 3.5 compare the loadings of 11 trace elements on each PC by plotting the loading of each element on PC2 vs. PC1, PC3 vs. PC1, and PC3 vs. PC2. These figures illustrate how different elemental concentrations display common patterns of variability; elements that plot near one another likely share common forcing mechanisms.

Each of the first three PCs is characterized by high loadings of different groups of elements. PC1 has high loadings of Mg, Sr, and Ba that likely reflect the effect of groundwater-bedrock interaction in the vadose zone. PC2 has high loadings of P, Cu, Sr, and U. These elements readily adsorb to colloidal particles and organic acids, suggesting that PC2 indicates the amount of dissolved or colloidal components that are washed into the cave from the overlying

soil. PC3 is the only remaining principal component that explains >8% of the total variance and has a pattern consistent with the inclusion of silicate particles in the turbulent banding layer; the highest positive elemental loadings in PC3 are Zn, Pb, Mn, and Si.

We note the large peaks in the scores of PCs 1-3 correspond to high trace element concentrations in the turbulent layer (e.g. Sr; Figure 3.4B). PCA of the LA-ICP-MS results minus the portion of the turbulent layer with peak trace element concentrations (Figure A3.10) gives similar PC scores and elemental loadings to those illustrated in Figure 3.5. This similarity indicates that the PCs in Figure 3.5 are not distorted by the turbulent layer.

4.3.3 Characterizing dripwater compositions

Another notable feature of the PCA results is the relation of Mg to Sr and Ba in PCs 1 and 2. Figure 3.5D shows that Mg, Sr and Ba have similar positive loadings on PC1, but Mg has a negative loading on PC2 while Sr and Ba have positive loadings. This conflicting pattern is comparable to the correlations seen in the ion microprobe data; strong positive correlations are observed between Mg-Sr and Mg-Ba in the outer portion of 5-3b, but these same correlations are weak in the inner portion (Table 3.1). We hypothesize that the first two principal components represent the same forcing mechanisms ascribed to the correlation data. As such, PC1 would illustrate the influence of groundwater residence time on Mg, Sr, and Ba concentration, while PC2 reflects the amount of colloidal material washed into the cave.

In order to test the similarity of the PCA and correlations results, we conducted PCA on the same inner and outer portions of 5-3b as used in the correlation treatment. The results (Figure A3.11) show that the first PC of the inner portion matches the variability of PC2 from the entire sample (Figure 3.5B); this pattern is dominated by similar variability in Sr, Ba, Cu, P, and U.

The first PC of the outer portion, however, is characterized by similar loadings of Mg, Sr, and Ba and has a comparable pattern of variability to PC1 of the entire sample (Figure 3.5A). Thus, we are confident that PCs 1 and 2 of the entire sample represent the same forcing mechanisms used to explain correlations in the outer and inner portions, respectively (Table 3.1).

Given the proposed forcing factors for PCs 1 and 2, Figure 3.5D is particularly interesting because it shows the loading of different elements with respect to both components. One feature that stands out is the strong positive loading of both Sr and Ba (outlined in red) on PCs 1 and 2. In this case, PCA illustrates how the two forcing factors overprint one another in the composite trace element record. On one hand, since Sr and Ba concentrate in groundwater that has decadal residence times in the dolomitic vadose zone, they reflect the proportion of vadose zone groundwater in dripwater (PC1). On the other hand, these elements are also delivered to the sample via colloidal particles flushed into the cave by intense wet season rains (PC2).

Therefore, trace element data reinforce the two-component hydrological routing model previously used to describe $\delta^{18}O$ and fluorescence variability in Soreq speleothems (Orland et al., 2009). While mixing of groundwater reservoirs is sufficient to explain the $\delta^{18}O$ variability of 5-3b, the seasonal delivery of colloidal particles is critical to understanding the variability of trace elements like Sr, Ba, U, P, and Cu.

With regard to the influence of colloidal particles, we emphasize one final observation from the PCA results. Panels D-F of Figure 3.5 illustrate the remarkably similar variability of fluorescence intensity and P and Cu concentrations across sample 5-3b; the loadings of P, Cu, and CLFM are grouped together (green outline) in each of the first three principal components. The similar patterns of variability support the hypothesis that organic molecules, which are

vehicles for P, Cu, and other elements (Borsato et al. 2007; Fairchild and Treble, 2009), cause the fluorescent banding in sample 5-3b.

5. CONCLUSIONS

We apply high-spatial-resolution analysis and imaging to a modern Soreq Cave stalagmite in order to evaluate the co-variation of $\delta^{18}O$, trace elements, and fluorescence on a seasonal scale. Records of rainfall amount and $\delta^{18}O$ collected above Soreq Cave during the period when the stalagmite grew allow us to test hypotheses regarding cave hydrology and the annual nature of fluorescent banding. The results of this study are generally applicable to high-resolution geochemical data from speleothems, including other speleothems from Soreq Cave. The results also demonstrate the benefits of a multi-proxy, high-resolution approach and lead to the following conclusions:

- Corroborating results were obtained from trace element analyses by ion microprobe and LA-ICP-MS.
- Oxygen isotope variability, fluorescent banding, and trace element variability were considered in tandem in order to distinguish annual growth bands for each year of speleothem growth (water years 1991–2008).
- Both correlation analysis of ion microprobe data as well as principal component analysis (PCA) of LA-ICP-MS data reflect two modes of variability: (1) During the drier period from 1999–2008, muted fluorescent banding and the correlation of Mg, Sr, and Ba concentrations – likely sourced from the dolomitic country rock – suggest minimal colloidal infiltration; (2) During the wetter period from 1991–1998, fluorescent bands are

distinct and seasonal infiltration of organic colloids appears to accentuate the variability of P, Cu, Sr, Na, and U.

- Results support the two-reservoir model of Soreq Cave hydrology described by Orland et al. (2009). The first reservoir is stored in pores in the unsaturated zone where it accumulates divalent cations from the dolomite country rock, has a decadal residence time, and supplies well-mixed "baseline" dripwater to the cave on a year-round basis. The second reservoir delivers wet season rainfall to the cave along more direct pathways and thus has a shorter, sub-annual residence time. PCA results also indicate that the variability of some trace elements (Sr, Ba, U, P, Cu) is overprinted by the delivery of colloidal particles during intense wet season rains.
- Similar variability of P, Cu, and fluorescence intensity in a PCA of sample 5-3b data supports the hypothesis that fluorescent banding is caused by organic acids washed into the cave from the overlying soil.

Acknowledgements

The authors thank S. Meyers and A. Carlson for fruitful discussions; N. Kita and T. Ushikubo for support at WiscSIMS; O. Dvir for assistance with LA-ICP-MS analysis; L. Rodenkirch for assistance at the W. M. Keck Laboratory for Biological Imaging at UW-Madison; D. Ortiz and J. Fournelle for guidance on the SEM; B. Hess for sample preparation; J. Kern for profilometer assistance; A. Pollington and E. Syracuse for MATLAB support. Funding for this project was provided by the NSF (AGS-1003487, EAR-0838058), the Comer Science and Education Foundation, and the United States-Israel Binational Science Foundation (2010316). WiscSIMS is partially supported by NSF-EAR(0319230, 0744079, 1053466).

References

Affek H. P., Bar-Matthews M., Ayalon A., Matthews A. and Eiler J. M. (2008) Glacial/interglacial temperature variations in Soreq cave speleothems as recorded by 'clumped isotope' thermometry. *Geochim. Cosmochim. Acta* **72**, 5351-5360.

Ayalon A., Bar-Matthews M. and Sass E. (1998) Rainfall-recharge relationships within a karstic terrain in the Eastern Mediterranean semi-arid region, Israel: $\delta^{18}O$ and δD characteristics. *J. Hydro.* **207**, 18-31.

Ayalon A., Bar-Matthews M. and Kaufman A. (1999) Petrography, strontium, barium and uranium concentrations, and strontium and uranium isotope ratios in speleothems as palaeoclimatic proxies: Soreq Cave, Israel. *The Holocene* **9,** 715-722.

Ayalon A., Bar-Matthews M. and Schilman B. (2004) Rainfall isotopic characteristics at various sites in Israel and the relationships with unsaturated zone water. In: Geological Survey of Israel Reports, GSI/16/04. The Ministry of National Infrastructures, Jerusalem.

Baldini J. U. L., McDermott F., Hoffmann D. L., Richards D. A., and Clipson N. (2008) Very high-frequency and seasonal cave atmosphere PCO_2 variability: Implications for stalagmite growth and oxygen isotope-based paleoclimate records. *Earth Planet. Sci. Lett.* **272**, 118-129.

Bar-Matthews M., Ayalon A., Matthews A., Sass E., and Halicz L. (1996) Carbon and oxygen isotope study of the active water-carbonate system in a karstic Mediterranean cave: Implications for paleoclimate research in semiarid regions. *Geochim. Cosmochim. Acta* **60**, 337-347.

Bar-Matthews M., Ayalon A. and Kaufman A. (1997) Late Quaternary paleoclimate in the eastern Mediterranean region from stable isotope analysis of speleothems at Soreq Cave, Israel. *Quat. Res.* **47,** 155-168.

Bar-Matthews M., Ayalon A., Kaufman A. and Wasserburg G. J. (1999) The Eastern Mediterranean paleoclimate as a reflection of regional events: Soreq Cave, Israel. *Earth Planet. Sci. Lett.* **166**, 85-95.

Bar-Matthews M., Ayalon A., Gilmour M., Matthews A. and Hawkesworth C. J. (2003) Sea-land oxygen isotopic relationships from planktonic foraminifera and speleothems in the Eastern Mediterranean region and their implication for paleorainfall during interglacial intervals. *Geochim. Cosmochim. Acta* **67,** 3181-3199.

Bar-Matthews M. and Ayalon A. (2011) Mid-Holocene climate variations revealed by high-resolution speleothem records from Soreq Cave, Israel and their correlation with cultural changes. *The Holocene* **21**, 163-171.

Boch R., Spötl C., and Frisia S. (2011) Origin and palaeoenvironmental significance of lamination in stalagmites from Katerloch Cave, Austria. *Sedimentology* **58**, 508-531.

Borsato A., Frisia S., Fairchild I. J., Somogyi A. and Susini J. (2007) Trace element distribution in annual stalagmite laminae mapped by micrometer-resolution X-ray fluorescence: Implications for incorporation of environmentally significant species. *Geochim. Cosmochim. Acta* **71**, 1494-1512.

Cheng H., Edwards R. L., Broecker W. S., Denton G. H., Kong X., Wang Y., Zhang R. and Wang X. (2009) Ice Age Terminations. *Science* **326**, 248-252.

Cheng H., Zhang P. Z., Spötl C., Edwards R. L., Cai Y. J., Zhang D. Z., Sang W. C., Tan M. and An Z. S. (2012) The climatic cyclicity in semi-arid central Asia over the past 500,000 years. *Geophys. Res. Lett.* **39**, L01705.

Davis J. C. (2002) *Statistics and Data Analysis in Geology*. John Wiley and Sons: New York, 638 p.

Deininger M., Fohlmeister J., Scholz D. and Mangini A. (2012) Isotope disequilibrium effects: The influence of evaporation and ventilation effects on the carbon and oxygen isotope composition of speleothems – A model approach. *Geochim. Cosmochim. Acta* **96**, 57-79.

Dvir O., and Kessel R. (*in prep*) The effect of cell geometry on alkali element fractionation during LA-ICP-MS analysis.

Fairchild I. J. and Treble P. C. (2009) Trace elements in speleothems as recorders of environmental change. *Quat. Sci. Rev.* **28**, 449-468.

Fairchild I. J., Borsato A., Tooth A. F., Frisia S., Hawkesworth C. J., Huang Y., McDermott F. and Spiro B. (2000) Controls on trace element (Sr–Mg) compositions of carbonate cave waters: implications for speleothem climatic records. *Chem. Geol.* **166**, 255-269.

Fairchild I. J., Baker A., Borsato A., Frisia S., Hinton R. W., McDermott F., and Tooth A. F. (2001) High-resolution, multiple-trace-element variation in speleothems. *J. Geol. Soc. Lon.* **158**, 831-841.

Fairchild I. J., Smith C. L., Baker A., Fuller L., Spötl C., Mattey D., McDermott F. and E.I.M.F. (2006) Modification and preservation of environmental signals in speleothems. *Earth Sci. Rev.* **75**, 105-153.

Finch A. A., Shaw P. A., Weedon G. P., and Holmgren K. (2001) Trace element variation in speleothem aragonite: potential for paleoenvironmental reconstruction. *Earth Planet. Sci. Lett.* **186**, 255-267.

Gabitov R. I., Watson E. B. and Sadekov A. (2012) Oxygen isotope fractionation between calcite and fluid as a function of growth rate and temperature: An in situ study. *Chem. Geol.* **306-307**, 92-102.

Hellstrom J., Paton C., Woodhead J. and Hergt J. (2008) Iolite: software for spatially resolved LA-(quad and MC) ICPMS analysis. In: *Mineralogical association of Canada short course.* Mineralogical Association of Canada: Vancouver **40**, pp. 343-348.

Huang H. M., Fairchild I. J., Borsato A., Frisia S., Cassidy N. J., McDermott F. and Hawkesworth C. J. (2001) Seasonal variations in Sr, Mg and P in modern speleothems (Grotta di Ernesto, Italy). *Chem. Geol.* **175**, 429-448.

Johnson K. R., Hu C., Belshaw N. S. and Henderson G. M. (2006) Seasonal trace-element and stable-isotope variations in a Chinese speleothem: The potential for high-resolution paleomonsoon reconstruction. *Earth Planet. Sci. Lett.* **2006**, 394-407.

Johnson R. A. and Bhattacharyya G. K. (2009) *Statistics: Principles and Methods*. John Wiley and Sons: Hoboken, 704 p.

Kaufman A., Wasserburg G. J., Porcelli D., Bar-Matthews M., Ayalon A. and Halicz L. (1998) U-Th isotope systematics from the Soreq cave, Israel and climatic correlations. *Earth Planet. Sci. Lett.* **156,** 141-155.

Kita N. T., Ikeda Y., Togashi S., Liu Y., Morishita Y., and Weisberg M. K. (2004) Origin of urelites inferred from a SIMS oxygen isotopic and trace element study of clasts in the Dar al Gani 319 polymict urelite. *Geochim. Cosmochim. Acta* **68**, 4213-4235.

Kita N. T., Ushikubo T., Fu B. and Valley J. W. (2009) High Precision SIMS Oxygen Isotope Analyses and the Effect of Sample Topography, *Chem. Geol.* **264**, 43-57.

Kolodny Y., Bar-Matthews M., Ayalon A. and McKeegan K. D. (2003). A high spatial resolution $\delta^{18}O$ profile of a speleothem using an ion microprobe. *Chem. Geol.* **197**, 21-28.

Kozdon R., Ushikubo T., Kita N. T., Spicuzza M. and Valley J. W. (2009) Intratest oxygen isotope variability in the planktonic foraminifer *N. pachyderma:* Real vs. apparent vital effects by ion microprobe. *Chem. Geol.* **258**, 327-337.

Kozdon R., Kelly D. C., Kita N. T., Fournelle J. H., and Valley J. W. (2011) Planktonic foraminiferal oxygen isotope analysis by ion microprobe technique suggests warm tropical sea surface temperatures during the Early Paleogene. *Paleoceanography* **26**, PA3206.

Kuczumow A. B., Vekemans B., Schalm Wahnberg P., and Van Grieken R. (2001) Analysis of speleothems by electron and X-ray microprobes. *J. Anal. At. Spectrom.* **16**, 90-95.

Lachniet M. S. (2009) Climatic and environmental controls on speleothem oxygen-isotope values. *Quat. Sci. Rev.* **28**, 412-432.

MATLAB version 7.11.0.584. (2010) Natick, Massachusetts: The MathWorks Inc.

Mattey D. P., Fairchild I. J., Atkinson T. C., Latin J.-P., Ainsworth M., and Durell R. (2010) Seasonal microclimate control of calcite fabrics, stable isotopes and trace elements in modern speleothem from St Michaels Cave, Gibraltar. *Geol. Soc. Lon. Spec. Pub.* **336**, 323-344.

Matthews A., Ayalon A. and Bar-Matthews M. (2000) D/H ratios of fluid inclusions of Soreq Cave Israel speleothems as a guide to the Eastern Mediterranean Meteoric Line relationships in the last 120 ky. *Chem. Geol.* **166,** 183-191.

McDermott F. (2004) Palaeo-climate reconstructions from stable isotope variations in speleothems: a review. *Quat. Sci. Rev.* **23**, 901-918.

McGarry S. F., Bar-Matthews M., Matthews A., Vaks A., Schilman B. and Ayalon A. (2004) Constraints on hydrological and paleotemperature variations in the eastern Mediterranean region in the last 140ka given by the δD values of speleothem fluid inclusions. *Quat. Sci. Rev.* **23,** 919-934.

Mix A. C., Ruddiman W. F., and McIntyre A. (1986) Late Quaternary Paleoceanography of the tropical Atlantic, 2: The seasonal cycle of sea surface temperatures, 0-20,000 years B. P. *Paleocean.* **1**, 339-353.

O'Neil J. R., Clayton R. N. and Mayeda T. K. (1969) Oxygen fractionation in divalent metal carbonates. *J. Chem. Phys.* **51**, 5547-5558.

Orland I. J, Bar-Matthews M., Kita N. T., Ayalon A., Matthews A. and Valley J. W. (2009) Climate deterioration in the eastern Mediterranean as revealed by ion microprobe analysis of a speleothem that grew from 2.2 to 0.9 ka in Soreq Cave, Israel. *Quat. Res.* **71**, 27-35.

Orland I. J. Bar-Matthews M., Ayalon A., Matthews A., Kozdon R., Ushikubo T., and Valley J. W. (2012) Seasonal resolution of Eastern Mediterranean climate change since 34 ka from a Soreq Cave speleothem. *Geochim. Cosmochim. Acta* **89**, 240-255.

Paillard D., Labeyrie L. and Yiou P. (1996) Macintosh program performs time-series analysis. *Eos Trans. AGU* **77**, 379.

Paton C., Hellstrom J., Paul B., Woodhead J. and Hergt J. (2011) Iolite: Freeware for the visualization and processing of mass spectrometric data. *J. Anal. At. Spectrom.* **26**, 2508-2518.

Rasband W.S. (2012) ImageJ. U. S. National Institutes of Health, Bethesda, Maryland, USA, http://imagej.nih.gov/ij/.

Richards D. A., and Dorale J. A. (2003) Uranium-series chronology and environmental applications of speleothems. *Rev. Min. Geol.* **52**, 407-460.

Sokal R. R., and Rohlf F. J. (1995) *Biometry: the principles and practice of statistics in biological research*. 3rd edition. W.H. Freeman and Co: New York, 887 pp.

Treble P., Shelley J. M. G., and Chappell J. (2003) Comparison of high resolution sub-annual records of trace elements in a modern (1911-1992) speleothem with instrumental climate data from southwest Australia. *Earth Planet. Sci. Lett.* **216**, 141-153.

Treble P. C., Chappell J., and Shelley J. M. G. (2005) Complex speleothem growth processes revealed by trace element mapping and scanning electron microscopy of annual layers. *Geochim. Cosmochim. Acta* **69**, 4855-4863.

Tremaine D. M., Froelich P. N., and Wang Y. (2011) Speleothem calcite farmed in situ: Modern calibration of $\delta^{18}O$ and $\delta^{13}C$ paleoclimate proxies in a continuously-monitored natural cave system. *Geochim. Cosmochim. Acta* **75**, 4929-4950.

Tukey J. W. (1977) *Exploratory Data Analysis*. Addison-Wesley Publishing Co., Reading.

Valley J. W. and Kita N. T. (2009) *In situ* Oxygen Isotope Geochemistry by Ion Microprobe. In *MAC Short Course: Secondary Ion Mass Spectrometry in the Earth Sciences* (ed. M. Fayek), v. 41, pp. 19-63.

von Storch H. and Zwiers F. W. (1999) *Statistical Analysis in Climate Research*. Cambridge Univ. Press: Cambridge, UK, 484 p.

Wassenburg J. A., Immenhauser A., Richter D. K., Jochum K. P., Fietzke J., Deininger M., Goos M., Scholz D. and Sabaoui A. (2012) Climate and cave control on Pleistocene/Holocene calcite-to-aragonite transitions in speleothems from Morocco: elemental and isotopic evidence. *Geochim. Cosmochim. Acta* **92**, 23-47.

Weidel B. C., Ushikubo T., Carpenter S. R., Kita N. T., Cole J. J., Kitchell J. F., Pace M. L., and Valley J. W. (2007) Diary of a bluegill (*Lepomis macrochirus*): daily $\delta^{13}C$ and $\delta^{18}O$ records in otoliths by ion microprobe. *Can. J. Fish. Aquat. Sci.* **64**, 1641-1645.

Wong C. I., Banner J. L. and Musgrove M. (2011) Seasonal dripwater Mg/Ca and Sr/Ca variations driven by cave ventilation: Implications for and modeling of speleothem paleoclimate records. *Geochim. Cosmochim. Acta* **75**, 3514-3529.

Figures

Figure 3.1: Map of Israel with the location of Soreq Cave (SC, star). J = Jerusalem, EM = Eastern Mediterranean Sea, DS = Dead Sea.

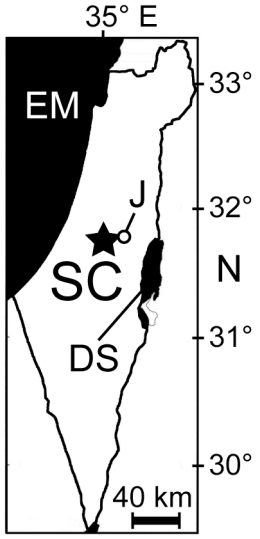

Figure 3.2: Average monthly rainfall totals and $\delta^{18}O$ values measured above Soreq Cave from 1995-2008 (based on Ayalon et al., 1998; Orland et al., 2009).

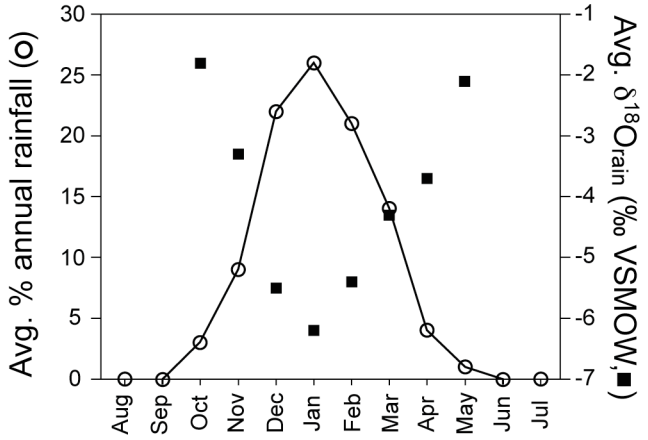

Figure 3.3: CLFM image of the polished surface of sample 5-3b, tiled together from smaller images. The dashed white line highlights a growth discontinuity, which appears to be a healed fracture (see text, Section 3.1). The rectangle outlines the area of sample 5-3b that includes the analytical traverse displayed in Figure 3.4. Yellow hashes mark 18 fluorescent bands, with shorter hashes acknowledging the more subtle bands. The white bracket shows the location of the turbulent banding that occurs immediately prior to the transition to more subtle fluorescent bands (Section 3.1). White ovals indicate the spot locations (pit size not to scale) for ion microprobe analyses of $\delta^{18}O$ along a single band. See Section 3.2 for results of the along-band analyses.

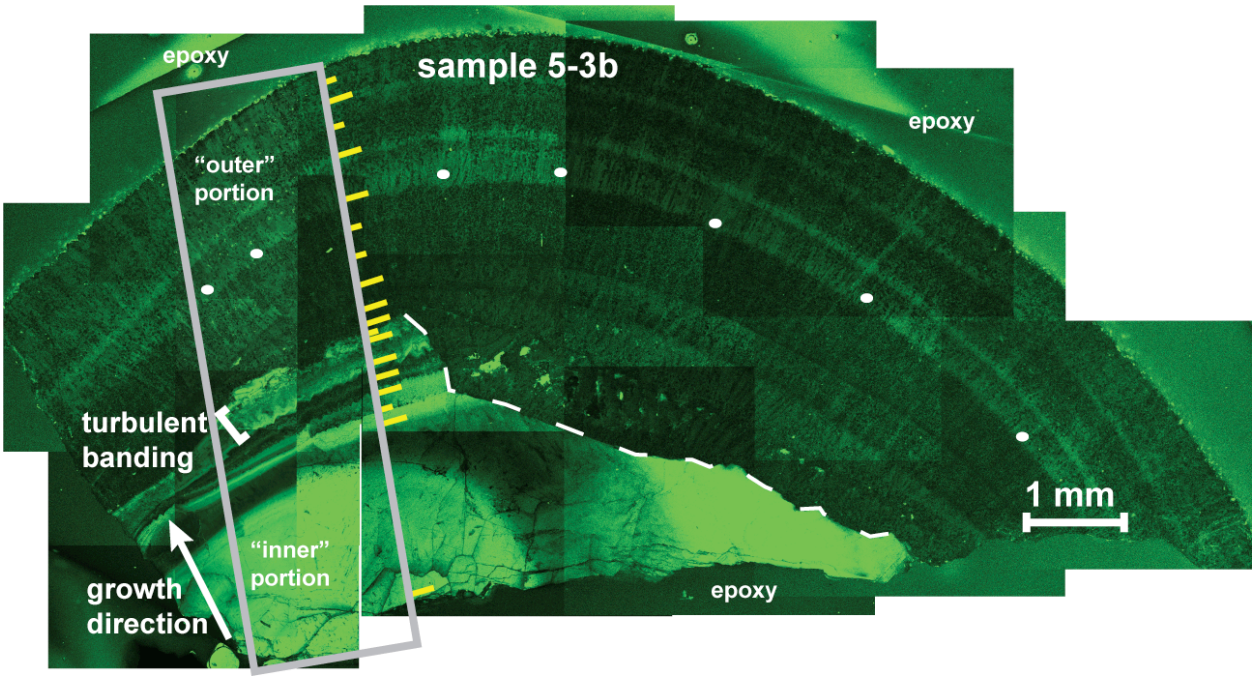

Figure 3.4 (next page): A is a stitched CLFM image of the area of analytical traverses shown in Figure 3.3. Ion microprobe pits for $\delta^{18}O$ are white circles, trace element pits are yellow circles. The location of the LA-ICP-MS laser trench is outlined with a yellow rectangle and the grayscale coloring within the traverse shows the Mg concentration. **B** shows values of $\delta^{18}O$, [Mg], [Sr], [P], and [Si]. The location of each ion microprobe pit was projected parallel to banding onto the laser traverse. For the four trace element profiles, spot analyses by ion microprobe are plotted as triangles with the continuous LA-ICP-MS traverse; there is good agreement between the two analytical methods. The grayscale legend for [Mg] applies to both panels A and B. The vertical dashed lines represent the inferred onset of winter wet-seasons (bright luminescence); as described in Section 4.1.2 a water year is assigned to the growth between each dashed line. The two thicker dashed lines at 1992 and 1999 mark years with extreme rainfall $\delta^{18}O$ values, shown in Figure 3.7.

Figure 3.4:

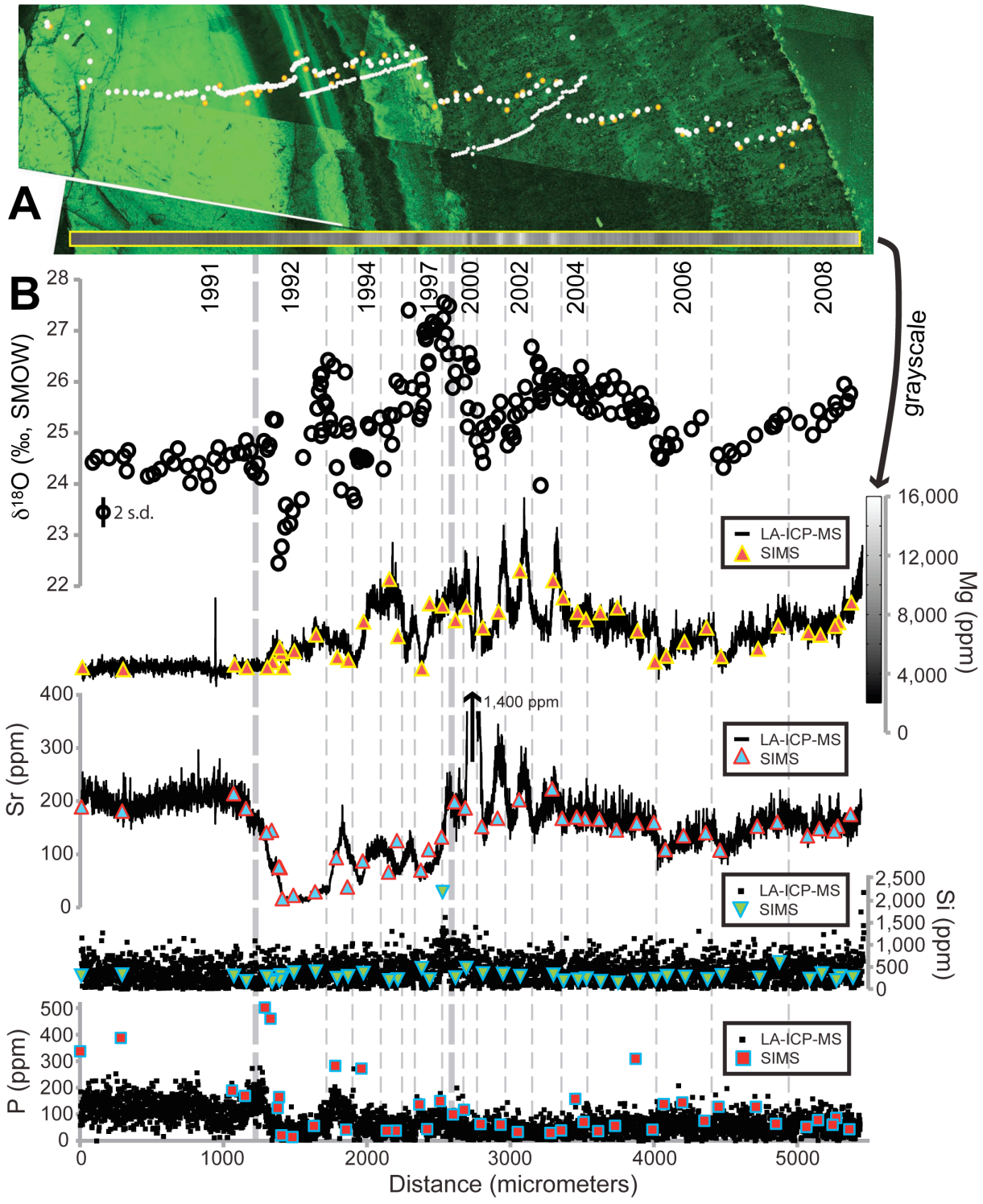
A
B
1991
1992
1994
1997
2000
2002
2004
2006
2008
grayscale
δ18O (‰, SMOW)
2 s.d.
LA-ICP-MS
SIMS
Mg (ppm)
16,000
12,000
8,000
4,000
0
Sr (ppm)
1,400 ppm
Si (ppm)
2,500
2,000
1,500
1,000
500
P (ppm)
0
1000
2000
3000
4000
5000
Distance (micrometers)

Figure 3.5 (next page): PCA results for 12 datasets that traverse sample 5-3b, including 11 records of trace element concentration from LA-ICP-MS analysis (Na, Mg, Si, P, Mn, Cu, Zn, Sr, Ba, Pb, U) and one record of fluorescence intensity acquired by CLFM. Section 3.4 explains the PCA terminology. **A-C** show the scores of PCs 1-3, respectively, plotted versus distance from the base of 5-3b. The percentage of total variance (%) represented by each PC is indicated in the upper-left corner of panels A-C. **D-F** show the loadings of the 12 observed datasets for PC2 vs. PC1, PC3 vs. PC1, and PC3 vs. PC2, respectively. Since the sum of the squared loading values of a trace element on all of the principal components equals 1, the unit circles in panels D-F outline the maximum range of possible loadings. For example, if one trace element has a loading of 1 on any principal component, it must have a loading of zero on all others. Notable classes of elements are highlighted in color to facilitate comparison of their relative loadings; divalent cations are colored blue (Mg) and red (Sr, Ba), while elements transported by organic colloids or silicates are green (P, Cu) and yellow (Si, Mn). The similar variability of fluorescence intensity (CLFM) to that of P and Cu likely indicates that fluorescence in sample 5-3b is caused by P- and Cu-laden organic colloids.

Figure 3.5:

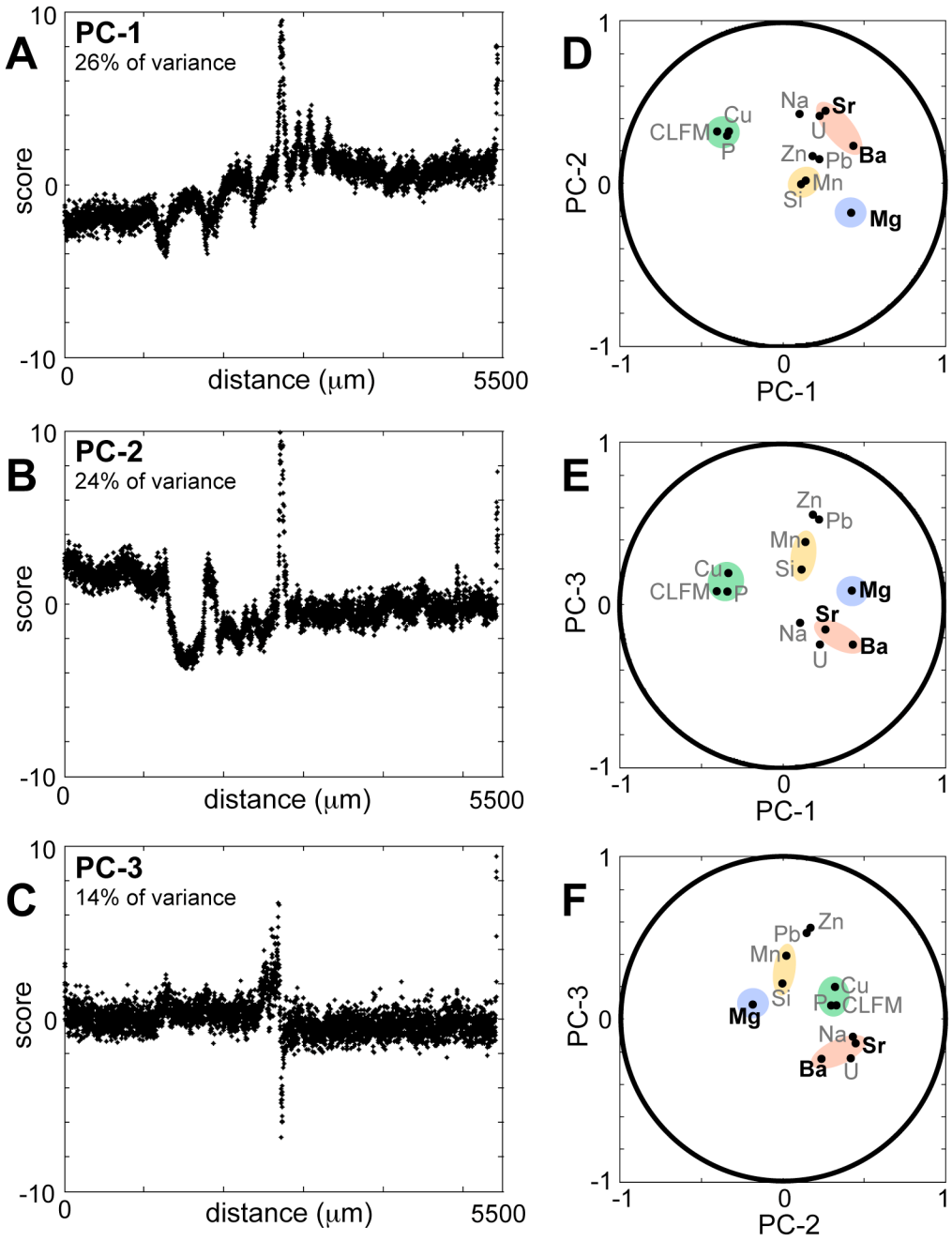
A
PC-1
26% of variance
score
distance (μm)
B
PC-2
24% of variance
C
PC-3
14% of variance
D
PC-2
PC-1
Na
Sr
U
CLFM
Cu
P
Zn
Pb
Ba
Mn
Si
Mg
E
PC-3
F

Figure 3.6: A and **B** show rainfall amounts and $\delta^{18}O$ values measured at Soreq Cave for the time period when sample 5-3b was growing. Monthly tabulation of the data (gray lines) is available beginning in water year 1996 (October 1995 – September 1996). The beginning of each water year is marked with a vertical dashed line. The annually averaged values of rainfall amount (triangles) and $\delta^{18}O$ (circles) are plotted at January of each year to show how annual $\delta^{18}O$ averages reflect the $\delta^{18}O$ values from the height of the wet season. **C** plots $\delta^{18}O$ (blue squares, right axis) and [Mg] (red diamonds, left axis) values in dripwater collected from inside Soreq Cave near the growth site of sample 5-3b.

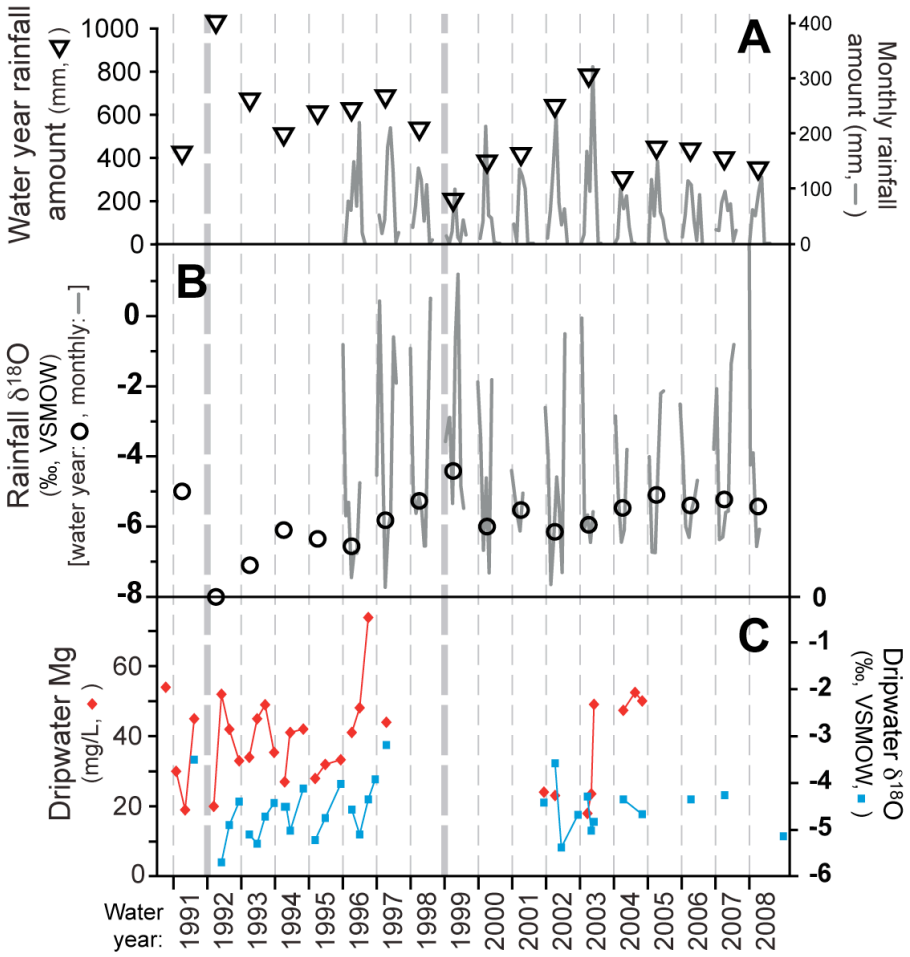

Figure 3.7 (next page): Rainfall record from above Soreq Cave plotted against $\delta^{18}O$ values measured in sample 5-3b. Annually averaged rainfall $\delta^{18}O$ values **(A)** and amounts **(B)** are reported from water years 1991-2008. The time axis of each record is scaled to match the analytical traverse across 5-3b **(C)** according to the criteria explained in Section 4.1. The vertical dashed lines represent the onset of winter wet seasons; a water year is assigned to the growth between each dashed line. The two years with extreme annual $\delta^{18}O$ values, 1992 and 1999, are marked with thicker dashed lines and used to anchor the 5-3b $\delta^{18}O$ data to the instrumental record. Plotted alongside the $\delta^{18}O$ results from 5-3b in **C** are yellow triangles showing the predicted $\delta^{18}O$ of calcite precipitated at 22.0°C. The predicted values are calculated using the annually averaged rainfall $\delta^{18}O$ values from **A**, which are corrected to dripwater $\delta^{18}O$ values by adding 1‰ (after Ayalon et al., 1998; Orland et al., 2009), and the water-calcite fractionation factor for $\delta^{18}O$ from Tremaine et al. (2011). Panel **D** shows the difference between the highest and lowest $\delta^{18}O$ values ($\Delta^{18}O$) measured in each of the proposed annual bands. Note the similar variation of $\Delta^{18}O$ values and annual rainfall totals, illustrated further in Figure 3.8.

Figure 3.7:

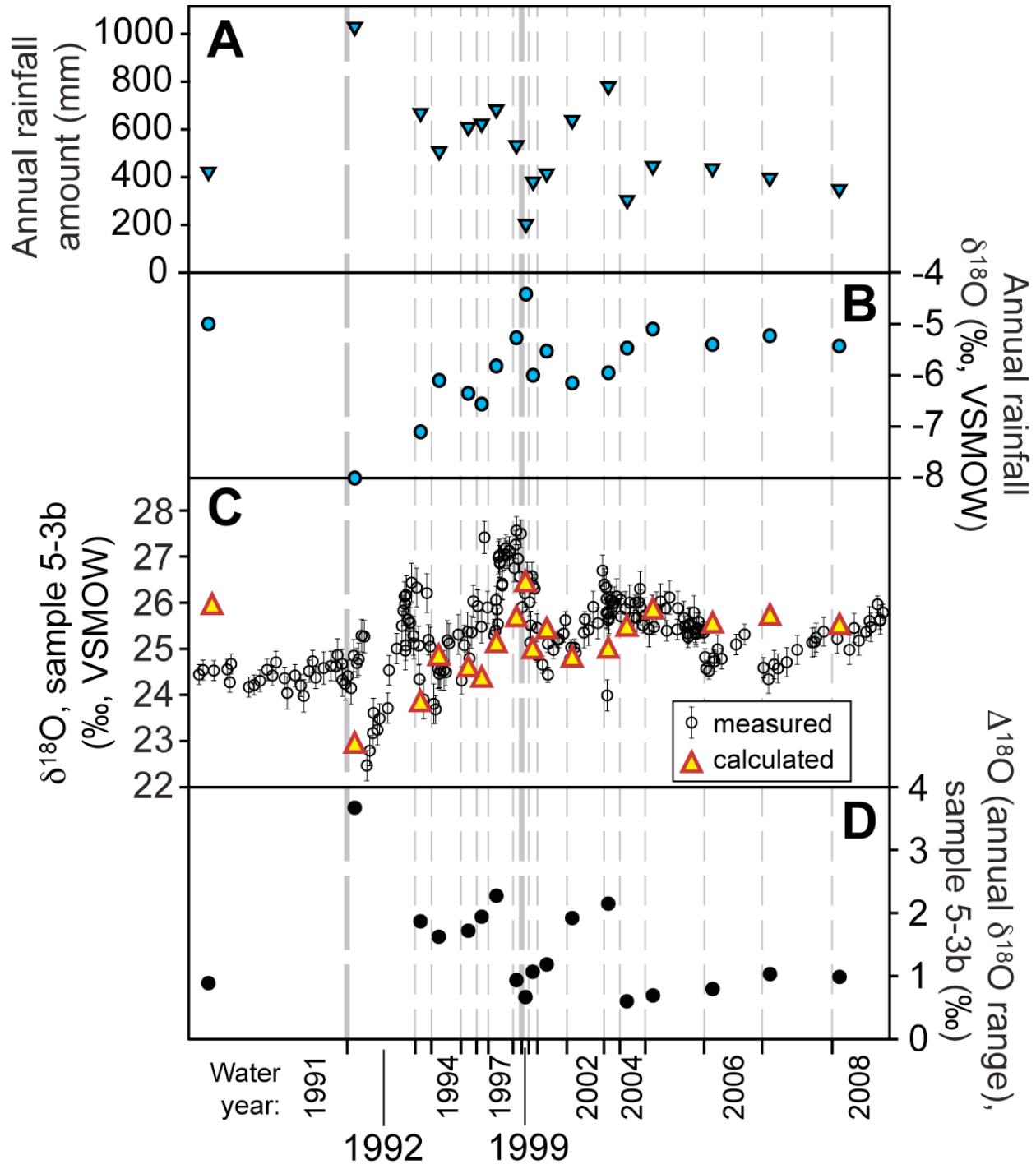
A
B
C
D
Annual rainfall amount (mm)
1000
800
600
400
200
0
Annual rainfall δ18O (‰, VSMOW)
-4
-5
-6
-7
-8
δ18O, sample 5-3b (‰, VSMOW)
28
27
26
25
24
23
22
measured
calculated
Δ18O (annual δ18O range), sample 5-3b (‰)
4
3
2
1
0
Water year:
1991
1992
1994
1997
1999
2002
2004
2006
2008

Figure 3.8: Illustrates the correlation between $\Delta^{18}O$ (range of $\delta^{18}O$ measured within each proposed annual band) and annual rainfall amount for sample 5-3b observed in Figure 3.7D.

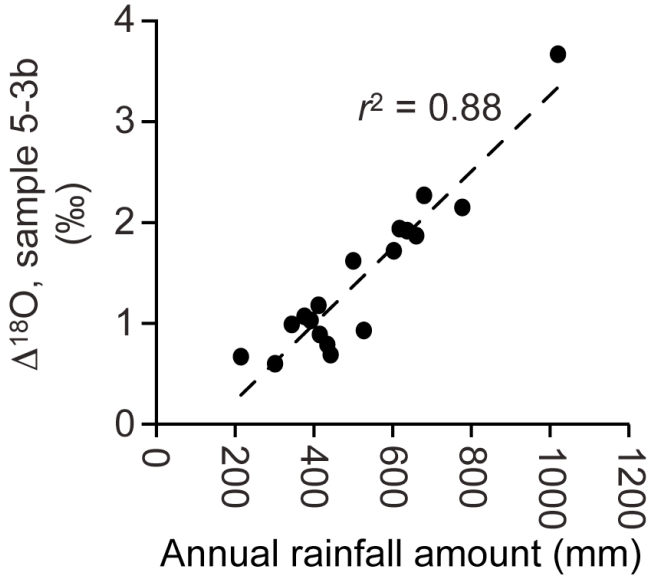

Tables

Table 3.1: Correlation coefficients (Pearson's *r*) of geochemical data acquired by ion microprobe – including $\delta^{18}O$ values as well as Mg, Si, P, Mn, Sr, Y, and Ba concentrations – from two portions of sample 5-3b excluding the turbulent layer shown in Figure 3.3. **A** shows the correlation of data between 0 and 2400 μm from the base of the sample. **B** includes data >2675 μm from the base of the sample. In each panel, the bolded, outlined values meet all three conditions that we use to identify significant correlations: (1) Pearson *r*-value >0.5, (2) Pearson p-value <0.02, and (3) Spearman rank correlation coefficient ρ-value >0.5. Note that for a p-value of 0.1, the familywise error rate (Dunn-Šidák correction; Sokal and Rohlf, 1995) for n=28 is 0.0038. Complete correlation results are available in the data repository, DR3.3.

A Pearson correlation coefficients (*r*) from inner portion of 5-3b.

	$\delta^{18}O$	Mg	Si	P	Mn	Sr	Y	Ba
$\delta^{18}O$	1	0.27	-0.27	0.18	-0.07	0.34	0.11	0.37
Mg		1	-0.14	-0.36	-0.32	-0.31	-0.33	0.05
Si			1	-0.15	**0.66**	-0.34	-0.23	-0.20
P				1	0.05	**0.61**	**0.67**	0.28
Mn					1	0.17	0.09	0.24
Sr						1	**0.81**	**0.62**
Y							1	0.49
Ba								1

B Pearson correlation coefficients (*r*) from outer portion of 5-3b.

	$\delta^{18}O$	Mg	Si	P	Mn	Sr	Y	Ba
$\delta^{18}O$	1	**0.69**	-0.24	-0.25	-0.04	**0.74**	0.19	0.38
Mg		1	-0.05	-0.41	0.16	**0.81**	0.19	**0.57**
Si			1	-0.11	0.32	0.07	0.03	0.30
P				1	0.06	-0.34	-0.27	-0.34
Mn					1	0.19	0.18	-0.03
Sr						1	0.11	**0.57**
Y							1	-0.21
Ba								1

Appendices

Figure A3.1: Images of sample 5-3b before and after being cast in a 25 mm epoxy round. In each view of the uncut sample, the dashed line shows the plane of the analytical surface. The arrows indicate growth direction, with the head of the arrow corresponding to younger growth. After casting the sample, a 1 mm-thick vertical section was cut from the middle of the epoxy round that exposed the desired analytical surface. The bottom-right panel shows the 1 mm-thick section laid flat between the remaining pieces of the epoxy round. The 1 mm-thick section was then trimmed of excess epoxy and mounted for analysis along with three UWC-3 calcite standard grains (Kozdon et al., 2009).

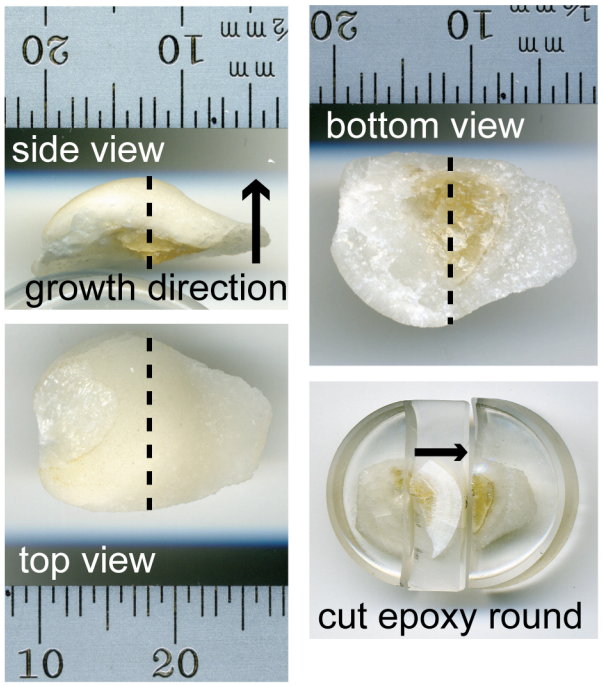

Table A3.2: Trace element concentrations (ppm-wt) in Sample 5-3b measured by WiscSIMS ion microprobe

Analysis #	band color*	Mg	Si	P	Mn	Fe	Zn	Sr	Y	Ba	distance (μm)**	pit condition$^{\Psi}$
5-3b-01	b	4429	302	338	1	30	6	197	0	18	0	1
5-3b-02	b	4284	327	388	0	17	9	189	0	18	284	0
5-3b-03	b	4608	299	189	0	12	6	223	0	19	1061	0
5-3b-04	b	4427	176	170	0	13	0	194	0	16	1147	0
5-3b-05	b	4425	277	502	0	19	10	147	0	15	1289	1
5-3b-06	i	4784	164	462	0	20	0	151	0	15	1325	1
5-3b-07	i	5764	202	123	0	0	10	80	0	7	1376	1
5-3b-08	i	5384	307	166	0	5	10	78	0	7	1385	0
5-3b-09	i	4425	263	21	0	15	9	17	0	2	1400	0
5-3b-10	d	6637	391	57	0	17	3	31	0	3	1629	0
5-3b-11	b	5116	247	284	0	17	4	98	0	19	1777	0
5-3b-12	i	4926	289	44	0	20	9	40	0	6	1854	0
5-3b-13	d	7521	363	272	0	22	9	91	0	20	1960	1
5-3b-14	d	10406	196	37	0	13	12	69	0	11	2140	0
5-3b-15	d	6531	217	40	0	24	10	131	0	38	2199	0
5-3b-16	d	4351	472	137	1	134	15	73	0	16	2365	0
5-3b-17	i	8753	215	46	0	13	22	113	0	11	2420	1
5-3b-18	b	7611	259	101	0	18	0	207	0	15	2600	1
5-3b-19	b	8520	474	117	0	44	4	195	0	15	2675	1
5-3b-20	d	7120	351	64	0	17	4	159	0	31	2790	1
5-3b-21	b	8189	341	61	0	20	14	175	0	47	2930	0
5-3b-22	d	10317	325	30	0	18	10	233	0	47	3280	0
5-3b-23	b	9146	188	40	0	19	15	175	0	36	3350	2
5-3b-24	d	8168	214	158	0	27	13	177	0	36	3451	1
5-3b-25	b	7675	237	71	0	5	19	174	0	37	3510	0
5-3b-26	d	8141	178	38	0	24	9	173	0	38	3609	2
5-3b-27	b	8472	143	58	0	24	3	152	0	29	3729	0
5-3b-28	d	4808	227	43	0	20	3	167	0	29	3990	0
5-3b-29	b	5203	293	140	0	28	13	114	0	31	4069	1
5-3b-30	d	7110	221	77	0	24	7	147	0	32	4350	0
5-3b-31	b	5177	308	129	0	19	15	112	0	34	4450	0
5-3b-32	d	5686	255	128	1	16	10	159	0	33	4710	0
5-3b-33	b	7250	605	65	0	18	6	167	0	42	4850	0
5-3b-34	b	6793	228	53	0	21	4	140	0	39	5060	0
5-3b-35	b	6620	351	80	1	12	6	155	0	33	5144	2
5-3b-36	d	7221	196	61	0	18	16	150	0	34	5245	1
5-3b-37	b	7481	289	85	0	24	17	160	0	35	5271	1
5-3b-38	d	8815	261	45	0	21	7	183	0	54	5360	0
5-3b-39	d	6152	275	145	0	18	20	141	0	28	4196	1
5-3b-40	d	6905	205	309	0	16	10	166	0	33	3870	1
5-3b-41	d	10974	292	33	1	28	12	211	0	39	3050	0
5-3b-42	i	8604	2182	150	3	409	9	138	0	10	2510	1
5-3b-43	d	5528	374	15	0	4	3	24	0	2	1477	1

Table notes:

*: band fluorescence classifications are as follows:
b = bright
d = dark
i = intermediate

**: distance is measured from the base of the sample

$^{\Psi}$: pit-bottoms of each analysis were imaged by SEM and classified as follows:
0 = regular (no cracks or pores)
1 = intermediate
2 = irregular (notable cracks or pores)

Table A3.3: Trace element profile (ppm-wt) of UWC-3 calcite standard measured by LA-ICP-MS at The Hebrew University in Jerusalem, Israel on Sept. 8, 2011. Two linear traverses were made using the same laser settings as described for sample analysis (no preclean pass). Trace element concentrations are calibrated by NIST-610 glass using ^{43}Ca as an internal standard with no matrix correction. The trace element concentrations of Si, P, Zn, Sr, Y, and Ba reported here (and **bolded** below) are used to find the relative sensitivity factors (RSF) that calibrate the trace element concentrations measured during the WiscSIMS analysis session on Feb. 21, 2011. Trace element concentrations in UWC-3 were also measured by ICP-AES and ICP-MS using acid-digestion techniques by SGS Mineral Services, Toronto, Canada; Nov. 10, 2011. These results and the quoted detection limits are in *italics*.

	Mg	Al	**Si**	**P**	K	Mn	Co	Ni	Cu
Mass analyzed	24	27	29	31	39	55	59	60	63
Analysis 1 (duration: 53.2 sec)									
Concentration (ppm)	5698	0.93	491	22.4	4.6	1452	0.47	0.23	0.31
2 s.e. (ppm)	(70)	(0.28)	(53)	(5.5)	(2.0)	(19)	(0.12)	(0.20)	(0.22)
Analysis 2 (duration: 44.2 sec)									
Concentration (ppm)	5635	0.33	588	30.0	2.6	1455	0.44	0.37	0.10
2 s.e. (ppm)	(69)	(0.23)	(63)	(6.1)	(2.3)	(15)	(0.12)	(0.30)	(0.24)
Avg. Concentration	5667	0.63	**540**	**26.2**	3.6	1454	0.46	0.30	0.21
Avg. 2 s.e.	(70)	(0.26)	(58)	(5.8)	(2.2)	(17)	(0.12)	(0.25)	(0.23)
SGS Mineral Services, acid-digestion ICP-AES and ICP-MS measurements									
Concentration (ppm)	*6400*			*100*		*1370*	*1.2*		
Detection limit (ppm)	*(100)*			*(100)*		*(10)*	*(0.5)*		

Table A3.3 (ctd)	**Zn**	**Sr**	**Y**	**Ba**	Pb	Th	U
Mass measured	66	88	89	137	208	232	238
Analysis 1 (duration: 53.2 sec)							
Concentration (ppm)	9.5	2766	7.8	12.9	5.6	0.24	0.057
2 s.e. (ppm)	(1.0)	(38)	(0.2)	(0.6)	(0.2)	(0.03)	(0.013)
Analysis 2 (duration: 44.2 sec)							
Concentration (ppm)	8.5	2718	7.8	12.1	5.6	0.21	0.045
2 s.e. (ppm)	(1.0)	(36)	(0.3)	(0.6)	(0.2)	(0.03)	(0.014)
Avg. Concentration	**9.0**	**2742**	**7.8**	**12.5**	5.6	0.23	0.051
Avg. 2 s.e. (ppm)	(1.0)	(37)	(0.2)	(0.6)	(0.2)	(0.03)	(0.014)
SGS Mineral Services, acid-digestion ICP-AES and ICP-MS measurements							
Concentration (ppm)	*5*	*2630*	*7.9*	*10.6*	*7*	*0.3*	*0.06*
Detection limit (ppm)	*(5)*	*(0.1)*	*(0.5)*	*(0.5)*	*(5)*	*(0.1)*	*(0.05)*

Table A3.4: Trace element profile of UWC-3 calcite standard measured by electron microprobe (EPMA; Kozdon et al., 2009) and LA-ICP-MS (this study). ICP-AES/MS measurements of UWC-3 by SGS Mineral Services are included to indicate accuracy. Also reported are the ^{40}Ca-normalized count rates of nine trace elements measured in five ion microprobe analyses of UWC-3. Relative sensitivity factors (RSF; in *italics* below) are calculated for each ion microprobe analysis of UWC-3 based on the trace element profile established by EPMA and LA-ICP-MS (**bold** values). The average RSF for the five UWC-3 measurements is used to calibrate each of the trace element concentrations measured during the WiscSIMS analysis session on Feb. 21, 2011.

	Mg	Si	P	Mn	Fe	Zn	Sr	Y	Ba
UWC-3 trace element concentrations, ppm-wt									
EPMA (UW$^{\alpha}$)	**5457**			**1222**	**4046**				
LA-ICP-MS (HUJI$^{\beta}$)	5667	**540**	**26.2**	1454		**9.0**	**2742**	**7.8**	**12.5**
ICP-AES/MS (SGS$^{\chi}$)	6400		(100)	1370	4100	(5)	2630	7.9	10.6
WiscSIMS measurements of UWC-3 (^{40}Ca-normalized count rate)									
UWC-3 Grain 11	5.59E-3	1.53E-5	1.16E-7	2.15E-4	7.65E-6	9.64E-8	2.47E-3	1.35E-6	8.38E-6
1 s.e. (%)	0.32%	10.18%	24.75%	0.11%	1.51%	59.92%	0.79%	5.18%	1.26%
*RSF**	*1.84E+4*	*6.62E+5*	*4.26E+6*	*1.07E+5*	*9.94E+6*	*1.76E+6*	*2.08E+4*	*1.08E+5*	*2.80E+4*
UWC-3 Grain 4	5.61E-3	1.88E-5	1.29E-7	2.21E-4	7.69E-6	7.53E-8	2.48E-3	1.36E-6	8.06E-6
1 s.e. (%)	0.28%	8.78%	23.43%	0.37%	2.10%	14.07%	0.76%	7.25%	4.40%
*RSF**	*1.83E+4*	*5.41E+5*	*3.81E+6*	*1.04E+5*	*9.89E+6*	*2.25E+6*	*2.08E+4*	*1.08E+5*	*2.92E+4*
UWC-3 Grain 5	5.77E-3	1.77E-5	1.61E-7	2.18E-4	7.11E-6	1.97E-8	2.50E-3	1.22E-6	8.10E-6
1 s.e. (%)	0.69%	10.24%	9.11%	0.33%	5.64%	–**	0.79%	5.76%	3.04%
*RSF**	*1.78E+4*	*5.74E+5*	*3.06E+6*	*1.05E+5*	*1.07E+7*	*8.58E+6*	*2.06E+4*	*1.20E+5*	*2.90E+4*
UWC-3 Grain 6	5.68E-3	1.63E-5	1.24E-7	2.14E-4	7.05E-6	1.87E-8	2.48E-3	1.17E-6	8.28E-6
1 s.e. (%)	0.52%	11.44%	12.98%	0.25%	1.90%	0.02%	0.97%	4.27%	0.84%
*RSF**	*1.81E+4*	*6.24E+5*	*3.98E+6*	*1.07E+5*	*1.08E+7*	*9.04E+6*	*2.08E+4*	*1.25E+5*	*2.84E+4*
UWC-3 Grain 9	5.59E-3	1.86E-5	1.36E-7	2.22E-4	7.68E-6	5.47E-8	2.49E-3	1.25E-6	8.31E-6
1 s.e. (%)	0.56%	9.99%	20.19%	0.40%	2.45%	20.23%	0.89%	9.76%	3.27%
*RSF**	*1.84E+4*	*5.47E+5*	*3.62E+6*	*1.03E+5*	*9.91E+6*	*3.09E+6*	*2.07E+4*	*1.17E+5*	*2.83E+4*
Average RSF	*1.82E+4*	*5.90E+5*	*3.75E+6*	*1.05E+5*	*1.02E+7*	*4.94E+6*	*2.08E+4*	*1.16E+5*	*2.86E+4*
1 s.d. (%)	1.34%	8.86%	12.06%	1.59%	4.47%	72.10%	0.44%	6.57%	1.70%

Table notes:

During each trace element analysis, WiscSIMS cycles through the suite of analyzed masses five times. The average ^{40}Ca-normalized count rate from all five cycles is reported above for all elements except Si and Zn. Due to decreasing count rates of Si and Zn in the first 2-3 cycles, perhaps resulting from surface contamination, the average value of the last 2 cycles is reported for these elements. Also note that the poor internal precision (s.e.) of Zn analyses is a result of low count rates caused by low ionization efficiency.

Symbol legend:

s.e. = standard error of ^{40}Ca-normalized counts measured in five (two for Si and Zn) analytical cycles

s.d. = standard deviation of the RSF values calculated from five UWC-3 analyses

α: EPMA measurements were made at UW-Madison (see Kozdon et al., 2009)

β: LA-ICP-MS measurements were made at The Hebrew University in Jerusalem, Israel. These concentration values were calibrated using the NIST-610 glass standard, so are not matrix-matched to the UWC-3 calcite standard. Matrix effects are assumed to be minor.

χ: ICP-AES/MS measurements from a commercial laboratory, SGS Mineral Services (Toronto, Canada). P and Zn concentrations (in parentheses) are at the detection limit quoted by SGS.

*: RSF values are calculated as follows (after Kita et al., 2004):
RSF = ppm / (^{40}Ca-normalized count rate x CaO wt%)
Trace element concentrations in Soreq speleothems are calculated using the mean RSF values listed above and observed ^{40}Ca-normalized count rates for each element. The CaO wt% in Soreq speleothems is assumed to match that of UWC-3.

**: The final analytical cycle in this spot returned no Zn counts, so standard error is not reported.

Figure A3.5: Data acquired with a reflected-light profilometer showing the depth-profile of a pre-cleaned LA-ICP-MS trench in a Soreq speleothem. Panel **A** plots the depth (in μm) of a profile measured across a pre-cleaned laser trench (shown in Panel **B**).

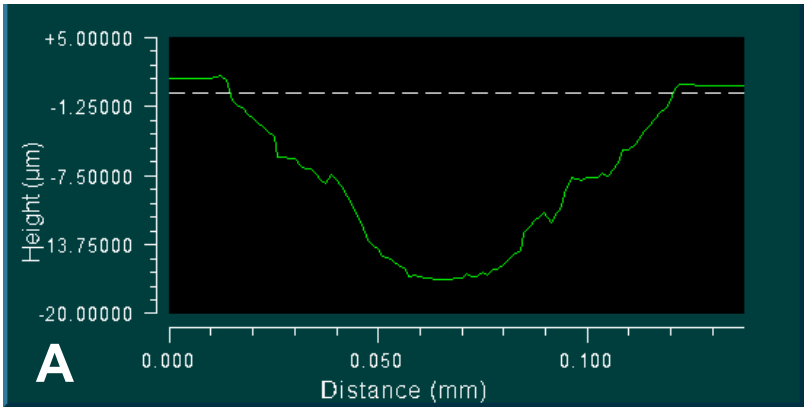

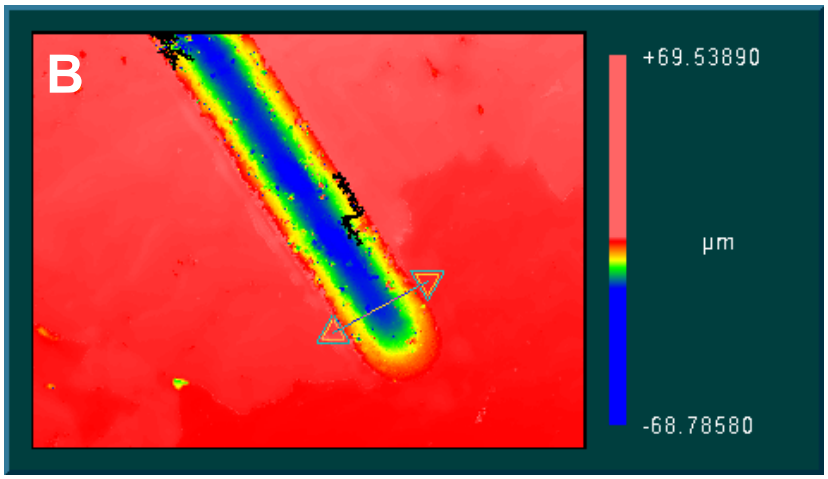

Figure A3.6: Data acquired with a reflected-light profilometer showing an axial depth-profile of an abruptly-stopped laser traverse. Panel **A** plots the depth (in μm) measured along the profile shown in Panel **B**. The consistent slope across the leading edge of the laser trench indicates that material on the analytical traverse is ablated at an approximately constant rate while the 55 μm-diameter laser beam passes over.

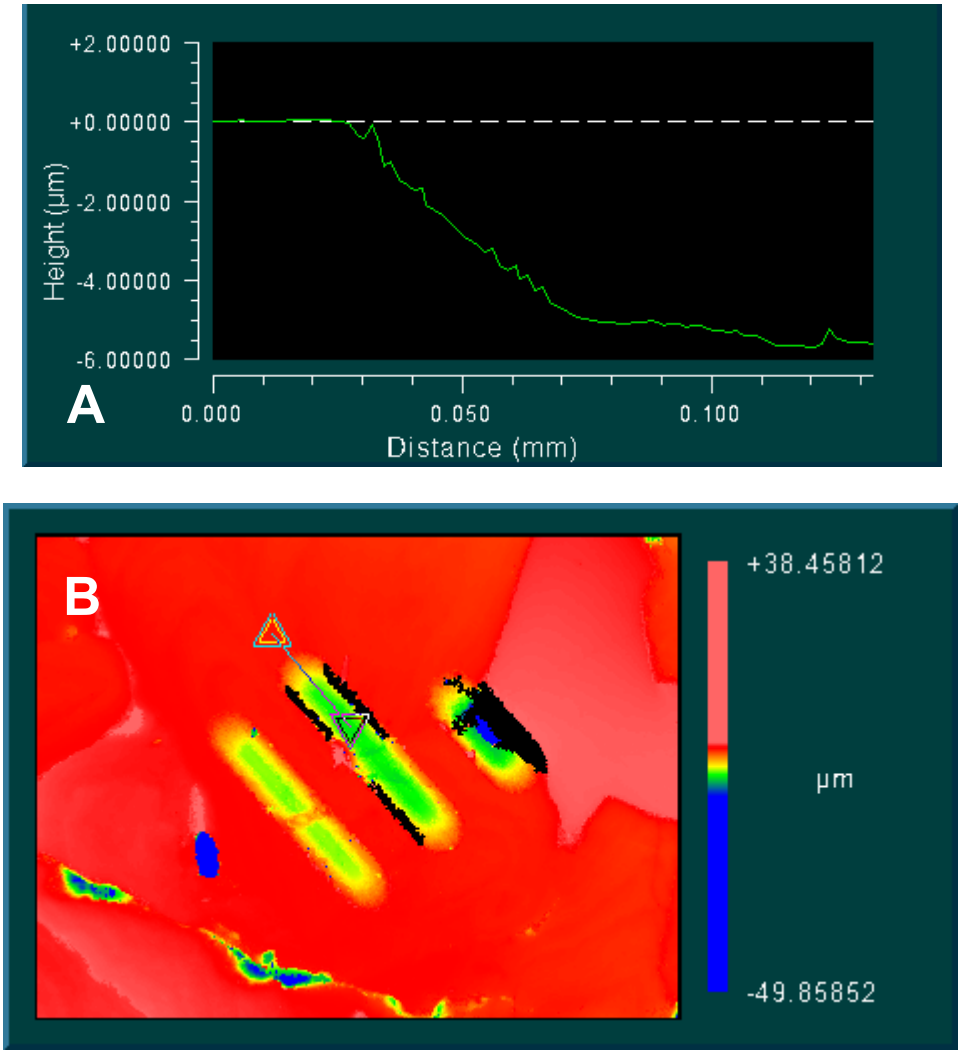

Figure A3.7 (next page): Trace element profiles (ppm) of all elements measured by both LA-ICP-MS (black squares) and ion microprobe (red squares) along the 5.4 cm analytical transect of sample 5-3b. We identified 11 elements as having a reliable signal during LA-ICP-MS analysis (Na, Mg, Si, P, Mn, Cu, Zn, Sr, Ba, Pb, and U). Colored vertical lines are included to aid visual comparison of the LA-ICP-MS plots. Trace element concentrations for K and Fe, which appeared to have coherent signals, were not classified as reliable because they have isobaric interferences with $^{38}Ar^{1}H$ and $^{40}Ar^{16}O^{1}H$, respectively. Ion microprobe measurements of Fe and Y are reported because their calibrations are independently confirmed by EPMA (Fe) and ICP-MS (Y) measurements of UWC-3 calcite standard (Table A3.4).

Figure A3.7:

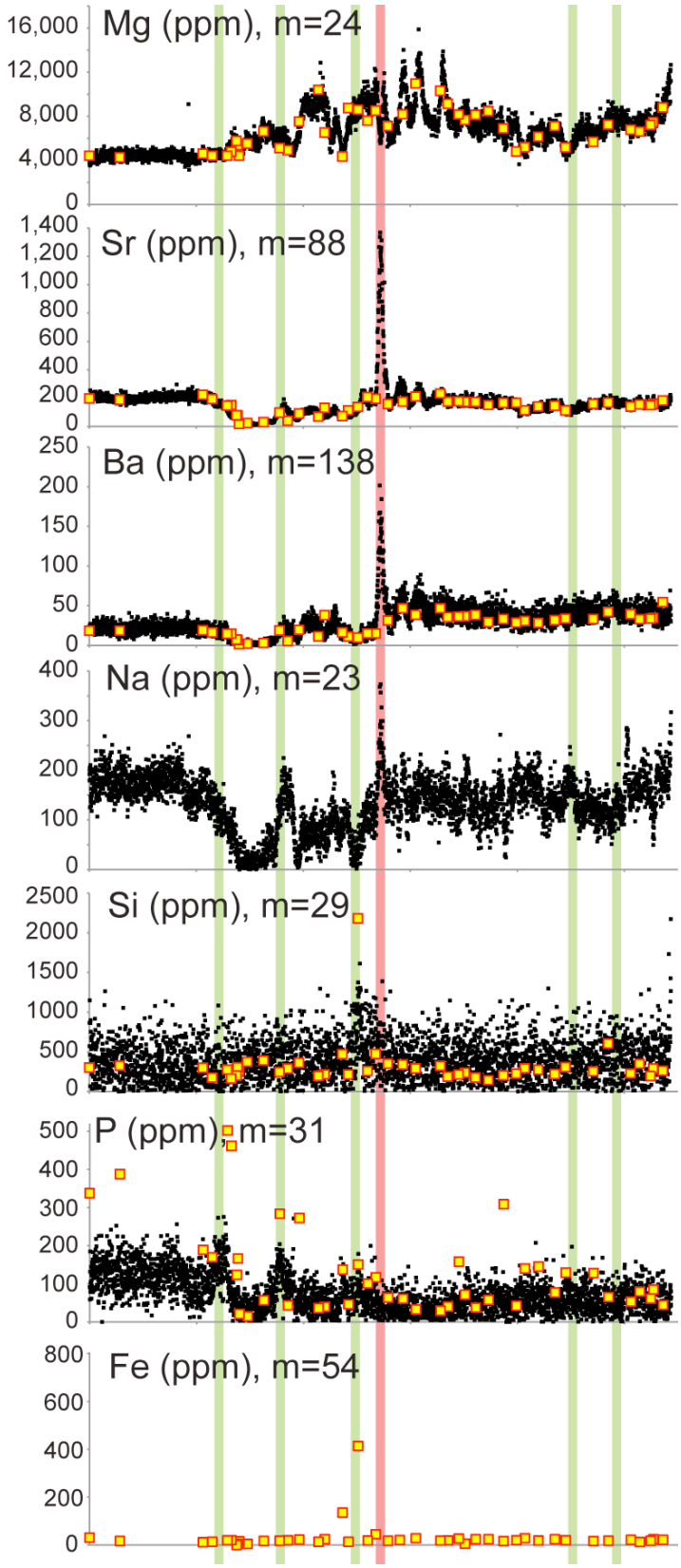
Mg (ppm), m=24
16,000
12,000
8,000
4,000
0
Sr (ppm), m=88
1,400
1,200
1,000
800
600
400
200
0
Ba (ppm), m=138
250
200
150
100
50
0
Na (ppm), m=23
400
300
200
100
0
Si (ppm), m=29
2500
2000
1500
1000
500
0
P (ppm), m=31
500
400
300
200
100
0
Fe (ppm), m=54
800
600
400
200
0

Figure A3.7 (ctd):

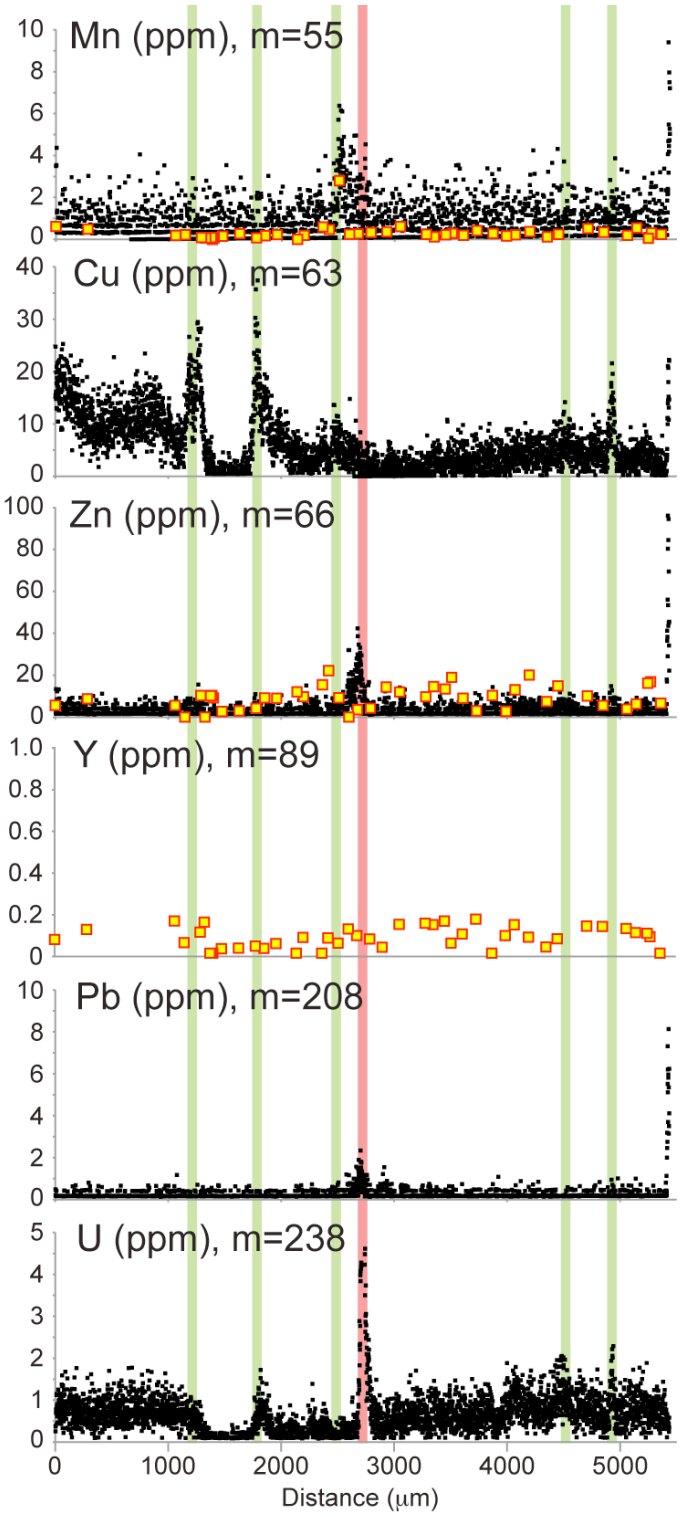

Table A3.8: Average trace element concentrations (ppm-wt) and 2 s.d. values (%) measured in five 30 s traverses of NIST-610 that bracket the analytical traverse of sample 5-3b. The index element for these concentration calculations is ^{29}Si. The nominal glass composition of NIST-610 is 72 wt% SiO_2, 12% CaO, 14% Na_2O, and 2% Al_2O_3. NIST-certified trace element concentrations are listed in the bottom row.

	Na	Mg	Al	P	K	Ca	Ca	Mn	Co	Ni
Mass measured	23	24	27	31	39	42	43	55	59	60
Avg. concentration (ppm)	102300	478.3	11110	352.9	497	84530	84520	499	416.7	472
2 s.d. (ppm)	29	0.9	4.6	0.7	27	130	78	0.47	0.21	0.56
2 s.d. (% conc.)	0.028	0.19	0.041	0.19	5.4	0.16	0.092	0.095	0.05	0.12
NIST concentration (ppm)*					(461)			457	(390)	458.7

Symbol legend:
*: Known concentrations are supplied by the National Institute of Standards and Technology (NIST) as follows:
- Certified values normal text
- Reference values in italics
- Values in parentheses are informational only

Table A3.8 (ctd)	Cu	Zn	Sr	Y	Ba	Au	Pb	Th	U
Mass measured	63	66	88	89	137	197	208	232	238
Avg. concentration (ppm)	442.4	468.7	530.6	463	447.6	23.66	438.3	470.5	474.9
2 s.d. (ppm)	1.2	1.9	0.52	0.74	0.28	0.041	1.1	0.75	0.4
2 s.d. (% conc.)	0.26	0.41	0.099	0.16	0.063	0.009	0.26	0.16	0.085
NIST concentration (ppm)*	*444*	(433)	515.5		453	(25)	426	457.2	461.5

Table A3.9: Dripwater $\delta^{18}O$ values and Mg concentrations measured in samples collected from a drip-site adjacent to sample 5-3b between 1990 and 2008. Each dripwater sample was collected in 125 cc Nalgene bottles that were pre-washed in the dripwater and filled to the top. Both $\delta^{18}O$ and [Mg] were measured at the time of sampling at the Geological Survey of Israel; [Mg] was analyzed using a Perkin Elmer 5300 V ICP-Optical Emission Spectrometer.

Sampling date (M/D/Y)	Mg (mg/L)	$\delta^{18}O$ (‰, VSMOW)
7/10/90	54	
10/30/90	30	
2/4/91	19	
5/13/91	45	-3.50
12/10/91	20	
3/2/92	52	-5.70
5/26/92	42	-4.90
9/9/92	33	-4.40
12/27/92	34	-5.10
3/22/93	45	-5.30
6/16/93	49	-4.72
9/21/93	35	-4.43
1/13/94	27	-4.51
1/30/94		-4.51
3/14/94	41	-5.02
8/2/94	42	-4.12
12/8/94	28	-5.22
3/27/95	32	-4.75
9/10/95	33	-4.02
1/7/96	41	-4.57
4/1/96	48	-5.10
7/3/96	74	-4.35
9/16/96		-3.92
1/14/97	44	-3.19
9/10/01	24	-4.42
1/8/02	23	-3.58
3/17/02		-5.38
9/12/02		-4.68
12/23/02	18	-4.29
2/3/03	24	-5.02
3/4/03	49	-4.83
1/14/04	47	-4.35
5/20/04	52	
8/5/04	50	-4.67
1/13/06		-4.35
1/11/07		-4.26
10/6/08		-5.14

Figure A3.10: PCA of LA-ICP-MS results from sample 5-3b, excluding trace element measurements from a portion of the "turbulent" layer (between 2675 and 2800 μm from the base of the sample). This PCA tested the influence of the excluded section, which contains notable changes in trace element concentrations (Figure 3.4B), on the PCA of the entire laser traverse (Figure 3.5). As in Figure 3.5, panels A and B show the respective scores and percent of variance explained by the first two principal components. Panel C illustrates elemental loadings on the first two principal components. The similarity of the patterns in panels A-C below to panels A, B, and D of Figure 3.5 suggests that trace element variability within the turbulent layer did not distort PCA of the entire laser traverse.

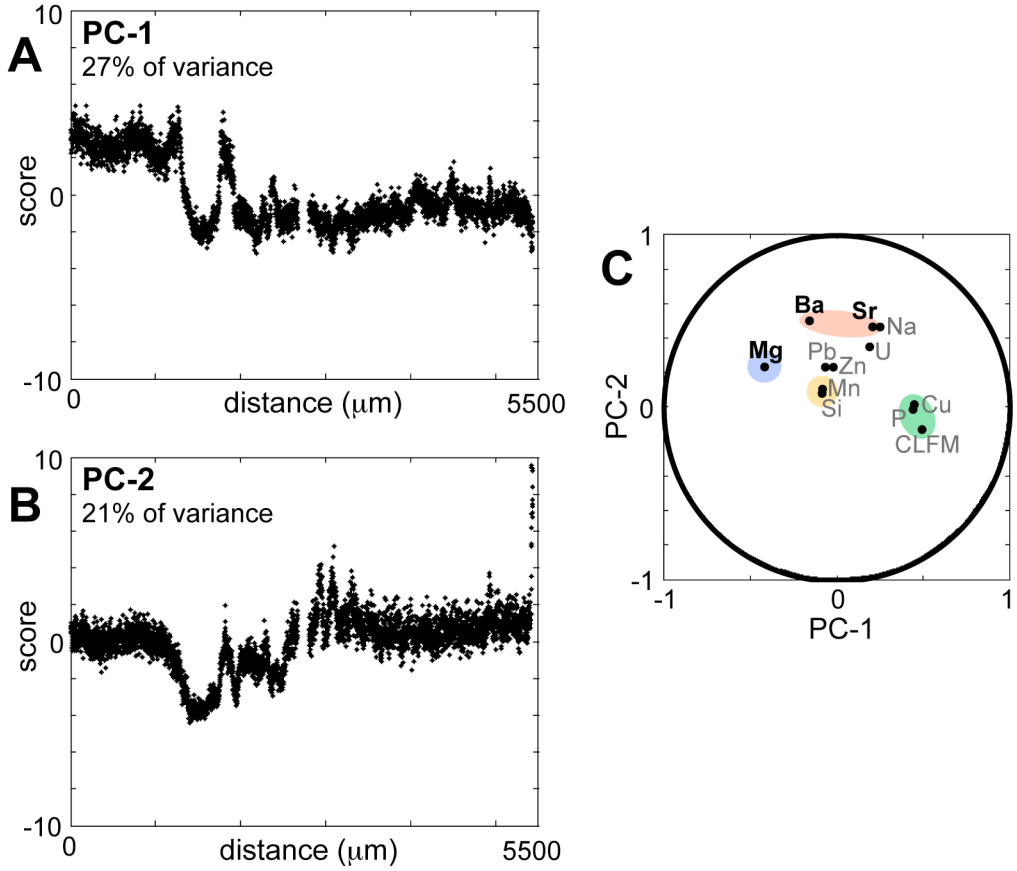

Figure A3.11-1 and 11-2: Results of PCA from the sample base to 2675 μm along the analytical traverse (A3.11-1) and from 2800 μm to the outer rim (A3.11-2). Each figure shows the respective scores and percent of variance explained by the first two principal components in panels A and B. Panel C in each figure illustrates elemental loadings on the first two principal components. Notable classes of elements are highlighted as in Figure 3.5.

Figure A3.11-1:

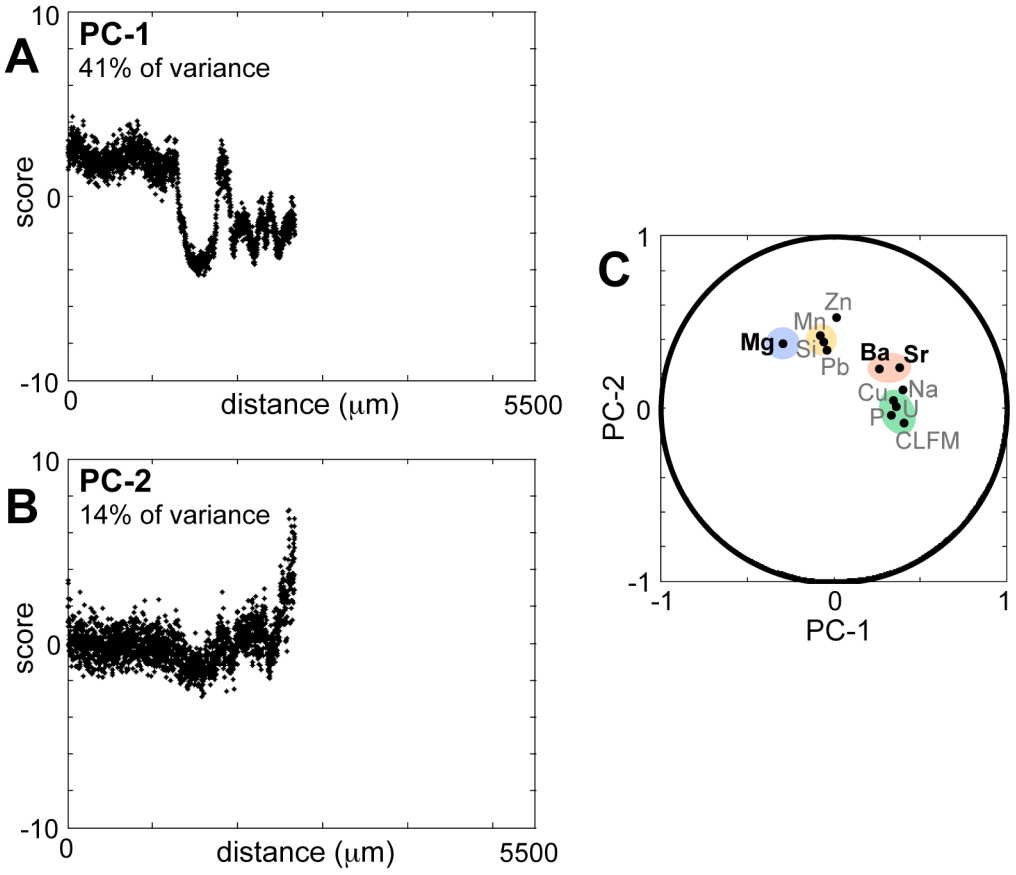

Figure A3.11-2:

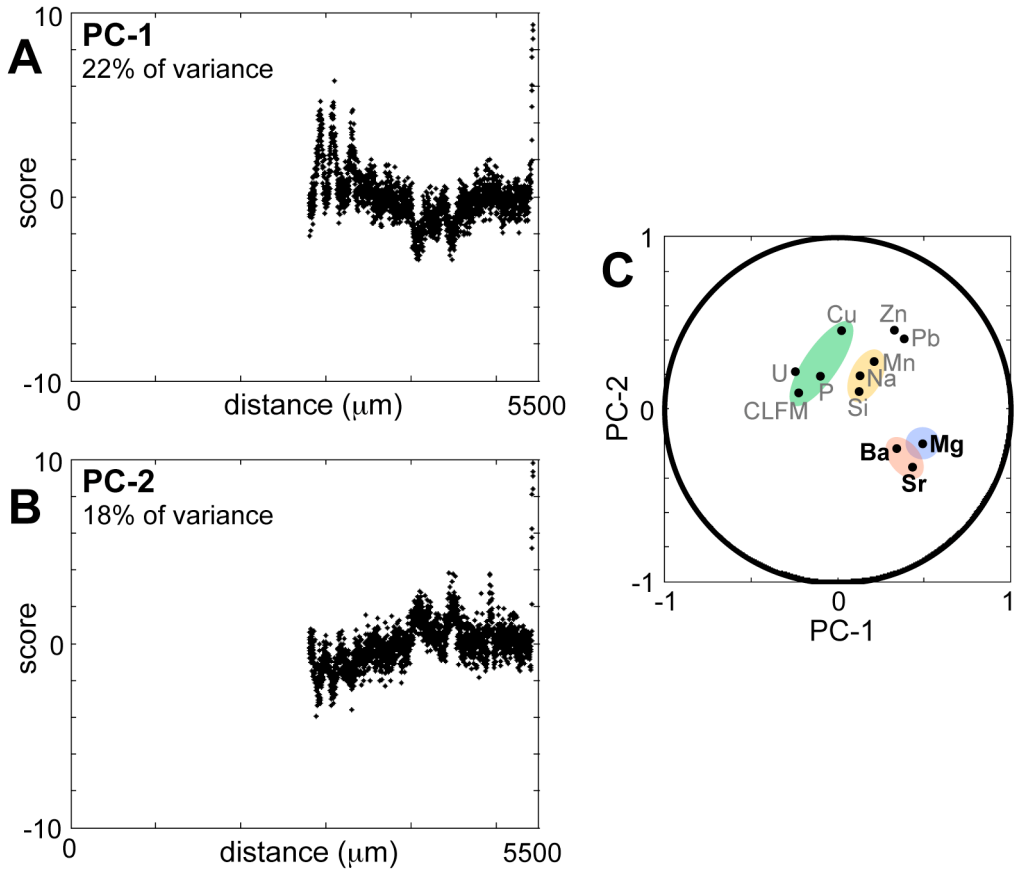

Data Repository Index

Large data tables and figures for each chapter are included in the supplementary files available with the online version of this dissertation.

DR3.1: Ion microprobe raw and corrected oxygen isotope ratios from 231 analyses of sample 5-3b from Soreq Cave.

DR3.2: High-resolution map of trace element and $\delta^{18}O$ ion microprobe analyses in sample 5-3b.

DR3.3: Correlation results (including Pearson's *r*- and p-values, as well as Spearman's ρ-value) of trace element concentrations measured by both ion microprobe and LA-ICP-MS analysis in two regions of sample 5-3b (the inner and outer portions shown in Figure 3.3).

DR3.4: Rainfall amount and $\delta^{18}O$ values measured above Soreq Cave from 1990-2008. Monthly tabulation of rainfall data began in 1995.

DR3.5: SEM images of ion microprobe pits from trace element and $\delta^{18}O$ analyses in sample 5-3b.

CHAPTER IV

New micro-proxy approach for assessing seasonal climate records in speleothems: Combining high-resolution geochemical analyses with quantitative characterization of fluorescent annual banding

Ian J Orland[1], Yuval Bursytn[2], Miryam Bar-Matthews[3], Reinhard Kozdon[1], Avner Ayalon[3], Stephen R Meyers[1], Alan Matthews[2], John W Valley[1]

[1]*WiscSIMS, Department of Geoscience, University of Wisconsin, 1215 W Dayton St., Madison, WI, 53706, USA*

[2]*The Institute of Earth Sciences, The Hebrew University, Givat Ram, Jerusalem, 91904, Israel*

[3]*Geological Survey of Israel, 30 Malchei Israel St., Jerusalem, 95501, Israel*

Abstract

Trace element, oxygen isotope ($\delta^{18}O$), and quantitative fluorescent banding analysis of a calcite Soreq Cave stalactite (sample 2N) are used to construct a coherent record of seasonal climate in the Eastern Mediterranean between 34 and 4 ka. A composite, 1-μm-resolution record of fluorescent banding patterns is acquired directly from digitized confocal laser fluorescent microscope (CLFM) images of fluorescent annual growth bands in sample 2N. A customized peak-finding algorithm was developed in order to count and categorize fluorescent banding patterns by measuring their width and characterizing the "shape" of their fluorescence (i.e. sawtooth, sinusoidal, or reverse-sawtooth). In order to quantify the shape of peak fluorescence within a band, the variable "fractional peak position" is defined as the ratio of the distance from a fluorescent peak to the preceding valley and the distance between the two valleys that bracket the peak. The algorithm finds a similar number of bands (2288) as counted by visual inspection (2328). Five sections of fluorescent banding patterns are distinguished in sample 2N by a combination of their band widths and fractional peak positions; the Holocene is split into three sections, the Younger Dryas represents a fourth section, and the portion of the sample older than 15 ka is the fifth section.

Trace element data were acquired at both seasonal- and annual-resolution along the 13.4 cm analytical traverse of sample 2N via discrete 10-μm-diameter ion microprobe pits (Mg, Sr, Ba, Si, P, Fe, Mn, Zn, Y) and a continuous 55-μm-resolution laser ablation (LA)-ICP-MS traverse (Mg, Sr, Ba, Na, Si, P, Mn, Cu, Zn, Y, Pb, U), respectively. LA-ICP-MS trace element profiles of the five sections delineated by fluorescent banding patterns are compared by principal component analysis (PCA) to test whether the changes in banding patterns are reflected in the trace element geochemistry of sample 2N.

PCA of the continuous trace element data from the four youngest fluorescent banding sections shows patterns of variability that are similar to those of a modern sample, suggesting that climate after 14 ka featured distinct wet- and dry-seasons as observed above Soreq Cave today. Trace element variability before 15 ka in sample 2N is notably dissimilar. Seasonal-resolution ion microprobe analyses show that the annual variability of Mg and P increase significantly after 15 ka, indicating the onset of a seasonal rainfall regime where annual dry-seasons permit these elements to accumulate in vadose zone groundwater and the overlying soil, respectively. Reduced seasonal variability of Sr during the Younger Dryas may be caused by the contribution of Sr from wind-blown dust to wet season dripwaters that would otherwise be Sr-poor. The combined results of trace element, $\delta^{18}O$, and fluorescent band analysis all point to a change in the seasonal rainfall distribution above Soreq Cave at 15 ka from more consistent rainfall throughout the year to distinct wet- and dry-seasons.

1. INTRODUCTION

1.1. Background and objectives

In the last decade, the time-resolution of speleothem paleoclimate records has increased in response to the development of micron-scale analytical techniques. Sub-annual measurements of trace elements (Fairchild et al., 2000; Treble et al., 2003, 2005a; Johnson et al., 2006; Borsato et al., 2007; Fairchild and Treble, 2009; Smith et al., 2009; Boch et al., 2011), oxygen isotopes (Treble et al., 2005b; Orland et al., 2009, 2012), and fluorescent banding (Baker et al., 1993; Baker and Genty, 1999; McGarry and Baker, 2000; Perrette et al., 2005; Tan et al., 2006; Asrat et al., 2007; Baker et al., 2008) have contributed valuable insight into the paleoenvironmental setting of different caves.

Chapter 3 of this dissertation, which examined a modern (1990–2008) Soreq Cave stalagmite, is the first study to assess all three of these sub-annual characteristics in parallel. The three analytical techniques used to obtain these data were: (1) ion microprobe for spot-analyses of $\delta^{18}O$ and trace element data (2) laser-ablation ICP-MS (LA-ICP-MS) for a continuous trace element transect, and (3) confocal laser fluorescent microscopy (CLFM) for imaging of fluorescent banding. The combination of these datasets forms the basis of a detailed explanation of how seasonal environmental changes are recorded in modern Soreq Cave speleothems. Notably, Chapter 3 was able to shape the interpretation of geochemical and fluorescent variability in the speleothem using observations of rainfall and dripwater chemistry that were collected as the sample grew. Because speleothem paleoclimate records cover much longer time periods and have no instrumental records for comparison, a different approach is needed to assess the seasonal climate information recorded in their geochemistry and fluorescent banding.

Here, we develop a multi-proxy strategy for examining the seasonal climate signal in speleothem paleoclimate records. The approach, which draws on the findings of Chapter 3, incorporates high-resolution trace element and $\delta^{18}O$ analyses as well as a new method for quantitative characterization of fluorescent bands. The method is tested in a speleothem (Soreq Cave sample 2N) where ion microprobe analyses of $\delta^{18}O$ indicate a change in the regional seasonal climate regime following the last glacial maximum at ~20 ka (Orland et al., 2012). This method establishes a protocol that can be either partly or fully implemented in other speleothems. Given the wide geographic distribution of caves and the rarity of low latitude and continental seasonal-resolution paleoclimate records, this approach provides a valuable means to assess past changes in seasonal climate around the globe as well as the associated shifts in atmospheric circulation.

1.2. Prior work

Speleothem samples from Soreq Cave (see inset map, Figure 4.1) provide an exceptional opportunity to study seasonal climate for two reasons. First, a large amount of work has established Soreq Cave as a well-characterized natural laboratory (Bar-Matthews et al., 1997, 1999, 2003, 2011; Ayalon et al., 1998, 1999; Matthews et al., 2000; Kaufman et al., 2003; Kolodny et al., 2003; Vaks et al., 2003; McGarry et al., 2004; Affek et al., 2008). These prior studies have identified Soreq samples that record significant climate change over the past 185 ky and provide insight into dripwater pathways, groundwater residence times, and isotopic reaction kinetics. Second, the modern climate regime has distinct wet and dry seasons both in terms of rainfall amount and isotopic composition.

Since 1995, when monthly tabulation of rainfall above Soreq Cave began, 95% of the rain above Soreq Cave fell during the annual "winter wet-season" between November and April (Ayalon et al., 2004; Orland et al., 2009). Ayalon et al. (1998) show that when monthly rainfall amounts are highest, rainfall $\delta^{18}O$ values are lowest. The $\delta^{18}O$ value of rainfall is transmitted to cave dripwaters, which also have lowest $\delta^{18}O$ values during winter months (Ayalon et al., 2004), and is subsequently recorded in speleothem calcite (Orland et al. 2009, 2012; previous chapter).

Orland et al. (2009) describe the co-variability of $\delta^{18}O$ values and fluorescence intensity in growth bands of a Soreq speleothem that grew from 2.2–0.9 ka. In this sample, fluorescence is brightest at the beginning of each band and gradually decreases until the onset of the next bright fluorescent band. This sawtooth pattern is also evident in $\delta^{18}O$ values, which are lowest in the bright portion of each band and gradually increase to their highest value at the non-fluorescent edge of each growth band. Orland et al. (2009) proposed that the annual flush of low-$\delta^{18}O$ rainfall during winter wet-seasons carries organic colloids, like humic or fulvic acids, from the overlying soil into the cave where they are entrained in speleothem calcite and cause the observed fluorescence. Thus, fluorescent bands are interpreted as annual.

Recent work found that the sawtooth patterns of fluorescence and $\delta^{18}O$ persist through the Holocene in Soreq sample 2N (34–4 ka), suggesting that the modern climate regime of distinct wet- and dry-seasons is persistent throughout the Holocene (Orland et al., 2012). Before 10.5 ka, however, different patterns of fluorescent banding and $\delta^{18}O$ variability are found in sample 2N. Qualitative classifications distinguish four types of growth bands in the pre-Holocene portion of the sample (Orland et al., 2012).

Fluorescent banding patterns are used to assign three of the four band-types identified in sample 2N; the fourth band-type is assigned based on the pattern of $\delta^{18}O$ variability. Figure 4.2

shows the three fluorescence classifications: (1) the sawtooth pattern described above, (2) a "sinusoidal" pattern where the transition from both bright-to-dark and dark-to-bright fluorescent domains is smooth, and (3) a reverse-sawtooth pattern where the beginning of a band is marked by a sharp, dark boundary and fluorescence gradually brightens to the end of the band. A classification is assigned to 165 bands in sample 2N where $\delta^{18}O$ was measured in both a bright- and dark-fluorescent domain. Assuming that the measured bands are representative of the whole sample, three regimes of seasonal climate are identified in the last 34 ky (Orland et al., 2012). From 10.5 ka to present, sawtooth fluorescent bands indicate a pattern of distinct wet and dry seasons similar to today. During the Younger Dryas cold period (13-11.5 ka) fluorescent bands are mostly sinusoidal, suggesting more consistent rainfall throughout the year. Before 15 ka, reverse-sawtooth patterns of fluorescence and $\delta^{18}O$ variability are common within growth bands, perhaps indicating regular winter snow cover or different vegetation over Soreq Cave.

In order to test the proposed changes in seasonal climate regime, the present study introduces a method to quantitatively count bands and assess their "shape" (i.e. sawtooth, sinusoidal, reverse-sawtooth) using digitized CLFM images of fluorescent banding along the entire analytical traverse. This information is used to subdivide the sample into sections with distinct banding patterns. Principal component analysis (PCA) is then used to identify common patterns of variability in continuous trace element profiles across each banding section. A suite of 10-μm-diameter spot analyses provides sub-annual trace element data that further refine seasonal climate interpretations. If applied to speleothems from other caves, this method for integrating high-resolution proxy records represents a way to begin cataloging continental patterns of seasonal climate change.

2. MATERIALS AND ANALYTICAL METHODS

High-resolution analyses of speleothem geochemistry and fluorescent banding are the foundation for the procedure developed in this study. Soreq Cave stalactite sample 2N (Figure 4.1) was chosen to test the approach because detailed geochronology and seasonal-resolution $\delta^{18}O$ records have already been acquired from it (Orland et al., 2012). As shown in Figure 4.1, the analytical traverse established by prior workers follows the longest radial axis of the sample in order to maximize the time-resolution of geochemical analyses. Details of sample preparation are reported in the Appendix, A4.1.

2.1. Trace element measurements

2.1.1. Laser-ablation ICP-MS

LA-ICP-MS analysis of trace elements in sample 2N was completed at The Hebrew University-Jerusalem (Israel) using a New Wave UP-193 nm laser ablation system coupled to an Agilent Technologies 7500 series ICP-MS. Each polished epoxy mount was loaded into a He-purged "super-cell" (Dvir and Kessel, *in prep*) along with a chip of NIST-610 standard glass. Concentrations of 12 trace elements (Na, Mg, Si, P, Mn, Cu, Zn, Sr, Y, Ba, Pb, and U were measured along the 13.4 cm analytical traverse of sample 2N. Because the sample was cut into ~1 cm-long chips for ion microprobe analysis (Figure 4.1), the complete traverse is composed of 13 linear traverses.

As described in further detail in the previous chapter, each of the twelve analytical traverses required two laser passes. The first pass used a low-power (50% laser power, 30 Hz, 10 μm/sec stage speed), 100 μm-diameter beam to remove ~5 μm of material in order to "preclean" the sample. After precleaning, the analytical pass used a high-power (65% power, 10 Hz, 4

μm/sec stage speed), 55 μm-diameter beam that removed a further 10 μm of sample. Ion counts measured in the ICP-MS were integrated three times per second; during the analytical traverse, each integration corresponds to a laser advancement of ~1.33 μm. Because the laser excavates material at a roughly constant rate within the analytical spot, the data series approximates a 55 μm running-mean of trace element concentrations along the analytical traverse. Figure A4.2 reports the results (in ppm) of LA-ICP-MS analyses in each chip.

Since a matrix-matched standard for LA-ICP-MS analysis did not exist, the trace element concentrations measured in sample 2N (Figure A4.2) are calibrated by NIST-610 standard glass. Prior work found excellent agreement between measurements of UWC-3 calcite standard by glass-standardized LA-ICP-MS and acid-digestion ICP-MS (see Table A3.3 in previous chapter), suggesting that no matrix correction is needed for LA-ICP-MS analysis of sample 2N. Therefore, the analytical pass of each chip from sample 2N was bracketed by four 30 s traverses in NIST-610 glass using the same laser settings (no precleaning pass). In addition, to calibrating trace element concentrations in sample 2N, the bracketing measurements of NIST-610 allow us to demonstrate the stability of the ICP-MS during the analytical session. Using ^{29}Si as an internal standard, the average 2 s.d. of the four bracketing analyses of Na, Mg, Al, Mn, and Cu concentrations in the 13 chips is <3% of their respective average concentrations (Table A4.3). For Zn, Sr, Ba, Au, Pb, and U measurements the average 2 s.d. is <6% of the average concentrations. After excluding one outlying NIST-610 measurement (out of 56 total NIST-610 analyses), the average 2 s.d. of P concentrations in the bracketing standards is <7% of the average concentration. The stability of trace element measurements in standard glass reflects the robustness of relative concentration values. This determination is important for the interpretive

methods used in this study, which rely on relative changes in trace element concentration and not their absolute value.

2.1.2. Ion microprobe

Growth bands in sample 2N are typically <20 μm in diameter. Thus, the 55 μm-diameter laser used for LA-ICP-MS analysis typically averaged elemental concentrations across multiple growth bands. In order to examine seasonal variability of trace element concentrations in sample 2N, a series of 70 10-μm-spot analyses were made with the WiscSIMS ion microprobe at the University of Wisconsin-Madison. These measurements were made during the same analytical session described in the previous chapter (Table A3.2) and an overview of the analytical settings is given below. Trace element concentrations of Mg, Si, P, Mn, Fe, Zn, Sr, Y, and Ba (in ppm-wt) measured in sample 2N are reported in Table 4.1.

A 1.0 nA beam of O^- ions with an accelerating voltage of 13 kV was used to sputter secondary ions from 10-μm-diameter pits on the polished sample surface. Positively charged secondary ions were accelerated across a 10 kV potential into a double-focusing mass spectrometer. Each analysis pit took 10 minutes to complete and was comprised of 120 s of pre-analysis sputtering followed by five 90 s cycles of the magnet scanning through a range of masses (6.5-138) that included the nine trace elements of interest (^{24}Mg, ^{28}Si, ^{31}P, ^{55}Mn, ^{57}Fe, ^{64}Zn, ^{88}Sr, ^{89}Y, and ^{137}Ba). The average count rate measured for each element during the analytical cycles was normalized by the concurrent count rate of ^{40}Ca. The ^{40}Ca-normalized count rate for each element was converted to concentration using relative sensitivity factors (RSF) determined for WiscSIMS measurements of calcite. The RSFs (Table A3.4, Chapter 3) were calculated at the beginning of the ion microprobe session by averaging the elemental count

rates of five analyses of UWC-3, which has a trace element profile measured by both electron microprobe and LA-ICP-MS (Kozdon et al., 2009; previous chapter).

As with the $\delta^{18}O$ pits in sample 2N, the pits from trace element analysis were imaged by scanning electron microscope (SEM) after the analytical session. Each pit-bottom was evaluated for evidence of cracks or porosity that might bias concentration measurements (Table 4.1). There does not appear to be a systematic bias in the trace element profiles of pits that have cracks or pores (n = 12); relatively high ppm values of Si and Mn measured in some pits are likely a result of detrital silicate inclusions in the speleothem. The effect of detrital silicate inclusions on the precision of trace element measurements in calcite is uncalibrated, so relative concentrations are emphasized instead of their absolute values.

2.2. Fluorescence data

2.2.1. Confocal laser fluorescence microscopy

The analytical traverse of sample 2N was imaged by confocal laser fluorescence microscopy (CLFM) on a Bio-Rad MRC-1024 scanning confocal microscope in the Keck Bio-imaging Lab at the University of Wisconsin-Madison. The images used in this study are published in Orland et al. (2012). Images were generated using a 488 nm incident laser (40 mW) and an emission filter that allowed the transmission of wavelengths between 505 and 539 nm, hence their green color. Each image was taken with a 10x objective lens (100x total magnification), which resulted in a pixel diameter of 0.94 μm.

Images from the same sample chip were stitched to create 13 composite chip images. Of note is the absence of a method to standardize fluorescence intensity in CLFM images. Imaging parameters were held constant while imaging each 1 cm chip, but this was not always feasible

when switching between chips. For this reason, we avoid interpreting absolute fluorescence intensity. Instead, relative fluorescence intensities were used to identify the positions of "peaks" and "valleys" of fluorescence in each band along the analytical traverse.

2.2.2. Digitizing a traverse across fluorescent bands

In order to automate the process of peak- and valley-picking, the fluorescence intensity of growth bands along the analytical traverse was digitized with ImageJ software (Rasband, 2012). Since growth bands in sample 2N do not always have a uniform width, and are thus not perfectly concentric, the linear traverse used for geochemical analyses is not always perpendicular to the bands. For calculation of band widths, however, measurements must be perpendicular to banding to avoid bias. Thus, the traverse of fluorescence intensity is broken into a series of rays for each chip such that all of the bands in the analytical traverse are measured along an approximately radial axis. Figures in the data repository (DR4.1) show the individual transects used to generate the composite record of fluorescence intensity across each sample chip.

ImageJ records the brightness of each pixel along the compound radial traverse on a scale from 0–255 (DR4.2). The final step before running a peak-picking script is to linearly scale the compound traverse across each chip to match the length of the LA-ICP-MS traverse.

2.2.3. Automated characterization of fluorescent bands

A publicly available MATLAB (2010) script, `peakfinder` (Yoder, 2011), is the basis for the customized algorithm `peakfinder_window` (DR4.3) that is used to record the location of peaks and valleys in the fluorescence intensity transect of sample 2N. The original `peakfinder` script requires the user to set a threshold for defining peaks, which is applied to

the entire dataset. If, for example, the threshold was set to 10 units, a local maximum must be at least 10 units above the previous local minimum before being considered a peak. In contrast, `peakfinder_window` uses a dynamic threshold defined by the standard deviation of fluorescence intensity within a sliding window. The width of the sliding window is assigned to be 200 μm, wider than >99% of the bands in sample 2N. The sliding-window concept is borrowed from a similar script developed for speleothem applications (`fpeakcount`; Smith et al., 2009). The peak and valley data generated with this methodology are used to count peaks, measure band-widths, and assess peak "shapes" across the entire analytical traverse of sample 2N. The shape of fluorescence variability within each band is measured by calculating the relative position of each peak between the two adjacent valleys. Sawtooth shapes have a peak that is close to the preceding valley, reverse-sawtooth bands have peaks close to the following valleys, and sinusoidal peaks bisect adjacent valleys.

When assessing the raw fluorescence intensity transect, noise in the fluorescence data can cause the incorrect identification of peaks and obfuscate peak-shape information because the intensity of a single "noisy" pixel can result in a false peak or valley. Two approaches were used to reduce the influence of noise on the peak-finding algorithm. First, the fluorescence dataset was smoothed with a Gaussian kernel (Bowman and Azzalini, 1997; MATLAB script `ksr`; Cao, 2008), which is a modified running mean that upweights points closer to the center of the moving window. The width of the Gaussian kernel (5 pixels) was chosen based on the desire to preserve a minimum band width of 10 pixels, which accounts for the majority of bands in 2N apparent by visual inspection.

The second method used to reduce the influence of noise on peak identification was to limit the minimum value of the dynamic threshold. We use the standard deviation (s.d.) of

CLFM "background noise" to define a minimum threshold so that fluorescence variability less than this quantity does not define peaks and valleys. Background noise in CLFM images is measured as the fluorescence intensity of blank epoxy in a sample mount. The s.d. of CLFM background noise (4.3 intensity units) was calculated as the average s.d. of fluorescence intensity in five ~200 μm transects across blank epoxy.

The viability of using the s.d. of background noise to define a minimum threshold was demonstrated on a dataset of synthetic noise – a sequence of 10,000 random values (pixels) distributed between 0 and 1 (s.d. = 0.29). After smoothing the synthetic noise with the 5-pixel Gaussian kernel described above, peaks and valleys in the smoothed noise were picked using a constant threshold of 0.29. The combined effect of smoothing and the s.d. threshold was to remove >94% of the peaks in the synthetic noise that would otherwise be identified as real peaks by the algorithm. Moreover, the remaining peaks were separated on average by >100 pixels; as the typical band-width is only ~10 pixels in sample 2N, the overprinting of real peaks will further reduce the number of false peaks caused by background noise. Thus, by employing a minimum threshold defined by the s.d. of background noise, the influence of CLFM noise on automated peak identification is greatly reduced. In both the case of the Gaussian smoothing and the minimum threshold, a fine balance is required so as not to apply unnecessary bias or eliminate too much signal.

One notable caveat arises from smoothing the fluorescence data. Namely, the "shape" of bands is biased by the smoothing operation. Figure 4.3 illustrates this concept by applying the 5-pixel Gaussian kernel to two idealized sawtooth patterns with different sawtooth widths. In the example with 10 pixel-wide (~10 μm) sawtooths, the sawtooth pattern is lost after smoothing

(Figure 4.3B). In order to quantify peak shapes and the effect of smoothing on them, we define a new variable called "fractional peak position."

The fractional position of each peak is calculated as the ratio of the distance between a peak and the preceding valley and the distance between the two adjacent valleys. For the idealized sawtooth plotted in Figure 4.3A, the fractional peak positions have values of 0.1; the distance from each peak to the preceding valley is 1 pixel and the distance between adjacent valleys is 10 pixels. In contrast, a reverse-sawtooth band (as in Figure 4.2C) would have a fraction peak position of ~0.9, while the value for a sinusoidal band is 0.5.

Figure 4.3C shows that the distance between the two valleys that bracket each peak ("band width") is unchanged by the 5-pixel Gaussian kernel. As illustrated in Figure 4.3D, however, the fractional peak positions increase from 0.1 to 0.5 as a result of smoothing the idealized, 10-pixel-wide sawtooth pattern with the 5-pixel Gaussian kernel. When the idealized sawtooth width is increased to 21 pixels (Figure 4.3E-H), the fractional peak positions (Figure 4.3H) of the smoothed data only increase to 0.33. Thus, when assessing peak shapes in sample 2N, bands with less than 21 pixels between the bracketing valleys are ignored.

Figure 4.4 shows a small portion of the fluorescence transect at ~9.0 ka to demonstrate how the `peakfinder_window` algorithm calculates values of band width and fractional peak position from the smoothed fluorescence data. Figure 4.4 also shows how the automated approach responds to two inherent features of the composite fluorescent transect. The two notable features are (1) the tie-point between sequential sections of the composite transect, and (2) a crack in the sample (partially hidden by the yellow line in Figure 4.4A). As shown in Figure 4.4B, careful placement of corresponding endpoints along the lateral extension of a fluorescent band allows the user to avoid false peaks at the tie-point between two sequential sections. The

artificial valley picked at the location of the (non-fluorescing) crack labeled in Figure 4.4B is harder to avoid. In this case, the crack causes the algorithm to identify two peaks with extreme, symmetric peak shapes (Figure 4.4D). Thus, depending on the width of a crack and its fluorescence intensity relative to the surrounding calcite, cracks may cause spurious peaks to be counted by the automated procedure.

2.3. Age model

We use the program `StalAge` to construct an age model for sample 2N based on 24 U-Th ages (Orland et al., 2012; Appendix A4.4). `StalAge` was developed by Scholz and Hoffman (2011) for the R software environment and uses a Bayesian approach to generate age models for U-Th ages measured in speleothems. One of the useful features of this program is its ability to interpolate the ages of proxy measurements within the sample. This feature was particularly effective for assigning ages to the LA-ICP-MS data from sample 2N, which include 95,084 discrete trace element measurements.

2.4. Principal component analysis

In order to identify common patterns of variability within the 12 trace element series generated by LA-ICP-MS, this study uses the same principal component analysis (PCA; Davis, 2002) approach as the previous chapter. The value of applying PCA to continuous trace element profiles of speleothems is demonstrated in a few recent studies (Borsato et al., 2007; Wassenburg et al., 2012; Chapter 3). PCA is an operation that distributes the variability observed in each of *n* variables (i.e. trace element concentrations) into *n* orthogonal, "principal components." Every resulting principal component is a time-series of "scores" that defines a pattern of variability

unique to that component. Each of the *n* principal components explains a "percentage of total variance" of the dataset and they are ranked according to these percentages (i.e. the first principal component, PC1, explains the highest percentage of total variance). Each of the *n* observed variables (trace elements) has a "loading" on a scale from -1 to 1 for each principal component that indicates how well the variability of that element is described by each principal component. If a trace element has a loading value of zero for a particular principal component, then that principal component does not correlate with the trace element in question. Conversely, an element loading of 1 indicates perfect positive correlation to a principal component. Negative loading values signify that an observed variable has inverse correlation to the principal component.

As in the previous chapter, PCA was performed on the z-score normalization of each trace element profile. PCA of the normalized trace element concentrations was performed using the built-in MATLAB function, `princomp`.

3. RESULTS

3.1. Trace elements

Figure 4.5 plots the concentration (in ppm) of 9 trace elements measured along the analytical traverse in sample 2N by both LA-ICP-MS and ion microprobe. The data are plotted using the age model calculated by `StalAge`, described above. There is good agreement between trace element concentrations measured at 10-μm scale by ion microprobe and 55-μm scale by LA-ICP-MS (Figure 4.5). The results of all 12 trace element traverses measured by LA-ICP-MS are plotted in Figure A4.2.

We note three features of interest in the LA-ICP-MS data shown in Figure 4.5. First are the long-term, anti-correlated trends of Mg and Sr concentration. As [Mg] generally increases from ~3500-6000 ppm between 35 and 10 ka, [Sr] decreases from ~200-60 ppm; both elements have consistent concentrations for the remainder of Holocene growth.

The second feature in Figure 4.5 is the sharp, simultaneous excursion of [Ba] and [Zn] at several points between 11 and 9 ka. Concentrations of both Ba and Zn, which are generally ~25 ppm in this part of the sample, are observed to increase to maxima between 100-500 ppm across narrow (<100-μm-wide) domains (blue circles, Figure A4.5). We note, however, that [Ba] and [Zn] peaks measured in the pre-cleaned laser traverses of chips G and H are not duplicated in the adjacent, non-pre-cleaned laser traverse (Figure A4.5). This disagreement suggests the presence of micron-scale inclusions. Backscatter electron imaging of the analytical traverse in chips G and H by SEM confirms that [Ba] and [Zn] peaks in this part of the sample coincide with inclusions (10-50 μm diameter) in the calcite (Figure A4.6).

The third feature is the similar pattern of [Si], [Mn], and [Y] variability across 2N. Increased concentrations of these elements in portions of the sample that grew from 30-25, 17-16, and intermittently after 14 ka indicate the presence of silicate particles trapped in the carbonate crystals of the stalactite. By visual inspection, [P] has a similar, but smoothed, pattern of variability.

Paired ion microprobe analyses of trace element concentrations within single, annual growth bands show that seasonal trace element variability changes across sample 2N. Figures 4.6 and 4.7 highlight trends in the seasonal variability of Mg, Sr, and P: the range of intra-band variability of both Mg and P increases notably after 15 ka. By comparison, the range of Sr

variability is relatively consistent across the sample except for a period of reduced variability between 15 and 10 ka.

From the perspective of the whole sample, ion microprobe measurements of Mg and Sr are anti-correlated (Figure 4.8A) as seen in LA-ICP-MS results. Within a Holocene portion of sample 2N, however, ion microprobe analyses reveal that Mg and Sr concentrations are positively correlated (circles in Figure 4.8A). Furthermore, within these growth bands the concentration of both Mg and Sr is negatively correlated to fluorescence intensity; the concentration of both Mg and Sr is lowest in the fluorescent domain of each analyzed band. Figure 4.8B shows that Mg and P concentrations are anti-correlated both across sample 2N and within Holocene bands, as predicted by the model of modern trace element transport (Chapter 3).

3.2. Fluorescent banding

The total number of bands counted by the `peakfinder_window` algorithm, 2288, is remarkably similar to the number that the author counted by eye (2328). Table 4.2 lists the algorithm-to-eye comparison for each of the 13 chips from sample 2N. In the nine chips where the automated count is less than the eye count, the offset in the number of counts is never >20%. In the four other chips (B, C, M, N), which have four of the five lowest band-counts, the offsets range from 10-76%. While this may suggest that background noise in CLFM images disproportionately affects the number of bands counted by the algorithm in chips with few real bands, it is also noted that portions of chips M and N contain “irregular calcite growth” (Figure 4.9) that may contribute to the band-counting offset in those chips.

The banding characteristics computed by `peakfinder_window` show notable changes in both peak shape and band-width across sample 2N (Figure 4.9). The red line in Figure 4.9B

shows a 39-point running average of the band-widths, which varies between 21 and 104 μm over the entire sample. The window-width of the running average was assigned based on the minimum number of peaks found in any single chip (39 peaks in chip O). Also plotted in Figure 4.9B is a horizontal dashed line that indicates the diameter (50 μm) of the laser beam used for LA-ICP-MS analyses; a majority of the bands in sample 2N are narrower than the laser beam.

Figure 4.9C plots the fractional peak position of each peak that fulfills two band-width requirements (n = 1863). The first requirement (explained in Section 2.2.3) is that adjacent valleys are wider than 21 μm since smoothing eliminates meaningful peak shape information in narrower bands. The second requirement aims to remove peaks that are artifacts of an intervening crack (like the symmetrically-shaped peaks in Figure 4.4). Therefore, adjacent bands with peaks closer than 10 μm are not included in the fractional peak position data. Table 4.2 lists how many peaks these two filters remove in each chip. The yellow line in Figure 4.9C shows the 31-point running average of the fractional peak positions. The window-width of the running average was assigned based on the number of peaks in chip O that passed the two filters. Over the entire sample, the running average of fractional peak positions ranges from 0.33 to 0.62.

Recall that qualitative observations divided Sample 2N into three periods, each with their own characteristic banding patterns (Orland et al., 2012). As might be expected, the comprehensive results generated by `peakfinder_window` make it possible to recognize differences in fluorescent banding characteristics that were not identified by the qualitative study. Five sections are differentiated by visual inspection of the new comprehensive record from sample 2N.

The five sections of fluorescent banding are differentiated based on their characteristic band-widths and fractional peak positions. The Holocene portion of the sample is divided into

three parts, sections 1-3 in Figure 4.9, defined by the age model as 5.3–4.0, 9.4–5.3, and 12.3–9.4 ka. Sections 1 and 3 have similar band-width and band-shape characteristics, but section 2 has wider bands with fluorescent patterns that are more consistently sawtooth. Note that the oldest section from the Holocene (section 3) includes the termination of the Younger Dryas cold period, which the Bayesian age model identifies as older (12.3 ka) but within error of the age (12.0 ka) determined by a linear age model (Orland et al., 2012).

Banding section 4 includes the Younger Dryas (12.3–14.0 ka), and is differentiated from section 3 by consistently narrower bands. The fifth banding section includes all of the calcite older than 14 ky, and is characterized by a prevalence of reverse-sawtooth patterns of fluorescent banding. The five banding divisions cover similar time periods to qualitative observations (Orland et al., 2012), except that this study finds three sections within the Holocene portion of the sample. While there is good spatial agreement between the quantitative and qualitative observations of fluorescent banding, we note that the automated measurements of peak shape (i.e. fractional peak position) are more variable than suggested by Orland et al. (2012). Figure 4.9C shows that in each of the five sections, a large range of fractional peak positions is measured.

Figure 4.10 plots the band-width and band-shape results versus age. After ~12 ka (Younger Dryas termination), band widths begin to steadily increase and fluorescent band patterns start to become more sawtooth in character.

We tested the reproducibility of the automated peak-picking approach by constructing two additional compound fluorescent transects, labeled “parallel” and “blind,” in chip E (Figure A4.6). The parallel transect runs alongside the original compound traverse of chip E, offset by ~2 pixels. The blind transect is a second attempt at constructing a composite traverse of chip E,

unguided by the original traverse. As a result, the blind transect is comprised of a different combination of radial segments from the original traverse. For both test transects, the `peakfinder_window` algorithm was used to measure the two variables of greatest interest for this study, the number of bands and the fractional peak position. The number of bands counted in both the parallel (150) and blind (148) transects are consistent with the total calculated in the original transect (150). The average fractional peak position of the parallel (0.46) and blind (0.45) transects are also similar to the value calculated in the original transect (0.45). These results indicate that the automated method of analyzing compound fluorescent transects is reproducible.

The importance of using band-perpendicular segments to construct compound fluorescent transects is demonstrated by measuring a continuous "control" transect parallel to the edge of each chip. For chip E, the total number of bands (182) and average peak position (0.51) from the control transect do not match the values of the original, parallel, or blind transects. Figure A4.7 documents the fluorescence intensity, band counts, and fractional peak positions measured in each of the four fluorescent profiles (original, parallel, blind, control) from chip E. The band counting totals and average fractional peak position from the control transect in each chip are listed in Table 4.2.

3.3. Principal components of trace element variability

The scores, percentage of total variance, and elemental loadings of the first two principal components derived from 13 datasets across sample 2N are reported in Figure 4.11. The 13 datasets include 12 trace element transects (Figure A4.2) as well as the raw fluorescence intensity dataset (Figure 4.5), which was re-sampled to match the spatial resolution of the LA-

ICP-MS data. In all plots of elemental loading values (e.g. Figure 4.11C), four notable sets of elements are highlighted in order to ease comparison of their relative loadings. The four sets of elements are colored as in Chapter 3: (1) Mg: blue; (2) Sr, Ba: red; (3) P, Cu: green; and (4) Si, Mn: yellow. The relative positions of these sets are used to compare sample 2N to the modern Soreq speleothem analyzed in the previous chapter.

The anti-correlated trends of [Mg] (increasing) and [Sr] (decreasing) measured across sample 2N (Figure 4.5) are represented by their opposite loadings on PC1 (Figure 4.11C), which gradually decreases across the sample. In contrast, PC2 has a higher degree of variability than PC1, generally increases across the sample, and has its highest loadings in Si, Mn, and Y.

We note that the fluorescence transect included in the whole-sample PCA results (Figure 4.11) was not attained from a traverse parallel to the LA-ICP-MS track; since these transects are not perfectly registered, any apparent similarities identified by PCA between fluorescence and trace element variability (e.g. Sr, U) do not include μm-scale variability across individual bands. Rather, these similarities likely reflect comparable variability on the mm- to cm-scale.

PCA is also administered to trace element data from each of the five banding sections in sample 2N that are delineated in Figure 4.9. Fluorescence data were not included in these PCA analyses since they are imperfectly registered to the LA-ICP-MS traverse and the top priority for this analysis was to identify common variability on short (annual to decadal) time scales. The loading of each trace element on PC2 vs. PC1 as determined for each section is plotted in Figure 4.12. In each of the loading plots for banding sections 1-4 (<14 ka), Mg (blue) lies directly across the origin from Sr and Ba (red), while P (green) and Si (yellow) are loaded in the same direction along an axis that is approximately orthogonal to the line between Mg and Sr. One logical

consequence of having the same loading pattern in four of the five sections is that the same pattern is pronounced in PCA of the complete sample traverse (Figure 4.11C).

PCA of the fifth banding section (>14 ka) reveals a different pattern of element loadings on PCs 1 and 2 (Figure 4.12E) than observed in the other four sections. In this section, Ba and Sr have the highest loadings on PC1, Mg has a loading near zero on both PCs 1 and 2, and elements associated with silicate or organic particles (Si, Mn, P, Cu) have the highest loadings on PC2.

4. DISCUSSION

There are two primary motivations for developing an automated method for counting and characterizing fluorescent bands in speleothems. First, is to be able to test visual band classifications like those described in Orland et al. (2012). Second, is to be able to acquire a continuous, high-resolution, quantitative characterization of fluorescent banding that can be interpreted alongside geochemical data, like the continuous LA-ICP-MS traverse measured in this study. We suggest that the `peakfinder_window` results plotted in Figures 4.9 and 4.10 realize both of these goals.

4.1. Utility of automated band characterization

In sample 2N, the results of automated band characterization reflect the qualitative observations of earlier work (Orland et al., 2012). Before 15 ka, when Orland et al. (2012) observe abundant reversed-sawtooth fluorescent bands, average fractional peak position values are >0.5. During the Younger Dryas cold period, where bands were observed to be narrow with a sinusoidal shape, fractional peak positions are accordingly ~0.5. In the Holocene portion of the sample, however, the automated results do not reflect pervasive sawtooth patterns as seen by

Orland et al. (2012). In fact, a strong signal of sawtooth fluorescent bands is only evident in section 2 (Figure 4.9C) as opposed to the entire Holocene (sections 1-3). Understanding the cause of this discrepancy will improve future applications of the automated method.

There are two potential explanations for the inconsistent distribution of peak shapes in the Holocene portion of sample 2N. Either the inconsistent distribution is real, or limitations of the automated process mute a more distinct signal. Visual inspection does not support such an inconsistent distribution. Furthermore, as illustrated in Figures 4.3 and 4.4, the accuracy of peak shape measurements by the `peakfinder_window` algorithm is susceptible to the Gaussian smoothing as well as to flaws in the sample surface. Also, the traverse used in the automated process is only a single pixel wide, and does not average fluorescence intensity along each band as is done by eye. With regard to banding in the Holocene, it appears that sawtooth peak-shapes measured in section 2 are enhanced because the bands are wider; the peak-shapes in section 2 are less susceptible to damping by Gaussian smoothing (Figure 4.3). Thus, we partially attribute the large spread of fractional peak positions in sample 2N to inherent vulnerabilities of the automated process. Despite this drawback, useful information is still attained by examining averaged peak shape measurements over multiple bands. The running mean plotted in Figure 4.9C illustrates the underlying tendencies of fractional peak positions across sample 2N and helps to distinguish between the five sections of fluorescent banding.

4.2. Multi-proxy climatic interpretation

Because this study incorporates a number of datasets (ion microprobe, LA-ICP-MS, fluorescent band characterization), the paleoclimate interpretation is broken into two parts. First, we examine the PCA of trace element concentrations measured in the five banding sections to

assess whether: (1) changes in fluorescent banding are reflected in trace element variability, and (2) trace element variability in sample 2N repeats the patterns observed in portions of a modern Soreq speleothem that grew during wet and dry periods (Chapter 3). In the second part of the interpretation, we consider the environmental factors that may contribute to both the long-term and seasonal patterns of trace element variation in sample 2N.

4.2.1. Implication of PCA results from sample 2N

With emphasis on the colored elemental loadings in Figures 4.11C and 4.12A-E, we identify two main points of interest from PCA of the LA-ICP-MS traverse. First, the relative pattern of trace element variability is the same in the youngest four banding sections (Figure 4.12A-D), but different in the fifth section (>15 ka). In this case, a change in fluorescent banding identifies a coincident change in the trace element profile of the speleothem.

The second point of interest is the similarity between the loading pattern of the youngest four sections of sample 2N (Figure 4.12A-D) and the plot of PC3 vs. PC2 from modern sample 5-3b (Figure 3.5F in Chapter 3). In the modern sample, which formed between 1990 and 2008, the variability of PC2 is attributed to a seasonal increase in colloids (some organic) embedded in the speleothem caused by increased rainfall in the wet-season. PC3 is proposed to record a supply of detrital clay-size silicates, perhaps wind-blown dust, which could be flushed into the cave following a particularly dry year. The similar patterns of relative variability suggest that the seasonal delivery of particulate material (including organic colloids and detrital clays) contributes to the patterns of trace element variability observed in the youngest four sections of sample 2N. Interestingly, this includes the Younger Dryas cold event (section 4), where fluorescent bands are generally narrow with a sinusoidal shape; one hypothesis proposed by

Orland et al. (2012) to explain this banding pattern is more consistent rainfall year-round. In the next section, we examine trace element concentrations in further detail to determine if they support a year-round rainfall regime during the Younger Dryas.

4.2.2. Trace element constraints on the paleoclimate interpretation of sample 2N

We begin by examining LA-ICP-MS measurements of [Mg] and [Sr] in sample 2N. As shown in Figure 4.5, these concentrations are negatively correlated; [Mg] increases while [Sr] decreases. In the modern sample 5-3b, however, the dominating mode of variability (PC1, Figure 3.5D in the previous chapter) is characterized by correlation of Mg, Sr, and Ba. Chapter 3 shows that these elements accumulate in vadose zone groundwaters that have decadal residence times in the dolomitic bedrock. In sample 2N, there must be another geochemical mechanism in play.

Prior workers found that high Sr concentrations in other speleothems from Israel that grew during the last glacial maximum (~20 ka) reflect an increase of wind-blown dust (predominantly silicates from the late Proterozoic Arabian-Nubian shield) and Mediterranean sea spray in the soil at that time (Bar-Matthews et al., 1999; Frumkin and Stein, 2004; Ayalon et al., *in press*). Figure 4.6B shows that $^{87}Sr/^{86}Sr$ ratios in Soreq Cave speleothems dropped after ~13 ka (Ayalon et al., *in press*), implying a reduced amount of dust and sea spray delivered to the soil above the cave.

In contrast, the long-term increase in [Mg] is likely a result of gradually lengthening groundwater residence times in the vadose zone above the cave. This inference corroborates the hypothesis that dripwater was more consistent year-round during the last glacial period (Bar-Matthews et al., 1997), perhaps as a result of more regular rainfall events (Orland et al., 2012).

By this interpretation, high Mg concentrations during the Holocene are a result of Mg accumulation in groundwater during prolonged dry seasons.

Given prolonged dry seasons, one would expect to see intra-band correlation of Mg and Sr concentrations as in the modern sample examined in Chapter 3. While the LA-ICP-MS trace element record in sample 2N can assess decadal changes in the residence time of vadose zone groundwater, seasonal variability is not generally resolved because the laser beam diameter (55 μm) is greater than the width of most bands (Figure 4.9B). For sub-annual measurements of trace element variability in sample 2N, we turn to ion microprobe analyses.

Figures 4.6 and 4.8A show that Holocene concentrations of both Mg and Sr are consistently lower in bright fluorescent domains than in dark domains. As demonstrated in the previous chapter, annual co-variability of Mg and Sr is evidence of a climate regime with distinct wet- and dry-seasons. These results reinforce the hypothesis that the seasonal climate regime in the Eastern Mediterranean was consistent throughout the Holocene (Orland et al., 2012).

Furthermore, Figure 4.8B shows that Mg and P concentrations during the Holocene are anti-correlated as predicted by the model of modern trace element transport (Chapter 3); the existence of a prolonged annual dry-season in the modern climate regime results in the storage of P in the overlying soil as well as the accumulation of Mg in vadose zone groundwater. Year-round rainfall would not facilitate either of these mechanisms. Figure 4.7 reveals that the seasonal range of both Mg and P increased after 15 ka and remained relatively consistent. Not only does this result support the inference of more consistent year-round rainfall before 15ka, but it also corroborates the suggestion based on PCA results from the previous section that the Younger Dryas has a seasonal rainfall gradient similar to that of the Holocene. This interpretation implies that the sinusoidal fluorescent bands in the Younger Dryas portion of

sample 2N were caused by something other than consistent rainfall; perhaps the overlying vegetation was different.

Contrary to Mg and P concentrations, [Sr] shows a consistent range of variability across sample 2N except during the Younger Dryas (Figure 4.7). During this cold period, when PCA results as well as the seasonal variability of Mg and P point to an increased seasonal rainfall gradient, we suggest that reduced inter-annual Sr variability is a result of two interfering signals: the contribution of wind-blown dust and the residence time of groundwaters. During the wet season, Sr is leached into groundwater from wind-blown dust in the overlying soil column (Bar-Matthews et al., 1999; Frumkin and Stein, 2004). The dry season would allow bedrock-derived Sr to accumulate in vadose zone groundwaters. This scenario allows relatively high concentrations of Sr to persist year-round, as shown in Figure 4.6B.

5. CONCLUSIONS

This study develops an automated approach for counting and characterizing fluorescent bands in speleothems and introduces a strategy for incorporating banding data with high-resolution geochemical records into a multi-proxy approach to obtaining seasonal climate information from speleothems. Seasonal-resolution spot-analyses of $\delta^{18}O$ and trace elements are integrated with continuous-traverse trace element and fluorescence datasets from a Soreq Cave stalactite that grew from 34–4 ka (sample 2N; Orland et al., 2012). The diverse suite of geochemical data collected at micron-scale resolution allows us to describe a coherent record of seasonal climate in the Eastern Mediterranean from 34–4 ka.

Two datasets span the entire 13.4 cm analytical traverse of sample 2N, a trace element profile measured by laser ablation (LA)-ICP-MS (55-μm-resolution; Mg, Sr, Ba, Na, Si, P, Mn,

Cu, Zn, Y, Pb, U) and a composite record of fluorescence intensity measured by confocal laser fluorescent microscopy (1-μm-resolution) across concentric annual growth bands. Together, these data are useful for identifying long-term changes in fluorescent banding patterns and trace element variability. The fluorescence intensity data are processed by a customized algorithm (`peakfinder_window`; MATLAB, 2010) that counts fluorescent growth bands, measures their width, and characterizes their "shape" (i.e. sawtooth, sinusoidal, or reverse-sawtooth fluorescence).

The new algorithm finds a similar number of bands (2288) in sample 2N as counted by visual inspection (2328). Likewise, the "shape" results corroborate qualitative observations that identify five sections of characteristic banding patterns in sample 2N that correspond to the Holocene (3 sections), Younger Dryas cold period, and the last glacial maximum (Orland et al., 2012).

Trace element variability as assessed by principal component analysis (PCA) in the youngest sections (Holocene and Younger Dryas) of sample 2N are similar to those observed in a modern Soreq Cave stalagmite (Chapter 3). It is inferred that the Holocene and Younger Dryas portions of sample 2N record a climate regime with distinct wet- and dry-seasons as observed today. In the section of sample 2N that grew before 15 ka, PCA results indicate a different seasonal climate regime.

Ion microprobe spot-analyses of trace element concentrations within single annual growth bands (10-μm-resolution) support the hypothesis that regional rainfall shifted at 15 ka from more consistent rainfall year-round to a distinct seasonal distribution. Furthermore, annual Sr variability indicates the persistence of wind-blown dust during the Younger Dryas (as in Bar-Matthews et al., 1999) even after the hypothesized onset of a seasonal rainfall regime.

Combined results of trace element, $\delta^{18}O$, and fluorescent banding analyses substantiate a shift in the seasonal climate regime of the Eastern Mediterranean at 15 ka from more consistent year-round rainfall to distinct wet- and dry-seasons.

Acknowledgements

The authors thank O. Dvir for guidance on the LA-ICP-MS at GSI; N. Kita and T. Ushikubo for support at WiscSIMS; L. Rodenkirch for assistance at the W. M. Keck Laboratory for Biological Imaging at UW-Madison; A. Pollington, D. Ortiz, and J. Fournelle for guidance on the SEM; B. Hess for sample preparation; J. Kern for profilometer assistance; A. Pollington and E. Syracuse for their invaluable input on MATLAB coding. Funding for this project was provided by the NSF (AGS-1003487), the Comer Science and Education Foundation, and the United States-Israel Binational Science Foundation (2010316). WiscSIMS is partially supported by NSF-EAR(0319230, 0744079, 1053466).

References

Affek H. P., Bar-Matthews M., Ayalon A., Matthews A. and Eiler J. M. (2008) Glacial/interglacial temperature variations in Soreq cave speleothems as recorded by 'clumped isotope' thermometry. *Geochim. Cosmochim. Acta* **72**, 5351-5360.

Asrat A., Baker A., Mohammed M. U., Leng M. J., van Calsteren P., and Smith C. (2007) A high-resolution multi-proxy stalagmite record from Mechara, Southeastern Ethiopia: palaeohydrological implications for speleothem palaeoclimate reconstruction. *J. Quat. Sci.* **22**, 53-63.

Ayalon A., Bar-Matthews M. and Sass E. (1998) Rainfall-recharge relationships within a karstic terrain in the Eastern Mediterranean semi-arid region, Israel: $\delta^{18}O$ and δD characteristics. *J. Hydro.* **207**, 18-31.

Ayalon A., Bar-Matthews M. and Kaufman A. (1999) Petrography, strontium, barium and uranium concentrations, and strontium and uranium isotope ratios in speleothems as palaeoclimatic proxies: Soreq Cave, Israel. *The Holocene* **9,** 715-722.

Ayalon A., Bar-Matthews M. and Schilman B. (2004) Rainfall isotopic characteristics at various sites in Israel and the relationships with unsaturated zone water. In: Geological Survey of Israel Reports, GSI/16/04. The Ministry of National Infrastructures, Jerusalem.

Ayalon A., Bar-Matthews M., Frumkin A., and Matthews A. (*in press*) Last Glacial warm events on Mount Hermon: the southern extension of the Alpine karst range of the east Mediterranean. *Quaternary Science Reviews*.

Baker A., Smart P. L., Edwards R. L., and Richards D. A. (1993) Annual growth banding in a cave stalagmite. *Nature* **364**, 518-520.

Baker A., and Genty D. (1999) Fluorescence wavelength and intensity variations of cave waters. *J. Hydro.* **217**, 19-34.

Baker A., Smith C. L., Jex C., Fairchild I. J., Genty D., and Fuller L. (2008) Annually laminated speleothems: a review. *Int. J. Spel.* **37**, 193-206.

Bar-Matthews M., Ayalon A. and Kaufman A. (1997) Late Quaternary paleoclimate in the eastern Mediterranean region from stable isotope analysis of speleothems at Soreq Cave, Israel. *Quat. Res.* **47,** 155-168.

Bar-Matthews M., Ayalon A., Kaufman A. and Wasserburg G. J. (1999) The Eastern Mediterranean paleoclimate as a reflection of regional events: Soreq Cave, Israel. *Earth Planet. Sci. Lett.* **166**, 85-95.

Bar-Matthews M., Ayalon A., Gilmour M., Matthews A. and Hawkesworth C. J. (2003) Sea-land oxygen isotopic relationships from planktonic foraminifera and speleothems in the Eastern Mediterranean region and their implication for paleorainfall during interglacial intervals. *Geochim Cosmochim. Acta* **67,** 3181-3199.

Bar-Matthews M. and Ayalon A. (2011) Mid-Holocene climate variations revealed by high-resolution speleothem records from Soreq Cave, Israel and their correlation with cultural changes. *The Holocene* **21**, 163-171.

Boch R., Spötl C., and Frisia S. (2011) Origin and palaeoenvironmental significance of lamination in stalagmites from Katerloch Cave, Austria. *Sediment.* **58**, 508-531.

Borsato A., Frisia S., Fairchild I. J., Somogyi A. and Susini J. (2007) Trace element distribution in annual stalagmite laminae mapped by micropmeter-resolution X-ray fluorescence:

Implications for incorporation of environmentally significant species. *Geochimica et Cosmochimica Acta* **71**, 1494-1512.

Bowman A. W. and Azzalini A. (1997) *Applied Smoothing Techniques for Data Analysis*. Oxford University Press: New York. 193 pp.

Cao Y. (2008) MATLAB File Exchange. BSD open source software license. Web. <http://www.mathworks.com/matlabcentral/fileexchange/19195>.

Davis J. C. (2002) *Statistics and Data Analysis in Geology*. John Wiley and Sons: New York, 638 p.

Dvir O., and Kessel R. (*in prep*) The effect of cell geometry on alkali element fractionation during LA-ICP-MS analysis.

Fairchild I. J., Borsato A., Tooth A. F., Frisia S., Hawkesworth C. J., Huang Y., McDermott F. and Spiro B. (2000) Controls on trace element (Sr–Mg) compositions of carbonate cave waters: implications for speleothem climatic records. *Chem. Geol.* **166**, 255-269.

Fairchild I. J. and Treble P. C. (2009) Trace elements in speleothems as recorders of environmental change. *Quat. Sci. Rev.* **28**, 449-468.

Frumkin A., and Stein M. (2004) The Sahara-East Mediterranean dist and climate connection revealed by strontium and uranium isotopes in a Jerusalem speleothem. *Earth Planet. Sci. Lett.* **217**, 451-464.

Johnson K. R., Hu C., Belshaw N. S. and Henderson G. M. (2006) Seasonal trace-element and stable-isotope variations in a Chinese speleothem: The potential for high-resolution paleomonsoon reconstruction. *Earth and Planetary Science Letters* **2006**, 394-407.

Kaufman A., Bar-Matthews M., Ayalon A., and Carmi I. (2003) The vadose flow above Soreq Cave, Israel: a tritium study of cave waters. *J. Hydro.* **273**, 155-163.

Kolodny Y., Bar-Matthews M., Ayalon A. and McKeegan K. D. (2003). A high spatial resolution $\delta^{18}O$ profile of a speleothem using an ion microprobe. *Chem. Geol.* **197**, 21-28.

Kozdon R., Ushikubo T., Kita N. T., Spicuzza M. and Valley J. W. (2009) Intratest oxygen isotope variability in the planktonic foraminifer *N. pachyderma:* Real vs. apparent vital effects by ion microprobe. *Chem. Geol.* **258**, 327-337.

MATLAB version 7.11.0.584. (2010) Natick, Massachusetts: The MathWorks Inc.

Matthews A., Ayalon A. and Bar-Matthews M. (2000) D/H ratios of fluid inclusions of Soreq Cave Israel speleothems as a guide to the Eastern Mediterranean Meteoric Line relationships in the last 120 ky. *Chem. Geol.* **166,** 183-191.

McGarry S. F., and Baker A. (2000) Organic acid fluorescence: applications to speleothem palaeoenvironmental reconstruction. *Quat. Sci. Rev.* **19**, 1087-1101.

McGarry S. F., Bar-Matthews M., Matthews A., Vaks A., Schilman B. and Ayalon A. (2004) Constraints on hydrological and paleotemperature variations in the eastern Mediterranean region in the last 140ka given by the δD values of speleothem fluid inclusions. *Quat. Sci. Rev.* **23,** 919-934.

Orland I. J, Bar-Matthews M., Kita N. T., Ayalon A., Matthews A. and Valley J. W. (2009) Climate deterioration in the eastern Mediterranean as revealed by ion microprobe analysis of a speleothem that grew from 2.2 to 0.9 ka in Soreq Cave, Israel. *Quat. Res.* **71**, 27-35.

Orland I. J. Bar-Matthews M., Ayalon A., Matthews A., Kozdon R., Ushikubo T., and Valley J. W. (2012) Seasonal resolution of Eastern Mediterranean climate change since 34 ka from a Soreq Cave speleothem. *Geochim. Cosmochim. Acta* **89**, 240-255.

Perrette Y., Delannoy J.-J., Desmet M., Lignier V., and Destombes J.-L. (2005) Speleothem organic matter content imaging. The use of a Fluorescence Index to characterize the maximum emission wavelength. *Chem. Geol.* **214**, 193-208.

Rasband W.S. (2012) ImageJ. U. S. National Institutes of Health, Bethesda, Maryland, USA. Web. <http://imagej.nih.gov/ij/>.

Scholz D., and Hoffman D. L. (2011) StalAge – An algorithm designed for construction of speleothem age models. *Quat. Geochron.* **6**, 369-382.

Smith C. L., Fairchild I. J., Spötl C., Frisia S., Borsato A., Moreton S. G., and Wyn P. M. (2009). Chronology building using objective identification of annual signals in trace element profiles of stalagmites. *Quat. Geochron*. **4**, 11-21.

Tan M., Baker A., Genty D., Smith C., Esper J., and Cai B. (2006) Applications of stalagmite laminae to paleoclimate reconstructions: Comparison with dendrochronology/climatology. *Quat. Sci. Rev.* **25**, 2103-2117.

Treble P., Shelley J. M. G., and Chappell J. (2003) Comparison of high resolution sub-annual records of trace elements in a modern (1911-1992) speleothem with instrumental climate data from southwest Australia. *Earth Planet. Sci. Lett.* **216**, 141-153.

Treble P. C., Chappell J., and Shelley J. M. G. (2005a) Complex speleothem growth processes revealed by trace element mapping and scanning electron microscopy of annual layers. *Geochim. Cosmochim. Acta* **69**, 4855-4863.

Treble P. C., Chappell J., Gagan M. K., McKeegan K. D., and Harrison T. M. (2005b) In situ measurement of seasonal $\delta^{18}O$ variations and analysis of isotopic trends in a modern speleothem from southwest Australia. *Earth Planet. Sci. Lett.* **233**, 17-32.

Vaks A., Bar-Matthews M., Ayalon A., Schilman B., Gilmour M., Hawkesworth C. J., Frumkin A., Kaufman A., and Matthews A. (2003) Paleoclimate reconstruction based on the timing of speleothem growth and oxygen and carbon isotope composition in a cave located in the rain shadow in Israel. *Quat. Res.* **59**, 182-193.

Valley J. W. and Kita N. T. (2009) *In situ* Oxygen Isotope Geochemistry by Ion Microprobe. In *MAC Short Course: Secondary Ion Mass Spectrometry in the Earth Sciences* (ed. M. Fayek), v. 41, pp. 19-63.

Wassenburg J. A., Immenhauser A., Richter D. K., Jochum K. P., Fietzke J., Deininger M., Goos M., Scholz D. and Sabaoui A. (2012) Climate and cave control on Pleistocene/Holocene calcite-to-aragonite transitions in speleothems from Morocco: elemental and isotopic evidence. *Geochim. Cosmochim. Acta* **92**, 23-47.

Yoder N. (2011) PeakFinder. MATLAB File Exchange. BSD open source software license. Web. <http://www.mathworks.com/matlabcentral/fileexchange/25500>.

Figures

Figure 4.1: The polished surface of stalactite sample 2N showing the location of the 13 ~1 cm^3 chips (A-I, M-P) removed for analysis. The dashed white line indicates the analytical traverse used for all geochemical analyses. Note that the analytical traverse in chip I makes a lateral step in order to include growth bands removed by the wide saw cut between chips H and I. White arrows show regions of the sample with irregular crystal growth (Orland et al., 2012). Cut-outs below the polished slab show how individual chips are mounted along with three UWC-3 calcite standard grains in 1-inch epoxy rounds for ion microprobe analysis. The inset map of Israel illustrates the location of Soreq Cave (star) in relation to Jerusalem (J), the Dead Sea (DS), and the Eastern Mediterranean Sea (EM). (after Orland et al., 2012).

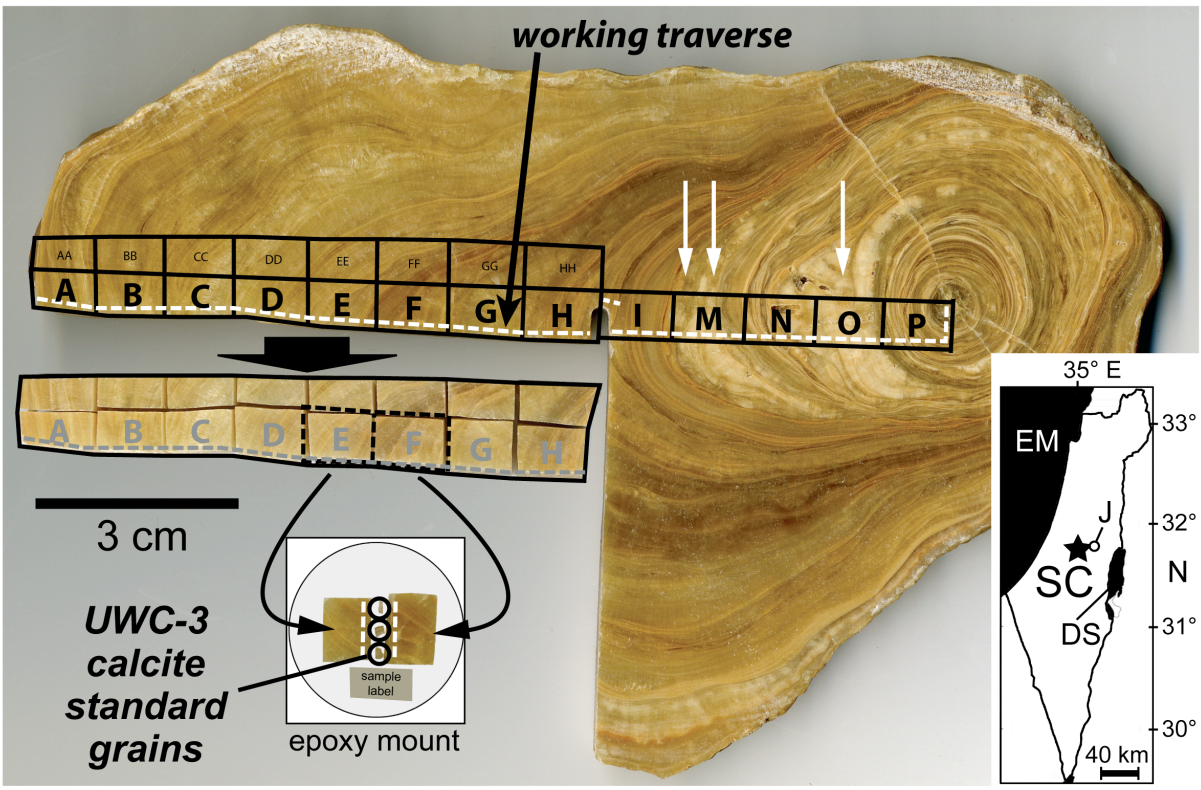

Figure 4.2: Examples of the three fluorescent band categories from Orland et al. (2012), with a transect of fluorescence intensity shown for each pattern. Sawtooth bands (**A**) have a sharp fluorescent onset and gradually darken until the next sharp fluorescent boundary. Sinusoidal bands (**B**) do not have sharp fluorescent boundaries and gradually transition from bright to dark fluorescence. Reverse-sawtooth bands (**C**) have a sharp, dark (non-fluorescent) onset and gradually increase in fluorescence until the next dark onset.

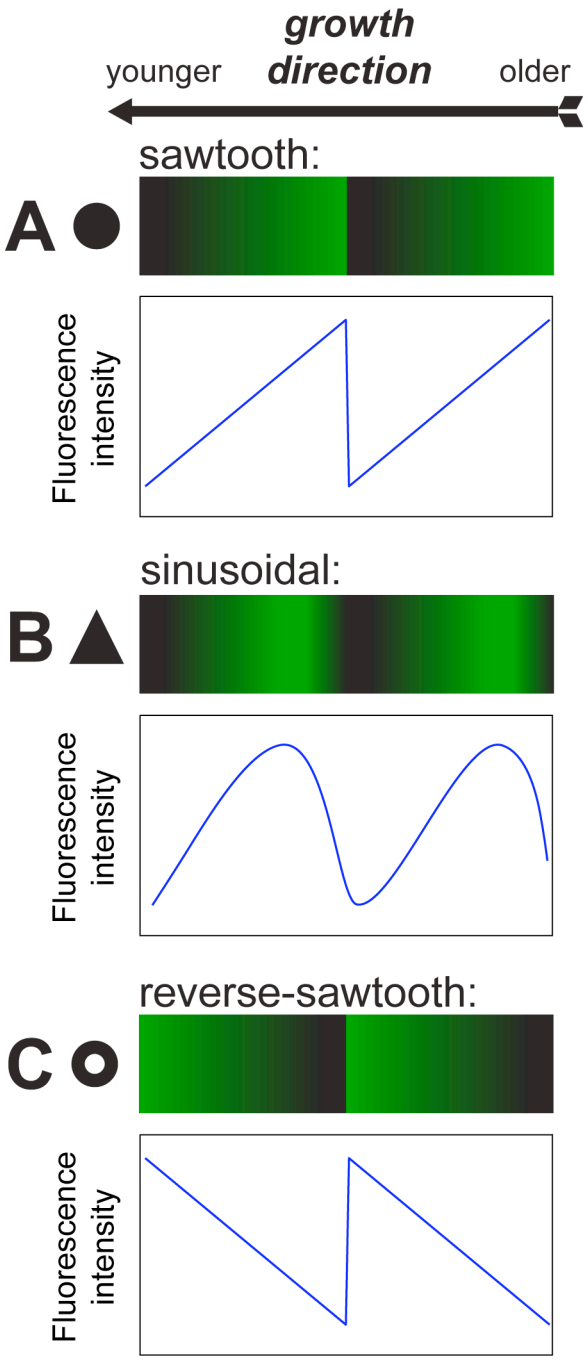

Figure 4.3 (next page): The automated peak-picking algorithm described in Section 2.2.3, called `peakfinder_window`, is demonstrated on synthetic patterns of sawtooth-shaped fluorescence intensity (**A**, **E**). The band width of the synthetic signal is 10 μm in **A**, 21 μm in **E**. Panel **B** (**F**) shows the results of Gaussian smoothing (5-pixel kernel) in blue along with the peaks (red circles) and valleys (black circles) identified using a threshold value (3.0) equal to the s.d. of the original dataset. Panel **C** (**G**) shows the band widths, in μm, calculated as the distance between adjacent valleys. Panel **D** (**H**) plots the "fractional peak position" variable for each band, which is the ratio of the distance from a peak to the preceding valley and the band width. Note the accuracy with which the algorithm picks the peaks and valleys and calculates band widths, with the minor exception of an edge-effect in the outermost bands caused by the smoothing operation. The bottom panels illustrate the effect of smoothing on the band "shape" measurements. The fractional peak position for the idealized bands in **A** (**E**) is 0.1 (0.05), but increases to 0.5 (0.33) after smoothing. Since a fractional peak position of 0.33 is the cut-off for our classification of sawtooth bands, only bands that are wider than 21 μm are included in interpretations of peak shape.

Figure 4.3:

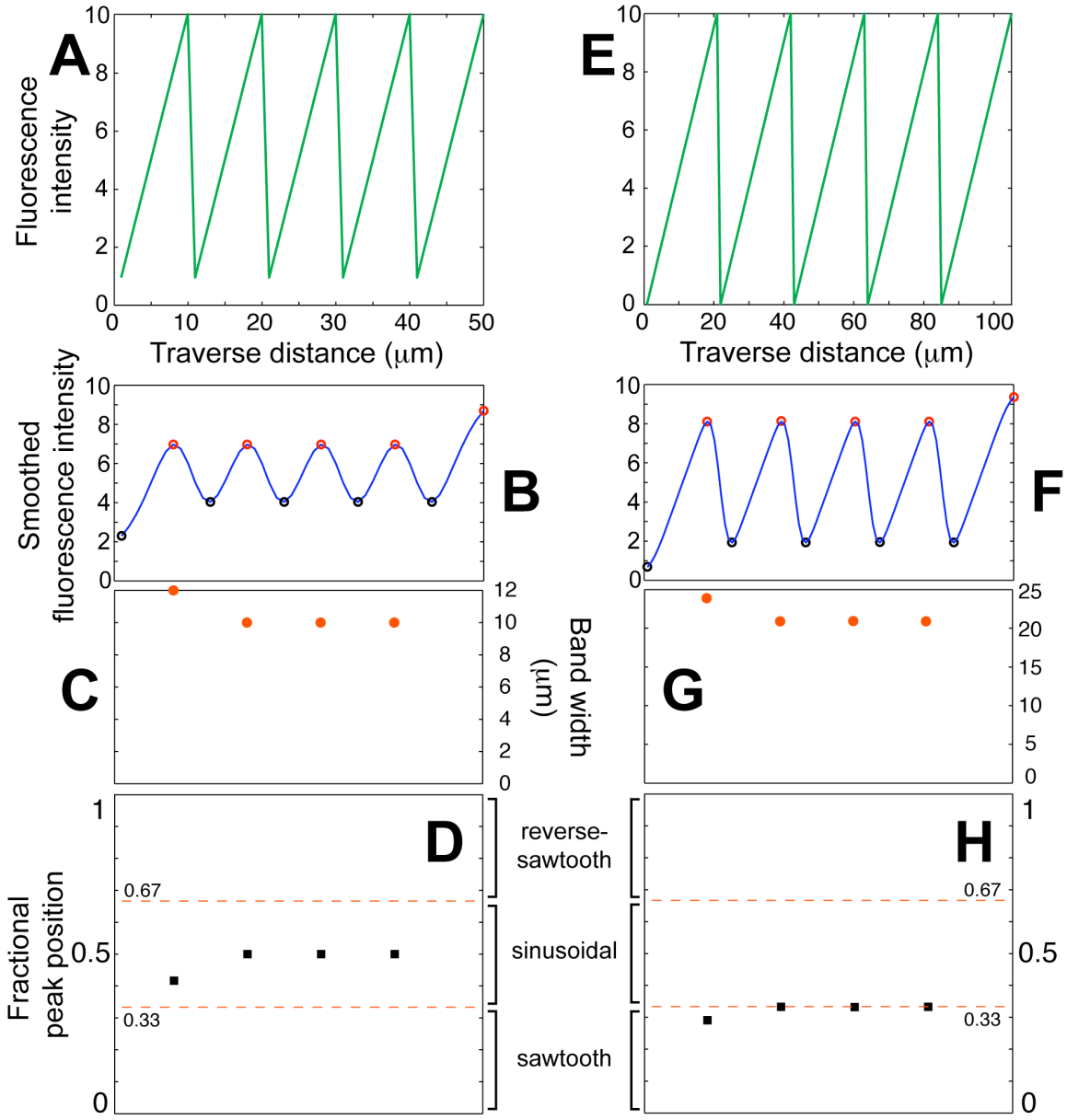
A
E
Fluorescence intensity
Traverse distance (μm)
Traverse distance (μm)
Smoothed fluorescence intensity
B
F
C
G
Band width (μm)
D
H
Fractional peak position
0.67
0.33
reverse-sawtooth
sinusoidal
sawtooth

Figure 4.4 (next page): A small portion of the fluorescence transect at ~9.0 ka (from chip E in Figure 4.1) that illustrates how the `peakfinder_window` algorithm picks peaks and valleys from the smoothed fluorescence intensity data. Panel **A** shows a CLFM image of fluorescent banding. **B** plots the composite traverse of fluorescence intensity measured across the radially-oriented yellow line segments in panel **A**; raw fluorescence intensity is colored gray and data smoothed by a 5-pixel Gaussian kernel are shown in blue. Peaks identified by the algorithm are marked with red circles, valleys with black circles. Dashed lines connect notable features in panel **B** to their location in the CLFM image (**A**). Note that the crack identified in Panel **B** is partially hidden by the yellow line in panel **A**. Panel **C** plots the width of each band identified by `peakfinder_window`. Band widths are calculated as the distance between sequential valleys. Panel **D** shows the "fractional peak position" calculated for each identified peak and shows the peak shape classification (i.e. sawtooth, sinusoidal, or reverse-sawtooth) each value represents. Each fractional peak position is calculated as the ratio of the distance from a peak to the preceding valley and the distance between the two valleys that bracket the peak. Two notable features of this example transect are: (1) the false peaks with extreme fractional peak positions that are picked as a result of a crack, and (2) the smooth connection between sequential fluorescent transects ("tie-point" in panel **B**) that is attained by carefully positioning the radial transects.

Figure 4.4:

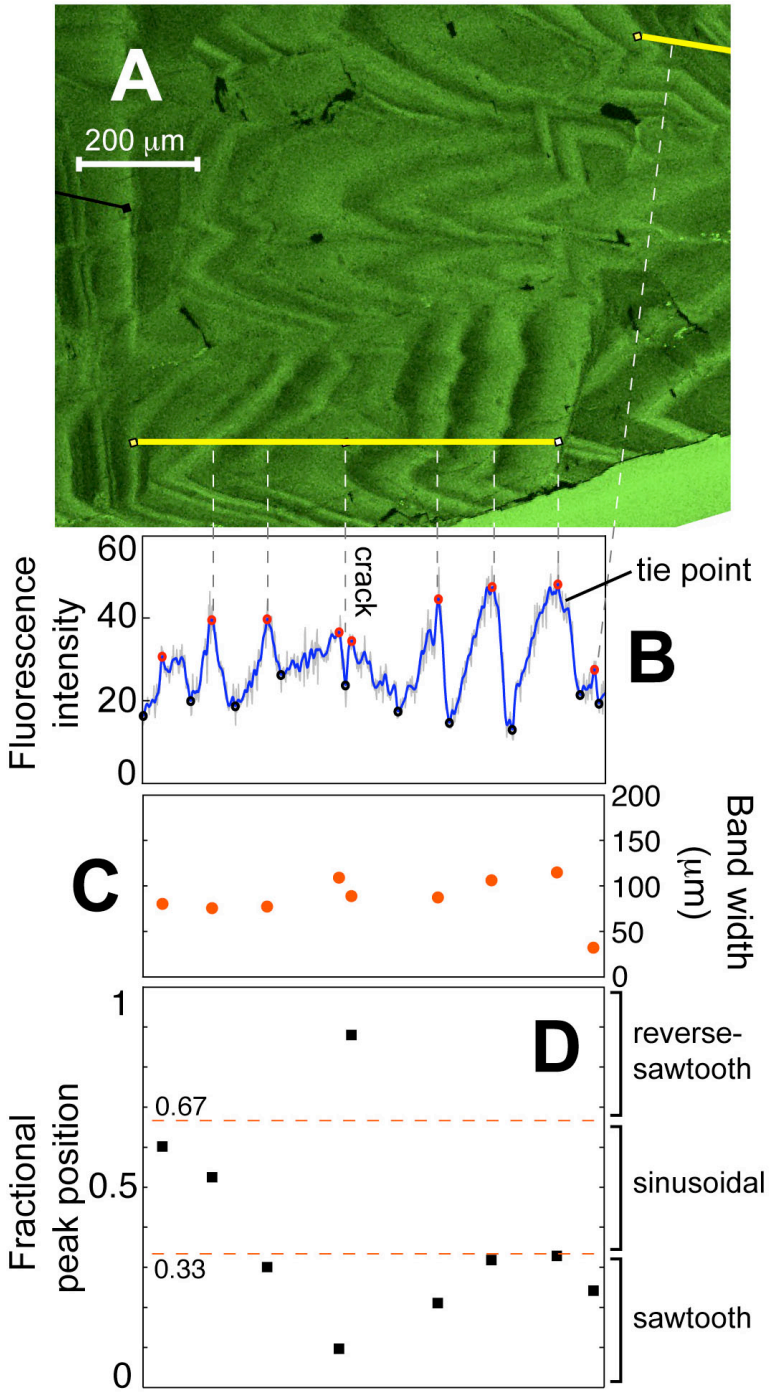
A
200 μm
B
Fluorescence intensity
60
40
20
0
crack
tie point
C
Band width (μm)
200
150
100
50
0
D
Fractional peak position
1
0.5
0
0.67
0.33
reverse-sawtooth
sinusoidal
sawtooth

Figure 4.5 (next page): The top nine panels show the concentration (in ppm) of Mg, Sr, Ba, Zn, Si, Mn, Fe, Y, and P in sample 2N as measured by LA-ICP-MS (filled circles) and ion microprobe (triangles and crosses). The data are plotted using interpolated ages from the Bayesian-derived age model calculated in `StalAge` (Scholz and Hoffman, 2011) from the 24 U-Th ages reported by Orland et al. (2012). For ion microprobe data, the fluorescence classification of each analysis is indicated by a symbol; blue cross = dark fluorescence, green triangle = bright fluorescence, black square = mixed. The bottom panel shows the fluorescence intensity measured across sample 2N by CLFM, also plotted versus age.

Figure 4.5:

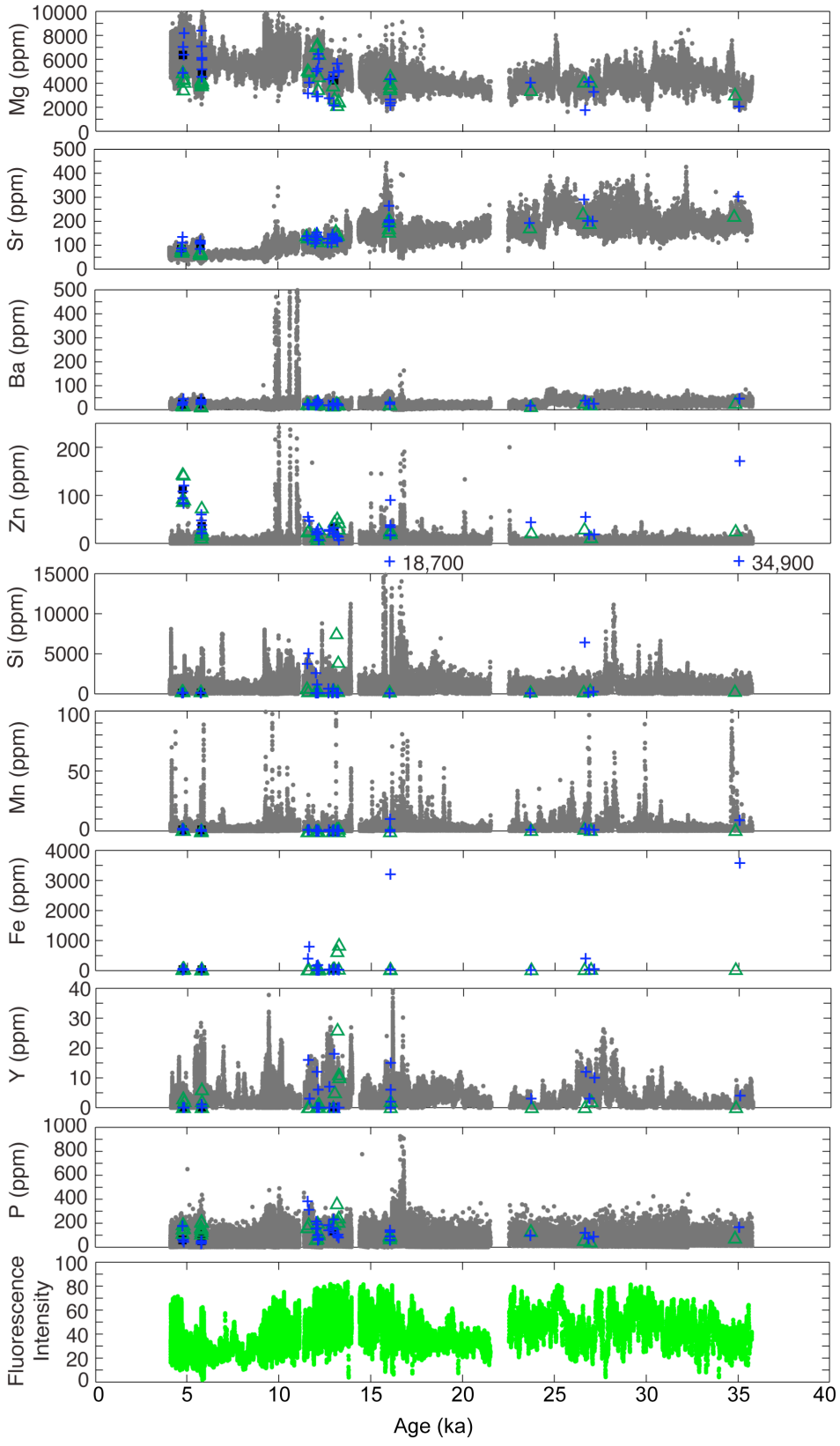
Mg (ppm)
Sr (ppm)
Ba (ppm)
Zn (ppm)
18,700
34,900
Si (ppm)
Mn (ppm)
Fe (ppm)
Y (ppm)
P (ppm)
Fluorescence Intensity
Age (ka)

Figure 4.6: Ion microprobe measurements of Mg (panel **A**), Sr (**B**), and P (**C**) concentrations (ppm) vs. age (ka). The symbols reflect the fluorescence classification of each analysis pit. The horizontal red bars identify the fluorescent banding sections sampled during this analysis. Each of the three sections (1, 4, and 5) is assigned a symbol used in Figure 4.8. In the panel that shows [Sr], grey diamonds plot $^{87}Sr/^{86}Sr$ ratios measured in Soreq Cave speleothems (see right axis; Ayalon et al., in press). The drop in $^{87}Sr/^{86}Sr$ values beginning at ~13 ka is interpreted to reflect decreased delivery of wind-blown dust to the landscape above Soreq.

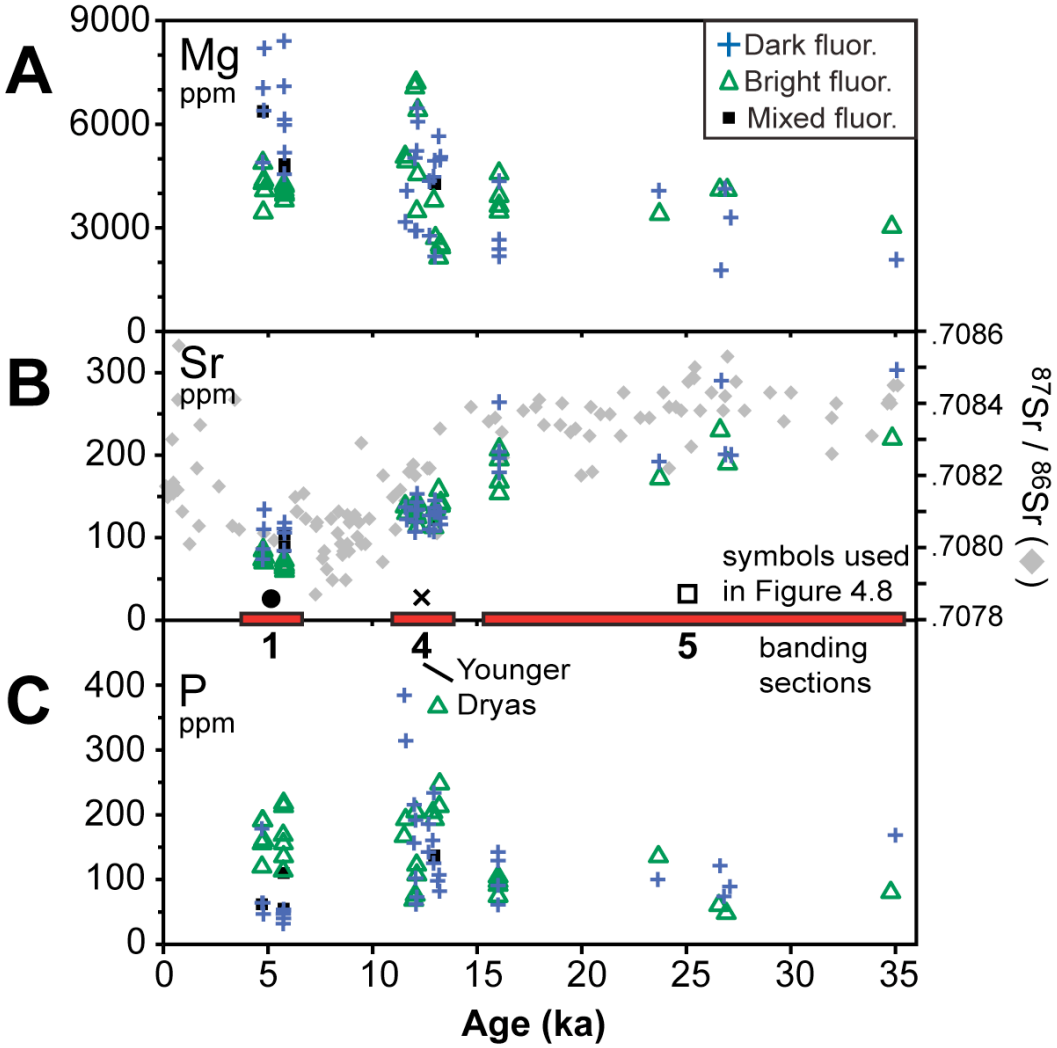

Figure 4.7: The difference (in ppm) between Mg (**A**), Sr (**B**), and P (**C**) concentrations measured by ion microprobe in the dark- and bright-fluorescent portions of single growth bands in sample 2N. Each difference is calculated as Δ(X) = X(dark)–X(bright) and categorized as one of the three fluorescent band-types established by Orland et al. (2012; symbols defined in Figure 4.2).

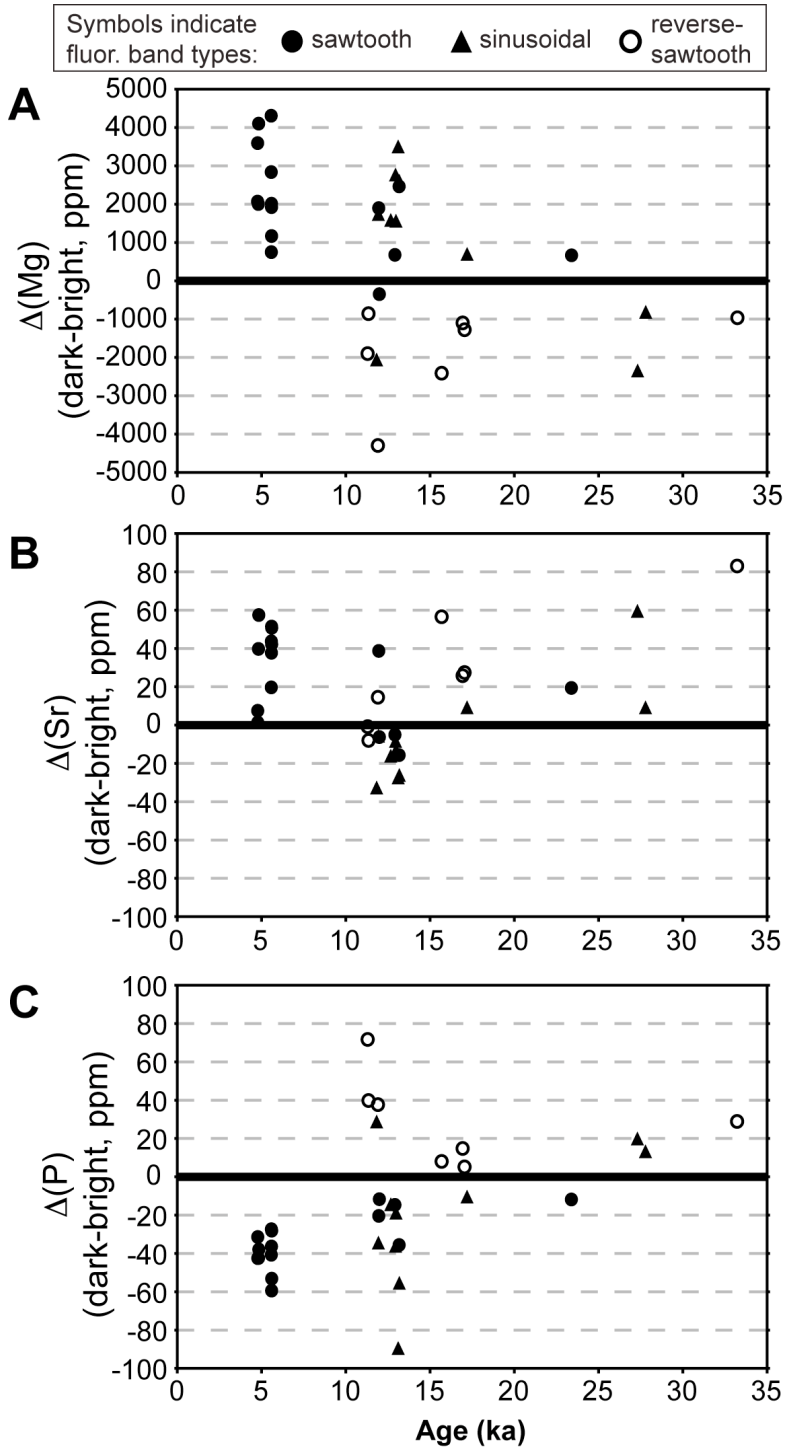

Figure 4.8: Comparison of trace element concentrations measured by ion microprobe in 43 pits across sample 2N. As designated in Figure 4.6, the symbol for each pit indicates the banding section in which it was measured; squares are oldest (LGM), followed by crosses (Younger Dryas), and then circles (Holocene). For the analyses in a Holocene banding section (circles; 4.0–5.3 ka), symbols are colored green or blue if the analysis is in bright- or dark-fluorescent calcite, respectively. Panel **A** plots Sr vs. Mg concentrations. The red arrow highlights the general trend of increasing [Mg] and decreasing [Sr] from the LGM (~20 ka) to the Holocene (< 10 ka). In the Holocene, bright fluorescent bands have lower [Mg] and [Sr] than dark bands, consistent with modern seasonal-scale observations. Panel **B** shows concentrations of P vs. Mg. Each banding section shows an anti-correlation between [Mg] and [P]. This anti-correlation reflects the model of modern trace element delivery described in the previous chapter; wet-season dripwaters deliver organic colloids (high P) and simultaneously dilute the contribution of high-Mg vadose zone groundwater (low Mg).

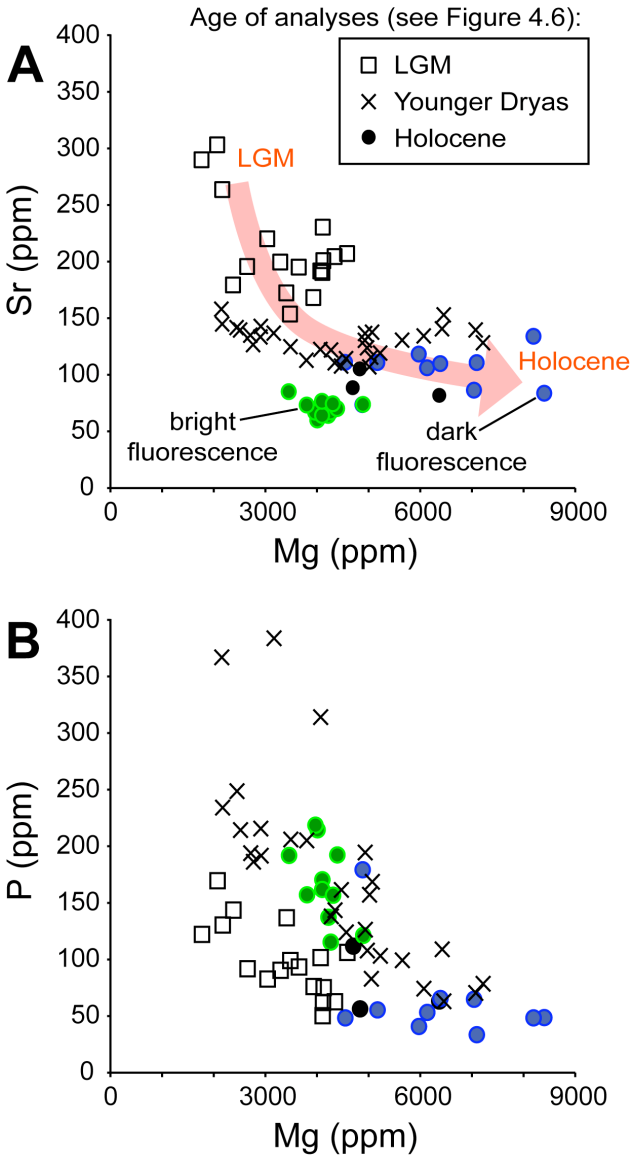

Figure 4.9 (next page): Results of the automated peak-picking algorithm, `peakfinder_window`, from the composite 13.4 cm traverse of fluorescence intensity values measured across sample 2N. Panel **A** shows the smoothed fluorescence intensity data (blue) along with the 2288 peaks (red circles) and valleys (black circles) identified by the algorithm. Panels **B** and **C** show band width and peak shape information, respectively, plotted vs. distance along the analytical traverse, except in portions of the sample with irregular crystal growth (described by Orland et al., 2012). The dashed horizontal line in **B** shows the diameter of the laser beam used for LA-ICP-MS. The red line in **B** shows the 39-point running average of band widths. In **C**, fractional peak positions are only plotted for bands wider than 21 μm (n = 1863). Horizontal lines show benchmark values of fractional peak position, while the yellow line shows the 31-point running average of fractional peak position. Vertical bars distinguish portions of sample 2N that have different fluorescence characteristics; the trace element data from these five sections are compared by principal component analysis.

Figure 4.9:

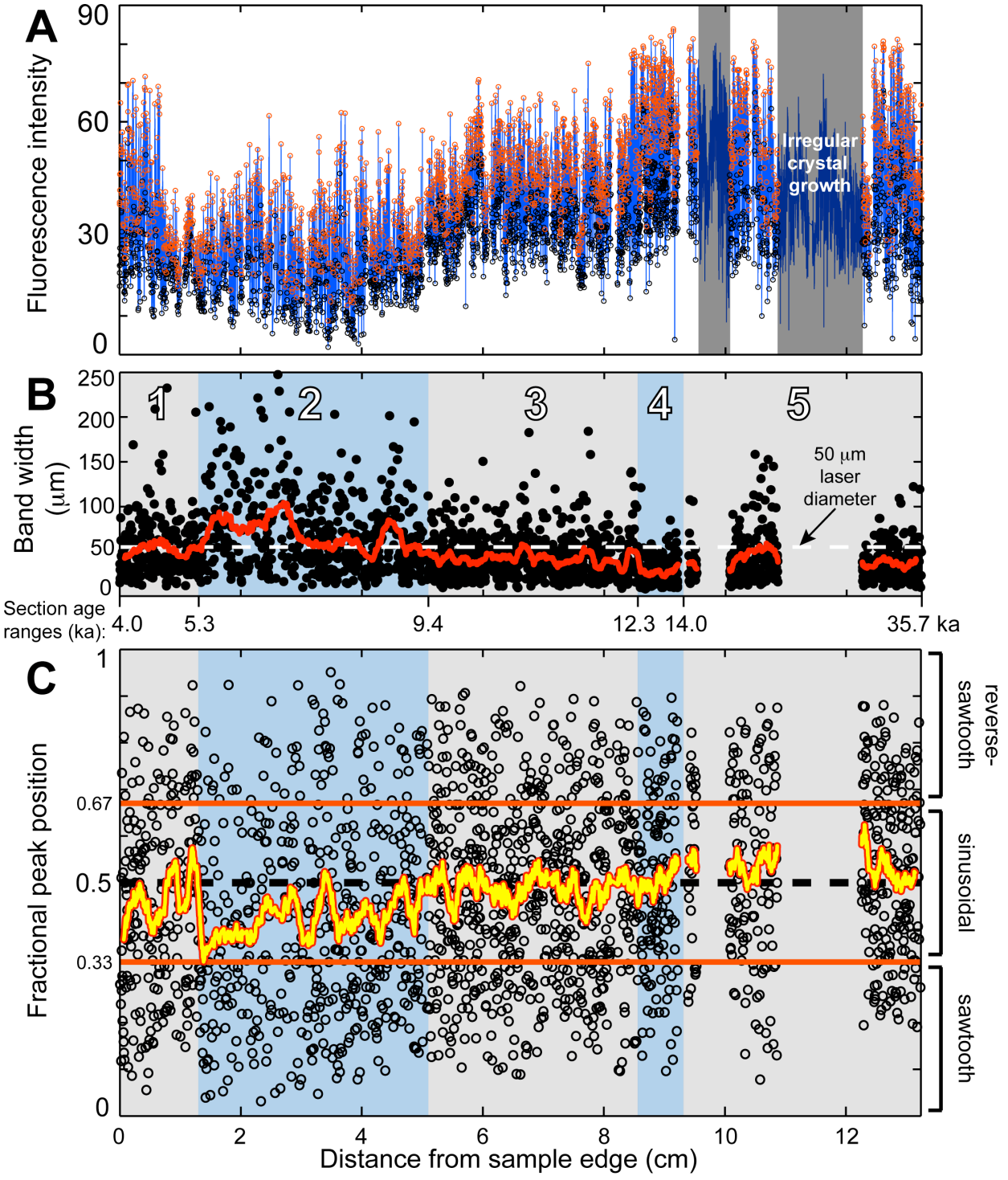
A
Fluorescence intensity
90
60
30
0
Irregular crystal growth
B
Band width (μm)
250
200
150
100
50
0
1
2
3
4
5
50 μm laser diameter
Section age ranges (ka):
4.0
5.3
9.4
12.3
14.0
35.7 ka
C
Fractional peak position
1
0.67
0.5
0.33
0
reverse-sawtooth
sinusoidal
sawtooth
0
2
4
6
8
10
12
Distance from sample edge (cm)

Figure 4.10: Banding characteristics of sample 2N (as in Figure 4.9) plotted versus age. Beginning near the termination of the Younger Dryas cold event at ~12 ka, band widths begin a steady increase (panel **A**) while their fluorescent patterns start to gradually become more "sawtooth" (panel **B**).

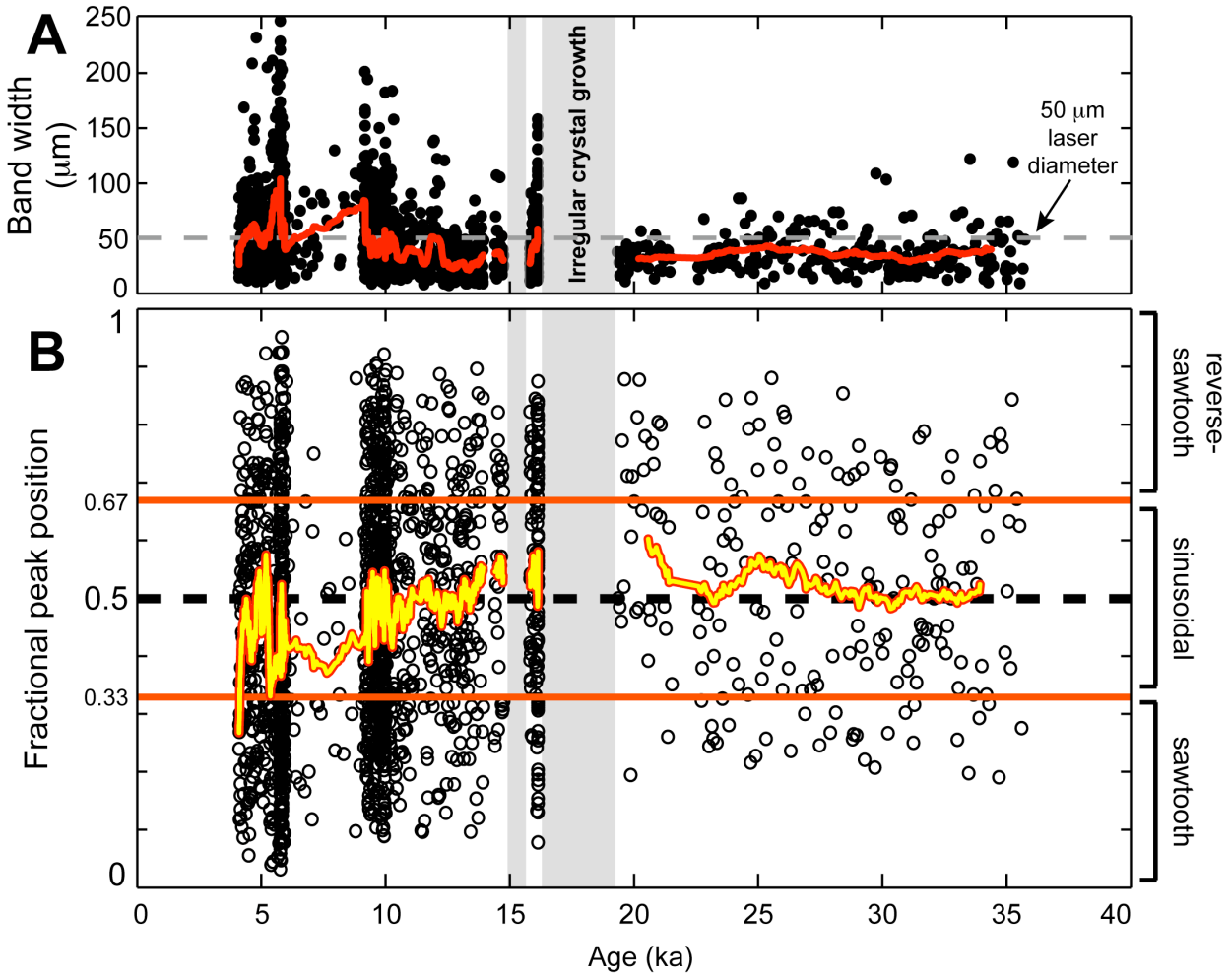

Figure 4.11: Principal component analysis (PCA) results from a dataset that includes 12 composite trace element traverses measured by LA-ICP-MS across sample 2N and the profile of raw fluorescence intensity obtained by CLFM. Definitions of PCA terminology are given in Section 2.4. Panels **A** and **B** plot the scores of principal components 1 and 2, respectively, for the entire LA-ICP-MS traverse of sample 2N. The percentage of total variance is listed for each principal component (PC). Panel **C** plots the loading factor of each element on PC2 versus PC1. Elements of note (see text) are highlighted by colored ellipses.

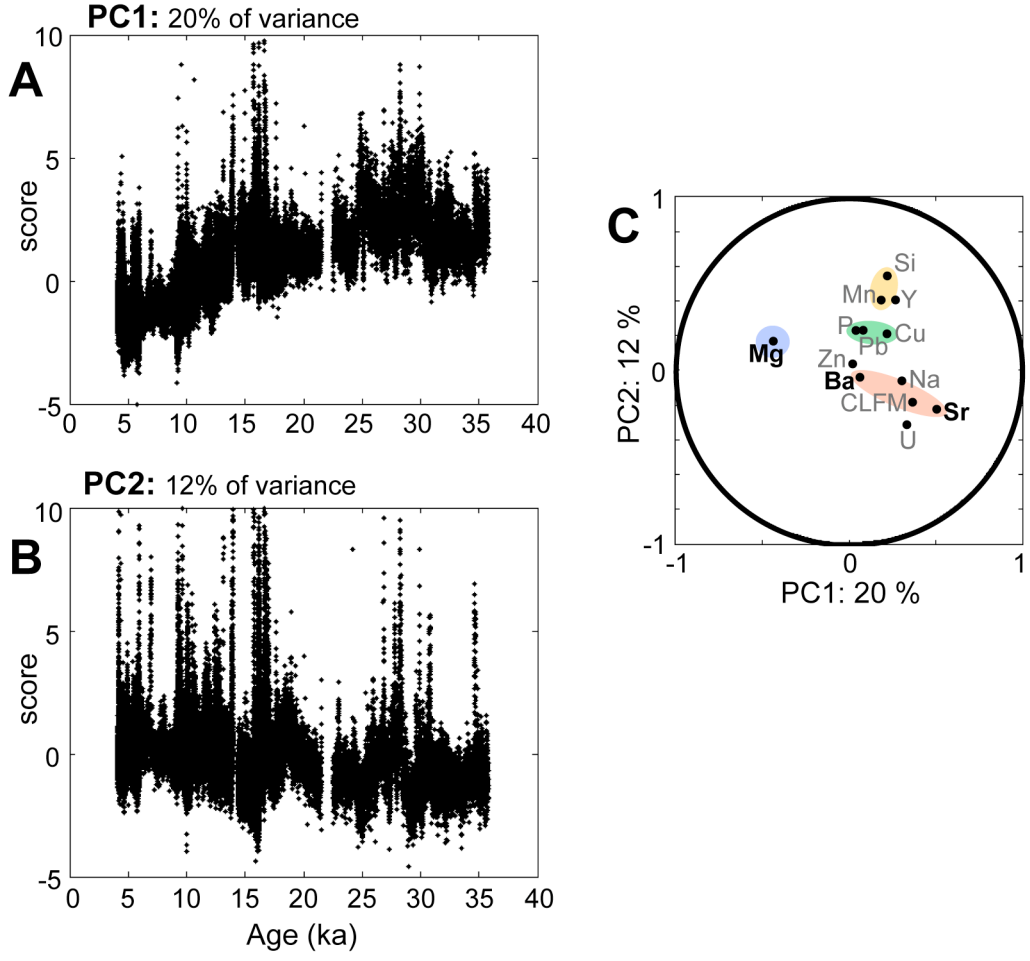

Figure 4.12: Panels **A-E** show PCA results from the sections 1-5, respectively, of sample 2N distinguished by characteristic fluorescent banding patterns in Figure 4.9. PCA terminology is defined in Section 2.4. Elements of note (Section 3.3) are colored with the same scheme as in Figure 4.11C.

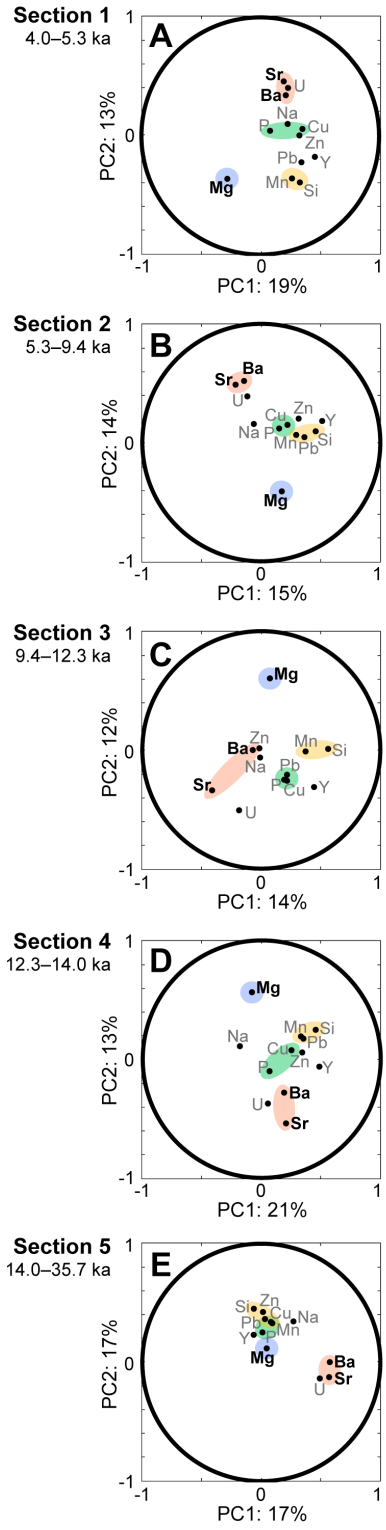

Tables

Table 4.1: Trace element concentrations (ppm-wt) in Sample 2N measured by WiscSIMS ion microprobe

Analysis #	band color*	Mg	Si	P	Mn	Fe	Zn	Sr	Y	Ba	distance (μm)**	model age (ka)$^{\Omega}$	pit condition$^{\Psi}$
2N-A-01	b	4097	83	162	1	54	90	77	2	19	7991	4749	0
2N-A-02	d	8192	110	48	1	37	120	134	0	45	7892	4752	0
2N-A-03	b	4390	163	192	1	62	142	70	0	18	7737	4752	2
2N-A-04	d	6387	104	65	1	47	83	110	0	32	7698	4754	0
2N-A-05	b	3454	121	192	1	49	94	85	3	22	7414	4756	1
2N-A-06	d	7040	85	65	2	60	108	86	0	24	7286	4768	0
2N-A-07	b	4307	94	157	1	31	87	74	0	21	7263	4793	1
2N-A-08	d	4880	89	179	1	20	94	74	0	20	7239	4797	1
2N-A-09	b	4891	111	121	1	51	144	74	0	21	7214	4811	0
2N-A-10	i	6368	101	63	1	38	112	82	0	23	7243	4820	1
2N-B-01	b	4006	115	214	1	54	74	60	2	15	19618	5763	1
2N-B-02	i	4693	90	111	1	31	36	89	0	24	19561	5764	0
2N-B-03	i	4828	124	56	0	23	29	105	0	34	19531	5767	0
2N-B-04	d	5169	82	55	1	17	21	111	0	35	19487	5770	0
2N-B-05	b	4217	97	137	0	30	27	64	0	17	19472	5774	0
2N-B-06	d	6132	85	53	1	56	38	106	0	35	19416	5778	0
2N-B-07	b	3965	96	219	0	37	19	67	0	17	19379	5782	0
2N-B-08	d	5971	75	41	0	25	29	118	0	42	19306	5783	1
2N-B-09	b	3802	78	157	0	31	21	73	6	18	19167	5784	0
2N-B-10	d	4544	79	48	0	22	29	111	0	30	19049	5785	0
2N-B-11	b	4261	77	115	0	26	17	67	0	17	18929	5786	0
2N-B-12	d	7092	115	33	1	27	48	111	0	38	18873	5787	1
2N-B-13	b	4099	82	170	0	21	11	64	0	16	18799	5787	0
2N-B-14	d	8400	87	48	0	30	60	84	1	24	18762	5788	0
2N-I-01	b	2445	3753	249	2	845	43	142	10	23	89567	11558	2
2N-I-02	d	5049	79	83	0	24	7	116	0	19	89542	11568	0
2N-I-03	b	2513	103	214	0	45	30	139	11	23	89524	11620	1
2N-I-04	d	4971	88	108	1	35	14	124	0	22	89487	11628	0
2N-I-05	b	2150	7339	367	2	630	52	158	26	29	89227	12019	2
2N-I-06	d	5649	104	99	0	34	16	131	0	25	89212	12028	0
2N-I-07	b	2711	285	194	0	54	44	135	5	19	88588	12034	1
2N-I-08	i	4273	106	138	0	40	32	122	0	19	88570	12084	0
2N-I-09	d	2166	618	234	1	55	32	145	18	22	88494	12102	2
2N-I-10	d	4932	110	126	0	27	20	136	0	26	88444	12107	0
2N-I-11	b	3797	84	205	0	45	23	113	0	18	88297	12114	0
2N-I-12	d	4468	96	161	0	29	25	108	0	18	88267	12126	0
2N-I-13	d	2764	83	186	0	26	28	127	7	19	87468	12151	1
2N-I-14	d	4345	625	143	1	42	26	110	0	18	87454	12156	0
2N-I-15	b	6421	234	109	0	53	29	141	1	31	85278	12162	1

Table 4.1 (ctd):

Analysis #	band color*	Mg	Si	P	Mn	Fe	Zn	Sr	Y	Ba	distance (μm)**	model age (ka)Ω	pit conditionΨ
2N-I-16	d	6067	77	74	0	15	7	134	0	31	85253	12718	0
2N-I-17	b	4563	87	124	0	20	15	114	0	23	85236	12721	0
2N-I-18	d	6455	72	63	0	17	20	153	0	40	85138	12921	0
2N-I-19	b	3488	248	206	0	51	16	125	1	23	85093	12928	0
2N-I-20	d	5223	69	103	0	15	21	119	0	23	85066	12965	0
2N-I-21	d	2913	1143	192	0	186	30	143	6	26	85044	12978	1
2N-I-22	b	7215	84	78	0	32	8	128	0	30	84976	12997	0
2N-I-23	d	2906	2582	216	1	164	25	133	12	24	84785	13002	1
2N-I-24	b	7073	86	70	0	23	13	140	0	29	84724	13160	1
2N-I-25	d	5014	82	157	0	18	19	107	0	19	84759	13163	1
2N-I-26	d	4066	5039	314	1	796	47	122	3	20	83192	13230	1
2N-I-27	b	4929	86	194	0	24	27	130	0	24	83161	13239	0
2N-I-28	d	3163	3742	384	1	399	55	137	16	24	82954	13244	1
2N-I-29	b	5068	515	168	0	26	24	138	0	25	82911	13250	0
2N-M-01	d	2167	58	130	1	46	38	264	6	31	105443	16050	2
2N-M-02	b	4584	79	106	0	48	27	207	2	26	105400	16050	1
2N-N-01	d	2649	39	92	0	33	34	196	0	24	106950	16051	1
2N-N-02	b	3931	43	76	0	37	21	168	0	23	106935	16051	0
2N-N-03	b	3647	44	93	0	27	20	195	0	24	107722	16052	0
2N-N-04	d	4342	52	62	0	33	17	204	2	27	107674	16052	1
2N-N-05	d	2375	18733	143	10	3209	90	179	15	25	106724	16052	2
2N-N-06	b	3479	40	99	0	31	25	154	2	25	106567	16054	2
2N-P-01	d	4066	55	101	1	20	44	192	3	17	125108	23688	1
2N-P-02	b	3407	45	137	1	29	22	172	0	16	125130	23724	2
2N-P-03	b	4112	50	62	2	32	30	230	0	31	126860	26610	0
2N-P-04	d	1766	6411	122	2	404	55	290	12	38	126895	26668	2
2N-P-05	d	4124	125	75	1	36	18	201	3	25	127010	26860	1
2N-P-06	b	4105	234	50	1	40	12	190	2	23	127075	26969	0
2N-P-07	d	3289	252	90	1	49	19	200	10	25	127175	27135	2
2N-P-08	b	3038	133	82	1	35	26	220	0	30	131820	34842	2
2N-P-09	d	2069	34942	169	9	3578	171	303	4	46	131950	35061	2

Table notes:

*: band fluorescence classifications are as follows:
- b = bright
- d = dark
- i = intermediate

**: distance is measured from the outer edge of the sample

Ω: Ages assigned according to the age model described in the text.

Ψ: pit-bottoms of each analysis were imaged by SEM and classified as follows:
- 0 = regular (no cracks or pores)
- 1 = intermediate
- 2 = irregular (notable cracks or pores)

Table 4.2: Results of automated peak-picking for each chip in sample 2N, including the total number of bands as counted by the author (by eye) and the `peakfinder_window` algorithm (auto). The "% offset" values show the fractional offset of the number of bands counted by the algorithm versus by eye. The number of bands with widths <21 μm, which are excluded from peak shape interpretations, is indicated as "# narrow bands." Also listed are the average fractional peak position (FPP) and percentage of peaks with fractional peak position ≤0.33 (% saw) calculated for each chip. The two columns labeled "control transects" show the number of bands and average fractional peak position calculated in the "control" traverse of each chip (see Section 3.2).

	Compound transects							Control transects	
Chip	Model age range (ka)	# bands (by eye)	# bands (auto)	% offset	# narrow bands	Avg. FPP	% saw	# bands (auto)	Avg. FPP
A	4.1-5.0	214	195	-8.9	17	0.46	32	226	0.52
B	5.1-5.7	130	144	+10.8	8	0.43	42	190	0.46
C	5.7-5.8	80	113	+41.3	5	0.43	37	158	0.50
D	5.8-5.9	188	175	-6.9	24	0.44	38	189	0.46
E	5.9-9.3	184	149	-19.0	9	0.45	33	181	0.51
F	9.3-9.8	252	248	-1.6	41	0.50	22	312	0.50
G	9.8-10.0	224	212	-5.4	31	0.49	24	234	0.48
H	10.0-11.1	300	250	-16.7	50	0.48	24	257	0.50
I	11.1-13.9	350	345	-1.4	141	0.49	18	254	0.49
M	14.4-16.1	75	122	+62.7	28	0.54	13	134	0.51
N	16.1-?	45	79	+75.6	12	0.53	25	105	0.48
O	?-21.5	41	39	-4.9	7	0.58	8	40	0.49
P	22.6-35.7	245	217	-11.4	40	0.51	20	292	0.52
Sample totals		**2,328**	**2,288**	**-1.7**	**413**			**2,573**	

Appendices

Appendix A4.1: Sample 2N is a 1 cm-thick horizontal slice through a Soreq Cave stalactite (Figure 4.1). Ion microprobe analysis required samples to be mounted in 1-inch epoxy rounds, so the portion of sample 2N that follows the 13.4 cm analytical traverse was cut into thirteen ~1 cm cubes with a thin-kerf jeweler's saw (Orland et al., 2012). Two cubes were arranged in each epoxy mount such that their analytical traverses were nearest the center of the mount. As shown in Figure 4.1, three grains of UWC-3 calcite standard (Kozdon et al., 2009) were mounted in each round between the pair of cubes. After casting in epoxy, the analytical face of each round was ground with a diamond mesh and polished with successive grits of diamond paste (6, 3, 1 μm) in order to minimize analytical bias caused by surface relief (Valley and Kita, 2009).

Before analysis, each epoxy round was cut to 5 mm thickness to fit into the ion microprobe sample holder. Next, each round was cleaned by successive 30 s sonication sessions in ethanol and distilled water. Each mount was then dried in a vacuum oven at 40°C for a minimum of 8 hours. After drying, the rounds were coated with a ~60 nm-thick gold coating. The final step before ion microprobe analysis was to create a map of the sample surface with a reflected-light microscope.

Following ion microprobe analysis, the gold coating was removed by lightly abrading the coated surface with a 0.25 μm diamond suspension. The uncoated surface was then ready for either imaging by confocal laser fluorescent microscopy or analysis by LA-ICP-MS. Before subsequent ion microprobe analysis sessions, the cleaning and coating steps were repeated.

Figure A4.2: Plots of 12 elemental concentrations (in ppm-wt) measured by LA-ICP-MS along the 13.4 cm analytical traverse of sample 2N. Data are plotted versus age.

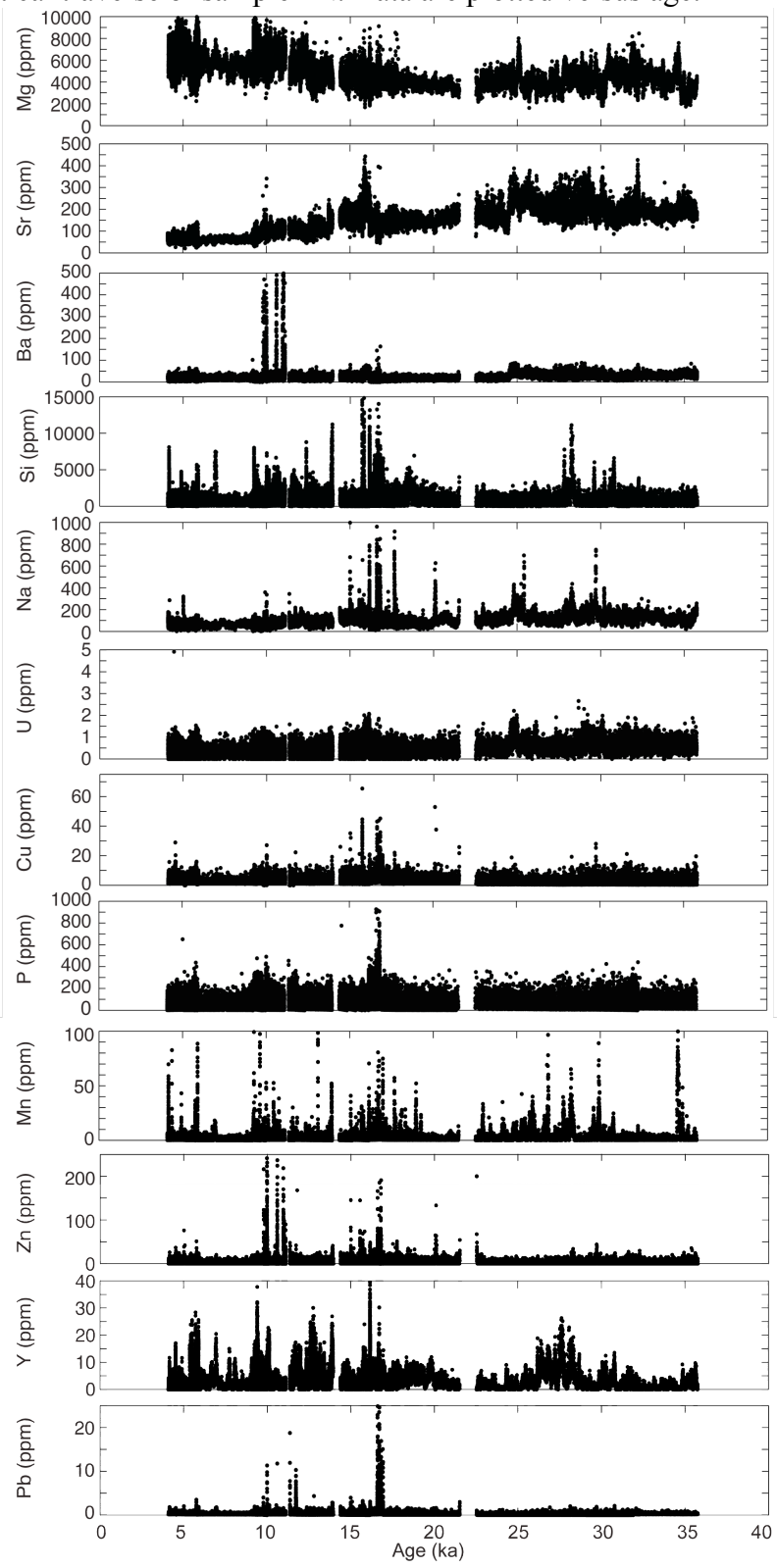

Table A4.3: Average trace element concentrations (ppm-wt) and 2 s.d. values (%) measured in 56 30 s traverses of NIST-610 that bracket the analytical traverses of sample 2N. The index element for these concentration calculations is ^{29}Si. The nominal glass composition of NIST-610 is 72 wt% SiO_2, 12% CaO, 14% Na_2O, and 2% Al_2O_3. NIST-certified trace element concentrations are listed in the bottom row (next page).

	Na	Mg	Al	P	K	Ca	Ca	Mn	Co	Ni	Cu	Zn	Sr	Y	Ba	Au	Pb	Th	U
Mass measured	23	24	27	31	39	42	43	55	59	60	63	66	88	89	137	197	208	232	238
2N-A (4 x NIST-610) Avg. conc. (ppm)	102250	477.0	11110	353.2	505	84200	84200	499	416.0	474	444.0	470	528	462	448	23.80	442	469	474
2 s.d. (ppm)	510	18	210	4.4	45	3600	3400	16	13	20	12	22	26	26	20	1.3	25	26	21
2 s.d. (% conc.)	0.5	3.7	1.9	1.3	9	4.3	4.1	3.2	3.1	4.1	2.7	4.8	5	5.7	4.5	5.6	5.6	5.5	4.5
2N-B (4 x NIST-610) Avg. conc. (ppm)	102150	478.6	11109	353	500.7	84700	84580	499.1	417.0	472	443.0	471	530	464	449	23.70	438	471	474
2 s.d. (ppm)	880	4.2	87	16	8.6	2100	930	9.3	10	14	12	23	19	14	22	2.0	21	19	22
2 s.d. (% conc.)	0.86	0.89	0.79	4.6	1.7	2.5	1.1	1.9	2.4	3	2.8	4.9	3.6	3	4.9	8.6	4.9	4	4.7
2N-C (4 x NIST-610) Avg. conc. (ppm)	102370	477.8	11110	352	500	84600	84500	497	417.0	471.8	442.1	471	531	464	448	23.80	440	472	476
2 s.d. (ppm)	770	7.7	130	25	17	2100	3100	14	12	5.7	6.6	27	26	23	27	1.6	24	29	31
2 s.d. (% conc.)	0.75	1.6	1.1	7	3.3	2.5	3.7	2.8	2.9	1.2	1.5	5.8	4.9	5	6.1	6.9	5.4	6.2	6.5
2N-D (4 x NIST-610) Avg. conc. (ppm)	102350	478.6	11107	352.8	499	84480	84490	499.2	416.8	472.2	442.4	469	531	462.9	447	23.70	437	470	475
2 s.d. (ppm)	860	4.5	46	2	18	660	680	5.7	2.7	6.3	5.3	12	5.9	7.7	10	0.87	9.2	11	11
2 s.d. (% conc.)	0.84	0.95	0.41	0.57	3.6	0.78	0.8	1.1	0.65	1.3	1.2	2.5	1.1	1.7	2.2	3.7	2.1	2.4	2.3
2N-E (4 x NIST-610) Avg. conc. (ppm)	102390	478.6	11120	353	506	84300	84700	498	416.0	471.8	442.0	469	531	463	447	23.90	435	467	472
2 s.d. (ppm)	1100	8.8	160	35	47	2700	2700	19	17	9.9	10	32	37	29	39	2.7	35	42	44
2 s.d. (% conc.)	1.1	1.8	1.4	9.9	9.2	3.2	3.2	3.7	4.2	2.1	2.3	6.7	7	6.3	8.6	11.0	8	9.1	9.3
2N-F (4 x NIST-610) Avg. conc. (ppm)	102350	478.8	11130	355	501	84500	84500	498	417.0	472	442.0	468	531	461	445	23.80	437	468	475
2 s.d. (ppm)	1600	7.8	260	20	48	2300	2500	18	13	17	14	8.2	30	29	29	1.3	29	42	36
2 s.d. (% conc.)	1.6	1.6	2.3	5.6	9.5	2.7	3	3.7	3.1	3.5	3.2	1.8	5.7	6.2	6.5	5.6	6.8	8.9	7.6
2N-G (4 x NIST-610) Avg. conc. (ppm)	102780	473.7	11140	353	503	84700	85100	504	415.1	472.4	444.5	467	529	461	447	23.52	448	468	481
2 s.d. (ppm)	740	2	120	32	37	1400	1500	11	2.4	6.4	6.1	22	17	17	24	0.76	21	25	25
2 s.d. (% conc.)	0.72	0.42	1.1	8.9	7.3	1.7	1.8	2.2	0.59	1.4	1.4	4.8	3.3	3.6	5.5	3.2	4.8	5.3	5.1
2N-H (4 x NIST-610) Avg. conc. (ppm)	103000	478.5	11050	353	504	84200	84500	501	419.0	475	447.0	470	531	462.1	450	24.10	447	471	478
2 s.d. (ppm)	3100	4.5	280	15	32	1300	1100	13	12	20	23	13	13	8.4	18	2.7	41	16	23
2 s.d. (% conc.)	3	0.94	2.5	4.4	6.4	1.6	1.2	2.5	2.8	4.1	5.2	2.8	2.5	1.8	4	11.0	9.1	3.5	4.9

Table A4.3 (ctd)	Na	Mg	Al	P	K	Ca	Ca	Mn	Co	Ni	Cu	Zn	Sr	Y	Ba	Au	Pb	Th	U
2N-I2 (4 x NIST-610) Avg. conc. (ppm)	102310	477.0	11090	352.9	499	84400	84100	499	417.0	473	443.3	470	530	457	446	23.65	438	470	475
2 s.d. (ppm)	460	15	320	6.4	32	3600	5400	15	12	11	8.2	17	32	30	23	0.35	16	33	26
2 s.d. (% conc.)	0.45	3.2	2.9	1.8	6.5	4.3	6.5	3	2.9	2.3	1.8	3.7	6.1	6.6	5.2	1.5	3.7	7.1	5.4
2N-I (4 x NIST-610) Avg. conc. (ppm)	102400	483.0	11100	390	540	84100	84500	498	416.0	470	442.2	469	535	462	449	23.65	443	467	474
2 s.d. (ppm)	1700	48	160	230	190	4800	6100	13	10	13	7	44	38	39	43	0.53	30	52	37
2 s.d. (% conc.)	1.7	9.9	1.4	58	36	5.7	7.2	2.7	2.5	2.8	1.6	9.3	7	8.4	9.6	2.3	6.9	11	7.8
2N-M (4 x NIST-610) Avg. conc. (ppm)	102770	479.0	11180	352	496	85100	84500	503	418.7	472	441.9	470	536	464	455	23.50	440	471	479
2 s.d. (ppm)	920	20	600	30	49	5700	4200	19	9.7	11	6.5	35	37	45	33	0.90	20	53	36
2 s.d. (% conc.)	0.89	4.1	5.3	8.4	10	6.7	5	3.8	2.3	2.3	1.5	7.5	6.9	9.8	7.3	3.8	4.5	11	7.4
2N-N (4 x NIST-610) Avg. conc. (ppm)	102420	477.5	11143	352.9	496	84580	84500	498.2	416.3	471.7	441.7	470	531	462	447	23.69	437	471	474
2 s.d. (ppm)	840	7.6	69	2.2	40	990	2000	9.3	8.8	5.8	6.5	16	12	15	19	0.76	27	16	21
2 s.d. (% conc.)	0.82	1.6	0.62	0.62	8.1	1.2	2.3	1.9	2.1	1.2	1.5	3.3	2.3	3.2	4.1	3.2	6.2	3.3	4.4
2N-O (4 x NIST-610) Avg. conc. (ppm)	102300	478.4	11100	354	501	84400	84600	498	415.9	472.1	443.0	469	528	459	446	23.71	437	464	472
2 s.d. (ppm)	560	5.1	250	54	36	3400	3600	14	7.6	9.5	12	5.9	23	26	21	0.87	15	35	27
2 s.d. (% conc.)	0.55	1.1	2.3	15	7.3	4	4.3	2.8	1.8	2	2.8	1.3	4.4	5.7	4.6	3.7	3.5	7.6	5.8
2N-P (4 x NIST-610) Avg. conc. (ppm)	102500	477.9	11130	352	503	84700	84470	499.1	417.7	471	443.2	471	531	464	449	23.70	444	475	479
2 s.d. (ppm)	1200	5	110	39	22	1700	730	2.5	6.3	10	7	21	15	11	12	0.80	25	23	27
2 s.d. (% conc.)	1.1	1	1	11	4.3	2.1	0.87	0.51	1.5	2.1	1.6	4.5	2.7	2.3	2.6	3.4	5.7	4.8	5.7
Statistics for averaged NIST-610 measurements from each traverse																			
Avg. conc. (ppm)	**102500**	**478.2**	**11120**	**355.6**	**504**	**84500**	**84520**	**499.3**	**416.8**	**472.2**	**443.0**	**470**	**531**	**462**	**448**	**23.73**	**440**	**470**	**476**
Avg. 2 s.d. (ppm)	1100	11	200	37	44	2600	2700	13	10	11	10	21	24	23	24	1.20	24	30	28
Avg. 2 s.d. (% conc.)	1.1	2.3	1.8	10.4	8.7	3.1	3.2	2.6	2.4	2.3	2.3	4.5	4.5	5.0	5.4	5.1	5.5	6.4	5.9
NIST conc. (ppm)*					(461)			457	(390)	458.7	*444*	(433)	515.5		453	(25)	426	457.2	461.5

Table notes:

The average values at the bottom of this table include all 56 30 s traverses measured in NIST-610 over the course of the analysis session. A single errant NIST-610 analysis in the bracket of traverse 2N-I causes a notable increase in the average precision of P measurements. Excluding the errant analysis reduces the average 2 s.d. of P measurements to <7% of the average concentration. As shown in Figure 4.1, the traverse of chip I is split into two portions, each with its own bracketing standards. Traverse I2 is the younger segment.

Symbol legend:

*: Known concentrations are supplied by the National Institute of Standards and Technology (NIST). Certified values are normal text, reference values are in italics, and values in parentheses are informational only.

Appendix A4.4: In constructing the complete age model, it was necessary to account for material removed by the jeweler's saw when the cubes were cut apart. Gap widths were assigned so that reference points in each chip aligned with their distance measured along the analytical traverse before the sample was cut. For cubes that were removed using the jeweler's saw, the bounding gaps were assigned a uniform width of 560 μm. This value is slightly larger than measurements of the kerf-width in a glass slide (450 μm), probably due to the longer cutting time required to remove each 1 cm-thick chip and the fact that calcite is softer than glass. The gaps between cubes H–I and I–M were cut by thicker saw blades and assigned values of 1050 and 1650 μm, respectively. The sum of the LA-ICP-MS traverse distances and the gap assignments matches the length of the analytical traverse before the sample was cut (134,300 microns).

Additional attention was given to sample chip P, which includes the oldest growth bands adjacent to the central growth axis. At the old end of chip P, the analytical traverse takes a right-angle turn in order to cross the first 2 mm of growth bands (Figure 4.1). Therefore, as with the $\delta^{18}O$ measurements in that chip (Orland et al., 2012), a simple algorithm is used to convert the location of each analytical point to a radial equivalent.

Figure A4.5: Concentrations of Ba and Zn (ppm) measured in chips G and H from adjacent laser traverses: pre-cleaned (blue) and non-pre-cleaned (red). The disagreement in the location of [Ba] and [Zn] peaks in the parallel transects suggests that they are caused by micron-scale inclusions.

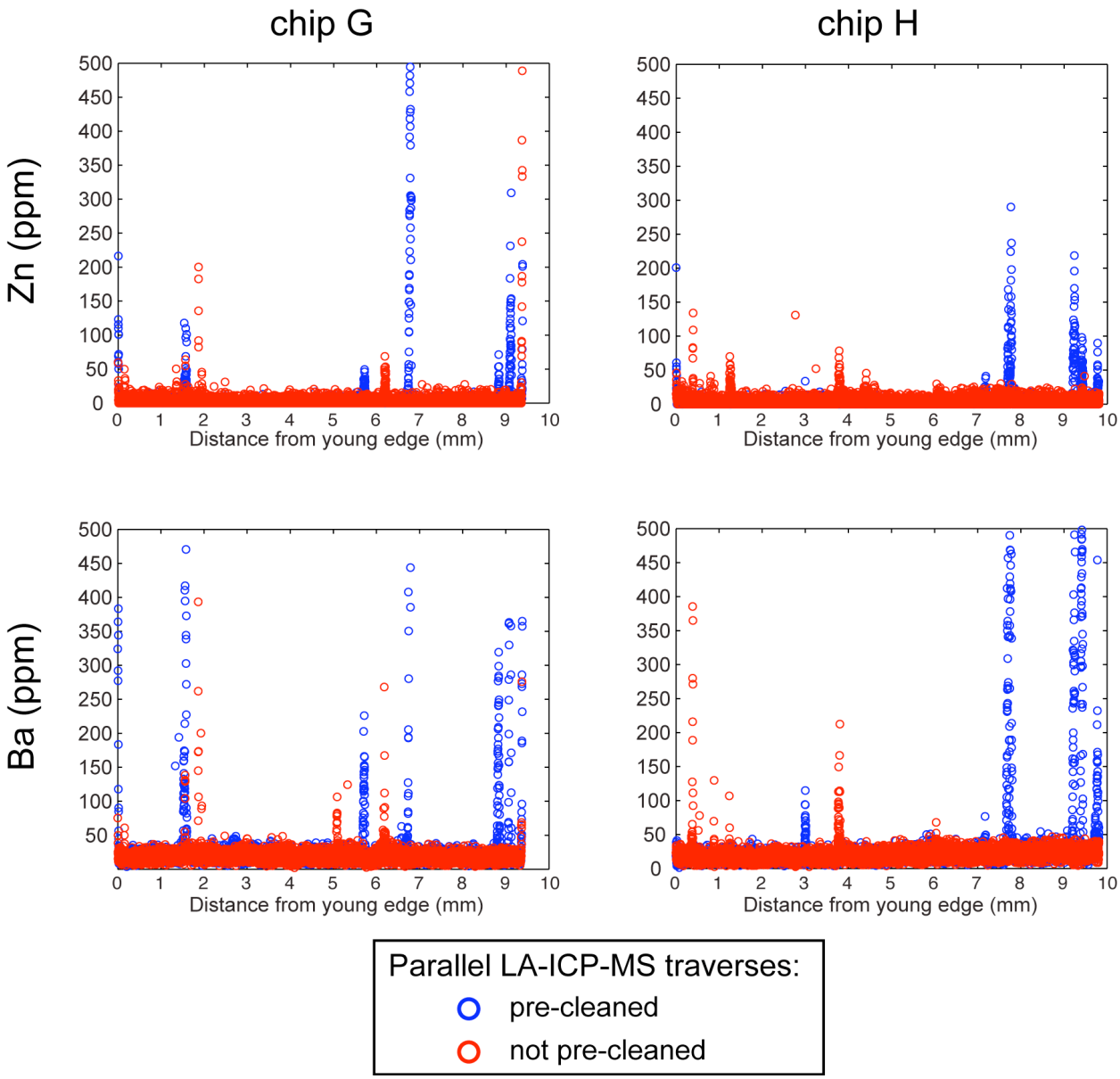

Figure A4.6: Backscatter electron image (by SEM) of a portion of the analytical traverse in chip G of sample 2N. Note the side-by-side laser trenches running north-south (pre-cleaned trench on the right, non-pre-cleaned trench on the left); the 50 μm-wide analytical trench on the right is coaxial with a 100 μm-wide pre-cleaning trench. The two white circles show inclusions at locations in the pre-cleaned analytical traverse that coincide with anomalously high concentrations of Ba and Zn.

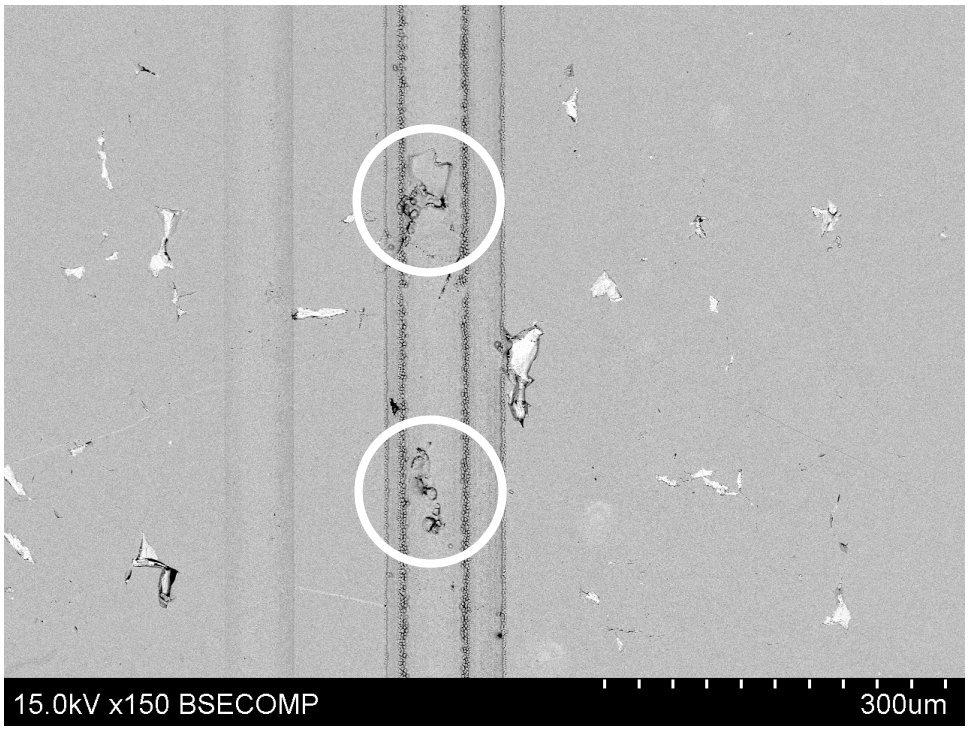

Figure A4.7: Testing the reproducibility of the automated peak-picking method. **A-D** show the Gaussian-smoothed fluorescence transects (with peaks and valleys indicated by circles) of four compound transects across chip E. In order from top to bottom, these transects include the original, blind, control, and parallel iterations. **E-H** plot the corresponding fractional peak positions from each transect along with the 31-point running average (as in Figure 4.9C). Note the similar fluorescence intensities and fractional peak positions measured in the original, blind and parallel transects. The control transect is composed of a single segment that stretches across the entire chip, parallel to the analytical traverse. Not only does the number of bands notably increase in the control transect (182), but the fractional peak positions are biased because the transect does not run perpendicular to the growth banding.

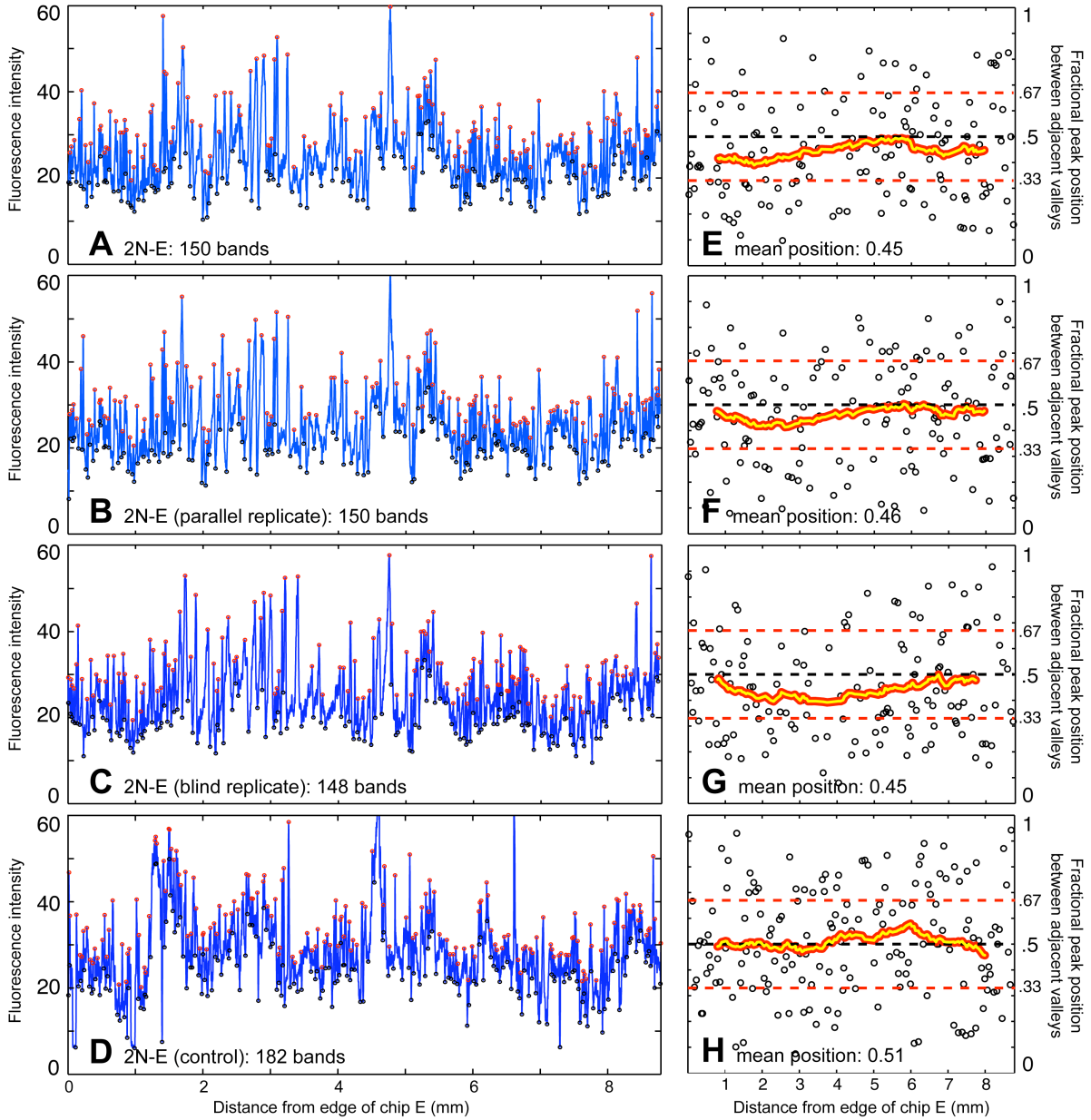

Data Repository Index

Large data tables and figures for each chapter are included in the supplementary files available with the online version of this dissertation.

DR4.1: Fluorescent images of sample 2N showing the tie-lines (yellow) used to generate fluorescence intensity profiles of each sample chip.

DR4.2: Fluorescence intensity values measured across each chip.

DR4.3: MATLAB code for `peakfinder_window`.

DR4.4: SEM images of ion microprobe pits from trace element analyses in sample 2N.

CHAPTER V

Otolith oxygen isotopes measured by high-precision secondary ion mass spectrometry reflect life history of a yellowfin sole (*Limanda aspera*)

Mary Elizabeth Matta[1], Ian J. Orland[2], Takayuki Ushikubo[2], Thomas E. Helser[1], Bryan A. Black[3], and John W. Valley[2]

[1]*Resource Ecology and Fisheries Management Division, Alaska Fisheries Science Center, National Marine Fisheries Service, National Oceanic and Atmospheric Administration, 7600 Sand Point Way NE, Seattle, WA 98115, USA*

[2]*WiscSIMS Laboratory, Department of Geoscience, University of Wisconsin-Madison, 1215 West Dayton Street, Madison, WI 53706, USA*

[3]*Hatfield Marine Science Center, Oregon State University, 2030 SE Marine Science Drive, Newport, OR 97365, USA*

Matta M. E., Orland I. J., Ushikubo T., Helser T. E., Black B. A., and Valley J. W. *in review*. Ototlith oxygen isotopes measured by high-precision secondary ion mass spectrometry reflect life history of a yellowfin sole (*Limanda aspera*).

Abstract

RATIONALE: The oxygen isotope ratio ($\delta^{18}O$) of aragonite fish otoliths is dependent on the temperature and $\delta^{18}O$ of ambient water and can thus reflect a fish's environmental history. Secondary ion mass spectrometry (SIMS) offers a spatial-resolution advantage over conventional acid-digestion techniques for stable isotope analysis of otoliths, especially given their compact nature.

METHODS: High-precision otolith $\delta^{18}O$ analysis was conducted with an IMS-1280 ion microprobe to investigate the life history of a yellowfin sole (*Limanda aspera*), a Bering Sea species known to migrate ontogenetically. The otolith was cut transversely through its core and one half was roasted to eliminate organic contaminants. Values of $\delta^{18}O$ were measured in 10-μm spots along three transects (two in roasted half, one in unroasted half) from the core toward the edge. Otolith annual growth zones were dated using the dendrochronology technique of crossdating.

RESULTS: Measured values of $\delta^{18}O$ ranged from 29.0-34.1‰ (relative to Vienna Standard Mean Ocean Water). Ontogenetic migration from shallow to deeper waters was reflected in generally increasing $\delta^{18}O$ values from age-0 to approximately age-7 and subsequent stabilization after the expected onset of maturity at age-7. Cyclical variations of $\delta^{18}O$ within juvenile otolith growth zones, up to 3.9‰ in magnitude, were caused by a combination of seasonal changes in the temperature and $\delta^{18}O$ of ambient water.

CONCLUSIONS: The IMS-1280 ion microprobe at WiscSIMS obtained a high-precision and high-resolution record of relative environmental conditions experienced by a yellowfin sole that is consistent with population-level studies of ontogeny. Furthermore, this study represents the first time crossdating has been used to ensure dating accuracy of $\delta^{18}O$ measurements in otoliths.

INTRODUCTION

Otoliths, paired calcified structures found within the inner ear of fish, have been widely used to study various aspects of fish ecology in marine and freshwater ecosystems (Campana and Thorrold, 2001; Mosegaard et al., 2002). Consisting of calcium carbonate (usually in the form of aragonite) precipitated over a protein matrix, otoliths accrete alternating concentric layers of opaque and translucent material around their cores, typically at a rate of one pair of layers, or a single annulus, per year. The seasonal deposition and contrasting optical properties of these layers (hereafter referred to as otolith growth zones) provide time-specific markers that have long been used by biologists to estimate fish age. In recent years, the relative widths of these growth zones have been used to develop biochronologies that reflect interannual variations in climate and ecosystem productivity (Black et al., 2008a, 2010; Rypel, 2009).

In addition to the visual properties of otoliths, chemical components may also be employed to reconstruct fish environmental and developmental histories (Campana, 1999; de Pontual and Geffen, 2002; Thorrold et al., 2007). Otoliths are well-suited for such applications given that they are acellular, metabolically inert, and grow from birth to death, all factors which allow the uptake and permanent retention of various elements and compounds (Campana, 1999; Campana and Thorrold, 2001). Isotope ratio analyses of oxygen, carbon, nitrogen, sulfur, lead, strontium, and boron have been applied in studies of fish trophic level, diet history, behavior, migration, thermal history, age validation, stock differentiation, and metabolism (Edmonds and Fletcher, 1997; Thorrold et al., 1998; Campana, 1999; Weidman and Millner, 2000; Weidel et al., 2007; Jones and Campana, 2009; Valley and Kita, 2009; Hanson et al., 2010). Specifically, the oxygen isotope composition ($\delta^{18}O$) of otolith aragonite is influenced by the temperature and isotopic composition of the ambient water, but is generally thought to be unaffected by

biological processes (Kalish, 1991; Thorrold et al., 1997; Campana, 1999; Høie et al., 2003). Due to the inverse relationship between $\delta^{18}O$ values and temperature, when measurements of otolith $\delta^{18}O$ are correlated with visible otolith growth zones they may provide a chronological record of a fish's thermal experience over its life history (Thorrold et al., 1997). Traditionally, $\delta^{18}O$ is measured using acid-digestion analytical methods, in which bulk samples weighing 0.01 to 10 mg are mechanically milled and homogenized into powders for analysis.

The relatively large sample mass necessary for high precision isotope analyses in gas-source mass spectrometers is a limitation in many otolith $\delta^{18}O$ studies. Given the compact nature of otoliths, providing sufficient sample mass while maintaining high temporal resolution of measurements is often difficult or impossible. Micro-milling, a method commonly used to extract otolith material for gas-source mass spectrometry, typically requires drilling continuously along a transect parallel to growth zones in order to obtain adequate $CaCO_3$ for analysis. Thus, these conventional analytical techniques often average isotopic information across multiple seasons or years (Valley and Kita, 2009). In contrast, secondary ion mass spectrometry (SIMS) has demonstrated marked improvements over conventional methods in temporal and spatial resolution of otolith $\delta^{18}O$ measurements (Weidel et al., 2007; Hanson et al., 2010). In particular, recent developments in the analytical capabilities of the IMS-1280, a focused ion beam coupled with a double-focusing mass spectrometer at the University of Wisconsin-Madison Secondary Ion Mass Spectrometer (WiscSIMS) ion microprobe laboratory, have allowed *in situ* analysis of otoliths on sub-annual, even daily, timescales (Weidel et al., 2007; Valley and Kita, 2009). The ion microprobe can analyze discrete samples that are less than one ten-thousandth of the mass required by conventional acid digestion/gas-source mass spectrometry (~1 ng vs. ≥ 10 μg). The increased spatial resolution of ion microprobe analyses (spot diameter = 10 μm with depth of ~1

μm) allows for finer temporal resolution of measurements while maintaining high accuracy and precision (Valley and Kita, 2009; Kita et al., 2009).

The analytical capabilities of the ion microprobe are particularly advantageous for characterizing the life history of fish that undertake ontogenetic migration; changes in the temperature and $\delta^{18}O$ of ambient water are recorded in the carbonate otolith as it grows. In this study, we analyze the otolith of a yellowfin sole (*Limanda aspera* Pallas, 1814), a common species in the eastern Bering Sea (EBS) that is the target of the largest flatfish fishery in the world (Wilderbuer et al., 2010). Population-level studies based on commercial catches and scientific surveys have demonstrated that juvenile yellowfin sole reside in shallow waters of the inner continental shelf (< 50 m) and gradually move deeper to waters of the middle and outer continental shelf (50-200 m) as they grow older (Bakkala, 1981; Wilderbuer et al., 1992; Nichol, 1997).

Recently, dendrochronology (tree-ring science) techniques were applied to the annulus widths of EBS yellowfin sole otoliths to develop an accurately dated, annually resolved biochronology (Matta et al., 2010). Central to any dendrochronology-based study is the concept that climate induces synchronous patterns of annulus width in all individuals from a given region. These synchronous patterns, which can be thought of as growth "bar codes", are matched among all sampled individuals using a technique called crossdating. Crossdating ensures that each annulus is assigned the correct calendar year of formation, subsequently allowing comparison of relative otolith growth with environmental variables and measures of ecosystem productivity over multi-year time scales. Given the high visual definition of their otolith growth zones and the synchronous growth pattern shared among individuals (Matta et al., 2010), modern

EBS yellowfin sole otolith annuli may be dated with a high degree of accuracy, thereby also allowing assignment of $\delta^{18}O$ measurements to the correct calendar year.

The main objective of the present study was to assess the feasibility of ion microprobe analysis as a tool to produce a detailed signature of otolith $\delta^{18}O$ measurements, thus revealing the environmental history of an individual EBS yellowfin sole in greater detail than would be allowed by conventional analyses. The WiscSIMS ion microprobe was used to measure $\delta^{18}O$ composition in a yellowfin sole otolith *in situ* at high spatial resolution to (1) generate a precise time series of $\delta^{18}O$ measurements from discrete samples within a single yellowfin sole otolith, with dating of $\delta^{18}O$ measurements verified through crossdating, (2) reconstruct the ontogenetic history of the fish based on otolith $\delta^{18}O$ measurements, and (3) assess relative intra- and inter-annual variability in $\delta^{18}O$ measurements.

EXPERIMENTAL

Otolith collection and preparation

An otolith pair was collected from a male yellowfin sole in the southeastern Bering Sea (56.7°N, 163.4°W; bottom depth = 74 m) during a standard National Marine Fisheries Service (NMFS) bottom trawl survey in June 2009 (Figure 5.1). This individual was selected for the present study due to the clarity of its otolith growth zones and its presumed old age, in order to increase the likelihood of observing the $\delta^{18}O$ signal of ontogenetic migration. The otoliths were preserved at sea in glycerol-thymol solution and returned to the laboratory where they were rinsed in distilled water and air-dried.

The left otolith was cut transversely through its core. One otolith half was placed in a small Pyrex cup and roasted in a 0.5 mTorr vacuum at 360°C for 2.5 hours to eliminate organic

materials that could contaminate spot samples. Roasting also allowed better contrast between opaque and translucent growth zones, a necessity for age determination (Matta and Kimura, 2012). The other otolith half was left unroasted for comparison of $\delta^{18}O$ values. Both otolith halves were cast in an epoxy resin, cut into separate blocks, and ground to the analytical surface using a 6 μm diamond mesh. After grinding, each otolith half was recast near the center of a 25 mm-diameter epoxy mount along with three grains of calcite standard UWC-3 (Kozdon et al., 2009) and polished to a smooth flat surface using a sequence of 6, 3, and 1 μm diamond pastes (Figure 5.2).

Total age was estimated to be 28 years from counting annuli (growth-zone pairs) visible on the roasted otolith cross section (Matta and Kimura, 2012). The age at maturity for this specimen was estimated to be 7 years based on published reports of maturity for male yellowfin sole (Wilderbuer et al., 1992) as well as the appearance of the growth zones, which became compressed after age-7 (i.e., the calendar year 1988; Figure 5.2A), possibly due to a slowing of growth following maturity (Francis and Horn, 1997; Geffen et al., 2002).

To ensure dating control of annuli in the otolith examined here, we visually and statistically related its annulus widths to an existing yellowfin sole biochronology that spans 1989 through 2006, and was generated from the otoliths of 21 EBS yellowfin sole collected during the 2008 NMFS bottom trawl survey (Matta et al., 2010). First, the growth pattern in the roasted cross section of the $\delta^{18}O$ otolith was crossdated by visual comparison with the published yellowfin sole biochronology (Matta et al., 2010). Next, the otolith was photographed and annulus widths were measured along the dorsal side of the sulcus near the location of Transect A. The axis of measurement was parallel to the direction of growth and one complete annulus was defined as the distance from the distal side of the previous year's translucent zone to the

distal side of the current year's translucent zone (Matta et al., 2010). The widths of the first four annuli were not measured due to difficulties in fitting a measurement axis through them. Crossdating was then statistically verified using the dendrochronology program COFECHA (Holmes, 1983; Grissino-Mayer, 2001). In COFECHA, each of the 21 otolith measurement time series from the original biochronology as well as the otolith measurement time series from the $\delta^{18}O$ otolith was fit with a cubic spline with a 50% frequency cutoff set at 15 years (Black et al., 2005; Black, 2009). Measurements were divided by the values predicted by the spline, thereby removing long-term trends including age-related growth declines and standardizing each time series to a mean of 1. A significant correlation between the $\delta^{18}O$ otolith and the average of all others corroborates that the synchronous growth pattern has been correctly identified and that each growth increments has been assigned the correct calendar year of formation.

Secondary ion mass spectrometry

Otolith oxygen isotope ratios were measured *in situ* from 10 μm spots using the CAMECA IMS-1280 large radius, multi-collector ion microprobe at the WiscSIMS Laboratory, University of Wisconsin-Madison. Before ion microprobe analysis, the polished epoxy round was cleaned with successive, 30-second sonication sessions in ethanol and distilled water, then dried in a vacuum oven at 40°C for 2.5 hours. The epoxy mount was then gold-coated with a coating thickness of ~60 nm and imaged with a reflected-light microscope for mapping purposes.

Each ion microprobe spot was sputtered by a ~1.7 nA primary beam of $^{133}Cs^{+}$ ions with a total accelerating voltage of 20 kV, focused to ~10 μm diameter at the sample surface. Both the gold coating applied to the sample surface as well as a normal-incidence electron flood gun prevented charging of the sample surface. The primary beam sputtered a ~1-μm-deep pit over the

course of each 4-minute analysis, which included choosing the analysis location (1-2 min), pre-sputtering (10 sec), automated centering of the secondary ion beam (90 sec), and 20 analytical cycles (80 sec). Secondary ions were accelerated by 10 kV into a double-focusing mass spectrometer that was configured to achieve high secondary-ion transmission (Kita et al., 2009). Average secondary-ion intensity ($^{16}O^-$ ion) during sample analyses was 2.7 x 10^9 cps. The mass resolving power for $\delta^{18}O$ measurements was 2200, which permitted separation of hydride interferences on ^{18}O; $^{16}O^-$ and $^{18}O^-$ ions were counted simultaneously on two Faraday cups (L1 and H1, respectively) in multicollection mode. Sample analyses were grouped in blocks of 10-15 and bracketed by eight analyses of UWC-3 calcite standard ($\delta^{18}O$ = 12.49‰ Vienna Standard Mean Ocean Water VSMOW; Kozon et al., 2009). This standard-sample-standard bracketing technique is used to correct for instrumental mass fractionation (bias) and to calculate the spot-to-spot precision of sample analyses (Kita et al., 2009; Kozdon et al., 2009; Orland et al., 2009). The average spot-to-spot precision measured during the analytical session was ±0.3‰ (2 standard deviations, S.D.).

Further description of WiscSIMS analytical methodology is discussed elsewhere (Kita et al., 2009; Orland et al., 2009; Valley and Kita, 2009). For this study, we compared relative values of $\delta^{18}O$, with no correction for any small differences in instrument bias for $\delta^{18}O$ between the calcite standard and aragonite otolith. All $\delta^{18}O$ values are reported here in permil (‰) relative to VSMOW. For raw $\delta^{18}O$ measurements and data reported on the Vienna Pee Dee Belemnite (VPDB) scale, please see the data repository (DR5.1).

Two transects, A and B, were analyzed for $\delta^{18}O$ in the roasted otolith cross section (Figure 5.2A). Transect A ran from the otolith's core (center) to its edge parallel to the sulcus, a prominent groove on the proximal side of the otolith. This area is a standard axis used to

enumerate annuli during routine age estimation (Matta and Kimura, 2012). Transect B was directed through the widest part of the first 10 annuli with the intent of capturing as much seasonal variability as possible during the juvenile and early adult life stages. A single transect in the unroasted cross section (Transect C), approximately parallel to Transect A in the roasted cross section, was analyzed to evaluate the effects of roasting (Figure 5.2B). Whenever possible, multiple samples were acquired within a single otolith annulus to capture seasonal trends in $\delta^{18}O$. The integrity of the polished otolith surface was verified post-analysis through scanning electron microscopy (SEM) to ensure no analysis pits contained contaminants or irregular surface topography that could bias $\delta^{18}O$ values (Weidel et al., 2007). In order to evaluate variability in measured oxygen isotope ratios in contemporaneously formed aragonite, a series of samples immediately adjacent to a single translucent growth zone in the roasted otolith cross section was analyzed (calendar year 2003; analyses 10, 152-158; Figure 5.2A).

RESULTS AND DISCUSSION

Otolith $\delta^{18}O$ measurements

A total of 73 spot analyses of $\delta^{18}O$ was acquired over Transect A, which spanned the years 1981 through 2007 (Figure 5.2A). No analyses were attempted in the growth band for 2008 as it was too narrow and close to the edge of the otolith. The number of 10-µm-diameter spot samples per annulus within Transect A ranged from 1 to 7. Transect B spanned the years 1981 through 1989, and the number of spot samples per annulus ranged from 3 to 23 (total n = 78; Figure 5.2A). The linear sampling density of both Transects A and B was approximately 50 spot analyses per mm. In the unroasted half of the otolith, a total of 45 spot samples was acquired along Transect C spanning the years 1981 through 2007 (Figure 5.2B). The number of spots per

annulus in Transect C ranged from 0 to 11. The linear sampling density of Transect C was approximately 38 spot analyses per mm.

In all three transects, multiple spot samples were taken per annulus prior to estimated maturity (age-7) to assess seasonal trends in $\delta^{18}O$. Due to compression of the annuli following age-7, several annuli in Transect A only had one associated spot sample (years 1988, 1989, 1992-1995, 1999, 2000, and 2006), and several calendar years in Transect C (1989, 2000-2003) were not sampled for $\delta^{18}O$. Yellowfin sole otoliths have extremely narrow translucent growth zones, and thus most of the spot samples were taken within opaque growth zones for all three transects.

Measured values of $\delta^{18}O$ ranged from 29.0 to 34.1‰ VSMOW (Figure 5.3) with average spot-to-spot reproducibility (2 S.D.) of ±0.3‰ in homogenous standards. Spot samples were checked by SEM for inclusions, porosity, and cracks; the integrity of each spot was verified and all analyses are included in the plots and interpretations presented here. Comparison of Transects A and B ($\delta^{18}O$ values averaged by year; Figure 5.3 bottom panel) revealed no significant difference ($t = 0.28$, $df = 16$, $P = 0.78$), indicating that growth axis (i.e., otolith accretion rate) did not affect $\delta^{18}O$ values. Spot samples taken immediately proximal to a single translucent growth zone to examine the variability of measured $\delta^{18}O$ values in contemporaneous growth ranged from 33.2 to 33.9‰ ($n = 8$; mean = 33.5‰, 2 S.D. = 0.4‰; Figure 5.4) with nearly the same precision as attained for the UWC-3 standard.

Annual resolution of life history provided by $\delta^{18}O$ values

Mean annual $\delta^{18}O$ values generally increased from the otolith center (age-0) until approximately age-7 (Figure 5.3), corresponding roughly to the age at maturity for male

yellowfin sole (Wilderbuer et al., 1992), after which $\delta^{18}O$ values were relatively stable. Because of the inverse relationship between $\delta^{18}O$ and temperature, the observed otolith $\delta^{18}O$ values suggest that this individual experienced an overall decrease in ambient temperatures from birth until maturity. This trend reflects the gradual ontogenetic migration yellowfin sole are known to make from shallow to deeper waters (Bakkala, 1981; Wilderbuer et al., 1992; Nichol, 1997). Similar lifetime patterns in $\delta^{18}O$ values have been documented for Pacific halibut (*Hippoglossus stenolepis*), a species also known to make an ontogenetic migration from shallow to deeper offshore waters (Gao and Beamish, 2003).

Sub-annual sampling was optimized in Transect B (Figure 5.3), which was directed through the widest part of the first 10 annuli. Within each annulus, the highest observed $\delta^{18}O$ values corresponded to the earliest deposited part of the opaque growth zone, and translucent growth zone formation coincided with or occurred soon after $\delta^{18}O$ minima (Figure 5.3). Within the juvenile portion of the otolith, sub-annual sampling revealed a recurring saw-toothed pattern of $\delta^{18}O$ values (Figure 5.3). Records of bottom temperatures from the Mooring 2 buoy (57°N, 164°W) in the middle domain of the EBS (Figure 5.1) share a similar saw-toothed pattern of slow warming and rapid cooling (Ladd, unpublished data). Thus, the saw-toothed pattern in otolith $\delta^{18}O$ values may reflect temperatures experienced on a small spatial scale, given that most juvenile yellowfin sole are believed to remain within the shallow waters of the inner continental shelf throughout the year (Bakkala, 1981; Wilderbuer et al., 1992; Nichol, 1997). The saw-toothed pattern is likely amplified by annual slowing or stopping of otolith growth during the colder months of the year when the narrow translucent growth zones form (December-May; Wakabayashi, 1989). Translucent zones in yellowfin sole otoliths are extremely narrow, and consequently most of our sampling occurred within the opaque zones, likely reflecting

environmental conditions experienced June-November. However, factors such as age, geographic region, and depth can influence individual otolith deposition rates (Kimura et al., 2007). Clearly, further studies of growth mechanisms and effects on uptake of $\delta^{18}O$ in yellowfin sole otoliths that account for these factors are warranted.

As is the case in most studies of oxygen isotope ratios in biogenic carbonate, the exact $\delta^{18}O$ of the ambient water encountered by this yellowfin sole is uncertain. Furthermore, an oxygen isotope fractionation equation does not currently exist for yellowfin sole; other studies have demonstrated that fractionation is species-specific (Høie et al., 2004). Thus, it is more practical to consider relative temperature changes experienced by this fish than to directly predict temperature from otolith $\delta^{18}O$ values. Below, we provide a brief outline of the variability in EBS $\delta^{18}O$ values in order to constrain our interpretation of relative temperatures from otolith $\delta^{18}O$ values.

The primary control on EBS water $\delta^{18}O$ variability is the fractional amount of runoff-sourced freshwater (negative $\delta^{18}O$ values, VSMOW) mixed into the seawater (~0‰, VSMOW). Thus, salinity is commonly used as a proxy for water $\delta^{18}O$. Within the Bering Sea, salinity can vary locally and seasonally (Stabeno et al., 2001; Tanaka et al., 2004). In particular, shallow coastal areas can be influenced by meltwater or continental freshwater runoff. Annual variability of inshore surface water salinity in the southeastern Bering Sea is as much as 3 parts per thousand (ppt); salinity is at its minimum in July due to river flow (Luchin et al., 1999). Salinity is far less variable (< 1 ppt) in the middle and outer domains of the EBS (Luchin et al., 1999). A decrease of 1‰ in ambient $\delta^{18}O$ in the Bering-Chukchi Sea region would correlate to a decrease in salinity of ~1.6 ppt (Yamamoto-Kawai et al., 2010), which is representative of the relatively shallow (< 50 m) coastal waters where juvenile yellowfin sole reside. Because freshening

occurred at shallow depths when water temperatures were highest, the resulting effect in the otolith would be a ~1‰ increase in the amplitude of the seasonal $\delta^{18}O$ signal.

The maximum range of $\delta^{18}O$ values observed within a single annulus was 3.9‰ (during the fish's second year), which, not taking ambient water $\delta^{18}O$ into account, translates into a range of experienced temperatures of approximately 18°C (Campana, 1999). Bottom temperatures below pack ice in the EBS are typically around -1.8°C, the freezing point of seawater, but during the summer months temperatures increase to 10°C or greater in shallow, well-mixed nearshore areas where juvenile yellowfin sole reside (Bakkala, 1981). A temperature range of 12°C would result in an aragonite $\delta^{18}O$ range of 2.8‰. The combined effects of temperature and the suggested 1‰ increase in $\delta^{18}O$ amplitude due to seasonal freshwater input could fully explain the $\delta^{18}O$ variation observed in the yellowfin sole otolith. Thus, our conclusions regarding the relative importance of temperature in explaining the overall observed trends in otolith $\delta^{18}O$ are valid.

In contrast to the highly variable juvenile phase, adult-phase otolith $\delta^{18}O$ values were much more stable over time. This stability could be explained in part by the temporal resolution of analysis spots in the outer annuli; the rate of otolith growth dramatically slowed after maturity, resulting in narrower annuli and potentially smoothing measurements of $\delta^{18}O$ variability. Alternatively, the $\delta^{18}O$ pattern in adult-phase annuli may have also been dampened by seasonal migrations between the inner and outer shelf; adults overwinter in outer continental shelf waters (100-270 m deep) and move to depths < 100 m to spawn and feed during the summer months (Bakkala, 1981; Wakabayashi, 1989; Wilderbuer et al., 1992; Bakkala, 1993). Adults appear to avoid ice cover and colder water temperatures associated with the inner and middle shelf waters during the winter months (Bakkala, 1981), and thus the relatively stable $\delta^{18}O$ values could reflect

active seeking of less variable ambient conditions. Overall, the otolith $\delta^{18}O$ profiles reflect the cyclical variability of seasonal temperatures, slightly amplified by seasonal freshwater input (Transect B), as well as longer-term habitat changes as the fish approached maturity (Transect A). Published population-level studies of yellowfin sole ontogenetic and seasonal movements lend further support to our interpretations of the $\delta^{18}O$ pattern (Bakkala, 1981; Wakabayashi, 1989).

Dating controls of $\delta^{18}O$ measurements

After detrending with cubic splines, the $\delta^{18}O$ otolith growth-increment widths (1985-2007) correlated strongly ($r = 0.62$, $P = 0.006$) with the average growth pattern from the 21 individuals used to develop the previously published EBS master chronology (Matta et al., 2010). Furthermore, the detrended $\delta^{18}O$ otolith growth-increment measurements strongly and positively ($r = 0.73$, $P < 0.001$) correlated to average summer bottom temperatures recorded during trawl surveys (NOAA, 2012). Thus, the growth pattern of the otolith analyzed here was consistent with other EBS yellowfin sole (Matta et al., 2010), providing a statistical corroboration of annulus dating (Black et al., 2008b), and by proxy, $\delta^{18}O$ spot sample dating. Due to lingering uncertainties about otolith accretion phenology in yellowfin sole, it was not possible to date $\delta^{18}O$ spots on a sub-annual scale, and thus, $\delta^{18}O$ measurements could not be directly compared to climate indices or increment width. However, dendrochronology-based dating controls allowed direct comparison of properties of the otolith with observational environmental records at the annual timestep. To ensure accuracy, we recommend that crossdating be a fundamental step of any sclerochronology analysis whenever annuli are

sufficiently well defined for mensuration and growth is synchronous among individuals from a given species and site.

Effects of roasting

Roasting resulted in an increase of approximately 1‰ in the raw value of $\delta^{18}O$ as compared to the unroasted sample, but did not change $\delta^{18}O$ trends (Figure 5.5). Conventional acid-digestion analyses of otoliths sometimes use roasting as a means to remove organic contaminants, and a shift in measured $\delta^{18}O$ values is expected (Guiguer et al., 2003). For this reason, we report the $\delta^{18}O$ values from the roasted otolith portion on the VSMOW scale. Preliminary (unpublished; DR5.2) *in situ* XRD analyses at UW-Madison, however, suggest that roasting converted some otolith aragonite to calcite, an unstudied effect in ion microprobe analyses. Since roasting is an imperfect solution to the removal of organic material from otolith analyses, we avoid interpreting absolute temperatures from values of $\delta^{18}O$. Notably, however, the similar trend of $\delta^{18}O$ values in both roasted and unroasted transects (Figure 5.5) suggests that our interpretations of relative temperatures from $\delta^{18}O$ values are valid.

Advantages of SIMS

The high spatial resolution of the ion microprobe allowed multiple sequential samples to be taken, often within a single year, to effectively describe the general ontogeny of an individual fish. This is the first case we know of where so many $\delta^{18}O$ analyses have been performed for a single individual, with measurements taken sub-annually over a time span of 27 years. In contrast, most conventional $\delta^{18}O$ studies have been directed at juveniles or short-lived fish with large otoliths, possibly in part due to limitations in spatial sample resolution. Yellowfin sole

otoliths are relatively small, and the individual in our study was extremely old. Had we directed our study at a species such as Pacific cod (*Gadus macrocephalus*), which has large otoliths and low longevity, even greater temporal resolution of $\delta^{18}O$ analyses could have been achieved (Valley and Kita, 2009).

Future applications

The present study was designed to explore the detailed information recorded by a single otolith and while such information may prove fundamental for understanding the life cycle of one fish, it was not intended to be used to make population-level inferences. However, based on this work, future studies can obtain the same level of information with far fewer analyses. Population-level studies focused on early life histories should consider transects similar to our Transect B, which maximized the number of potential $\delta^{18}O$ measurements obtainable by traversing the widest part of each annulus. Conversely, those studies interested in overall lifelong variation would be best suited by core-to-edge transects such as our Transect A. Furthermore, researchers should consider placement of spot analyses relative to growth zone borders. Potential variation would be maximized and the number of analyses minimized by sampling the distal edge of each translucent zone and several spots evenly distributed across each opaque zone.

CONCLUSIONS

Otolith $\delta^{18}O$ values obtained via ion microprobe provide an indicator of the relative environmental conditions to which a yellowfin sole was exposed during its lifetime in the EBS. The combined spatial resolution (10 μm spot diameter), sampling density (~50 discrete spots per mm in the roasted transect), and precision (0.3‰, 2 S.D.) achieved in this study reveal new

information about both ontogeny of a long-lived individual and annual variability in $\delta^{18}O$ that could not have been attained by conventional micro-mill techniques. Overall, the apparent ontogenetic and seasonal trends in observed otolith $\delta^{18}O$ values are consistent with population-level work on yellowfin sole movements (Bakkala, 1981; Wakabayashi, 1989; Wilderbuer et al., 1992; Nichol, 1997). Though the $\delta^{18}O$ composition of the ambient water was uncertain, evidence suggests that temperature played a primary role in controlling otolith $\delta^{18}O$ values and was largely responsible for the relative variation observed. A unique aspect of this study was the use of crossdating in conjunction with highly precise *in situ* measurements of $\delta^{18}O$ to ensure that all growth zones and $\delta^{18}O$ spot samples were assigned the correct calendar year of formation. These results demonstrate that $\delta^{18}O$ analysis with an ion microprobe is a useful tool in hindcasting detailed life histories of individual fish. Given sufficient resources, the ion microprobe can also be used to make population-level inferences regarding large-scale migrations, often poorly understood for many species of fish.

Acknowledgements

We thank Carla Stehr (retired, Northwest Fisheries Science Center, NOAA) for otolith scanning electron microscopy, Brian Hess (UW-Madison) for ion microprobe sample preparation, and Mike Spicuzza (UW-Madison) for vacuum-roasting assistance. Craig Kastelle, Dan Nichol, and Tom Wilderbuer (Alaska Fisheries Science Center, NOAA) and Michael Hoopmann (Institute for Systems Biology) provided constructive reviews of earlier versions of this manuscript. This research was supported by DOE (93ER14389) and NSF-EAR (0628719, 0838058). WiscSIMS is partly supported by NSF-EAR (0319230, 0744079, 1053466). The

findings and conclusions in the paper are those of the authors and do not necessarily represent the views of the National Marine Fisheries Service, NOAA.

References

Bakkala R. G. (1981) Population characteristics and ecology of yellowfin sole. In 'The Eastern Bering Sea Shelf: Oceanography and Resources'. Vol. 1. (Eds D. W. Hood and J. A. Clader.) pp. 553–574. (US Department of Commerce, NOAA: Washington, DC.)

Bakkala R. G. (1993) Structure and historical changes in the groundfish complex of the eastern Bering Sea. NOAA Technical Report NMFS 114, 91 p.

Black B. A. (2009) Climate-driven synchrony across tree, bivalve, and rockfish growth-increment chronologies of the northeast Pacific. *Mar. Ecol. Prog. Ser.* **378**, 37–46.

Black B. A., Boehlert G. W., and Yoklavich M. M. (2005) Using tree-ring crossdating techniques to validate annual growth increments in long-lived fishes. *Can. J. Fish. Aq. Sci.* **62**, 2277–2284.

Black B. A, Boehlert G. W., and Yoklavich M. M. (2008a) Establishing climate-growth relationships for yelloweye rockfish (*Sebastes ruberrimus*) in the northeast Pacific using a dendrochronological approach. *Fish. Ocean.* **17**, 368–379.

Black B. A., Gillespie D. C., MacLellan S. E., and Hand C. M. (2008b) Establishing highly accurate production-age data using the tree-ring technique of crossdating: a case study for Pacific geoduck (*Panopea abrupta*). *Can. J. Fish. Aq. Sci.* **65**, 2572–2578.

Black B. A., Schroeder I. D., Sydeman W. J., Bograd S. J., and Lawson P. W. (2010) Wintertime ocean conditions synchronize rockfish growth and seabird reproduction in the central California Current ecosystem. *Can. J. Fish. Aq. Sci.* **67**, 1149–1158.

Campana S. E. (1999) Chemistry and composition of fish otoliths: pathways, mechanisms and applications. *Mar. Ecol. Prog. Ser.* **188**, 263–297.

Campana S. E., and Thorrold S. R. (2001) Otoliths, increments, and elements: keys to a comprehensive understanding of fish populations? *Can. J. Fish. Aq. Sci.* **58**, 30–38.

de Pontual H., and Geffen A. J. (2002) Otolith microchemistry. In 'Manual of Fish Sclerochronology'. (Eds J. Panfili, H. de Pontual, H. Troadec and P. J. Wright.) pp. 245–302. (Ifremer-IRD: Brest, France.)

Edmonds J. S., and Fletcher W. J. (1997) Stock discrimination of pilchards *Sardinops sagax* by stable isotope ratio analysis of otolith carbonate. *Mar. Ecol. Prog. Ser.* **152**, 241–247.

Francis R. I. C. C., and Horn P. L. (1997) Transition zone in otoliths of orange roughy (*Hoplostethus atlanticus*) and its relationship to the onset of maturity. *Mar. Biol.* **129**, 681–687.

Gao Y., and Beamish R. J. (2003) Stable isotope variations in otoliths of Pacific halibut (*Hippoglossus stenolepis*) and indications of the possible 1990 regime shift. *Fish. Res.* **60**, 393–404.

Geffen A. J., de Pontual H., Wright P. J., and Mosegaard H. (2002) Life history events. In 'Manual of Fish Sclerochronology'. (Eds J. Panfili, H. de Pontual, H. Troadec and P. J. Wright.) pp. 99–104. (Ifremer-IRD: Brest, France.)

Grissino-Mayer H. D. (2001) Evaluating crossdating accuracy: a manual and tutorial for the computer program COFECHA. *Tree-Ring Res.* **57**, 205–221.

Guiguer K. R. R. A., Drimmie R., and Power M. (2003) Validating methods for measuring $\delta^{18}O$ and $\delta^{13}C$ in otoliths from freshwater fish. *Rap. Comm. Mass Spec.* **17**, 463–471.

Hanson N. N., Wurster C. M., E. I. M. F., and Todd C. D. (2010) Comparison of secondary ion mass spectrometry and micromilling/continuous flow isotope ratio mass spectrometry

techniques used to acquire intra-otolith $\delta^{18}O$ values of wild Atlantic salmon (*Salmo salar*). *Rap. Comm. Mass Spec.* **24**, 2491–2498.

Høie H., Folkvord A., and Otterlei E. (2003) Effect of somatic and otolith growth rate on stable isotopic composition of early juvenile cod (*Gadus morhua* L) otoliths. *J. Exper. Mar. Biol. Ecol.* **289**, 41–58.

Høie H., Otterlei E., and Folkvord A. (2004) Temperature-dependent fractionation of stable oxygen isotopes in otoliths of juvenile cod (*Gadus morhua* L.) *ICES J. Mar. Sci.* **61**, 243–251.

Holmes R. L. (1983) Computer-assisted quality control in tree-ring dating and measurement. *Tree-Ring Bull.* **43**, 69–78.

Jones J. B., and Campana S. E. (2009) Stable oxygen isotope reconstruction of ambient temperature during the collapse of a cod (*Gadus morhua*) fishery. *Ecol. Apps.* **19**, 1500–1514.

Kalish J. E. (1991) ^{13}C and ^{18}O isotopic disequilibria in fish otoliths: metabolic and kinetic effects. *Mar. Ecol. Prog. Ser.* **75**, 191–203.

Kimura D. K., Anderl D. M., and Goetz B. J. (2007) Seasonal marginal growth on otoliths of seven Alaska groundfish species support the existence of annual patterns. *Alaska Fish. Res. Bull.* **12**, 243–251.

Kita N. T., Ushikubo T., Fu B., and Valley J. W. (2009) High precision SIMS oxygen isotope analyses and the effect of sample topography. *Chem. Geol.* **264**, 43–57.

Kozdon R., Ushikubo T., Kita N. T., Spicuzza M., and Valley J. W. (2009) Intratest oxygen isotope variability in planktonic foraminifera: new insights from in situ measurements by ion microprobe. *Chem. Geol.* **258**, 327–337.

Ladd C., Unpublished data. Pacific Marine Environmental Laboratory, National Oceanic and Atmospheric Administration, Seattle, WA.

Luchin V. A., Menovshchikov V. A., and Lavrentiev V. M. (1999) Thermohaline structure and water masses in the Bering Sea. In 'Dynamics of the Bering Sea'. (Eds T. R. Loughlin and K. Ohtani K.) pp. 61–91. (University of Alaska Sea Grant: Fairbanks, AK.)

Matta M. E., and Kimura D. K. (2012) Age determination manual of the Alaska Fisheries Science Center Age and Growth program. *NOAA Professional Paper NMFS* **13**.

Matta M. E., Black B. A., and Wilderbuer T. K. (2010) Climate-driven synchrony in otolith growth-increment chronologies for three Bering Sea flatfish species. *Mar. Ecol. Prog. Ser.* **413**, 137–145.

Mosegaard H., Folkvord A., and Wright P. J. (2002) Ecological applications. In 'Manual of Fish Sclerochronology'. (Eds J. Panfili, H. de Pontual, H. Troadec and P. J. Wright.) pp. 167–178. (Ifremer-IRD: Brest, France.)

Nichol D. G. (1997) Effects of geography and bathymetry on growth and maturity of yellowfin sole, *Pleuronectes asper*, in the eastern Bering Sea. *Fish. Bull.* **95**, 494–503.

Nichol D. G. (1998) Annual and between-sex variability of yellowfin sole, *Pleuronectes asper*, spring-summer distributions in the eastern Bering Sea. *Fish. Bull.* **96**, 547–561.

NOAA (2012) 'Bering Climate: A Current View of the Bering Sea Ecosystem and Climate.' Available at http://www.beringclimate.noaa.gov. (accessed December 4, 2012)

Orland I. J., Bar-Matthews M., Kita N. T., Ayalon A., Matthews A., and Valley J. W. (2009) Climate deterioration in the eastern Mediterranean from 200 BC to 1100 AD as revealed by ion microprobe analysis of speleothems from Soreq Cave, Israel. *Quat. Res.* **71**, 27–35.

Rypel A. L. (2009) Climate-growth relationships for largemouth bass (*Micropterus salmoides*) across three southeastern USA states. *Ecol. Fresh. Fish* **18**, 620–628.

Stabeno P. J., Bond N. A., Kachel N. B., Salo S. A., and Schmuacher J. D. (2001) On the temporal variability of the physical environment over the south-eastern Bering Sea. *Fish. Ocean.* **10**, 81–98.

Tanaka T., Laodong G., Deal C., Tanaka N., Whitledge T., and Murata A. (2004) N deficiency in a well-oxygenated cold bottom water over the Bering Sea shelf: influence of sedimentary denitrification. *Cont. Shelf Res.* **24**, 1271–1283.

Thorrold S. R., Campana S. E., Jones C. M., and Swart P. K. (1997) Factors determining $\delta^{13}C$ and $\delta^{18}O$ fractionation in aragonitic otoliths of marine fish. *Geochim. Cosmochim. Acta* **61**, 2909–2919.

Thorrold S. R., Jones C. M., Swart P. K., and Targett T. E. (1998) Accurate classification of juvenile weakfish *Cynoscion regalis* to estuarine nursery areas based on chemical signatures in otoliths. *Mar. Ecol. Prog. Ser.* **173**, 253–265.

Thorrold S. R., Zacherl D. C., and Levin L. A. (2007) Population connectivity and larval dispersal using geochemical signatures in calcified structures. *Oceanography* **20**, 80–89.

Valley J. W., and Kita N. T. (2009) *In situ* oxygen isotope geochemistry by ion microprobe. In 'Secondary Ion Mass Spectrometry in the Earth Sciences'. (Ed M. Fayek.) pp. 19–63. (Mineralogical Association of Canada Short Course 41: Toronto, Ontario, Canada.)

Wakabayashi K. (1989) Studies on the fishery biology of yellowfin sole in the eastern Bering Sea [in Japanese, English summary]. *Bull. Far Seas Fish. Res. Lab.* **26**, 21–152.

Weidel B. C., Ushikubo T., Carpenter S. R., Kita N. T., Cole J. J., Kitchell J. F., Pace M. L., and Valley J. W. (2007) Diary of a bluegill (*Lepomis macrochirus*): daily $\delta^{13}C$ and $\delta^{18}O$ records in otoliths by ion microprobe. *Can. J. Fish. Aq. Sci.* **64**, 1641–1645.

Weidman C. R., and Millner R. (2000) High-resolution stable isotope records from North Atlantic cod. *Fish. Res.* **46**, 327–342.

Wilderbuer T. K., Walters G. E., and Bakkala R. G. (1992) Yellowfin sole, *Pleuronectes asper*, of the eastern Bering Sea: biological characteristics, history of exploitation, and management. *Mar. Fish. Rev.* **54**, 1–18.

Wilderbuer T. K., Nichol D. G., and Ianelli J. (2010) Yellowfin sole. In 'Stock Assessment and Fishery Evaluation Report for the Groundfish Resources of the Bering Sea/Aleutian Islands Regions'. pp. 565–644. (North Pacific Fishery Management Council: Anchorage, AK.)

Yamamoto-Kawai M., Carmack E. C., McLaughlin F. A., and Falkner K. K. (2010) Oxygen isotope ratio, barium, and salinity in waters around the North American coast from the Pacific to the Atlantic: implications for freshwater sources to the Arctic throughflow. *J. Mar. Res.* **68**, 97–117.

Figures

Figure 5.1: Summer 2009 distribution of yellowfin sole (catch per unit effort, CPUE, in number per hectare), capture location of $\delta^{18}O$ specimen (star; 74 m depth), and oceanographic buoy Mooring 2 (flag). Bathymetric contour lines (50 and 100 m) delineate oceanic domains (inner, middle, outer continental shelf). Data source: National Marine Fisheries Service eastern Bering Sea summer bottom trawl survey, 2009.

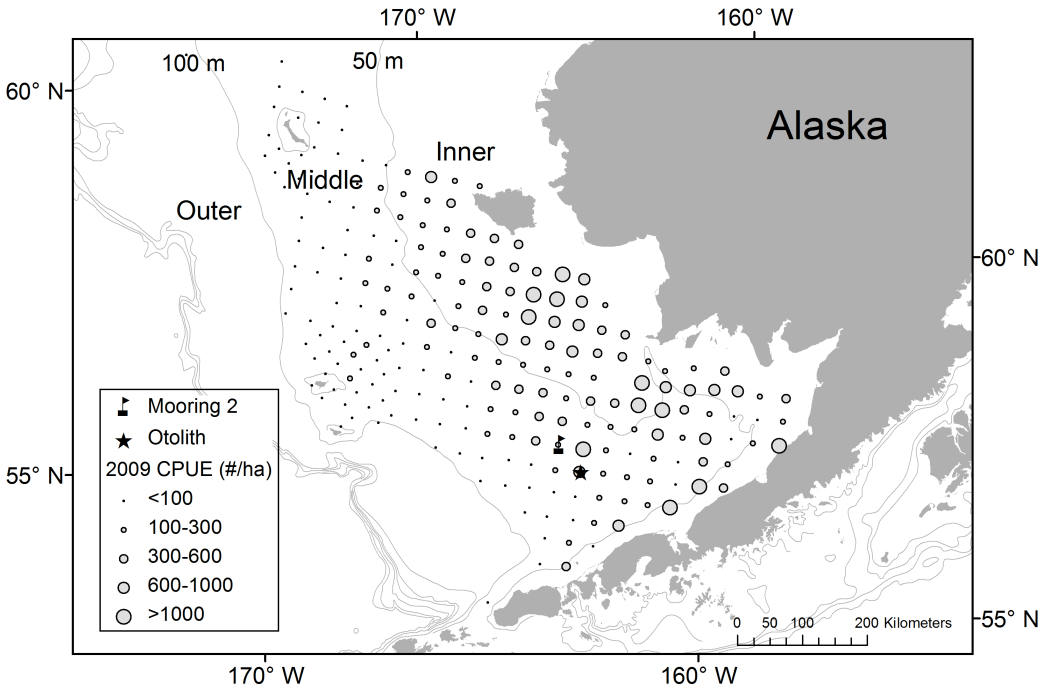

Figure 5.2: Composite photographs of polished surfaces of matching (**A**) roasted and (**B**) unroasted yellowfin sole otolith cross sections labeled with $\delta^{18}O$ spot analysis locations (white numbering) and calendar year assignments (black numbering) for each transect. Inset: Roasted (darker) and unroasted otolith halves embedded in epoxy mount. Oxygen isotope ratios for each spot analysis are available in the data repository (DR5.1).

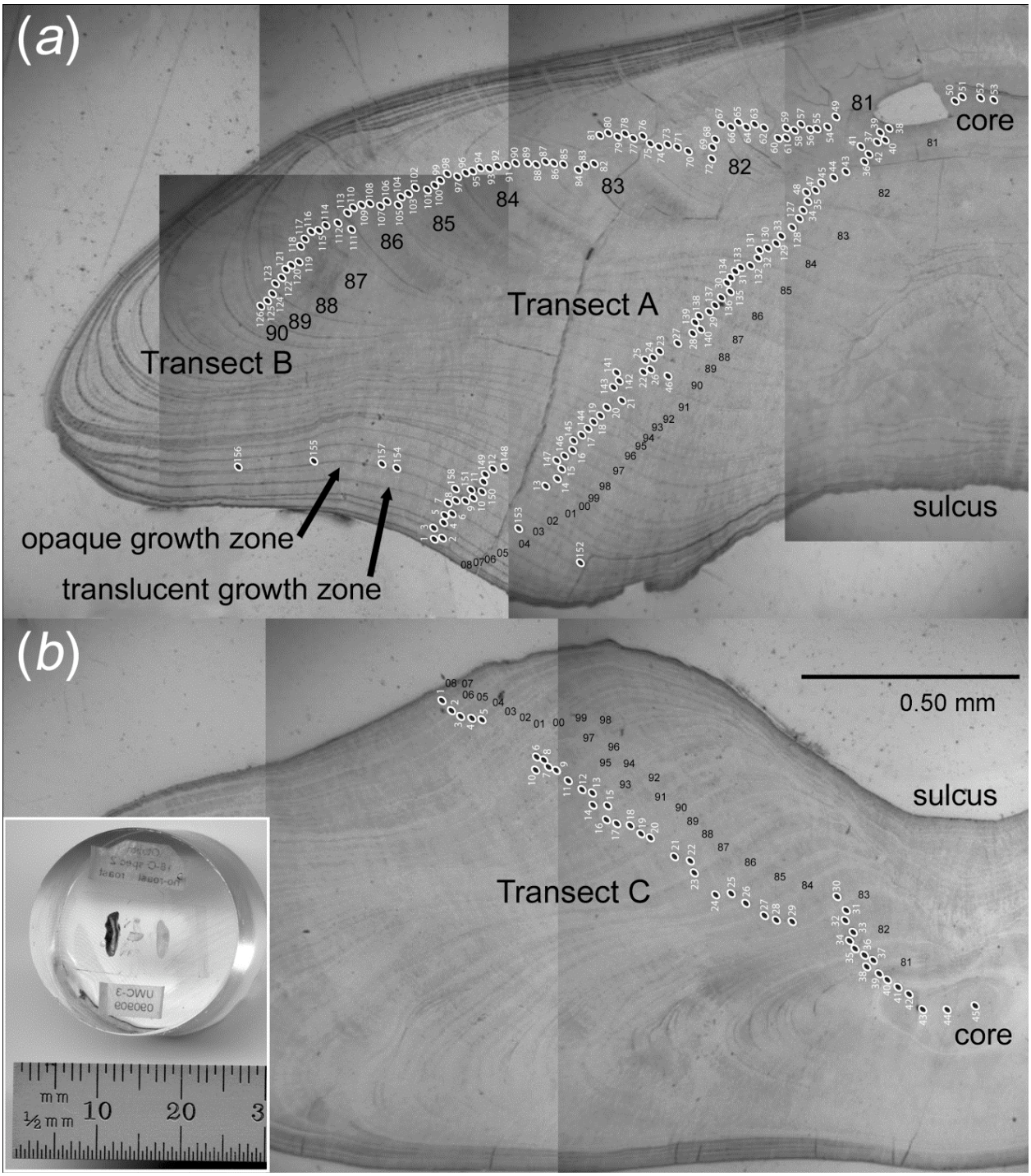

Figure 5.3 (next page): Measurements of $\delta^{18}O$ (‰ VSMOW, ±2 S.D.) made at WiscSIMS from the otolith center to the edge of Transect A (**upper panel**) and Transect B (**middle panel**) of the roasted otolith half. Solid vertical lines indicate estimated transition between juvenile and adult phases (age-7). Dashed vertical lines indicate locations of translucent growth zones, with calendar years of formation labeled at top of each panel in italic type (1981-2007). **Bottom panel** shows direct comparison of $\delta^{18}O$ values between transects averaged by year. Dashed line is 1:1.

Figure 5.3:

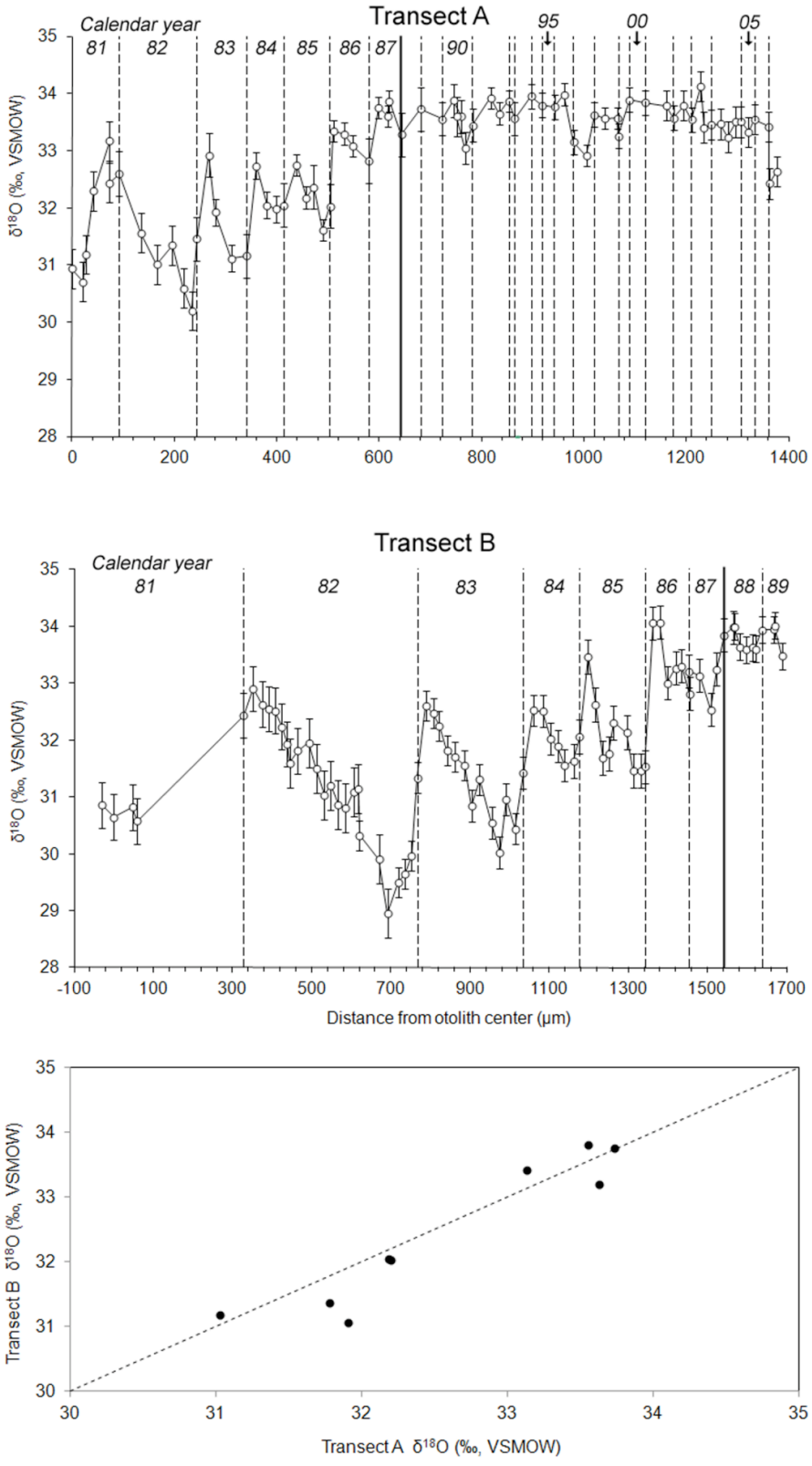
Transect A
Calendar year
81
82
83
84
85
86
87
90
95
00
05
δ18O (‰, VSMOW)
Transect B
Distance from otolith center (µm)
Transect B δ18O (‰, VSMOW)
Transect A δ18O (‰, VSMOW)

Figure 5.4: Measurements of $\delta^{18}O$ made at WiscSIMS from individual 10-μm spots (n = 8) taken to evaluate intra-growth zone variation. Mean (dashed line) = 33.5‰ VSMOW; 2 S.D. (bars) = 0.4‰.

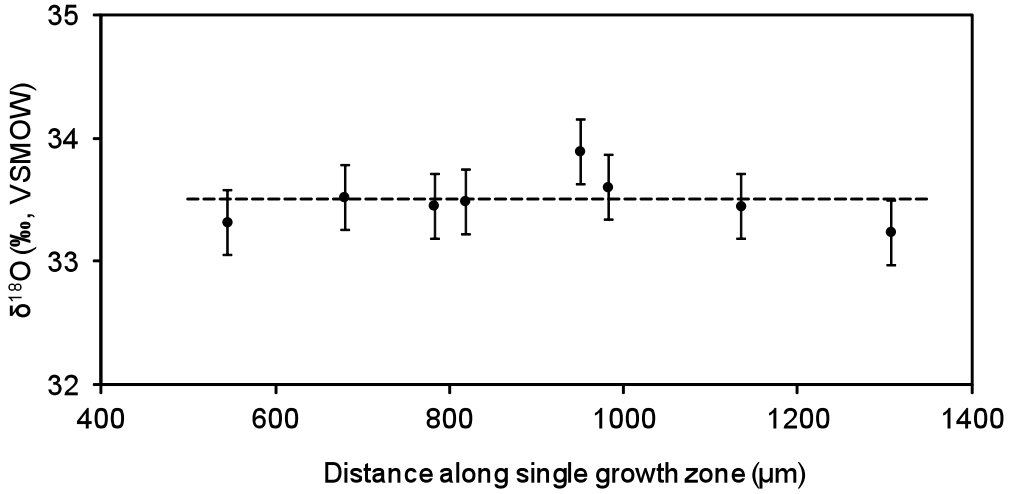

Figure 5.5: (**A**) Comparison of all spot analyses from Transect A (roasted; filled squares) and Transect C (unroasted; open diamonds) to assess the effects of roasting, which removes volatile organic contaminants, on $\delta^{18}O$ values. The unroasted data are interpreted to be biased by organic components and thus not be accurate. Error bars represent ±2 S.D. (**B**) Difference between roasted and unroasted $\delta^{18}O$ values averaged by year. Dashed line is 1:1. Roasted values were on average 1.18‰ higher (solid line) than unroasted values.

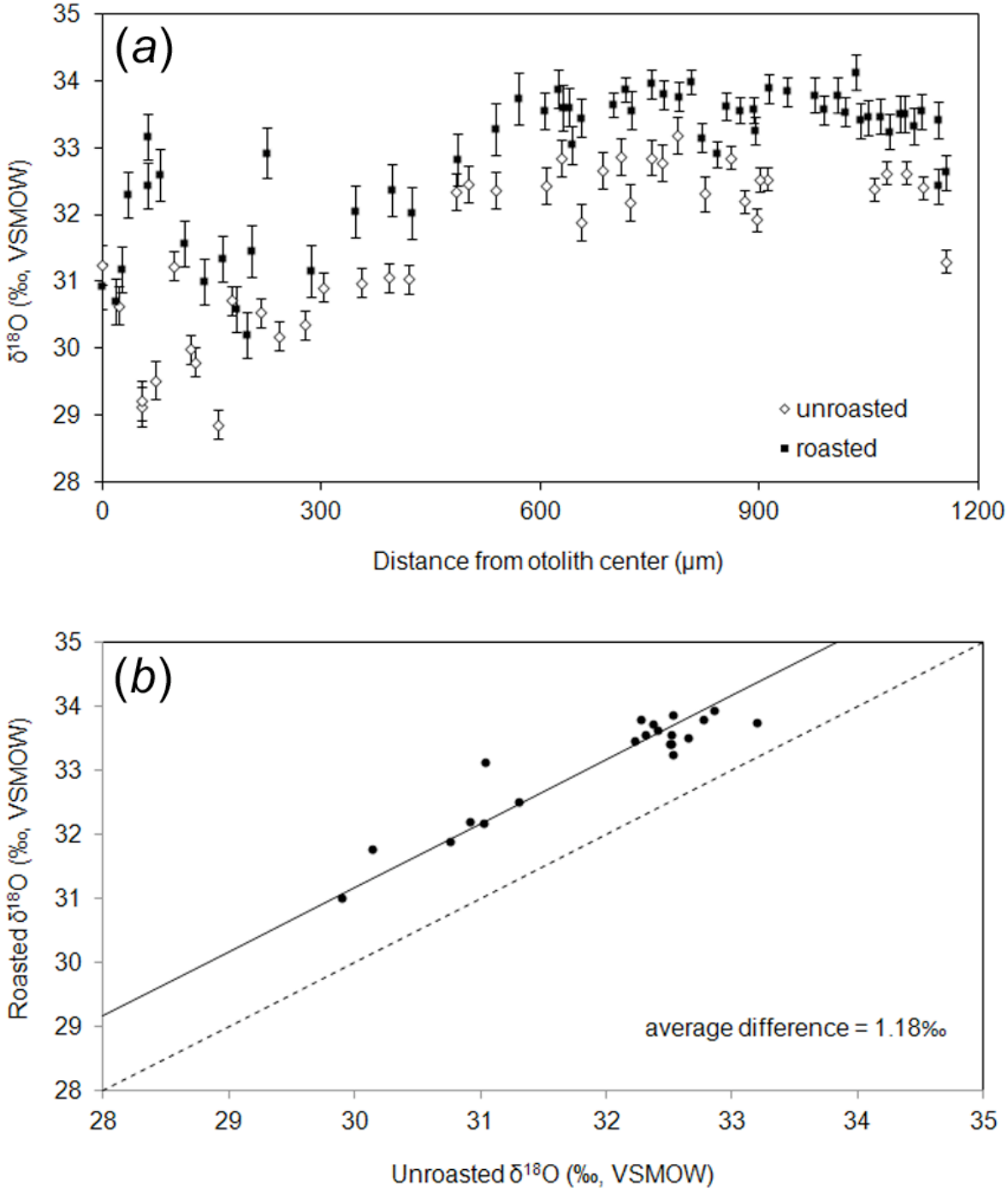

Data Repository Index

Large data tables and figures for each chapter are included in the supplementary files available with the online version of this dissertation.

DR5.1: Ion microprobe raw and corrected oxygen isotope ratios from analysis of an otolith from a yellowfin sole.

DR5.2: Single-crystal XRD results measured in the roasted and unroasted halves of the (right-hand) yellowfin sole otolith that mirrors the (left-hand) specimen investigated in this study.

Supplemental Appendices

Supplement A: Characterization of WiscSIMS aragonite standard UWArg-7

Table A.1: Summary of ion microprobe and acid-digestion analyses of $\delta^{18}O$ and $\delta^{13}C$ in aragonite standard UWArg-7 (WiscSIMS mount WI-STD-72; Figure A.2)

Mineral/ Sample	2 s.d., $\delta^{18}O_{SIMS, raw}$ (‰)*	$\delta^{18}O$ (‰, VSMOW)**	$\delta^{13}C$ (‰, VPDB)**	Calibration citation
Aragonite/ UWArg-7	0.56	20.03	5.99	Orland, 2012 (PhD thesis)

*: The 2 s.d. value is calculated from a total of 54 $\delta^{18}O$ analyses by ion microprobe in 17 grains of UWArg-7 (Table A.6).
**: Results from acid-digestion analysis of powdered UWArg-7 (Table A.7).

Note that the aragonite standard UWArg-7 was developed in tandem with the otolith study reported in Chapter 5; the Soreq Cave speleothem samples analyzed in this dissertation are calcite.

Sixteen carbonate specimens (Table A.3) were evaluated as part of the effort to develop an aragonite standard for $\delta^{18}O$ and $\delta^{13}C$ measurements by the WiscSIMS ion microprobe. These specimens were acquired from multiple sources of varying reliability, so a ~1 mg chip of each sample was analyzed by X-ray diffraction (XRD) to confirm aragonite mineralogy before chemical analysis. A Rigaku single-crystal XRD (Huifang Xu lab, measurements by Hiromi Konishi and Ian Orland) was used to determine the crystal structure of each specimen. Samples were analyzed for 10 min with a collimated, 0.1 mm-diameter X-ray beam emanating from a Mo target. X-rays (Mo Kα) were generated at the target by a 50 mA electron beam with a 50 kV potential. With this set-up, the collimated X-rays penetrate ~100 μm into the carbonate chips. During X-ray exposure, the sample chip is continuously rotated such that the X-ray beam diffracts off of the crystal lattice at a wide range of angles; stage rotation in the horizontal plane

(Ω) ranged from 0-60° while the spin axis (Ψ) of the oblique fiber that held each chip was rotated at a constant 2°/sec. The diffraction pattern of each chip was classified using the default index patterns in the *Jade 9* software, the results of which are reported in the "crystal structure" column of Table A.3. Figure A.4 shows the diffraction pattern of UWArg-7.

Approximately 1 g of each of the nine samples identified as aragonite was then crushed and dry-sieved into three size-fractions: <250 μm, 250–500 μm and >500 μm. Between 15 and 20 grains were selected from the 250-500 μm fraction of each aragonite sample and mounted for casting in one of two epoxy rounds, WI-STD-72 (Figure A.2) or WI-STD-65 (Figure A.5). In addition to the sieved aragonite grains, each epoxy round includes 4–5 grains of UWC-3 calcite standard (Kozdon et al., 2009). The mounting procedure for WiscSIMS samples described by Orland et al. (2009) was used to prepare each round. After a sequence of grinding and polishing with diamond pastes, the final polish was applied to each mount with a 0.05 μm colloidal alumina suspension.

Each mount was then analyzed by electron back-scatter diffraction on the Hitachi S3400 scanning electron microscope in the UW Dept. of Geoscience to assess the structural homogeneity of each potential standard (assistance from John Fournelle, Dayi Ortiz, Phil Gopon, Chloe Bonamici and Jason Huberty). Each mounted grain was analyzed in 3-5 different locations by electron back-scatter diffraction; six of the nine specimens showed consistent aragonite diffraction patterns in every grain, the other three specimens did not and were not considered further.

The remaining six aragonites were analyzed by ion microprobe for $\delta^{18}O$ homogeneity in two separate analysis sessions in the WiscSIMS lab. Since these tests were for oxygen isotope homogeneity, we used the known carbonate standard for $\delta^{18}O$ (UWC-3) and the instrumental

mass fractionation (IMF) value of calcite to calibrate each bracket of aragonite $\delta^{18}O$ measurements onto a common scale. For both sessions, each block of 10-15 aragonite analyses was bracketed by two groups of typically 4 UWC-3 analyses. Two times the standard deviation (s.d.) of the eight bracketing $\delta^{18}O$ values measured in UWC-3 was used to define the spot-to-spot precision of each aragonite analysis (Table A.6). Sample 6510 ("UWArg-7") shows the least heterogeneity in terms of $\delta^{18}O$, with a 2 s.d. of 0.56‰ across all 54 $\delta^{18}O$ measurements.

In order to test whether ion microprobe analyses of calcite and aragonite have different IMF values, bulk $\delta^{18}O$ analysis of UWArg-7 was conducted on a MAT 251 gas-source mass spectrometer using a conventional phosphoric acid-digestion technique at 25°C (analysis at UW by Mike Spicuzza and Ian Orland). Multiple grains from the 250-500 μm size fraction were crushed into 32.45 mg of powder using a dry mortar and pestle. Four aliquots of the powder, between 5 and 6 mg each, were loaded into pyrex Y-tubes and analyzed alongside two aliquots each of the calcite standards NBS-19 and UWC-3. The average NBS-corrected $\delta^{18}O$ value of the four UWArg-7 measurements was 20.03‰ (VSMOW; Table A.7). Analyses from the ion microprobe session on 2/22/2012 (Table A.6) demonstrate that there was a 0.98‰ difference between calcite and aragonite IMF values. Given this IMF offset, ion microprobe measurements of $\delta^{18}O$ versus VSMOW in UWArg-7 during that analytical session are 0.98‰ lower than if the values were calibrated by UWC-3 (Table A.6).

UWC-3 can be used as the bracketing standard for future WiscSIMS analyses of aragonite $\delta^{18}O$. In order to report $\delta^{18}O$ measurements on the VSMOW scale, the IMF difference between calcite and aragonite should be evaluated before each analytical session by comparing values of $\delta^{18}O$ measured by ion microprobe in UWArg-7 and UWC-3 to the bulk $\delta^{18}O$ values measured by acid-digestion techniques.

Table A.8 lists the results of gas source mass spectrometer analysis of $\delta^{18}O$ in aragonite specimens UWArg-4.1 and UWArg-5. Although ion microprobe measurements of $\delta^{18}O$ in these samples are more heterogeneous than in UWArg-7, their NBS-corrected $\delta^{18}O$ values reflect a similar offset between calcite and aragonite IMF values.

Figure A.2: Reflected-light image of the gold-coated aragonite standard mount, WI-STD-72. Grains of seven potential aragonite standards are arranged around a central group of UWC-3 calcite standard grains. The diameter of the circular arrangement is ~1 cm. The original sample names are listed next to each group of grains; grain numbers (used in Table A.6) are shown for samples identified by electron back-scatter detection as having homogeneous (aragonite) crystal structure (Table A.3).

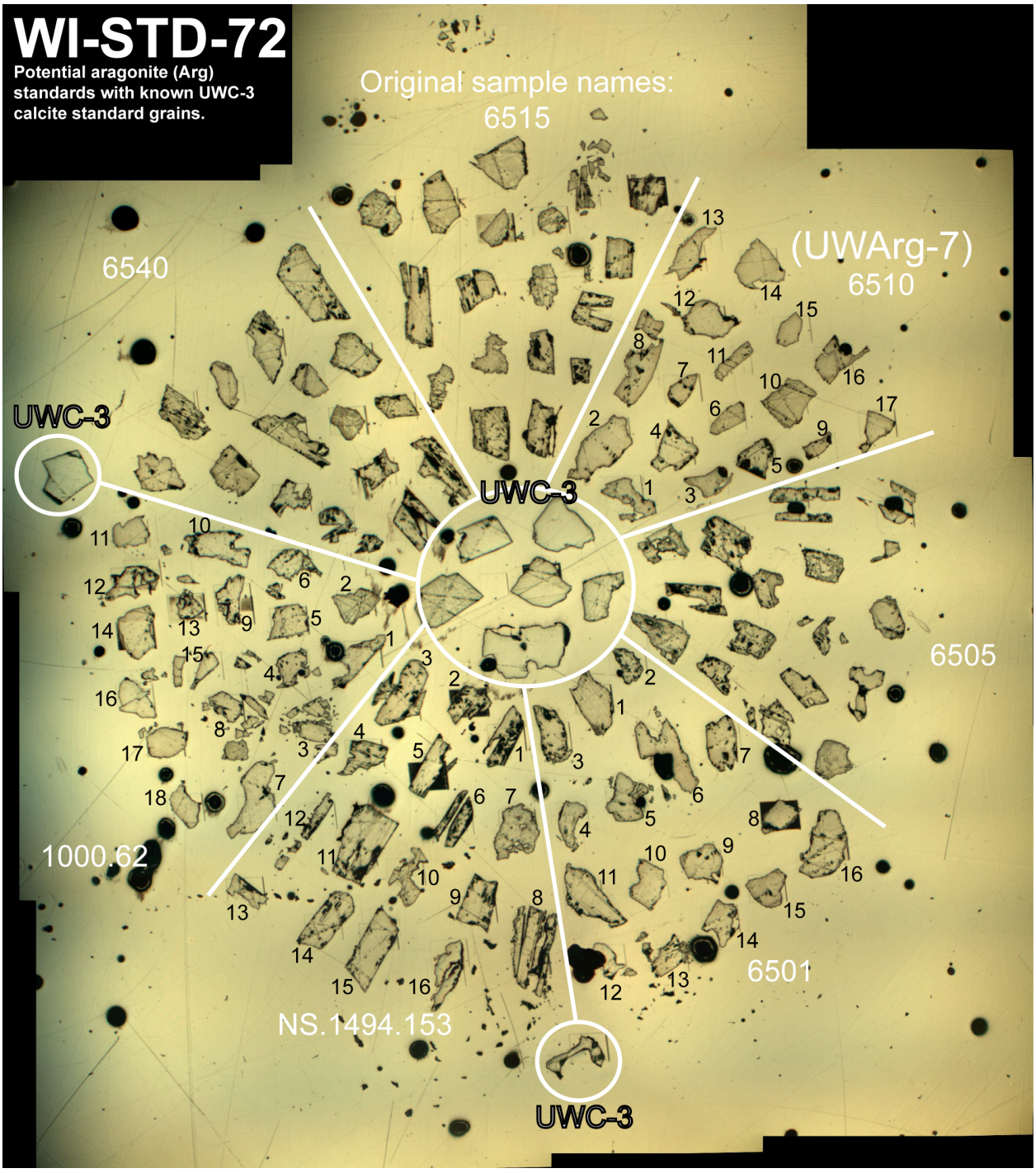

Table A.3: Results of mineral structure (XRD & EBSD) analysis in potential aragonite standards.

Sample name	Locality if known	Source[++]	WiscSIMS grain mount	UW-series name	Crystal structure (homogeneous?)*	Avg. $\delta^{13}C$ (‰, VPDB)[α]	Avg. $\delta^{18}O$ (‰, VSMOW)[β]
6510	***Herrengrund, Hungary***	***Geoscience Mineral. Coll.***	***WI-STD-72***	***UWArg-7***	***aragonite (y)***	***5.99***	***20.03***
6501	Cumberland	Geoscience Mineral. Coll.	WI-STD-72		**aragonite (y)**		
NS.1494.153	–	UW Geology Museum	WI-STD-72		**aragonite (y)**		
1000.62	–	UW Geology Museum	WI-STD-72		**aragonite (y)**		
–	Morocco	eBay	WI-STD-65	UWArg-4.1	**aragonite (y)**	7.48	23.35
–	Czech Rep.	eBay	WI-STD-65	UWArg-5	**aragonite (y)**	2.87	22.26
6505	Livermore, CA	Geoscience Mineral. Coll.	WI-STD-72		**aragonite (n)**		
6515	Chester Co., PA	Geoscience Mineral. Coll.	WI-STD-72		**aragonite (n)**		
6540	Tucson, AZ	Geoscience Mineral. Coll.	WI-STD-72		**aragonite (n)**		
–	Argentina	eBay	WI-STD-65	UWArg-3	calcite		
–	Argentina	eBay	WI-STD-65	UWArg-6	prehnite		
NS.1500.356	–	UW Geology Museum			calcite		
6506	Walcott Divide Eagle Co. CO	Geoscience Mineral. Coll.			calcite		
6550	New Mexico	Geoscience Mineral. Coll.			calcite		
96 G.10	Cyclades, Greece	J. W. Valley			calcite		
96 G.11	Cyclades, Greece	J. W. Valley			calcite		

Table notes:

[++]: Samples borrowed from the UW Dept. of Geoscience Mineralogy Collection and the UW Geology Museum, including bottles of sieved material, were returned to their respective source.

*: The potential standards were analyzed by XRD to determine their crystal structure; results indicate the mineral composition of each sample. Next, each aragonite sample was analyzed by EBSD to test for structural homogeneity, indicated in parentheses; y = homogeneous structure, n = non-homogeneous structure.

α: Average of $\delta^{13}C$ values measured by phosphoric acid digestion, reported in Tables A.7 (UWArg-7) and A.8 (others).

β: Average of $\delta^{18}O$ values measured by phosphoric acid digestion, reported in Tables A.7 (UWArg-7) and A.8 (others).

Figure A.4: Single-crystal XRD results from two analyses of a ~1 mg chip of aragonite sample 6510 (UWArg-7). Panel **A** plots intensity versus diffraction angle for the first experiment, with spin-axis rotation (Ψ) at 2°/sec and no horizontal stage rotation (Ω). Panel **B** shows results of the second experiment, which also had spin-axis rotation (Ψ) at 2°/sec but added horizontal stage rotation (Ω) between 0-70° at 1°/sec. At the bottom of each panel are the index patterns of aragonite and calcite for comparison.

Panel A:

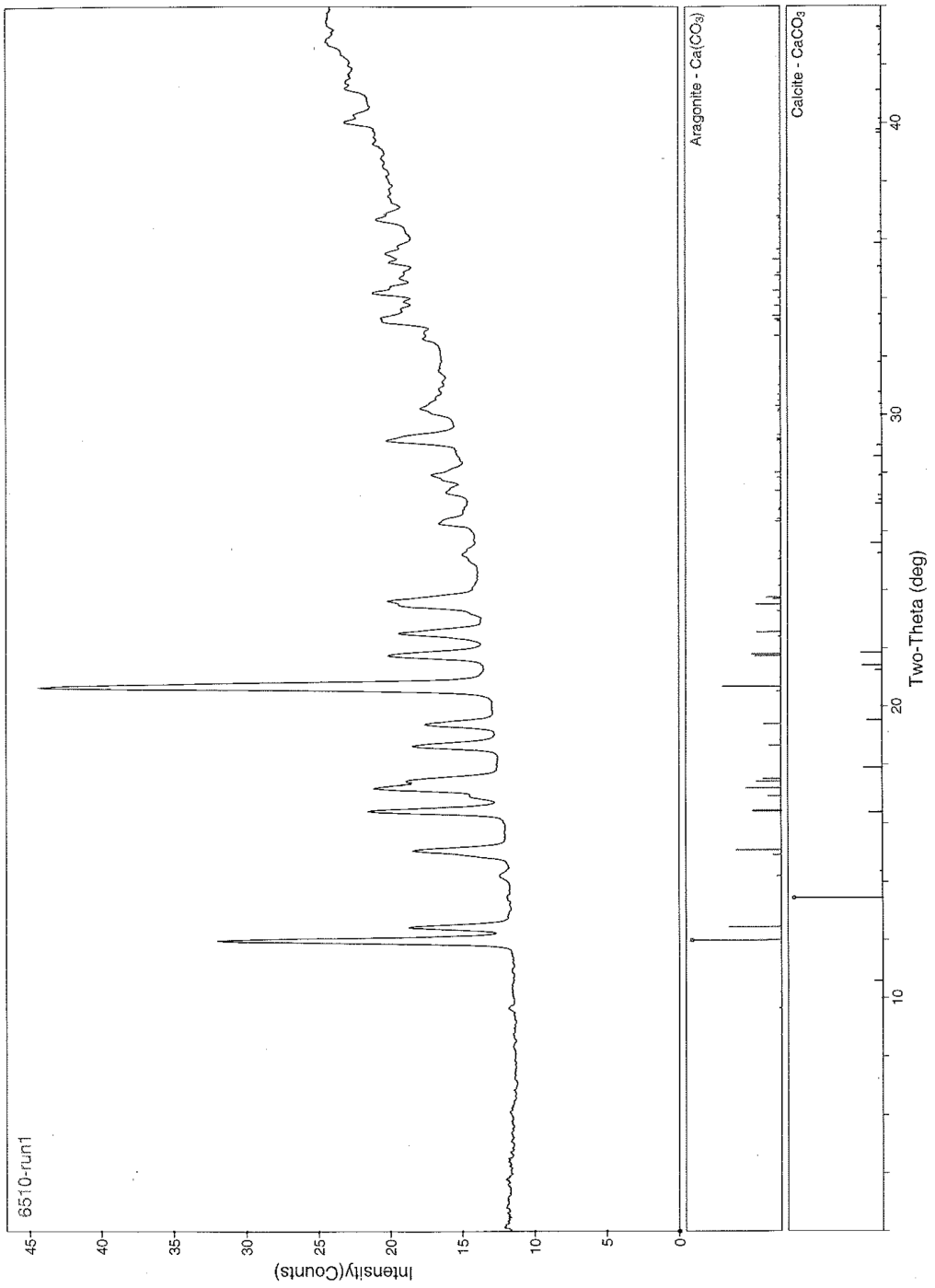

Figure A.4, panel B:

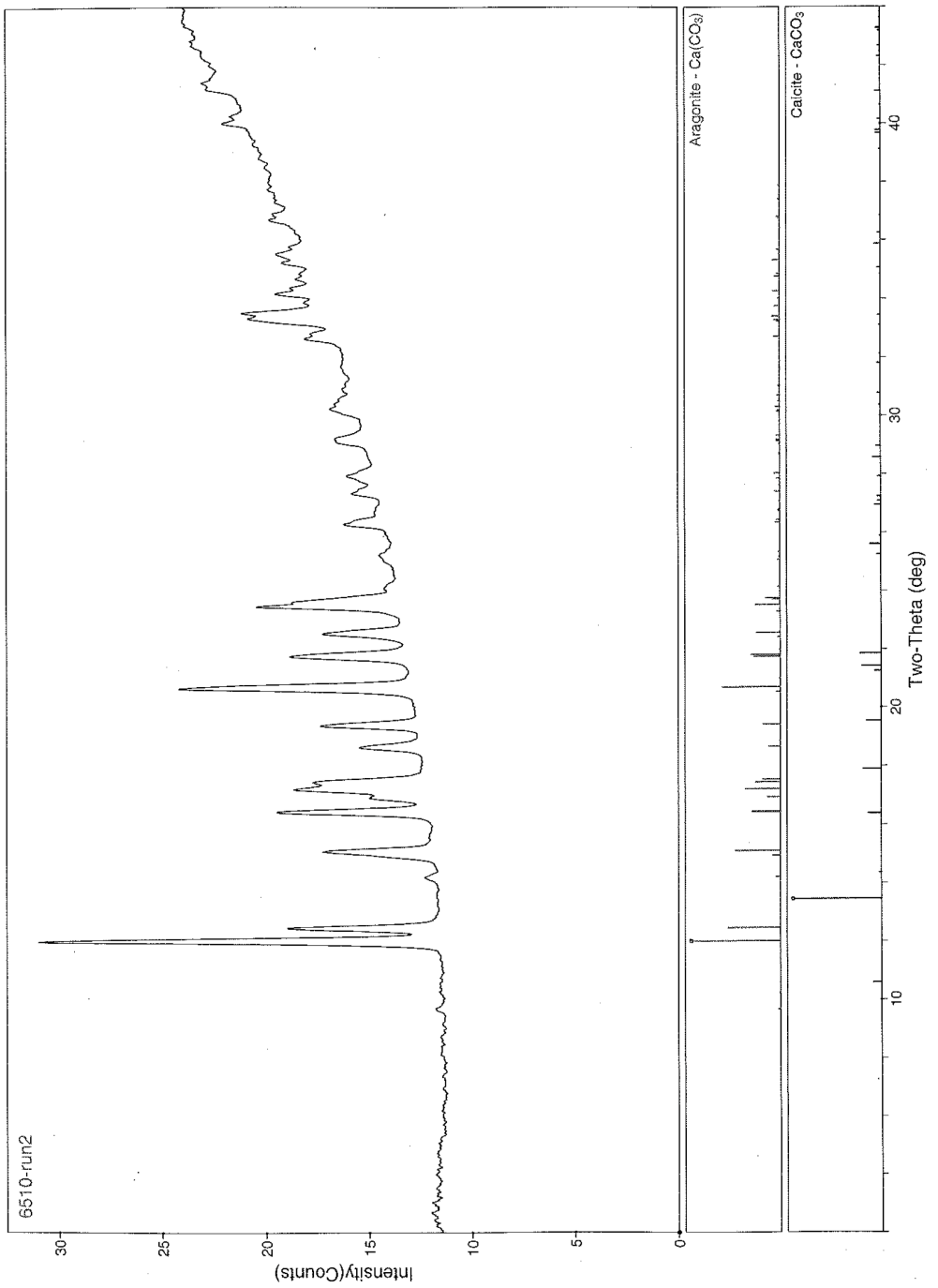

Figure A.5: Reflected-light image of the gold-coated aragonite standard mount, WI-STD-65. Grains of four potential aragonite standards and two dolomite standards are arranged around a central group of UWC-3 calcite standard grains. The diameter of this image is ~1 cm.

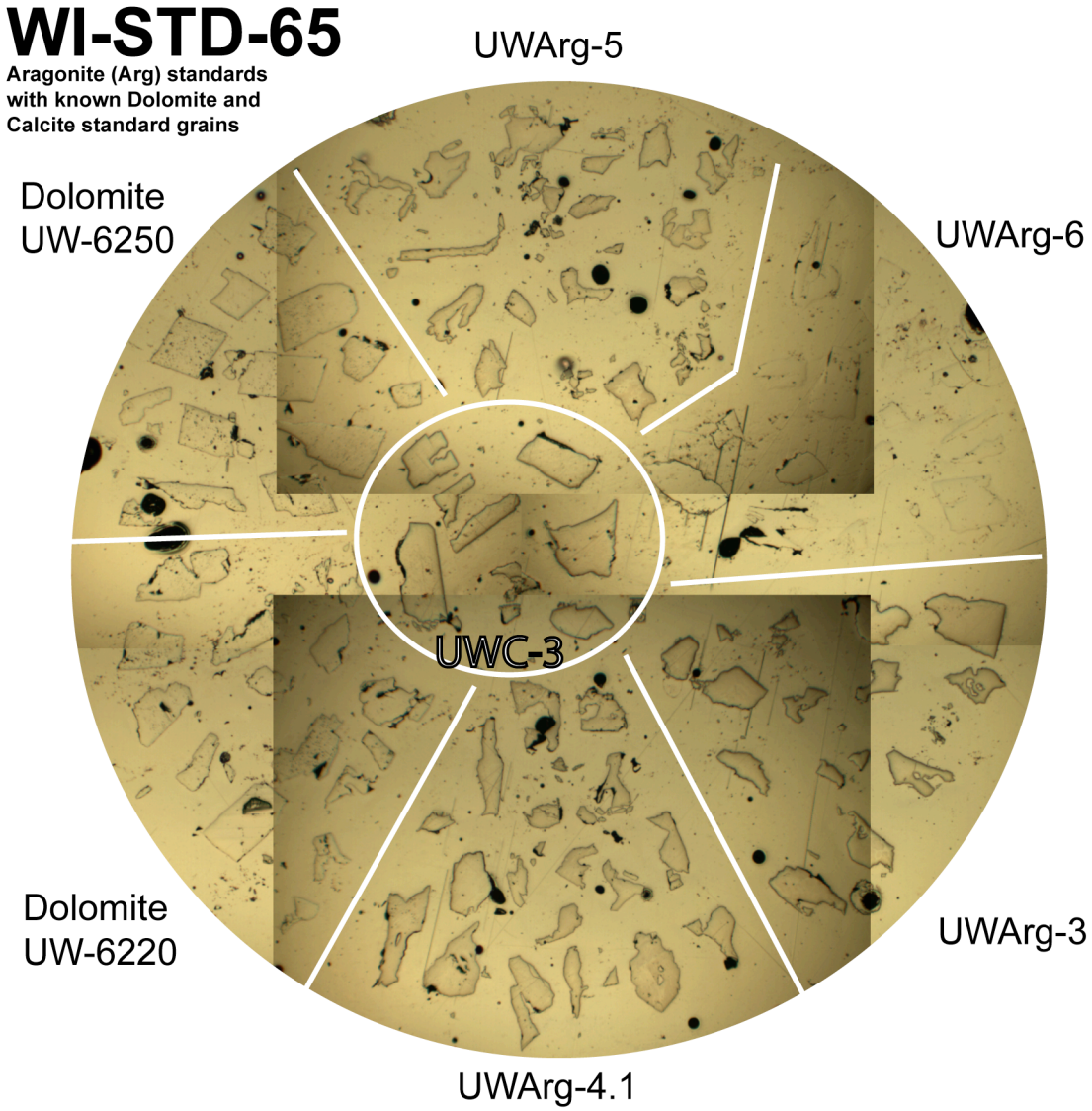

Table A.6: Ion microprobe analysis of $\delta^{18}O$ in six potential aragonite standards.

Mount, sample name, grain #	$\delta^{18}O$ (‰, VSMOW)*	2 s.d.	$\delta^{18}O_{raw}$ (‰)	Internal precision (‰)	IP (nA)	Yield (10^6 cps/nA)
Analysis session 1 (8/19/2011)						
UWC-3 G1 #01			6.34	0.51	1.40	2.07
UWC-3 G1 #02			6.42	0.47	1.40	2.07
UWC-3 G1 #03			6.41	0.46	1.41	2.05
UWC-3 G1 #04			6.36	0.44	1.41	2.05
WI-STD-65, UWArg-5, G1-01		0.23	18.67	0.51	1.40	1.97
WI-STD-65, UWArg-5, G2-01		0.23	17.80	0.48	1.41	1.98
WI-STD-65, UWArg-5, G3-01		0.23	18.89	0.49	1.41	1.98
WI-STD-65, UWArg-5, G4-01		0.23	18.48	0.45	1.41	1.98
WI-STD-65, UWArg-5, G5-01		0.23	18.41	0.47	1.42	1.99
WI-STD-65, UWArg-5, G6-01		0.23	18.65	0.54	1.43	1.99
WI-STD-65, UWArg-5, G7-01		0.23	16.80	0.49	1.43	1.98
WI-STD-65, UWArg-5, G8-01		0.23	16.72	0.48	1.42	1.99
UWC-3 G1 #05			6.65	0.49	1.43	2.05
UWC-3 G1 #06			6.42	0.41	1.43	2.06
UWC-3 G1 #07			6.41	0.51	1.43	2.10
UWC-3 G1 #08			6.24	0.41	1.43	2.09
Bracket UWC-3 1-8		**0.23**	**6.41**			
WI-STD-65, UWArg-5, G9-01		0.33	17.20	0.46	1.45	1.99
WI-STD-65, UWArg-5, G10-01		0.33	17.25	0.51	1.46	2.00
WI-STD-65, UWArg-5, G11-01		0.33	17.09	0.47	1.46	2.00
WI-STD-65, UWArg-5, G12-01		0.33	17.55	0.52	1.48	1.97
WI-STD-65, UWArg-5, G13-01		0.33	16.90	0.48	1.49	1.95
WI-STD-65, UWArg-5, G14-01		0.33	18.21	0.49	1.49	1.95
WI-STD-65, UWArg-5, G15-01		0.33	17.04	0.52	1.51	1.94
WI-STD-65, UWArg-5, G16-01		0.33	18.26	0.41	1.52	1.94
WI-STD-65, UWArg-5, G17-01		0.33	16.89	0.53	1.53	1.94
WI-STD-65, UWArg-5, G18-01		0.33	16.37	0.47	1.52	1.96
UWC-3 G1 #09			6.22	0.48	1.54	2.02
UWC-3 G1 #10			6.32	0.45	1.55	2.04
UWC-3 G1 #11			6.10	0.41	1.55	2.04
UWC-3 G1 #12			6.31	0.45	1.55	2.05
Bracket UWC-3 5-12		**0.33**	**6.33**			
WI-STD-65, UWArg-4.1, G1-01		0.29	18.31	0.48	1.55	1.92
WI-STD-65, UWArg-4.1, G2-01		0.29	17.97	0.50	1.54	1.94
WI-STD-65, UWArg-4.1, G3-01		0.29	18.36	0.44	1.55	1.94
WI-STD-65, UWArg-4.1, G4-01		0.29	17.96	0.52	1.55	1.94
WI-STD-65, UWArg-4.1, G5-01		0.29	17.26	0.46	1.54	1.95
WI-STD-65, UWArg-4.1, G6-01		0.29	18.50	0.50	1.54	1.93
WI-STD-65, UWArg-4.1, G7-01		0.29	18.12	0.48	1.55	1.93
WI-STD-65, UWArg-4.1, G8-01		0.29	17.71	0.52	1.54	1.94
UWC-3 G1 #13			6.01	0.48	1.56	2.03
UWC-3 G1 #14			6.20	0.35	1.56	2.05
UWC-3 G1 #15			6.22	0.42	1.56	2.06
UWC-3 G1 #16			5.91	0.47	1.56	2.07
Bracket UWC-3 9-16		**0.29**	**6.16**			

Mount, sample name, grain #	$\delta^{18}O$ (‰, VSMOW)*	2 s.d.	$\delta^{18}O_{raw}$ (‰)	Internal precision (‰)	IP (nA)	Yield (10^6 cps/nA)
WI-STD-65, UWArg-4.1, G9-01		0.28	18.68	0.49	1.55	1.95
WI-STD-65, UWArg-4.1, G10-01		0.28	18.68	0.49	1.55	1.96
WI-STD-65, UWArg-4.1, G11-01		0.28	18.20	0.45	1.56	1.94
WI-STD-65, UWArg-4.1, G12-01		0.28	17.71	0.42	1.56	1.95
WI-STD-65, UWArg-4.1, G13-01		0.28	18.18	0.51	1.56	1.94
WI-STD-65, UWArg-4.1, G14-01		0.28	17.22	0.50	1.55	1.95
WI-STD-65, UWArg-4.1, G15-01		0.28	17.45	0.49	1.55	1.94
WI-STD-65, UWArg-4.1, G16-01		0.28	18.08	0.47	1.56	1.91
WI-STD-65, UWArg-4.1, G17-01		0.28	17.52	0.48	1.56	1.94
WI-STD-65, UWArg-4.1, G18-01		0.28	17.61	0.50	1.56	1.91
UWC-3 G1 #17			6.31	0.41	1.56	2.02
UWC-3 G1 #18			6.18	0.45	1.56	2.04
UWC-3 G1 #19			6.25	0.42	1.56	2.03
UWC-3 G1 #20			6.30	0.46	1.56	2.02
Bracket UWC-3 13-20		**0.28**	**6.17**			
WI-STD-65, UWArg-5, G4-02		0.11	18.53	0.54	1.53	1.99
WI-STD-65, UWArg-5, G4-03		0.11	18.36	0.51	1.54	1.96
WI-STD-65, UWArg-5, G4-04		0.11	18.46	0.51	1.54	1.95
WI-STD-65, UWArg-5, G7-02		0.11	16.79	0.48	1.54	1.95
WI-STD-65, UWArg-5, G7-03		0.11	16.55	0.48	1.53	1.97
WI-STD-65, UWArg-5, G7-04		0.11	16.59	0.48	1.52	1.99
WI-STD-65, UWArg-5, G13-02		0.11	16.94	0.47	1.51	1.94
WI-STD-65, UWArg-5, G13-03		0.11	16.69	0.42	1.51	1.99
WI-STD-65, UWArg-5, G13-04		0.11	17.10	0.50	1.51	1.94
WI-STD-65, UWArg-5, G14-02		0.11	17.95	0.48	1.50	1.96
WI-STD-65, UWArg-5, G14-03		0.11	18.04	0.56	1.50	1.99
WI-STD-65, UWArg-5, G14-04		0.11	18.00	0.55	1.50	1.95
WI-STD-65, UWArg-5, G12-02		0.11	17.07	0.46	1.50	2.00
WI-STD-65, UWArg-5, G12-03		0.11	17.40	0.51	1.49	1.98
WI-STD-65, UWArg-5, G12-04		0.11	17.72	0.50	1.50	1.99
UWC-3 G1 #21			6.33	0.44	1.49	2.06
UWC-3 G1 #22			6.35	0.49	1.49	2.07
UWC-3 G1 #23			6.29	0.45	1.49	2.07
UWC-3 G1 #24			6.24	0.47	3.06	1.49
Bracket UWC-3 17-24		**0.110**	**6.281**			
Analysis session 2 (2/22/2012)						
UWC-3 G1 #05			8.33	0.47	2.23	2.89
UWC-3 G1 #06			8.07	0.41	2.22	2.88
UWC-3 G1 #07			8.08	0.42	2.24	2.90
UWC-3 G1 #08			8.14	0.44	2.25	2.88
WI-STD-72, 6501, G01	27.27	0.26	23.91	0.43	2.16	2.77
WI-STD-72, 6501, G02	27.12	0.26	23.76	0.50	2.20	2.81
WI-STD-72, 6501, G03	27.05	0.26	23.69	0.47	2.21	2.81
WI-STD-72, 6501, G04	27.05	0.26	23.69	0.44	2.20	2.83
WI-STD-72, 6501, G05	27.34	0.26	23.98	0.41	2.16	2.78
WI-STD-72, 6501, G06	28.32	0.26	24.95	0.40	2.11	2.84
WI-STD-72, 6501, G07	27.04	0.26	23.68	0.50	2.11	2.84
WI-STD-72, 6501, G08	27.96	0.26	24.59	0.48	2.09	2.78
UWC-3 G1 #09			8.18	0.47	2.23	2.98

Mount, sample name, grain #	$\delta^{18}O$ (‰, VSMOW)*	2 s.d.	$\delta^{18}O_{raw}$ (‰)	Internal precision (‰)	IP (nA)	Yield (10^6 cps/nA)
UWC-3 G1 #10			8.43	0.45	2.23	2.97
UWC-3 G1 #11			8.33	0.41	2.22	2.98
UWC-3 G1 #12			8.16	0.38	2.21	3.00
Bracket UWC-3 5-12		**0.26**	**8.21**			
WI-STD-72, 6501, G09	27.53	0.48	24.40	0.43	2.09	2.87
WI-STD-72, 6501, G10	25.44	0.48	22.32	0.41	2.06	2.89
WI-STD-72, 6501, G11	27.22	0.48	24.08	0.46	2.06	2.90
WI-STD-72, 6501, G12	27.78	0.48	24.65	0.41	2.01	2.87
WI-STD-72, 6501, G13	27.16	0.48	24.03	0.36	2.03	2.97
WI-STD-72, 6501, G14	27.44	0.48	24.31	0.46	2.04	2.92
WI-STD-72, 6501, G15	24.94	0.48	21.82	0.54	2.05	2.89
WI-STD-72, 6501, G16	27.26	0.48	24.13	0.44	2.05	2.88
UWC-3 G1 #13			8.98	0.35	2.14	2.99
UWC-3 G1 #14			8.53	0.42	2.12	3.04
UWC-3 G1 #15			8.44	0.40	2.09	3.08
UWC-3 G1 #16			8.47	0.51	2.09	3.10
UWC-3 G1 #17			8.45	0.35	2.11	3.09
Bracket UWC-3 9-17		**0.48**	**8.44**			
WI-STD-72, **UWArg-7**, G01	20.01	0.40	17.09	0.41	2.00	2.93
WI-STD-72, **UWArg-7**, G02	20.02	0.40	17.10	0.48	2.00	2.95
WI-STD-72, **UWArg-7**, G03	20.39	0.40	17.46	0.48	1.99	2.94
WI-STD-72, **UWArg-7**, G04	20.43	0.40	17.51	0.46	2.02	2.92
WI-STD-72, **UWArg-7**, G05	19.94	0.40	17.02	0.47	1.97	2.92
WI-STD-72, **UWArg-7**, G06	20.09	0.40	17.17	0.45	1.95	2.96
WI-STD-72, **UWArg-7**, G07	19.99	0.40	17.07	0.41	1.94	2.95
WI-STD-72, **UWArg-7**, G08	19.85	0.40	16.93	0.33	1.95	2.99
UWC-3 G1 #18			8.66	0.38	2.02	3.10
UWC-3 G1 #19			8.48	0.38	2.01	3.12
UWC-3 G1 #20			8.73	0.47	2.02	3.13
UWC-3 G1 #21			8.85	0.35	2.01	3.15
Bracket UWC-3 13-21		**0.40**	**8.62**			
UWC-3 G1 #22			8.46	0.37	2.22	3.07
UWC-3 G1 #23			8.17	0.41	2.30	2.97
UWC-3 G1 #24			8.13	0.48	2.34	2.94
UWC-3 G1 #25			8.15	0.47	2.35	2.90
UWC-3 G1 #26			8.11	0.42	2.38	2.92
WI-STD-72, **UWArg-7**, G09	20.33	0.22	16.99	0.48	2.27	2.72
WI-STD-72, **UWArg-7**, G10	20.03	0.22	16.69	0.35	2.28	2.76
WI-STD-72, **UWArg-7**, G11	19.64	0.22	16.30	0.47	2.26	2.77
WI-STD-72, **UWArg-7**, G12	20.19	0.22	16.85	0.49	2.23	2.76
WI-STD-72, **UWArg-7**, G13	19.82	0.22	16.48	0.41	2.21	2.79
WI-STD-72, **UWArg-7**, G14	19.68	0.22	16.34	0.45	2.21	2.80
WI-STD-72, **UWArg-7**, G15	20.30	0.22	16.96	0.39	2.18	2.78
WI-STD-72, **UWArg-7**, G16	20.33	0.22	16.99	0.40	2.13	2.82
WI-STD-72, **UWArg-7**, G17	20.20	0.22	16.86	0.39	2.11	2.81
UWC-3 G1 #27			8.18	0.43	2.24	2.98
UWC-3 G1 #28			8.13	0.42	2.25	2.99
UWC-3 G1 #29			8.22	0.39	2.26	2.99
UWC-3 G1 #30			8.29	0.44	2.23	2.99

Mount, sample name, grain #	$\delta^{18}O$ (‰, VSMOW)*	2 s.d.	$\delta^{18}O_{raw}$ (‰)	Internal precision (‰)	IP (nA)	Yield (10^6 cps/nA)
Bracket UWC-3 22-30		**0.22**	**8.20**			
WI-STD-72, 1000.62, G01	23.38	0.16	20.02	0.43	2.12	2.85
WI-STD-72, 1000.62, G02	24.38	0.16	21.02	0.54	2.13	2.84
WI-STD-72, 1000.62, G03	24.65	0.16	21.28	0.40	2.11	2.87
WI-STD-72, 1000.62, G04	24.58	0.16	21.22	0.53	2.10	2.88
WI-STD-72, 1000.62, G05	24.57	0.16	21.20	0.41	2.11	2.90
WI-STD-72, 1000.62, G06	24.70	0.16	21.33	0.42	2.13	2.89
WI-STD-72, 1000.62, G07	24.31	0.16	20.95	0.43	2.12	2.87
WI-STD-72, 1000.62, G08	24.27	0.16	20.90	0.50	2.13	2.88
WI-STD-72, 1000.62, G09	23.20	0.16	19.84	0.51	2.15	2.88
WI-STD-72, 1000.62, G10	24.76	0.16	21.40	0.50	2.15	2.85
UWC-3 G1 #31			8.19	0.43	2.28	2.96
UWC-3 G1 #32			8.05	0.45	2.27	2.96
UWC-3 G1 #33			8.25	0.38	2.28	2.97
UWC-3 G1 #34			8.27	0.50	2.26	2.97
Bracket UWC-3 27-34		**0.16**	**8.20**			
WI-STD-72, 1000.62, G11	24.53	0.24	21.20	0.38	2.12	2.87
WI-STD-72, 1000.62, G12	24.36	0.24	21.03	0.40	2.12	2.89
WI-STD-72, 1000.62, G13	22.76	0.24	19.44	0.47	2.17	2.88
WI-STD-72, 1000.62, G14	24.33	0.24	21.00	0.40	2.19	2.86
WI-STD-72, 1000.62, G15	24.56	0.24	21.23	0.53	2.17	2.87
WI-STD-72, 1000.62, G16	24.40	0.24	21.07	0.45	2.12	2.87
WI-STD-72, 1000.62, G17	24.71	0.24	21.38	0.40	2.14	2.89
WI-STD-72, 1000.62, G18	24.43	0.24	21.10	0.54	2.15	3.01
UWC-3 G1 #35			8.48	0.49	2.24	2.94
UWC-3 G1 #36			8.21	0.38	2.24	2.96
UWC-3 G1 #37			8.16	0.50	2.26	2.98
UWC-3 G1 #38			8.26	0.45	2.29	2.97
Bracket UWC-3 31-38		**0.24**	**8.23**			
WI-STD-72, NS.1494.153, G01	20.79	0.24	17.55	0.61	2.21	2.78
WI-STD-72, NS.1494.153, G02	21.59	0.24	18.34	0.50	2.22	2.79
WI-STD-72, NS.1494.153, G03	20.14	0.24	16.90	0.45	2.20	2.84
WI-STD-72, NS.1494.153, G04	22.03	0.24	18.78	0.47	2.20	2.81
WI-STD-72, NS.1494.153, G05	21.21	0.24	17.97	0.41	2.16	2.86
WI-STD-72, NS.1494.153, G06	20.63	0.24	17.39	0.42	2.14	2.86
WI-STD-72, NS.1494.153, G07	20.98	0.24	17.73	0.49	2.17	2.93
WI-STD-72, NS.1494.153, G08	22.39	0.24	19.14	0.38	2.10	2.85
UWC-3 G1 #39			8.31	0.50	2.21	3.00
UWC-3 G1 #40			8.24	0.35	2.20	3.00
UWC-3 G1 #41			8.49	0.44	2.22	3.01
UWC-3 G1 #42			8.28	0.41	2.24	2.97
Bracket UWC-3 35-42		**0.24**	**8.30**			
WI-STD-72, NS.1494.153, G09	22.91	0.27	19.78	0.45	2.14	2.85
WI-STD-72, NS.1494.153, G10	18.97	0.27	15.85	0.48	2.15	2.86
WI-STD-72, NS.1494.153, G11	23.41	0.27	20.28	0.43	2.12	2.82
WI-STD-72, NS.1494.153, G12	23.22	0.27	20.08	0.51	2.10	2.92
WI-STD-72, NS.1494.153, G13	19.80	0.27	16.68	0.48	2.05	2.91
WI-STD-72, NS.1494.153, G14	23.34	0.27	20.20	0.47	2.07	2.93
WI-STD-72, NS.1494.153, G15	21.50	0.27	18.37	0.43	2.07	2.91

Mount, sample name, grain #	$\delta^{18}O$ (‰, VSMOW)*	2 s.d.	$\delta^{18}O_{raw}$ (‰)	Internal precision (‰)	IP (nA)	Yield (10^6 cps/nA)
WI-STD-72, NS.1494.153, G16	17.81	0.27	14.70	0.32	2.11	2.98
UWC-3 G1 #43			8.53	0.44	2.13	3.03
UWC-3 G1 #44			8.43	0.38	2.08	3.05
UWC-3 G1 #45			8.61	0.45	2.07	3.09
UWC-3 G1 #46			8.50	0.38	2.08	3.11
Bracket UWC-3 39-46		**0.27**	**8.42**			
UWC-3 G1 #47			8.03	0.37	2.38	2.97
UWC-3 G1 #48			7.97	0.43	2.47	2.89
UWC-3 G1 #49			7.63	0.51	2.51	2.86
UWC-3 G1 #50			7.78	0.40	2.51	2.86
UWC-3 G1 #51			7.77	0.46	2.51	2.86
WI-STD-72, **UWArg-7**, G08-2	19.91	0.47	16.37	0.43	2.35	2.67
WI-STD-72, **UWArg-7**, G08-3	19.76	0.47	16.22	0.46	2.37	2.69
WI-STD-72, **UWArg-7**, G08-4	19.75	0.47	16.21	0.46	2.38	2.72
WI-STD-72, **UWArg-7**, G08-5	19.97	0.47	16.42	0.40	2.35	2.69
WI-STD-72, **UWArg-7**, G07-2	19.85	0.47	16.31	0.48	2.31	2.72
WI-STD-72, **UWArg-7**, G07-3	20.45	0.47	16.90	0.39	2.29	2.75
WI-STD-72, **UWArg-7**, G07-4	20.06	0.47	16.52	0.37	2.25	2.73
WI-STD-72, **UWArg-7**, G06-2	20.14	0.47	16.59	0.48	2.25	2.75
WI-STD-72, **UWArg-7**, G06-3	19.97	0.47	16.43	0.47	2.25	2.77
WI-STD-72, **UWArg-7**, G06-4	20.09	0.47	16.54	0.39	2.23	2.78
UWC-3 G1 #52			8.21	0.43	2.32	2.94
UWC-3 G1 #53			8.20	0.40	2.33	2.93
UWC-3 G1 #54			8.32	0.45	2.32	2.93
UWC-3 G1 #55			8.11	0.35	2.32	2.93
Bracket UWC-3 47-55		**0.47**	**8.00**			
WI-STD-72, **UWArg-7**, G05-2	19.59	0.36	16.35	1.25	2.08	2.73
WI-STD-72, **UWArg-7**, G05-3	20.41	0.36	17.16	0.44	2.08	2.85
WI-STD-72, **UWArg-7**, G05-4	19.68	0.36	16.44	0.38	2.12	2.86
WI-STD-72, **UWArg-7**, G09-2	20.57	0.36	17.32	0.42	2.13	2.81
WI-STD-72, **UWArg-7**, G09-3	20.52	0.36	17.27	0.46	2.15	2.79
WI-STD-72, **UWArg-7**, G09-4	20.46	0.36	17.21	0.48	2.14	2.74
WI-STD-72, **UWArg-7**, G17-2	19.71	0.36	16.46	0.43	2.14	2.81
WI-STD-72, **UWArg-7**, G17-3	20.25	0.36	17.00	0.43	2.12	2.77
WI-STD-72, **UWArg-7**, G17-4	19.88	0.36	16.64	0.46	2.13	2.79
WI-STD-72, **UWArg-7**, G10-2	20.31	0.36	17.06	0.43	2.16	2.82
WI-STD-72, **UWArg-7**, G10-3	20.21	0.36	16.96	0.44	2.16	2.82
WI-STD-72, **UWArg-7**, G10-4	20.16	0.36	16.91	0.45	2.12	2.81
UWC-3 G1 #56			8.61	0.41	2.20	3.01
UWC-3 G1 #57			8.39	0.41	2.22	3.00
UWC-3 G1 #58			8.44	0.45	2.24	3.00
UWC-3 G1 #59			8.09	0.37	2.26	3.00
Bracket UWC-3 52-59		**0.36**	**8.30**			
WI-STD-72, **UWArg-7**, G11-2	19.61	0.37	16.55	0.43	2.16	2.80
WI-STD-72, **UWArg-7**, G11-3	19.73	0.37	16.68	0.43	2.15	2.82
WI-STD-72, **UWArg-7**, G12-2	19.68	0.37	16.62	0.45	2.14	2.80
WI-STD-72, **UWArg-7**, G13-2	19.53	0.37	16.47	0.40	2.14	2.82
WI-STD-72, **UWArg-7**, G14-2	19.58	0.37	16.52	0.38	2.11	2.82
WI-STD-72, **UWArg-7**, G15-2	20.27	0.37	17.21	0.51	2.11	2.83

Mount, sample name, grain #	$\delta^{18}O$ (‰, VSMOW)*	2 s.d.	$\delta^{18}O_{raw}$ (‰)	Internal precision (‰)	IP (nA)	Yield (10^6 cps/nA)
WI-STD-72, **UWArg-7**, G16-2	20.30	0.37	17.24	0.46	2.13	2.76
WI-STD-72, **UWArg-7**, G02-2	19.83	0.37	16.77	0.50	2.16	2.82
WI-STD-72, **UWArg-7**, G01-2	20.09	0.37	17.03	0.35	2.14	2.81
WI-STD-72, **UWArg-7**, G03-2	19.63	0.37	16.57	0.43	2.14	2.79
WI-STD-72, **UWArg-7**, G04-2	20.26	0.37	17.20	0.42	2.14	2.85
WI-STD-72, **UWArg-7**, G04-3	19.91	0.37	16.85	0.40	2.12	2.84
WI-STD-72, **UWArg-7**, G04-4	20.36	0.37	17.30	0.38	2.10	2.82
WI-STD-72, **UWArg-7**, G02-3	20.01	0.37	16.95	0.46	2.08	2.90
WI-STD-72, **UWArg-7**, G02-4	20.06	0.37	17.00	0.43	2.06	2.90
UWC-3 G1 #60			8.63	0.44	2.18	3.03
UWC-3 G1 #61			8.58	0.42	2.18	3.02
UWC-3 G1 #62			8.66	0.42	2.17	3.02
UWC-3 G1 #63			8.46	0.36	2.17	3.03
Bracket UWC-3 56-63		**0.37**	**8.48**			

Symbols:

*: $\delta^{18}O$ values are only reported on the VSMOW scale for Analysis Session 2, when ion microprobe measurements of UWArg-7 calibrate the instrumental mass fractionation difference (0.98 ‰) between aragonite and calcite. Data from Analysis Session 1 are uncalibrated.

2 s.d. of $\delta^{18}O$ values for each aragonite sample:

UWArg-4.1 (n=18): 0.91‰
UWArg-5 (n=33): 1.49‰
6501 (n=16): 1.68‰
1000.62 (n=18): 1.12‰
NS.1494.153 (n=16): 3.21‰
UWArg-7* (n=54)*: 0.56‰

Table A.7: Conventional analyses of $\delta^{18}O$ and $\delta^{13}C$ in UWArg-7 by phosphoric acid-digestion. Analysis by Mike Spicuzza and Ian Orland, 3/5/2012.

Book #	Sample #	mg powder	$\delta^{13}C$ (‰, VPDB)	$\delta^{18}O$ (‰, VSMOW)
C4-234-5	UWArg-7	5.22	6.01	20.04
C4-234-6	UWArg-7	4.89	6.00	20.03
C4-234-7	UWArg-7	5.20	5.94	20.02
C4-234-8	UWArg-7	5.21	5.99	20.03
		Average:	**5.99**	**20.03**
		2 s.d.	**0.06**	**0.02**

Note: Delta values are calculated using the CO_2(acid-aragonite) fractionation factor (α-value) at 25°C of 1.01034 (Friedman and O'Neil, 1977), and corrected to the VPDB and VSMOW scales by using the average values of NBS-19 calcite standard (*n*=2) measured during this analytical session (α=1.01025; Friedman and O'Neil, 1977). All measurements were performed with high-density (1.94) phosphoric acid (McCrea, 1950; Sharma and Clayton, 1965), with accepted values of NBS-19 from Gonfiantini et al. (1995).

Table A.8: Conventional analyses of $\delta^{18}O$ and $\delta^{13}C$ in UWArg-4.1 and UWArg-5 by phosphoric acid-digestion. Analysis by Mike Spicuzza and Ian Orland, 9/27/2011.

Book #	Sample #	mg powder	$\delta^{13}C$ (‰, VPDB)	$\delta^{18}O$ (‰, VSMOW)	Remark
C4-233-3	UWArg-4.1	6.72	7.52	23.45	
C4-233-4	UWArg-4.1	5.73	7.46	23.28	
C4-233-5	UWArg-4.1	7.28	7.46	23.32	
	Average (UWArg-4.1):		**7.48**	**23.35**	
C4-233-6	~~UWArg-5~~	7.58			lost during analysis
C4-233-7	UWArg-5	6.85	2.87	22.27	
C4-233-8	UWArg-5	6.58	2.87	22.24	
	Average (UWArg-5):		**2.87**	**22.26**	

Note: Delta values are calculated using the CO_2(acid-aragonite) fractionation factor (α-value) at 25°C of 1.01034 (Friedman and O'Neil, 1977), and corrected to the VPDB and VSMOW scales by using the value of NBS-19 calcite standard (*n*=1) measured during this analytical session (α=1.01025; Friedman and O'Neil, 1977). All measurements were performed with high-density (1.94) phosphoric acid (McCrea, 1950; Sharma and Clayton, 1965), with accepted values of NBS-19 from Gonfiantini et al. (1995).

Supplement A References:

Friedman I., and O'Neil J. R. (1977) Compilation of stable isotope fractionation factors of geochemical interest. In: Fleischer M. (Ed.), Data of Geochemistry Sixth Edition. U. S. Government Printing Office, Washington.

Gonfiantini R., Stichler W., and Rozanski K. (1995) Standards and intercomparison materials distributed by the International Atomic Energy Agency for stable isotope measurements. Reference and Intercomparison Materials For Stable Isotopes Of Light Elements: International Energy Agency, Vienna, Austria. 13–29.

Kozdon R., Ushikubo T., Kita N. T., Spicuzza M. and Valley J. W. (2009) Intratest oxygen isotope variability in the planktonic foraminifer *N. pachyderma:* Real vs. apparent vital effects by ion microprobe. *Chem. Geol.* **258**, 327-337.

McCrea J. M. (1950) On the isotopic chemistry of carbonates and a paleotemperature scale. *J. Chem. Phys.* **18**, 849–857.

Orland I. J, Bar-Matthews M., Kita N. T., Ayalon A., Matthews A. and Valley J. W. (2009) Climate deterioration in the eastern Mediterranean as revealed by ion microprobe analysis of a speleothem that grew from 2.2 to 0.9 ka in Soreq Cave, Israel. *Quat. Res.* **71**, 27-35.

Sharma T. and Clayton R.N. (1965) Measurement of O^{18}/O^{16} ratios of total oxygen of carbonates. *Geochim. Cosmochim. Acta* **29**, 1347–1353.

Supplement B: Preliminary results of $^{16}OH/^{16}O$ ratios measured during $\delta^{18}O$ analysis of carbonates by ion microprobe.

A number of workers in the WiscSIMS lab (Ian Orland, Reinhard Kozdon, Taka Ushikubo, Ken Williford, Ben Linzmeier) have an interest in assessing the influence of entrained organic material on isotope ratios measured by ion microprobe. Consequently, relative amounts of ^{16}OH sputtered during $\delta^{18}O$ analyses were assessed in selected carbonate samples by measuring the ^{16}OH peak (using a Faraday cup), which is separated from the ^{17}O peak at a mass resolving power of 5000. This measurement is particularly interesting for ion microprobe analysis of biogenic carbonates (e.g. foraminifera, otoliths, mollusks), where organic components (e.g. proteins) may be integrated into the carbonate matrix. We found that the $^{16}OH/^{16}O$ ratio could be used to evaluate the relative contribution of organic components to $\delta^{18}O$ measurements; no calibration exists for calculating the real $^{16}OH/^{16}O$ ratio. Since there is no analytical penalty for measuring $^{16}OH/^{16}O$ during $\delta^{18}O$ analyses using the multi-collector, this value is now measured routinely during WiscSIMS analyses of $\delta^{18}O$ in carbonates. This appendix documents $^{16}OH/^{16}O$ data collected since October 2011, when this ratio was first added to the $\delta^{18}O$ analysis routine.

Figure B.1 plots the raw $\delta^{18}O$ and $^{16}OH/^{16}O$ data from four analytical sessions of calcium carbonates with markedly different formation environments. Samples include three biogenic carbonates (nautilus, mollusk, and foraminifera tests) and two speleothems from Soreq Cave. Also included in the figure are analyses of UWC-3 (filled squares) from the nautilus session. Note that $^{16}OH/^{16}O$ ratios in UWC-3 are lower and more tightly grouped than any of the sample data. This result supports the hypothesis that $^{16}OH/^{16}O$ ratios are a proxy for organic content

since UWC-3 is an amphibolite facies marble from the Adirondacks (Kozdon et al., 2009). In the mollusk (Olson et al., 2012), foraminifera, and speleothem sessions, $^{16}OH/^{16}O$ values are generally <0.02 and there is no correlation between $\delta^{18}O$ and $^{16}OH/^{16}O$ values. Analyses of the nautilus (Linzmeier, 2012; UW MS thesis), however, return $^{16}OH/^{16}O$ values as high as 0.1 and show anti-correlation between $\delta^{18}O$ and $^{16}OH/^{16}O$ in subsets of the data.

Figures B.2 and 3 plot all values of $\delta^{18}O$ (uncorrected) and secondary ion yield against $^{16}OH/^{16}O$ ratios measured during the nautilus session. There are two notable features in these plots. First, there is a negative linear trend in Figure B.2 ($\delta^{18}O$ vs. $^{16}OH/^{16}O$) within both the main cloud of the nautilus data (black circles) as well as the measurements with elevated $^{16}OH/^{16}O$ ratios (red circles). These trends suggest that each nautilus measurement may represent a mix of two or possibly three components. Potential candidates for the non-aragonite components in this system include organic material and micron-scale fluid inclusions. The second notable feature is the elevated secondary ion yield (Figure B.3) of measurements with elevated $^{16}OH/^{16}O$ ratios (red circles). The increased yield in these analyses suggests that whatever additional components are included in the aragonite shell are ionized more efficiently than the aragonite itself.

Two pre-treatments were applied to separate portions of the nautilus sample in an attempt to remove the influence of organic material from ion microprobe analyses. Figure B.1 illustrates the effect that roasting (red circles) and hydrogen peroxide (green circles) have on nautilus $\delta^{18}O$ and $^{16}OH/^{16}O$ values. Roasting at 356°C for 3 hours in an evacuated quartz tube does not appear to change $\delta^{18}O$ or $^{16}OH/^{16}O$ values measured in the nautilus shell; results from the roasted portion reflect the pattern observed in the untreated shell. On the other hand, treating the analytical surface with hydrogen peroxide (Linzmeier, 2012) appears to systematically increase the

$^{16}OH/^{16}O$ value measured in the nautilus shell. Thus, these pre-treatment techniques do not appear to remove the organic signal.

Figure B.1: Raw (uncorrected) values of $\delta^{18}O$ versus the $^{16}OH/^{16}O$ ratio measured in five different types of calcium carbonates. Analyses in mollusk (open squares; Olson et al., 2012), foraminifera (diamonds), and speleothem (triangles) samples show little co-variance between $\delta^{18}O$ and $^{16}OH/^{16}O$. Two different speleothems are indicated by the shading of the triangle symbols: a portion of sample "2-20" (~9.5–7.0 ka; black triangles) and SO-38 (last ~50 years, gray triangles). Circles show results from ion microprobe analysis of a nautilus shell (Linzmeier, 2012). The colors illustrate the effect of two different pre-treatments on the untreated (blue) results. Roasting for 3 hours at 356°C in an evacuated quartz tube (red) does not appear to change the pattern of $\delta^{18}O$ vs. $^{16}OH/^{16}O$ variability. In contrast, the application of hydrogen peroxide to the sample surface (green) increases the $^{16}OH/^{16}O$ ratio measured on average in the nautilus. Analyses of UWC-3 calcite standard (amphibolite facies marble) are included here (filled squares) from the nautilus session as an example of a carbonate with no expected organic content (and a correspondingly low $^{16}OH/^{16}O$ ratio).

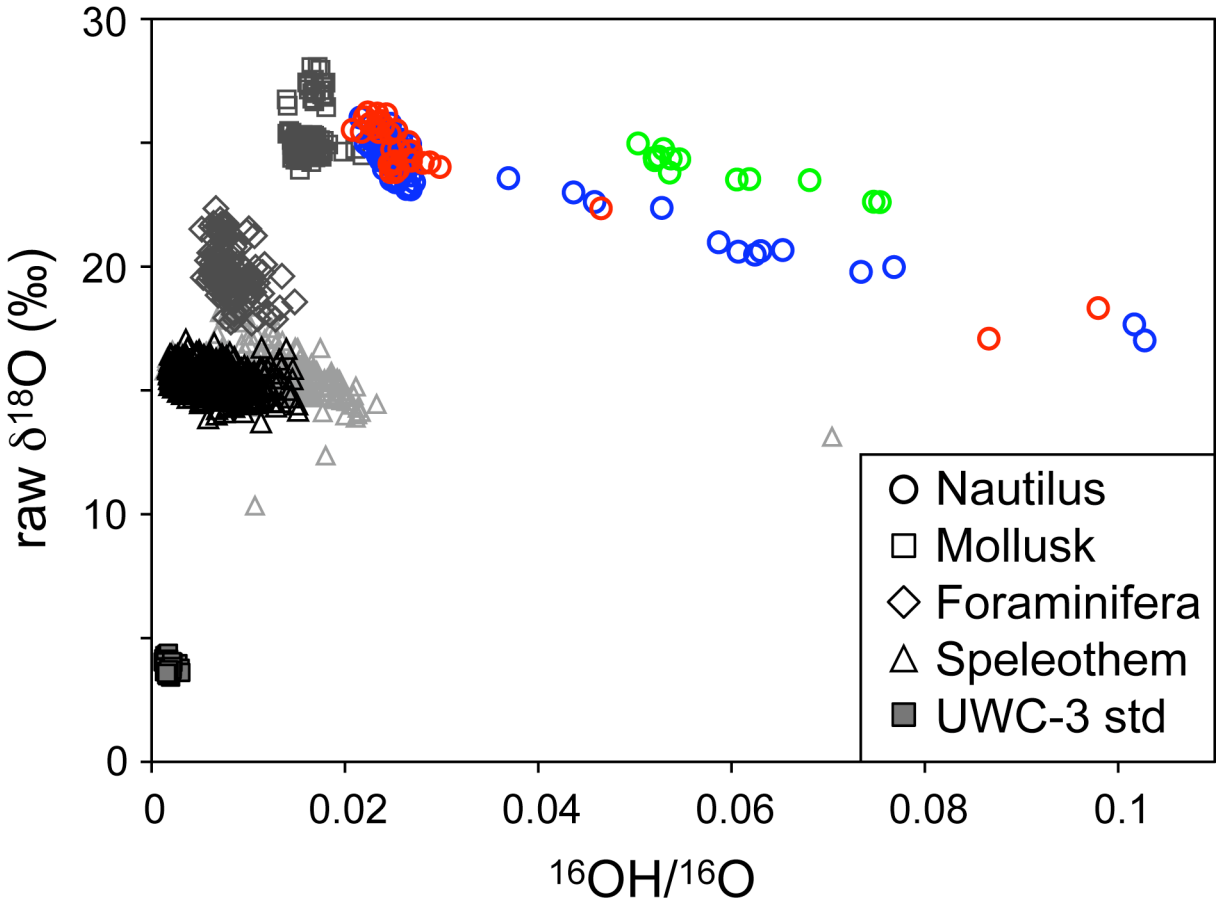

Figure B.2: Values of uncorrected $\delta^{18}O$ vs. $^{16}OH/^{16}O$ in an aragonite nautilus shell (circles; Linzmeier, 2012). Measurements with elevated $^{16}OH/^{16}O$ values are highlighted in red; the notable anti-correlation between $\delta^{18}O$ and $^{16}OH/^{16}O$ in these spots may be caused by variable amounts of organic material distributed within the aragonite shell structure (see text for discussion). Filled squares show measurements of UWC-3 calcite standard during the same analytical session.

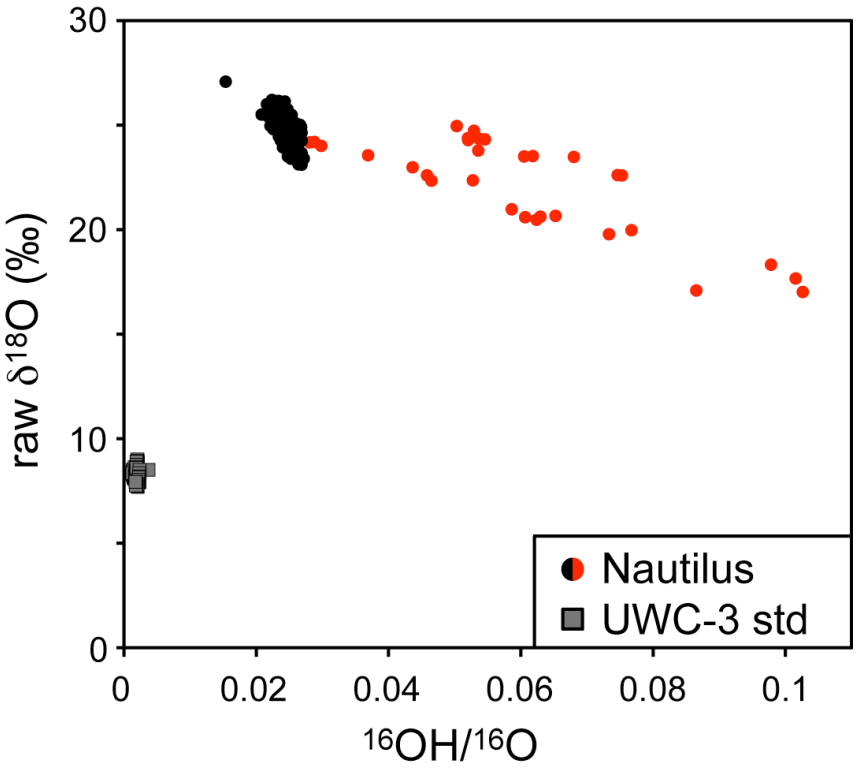

Figure B.3: Secondary ion yield (relative to the average yield of the bracketing UWC-3 analyses) and $^{16}OH/^{16}O$ values measured during $\delta^{18}O$ analysis of an aragonite nautilus shell (circles; Linzmeier, 2012). As in Figure B.2, analyses with elevated $^{16}OH/^{16}O$ values are highlighted in red. Increased secondary ion yields in the highlighted analyses suggest that whatever substance is causing the elevated $^{16}OH/^{16}O$ values is ionized more efficiently than aragonite. For reference, filled squares show results from UWC-3 calcite standard measurements made during the same analytical session.

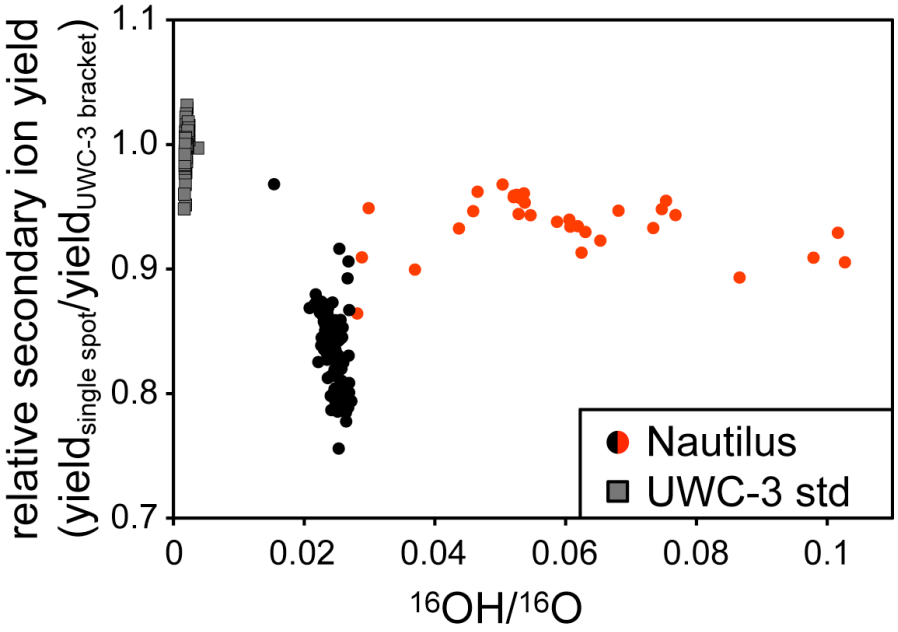

Supplement B References:

Friedman I., and O'Neil J. R. (1977) Compilation of stable isotope fractionation factors of geochemical interest. In: Fleischer M. (Ed.), Data of Geochemistry Sixth Edition. U. S. Government Printing Office, Washington

Kozdon R., Ushikubo T., Kita N. T., Spicuzza M. and Valley J. W. (2009) Intratest oxygen isotope variability in the planktonic foraminifer *N. pachyderma:* Real vs. apparent vital effects by ion microprobe. *Chem. Geol.* **258**, 327-337.

Linzmeier B. (2012) Depth migratory behavior elucidated by ion microprobe analysis of $\delta^{18}O$ within *Nautilus macromphalus* shell aragonite. University of Wisconsin-Madison, MS thesis.

Olson I. C., Kozdon R., Valley J. W., and Gilbert P.U.P.A. (2012) Mollusk shell nacre ultrastructure correlates with environmental temperature and pressure. *J. Amer. Chem. Soc.* **134**, 7351-7358.

Supplement C: Raman spectroscopy of Soreq Cave stalactite sample 2N.

The cause of the fluorescent banding in Soreq Cave speleothems remains to be fully resolved. In speleothems from many caves, natural organic matter is the common cause of fluorescence (Lauritzen et al., 1986; White and Brennan, 1989; Tan et al., 2006; Baker et al., 2008). In Soreq Cave, trace element analyses of the modern stalagmite 5-3b (see Chapter 3) find a co-variation between fluorescence intensity and concentrations of P and Cu, which have been linked to organic colloid transport in other cave settings (Borsato et al., 2007; Fairchild and Treble, 2009). These observations support the inference that organic molecules are the source of fluorescence in Soreq speleothems (Orland et al., 2009). However, direct chemical evidence of the type or abundance of organic molecules is yet to be measured.

Chemical characterization of lipid biomarkers within speleothems has been achieved with bulk-analysis techniques (Blyth et al., 2007; Rushdi et al., 2011), but these studies have low temporal resolution because of the amount of material required to obtain a sufficient signal. Spectral imaging of fluorescence (Perrette et al., 2005; Jex et al., 2008) is capable of annual resolution, but signal calibration is lacking. Raman spectroscopy has been used to characterize organic material in Precambrian microfossils (Schopf et al., 2002), but similar interpretations are unreported in speleothems. We collaborated with Prof. J. W. Schopf at UCLA to analyze a portion of Soreq sample 2N by Raman, with hopes of identifying (1) an "organic" signal that varies with fluorescence across individual bands, and (2) changes in the character of the organic signal that may reflect variability of the overlying vegetation.

The epoxy mount with chips A and B (~4.0–5.0 ka) from sample 2N were sent to Prof. Schopf. We chose to target an area in chip B with distinct, wide, sawtooth fluorescent bands

(Figure C.1). A rectangular Raman transect was made across one of the highly fluorescent bands (blue box, Figure C.2) using the UCLA T64000 (JY Horiba, Edison NJ) triple-stage laser-Raman system. Three Raman spectra were then integrated at depths of 0, 3, and 5 μm below the sample surface over the portion of the rectangular transect with the brightest fluorescence (black box, Figure C.2). All three spectra returned similar results, one of which is shown in Figure C.3. Figure C.3 shows the distinct spectral lines for calcite, but nothing more. Where spectral lines of kerogen might be expected (red lines, Figure C.3), there are no resolved peaks. Thus, unfortunately, it was not possible to characterize organic material in sample 2N.

There are two possible explanations for these results. Either there is no organic material present, or it is present but below detection limit. Prof. Schopf preferred the latter interpretation, namely that organic material may exist in the sample but its spectral signal is “swamped out” by the bright green fluorescence shown in the lower panel of Figure C.1.

Figure C.1: Upper panel shows a reflected light image (0.8 x 0.8 mm field of view, growth direction is right-to-left) of the portion of sample 2N (chip B) targeted for Raman spectroscopy. The red lines indicate potential traverse locations suggested prior to analysis. The gray box outlines the area shown in Figure C.2, note the black spot (small pore in the sample) used as a location reference. The **lower panel** is the same field of view imaged with a confocal laser fluorescent microscope in order to show to location of the fluorescent banding.

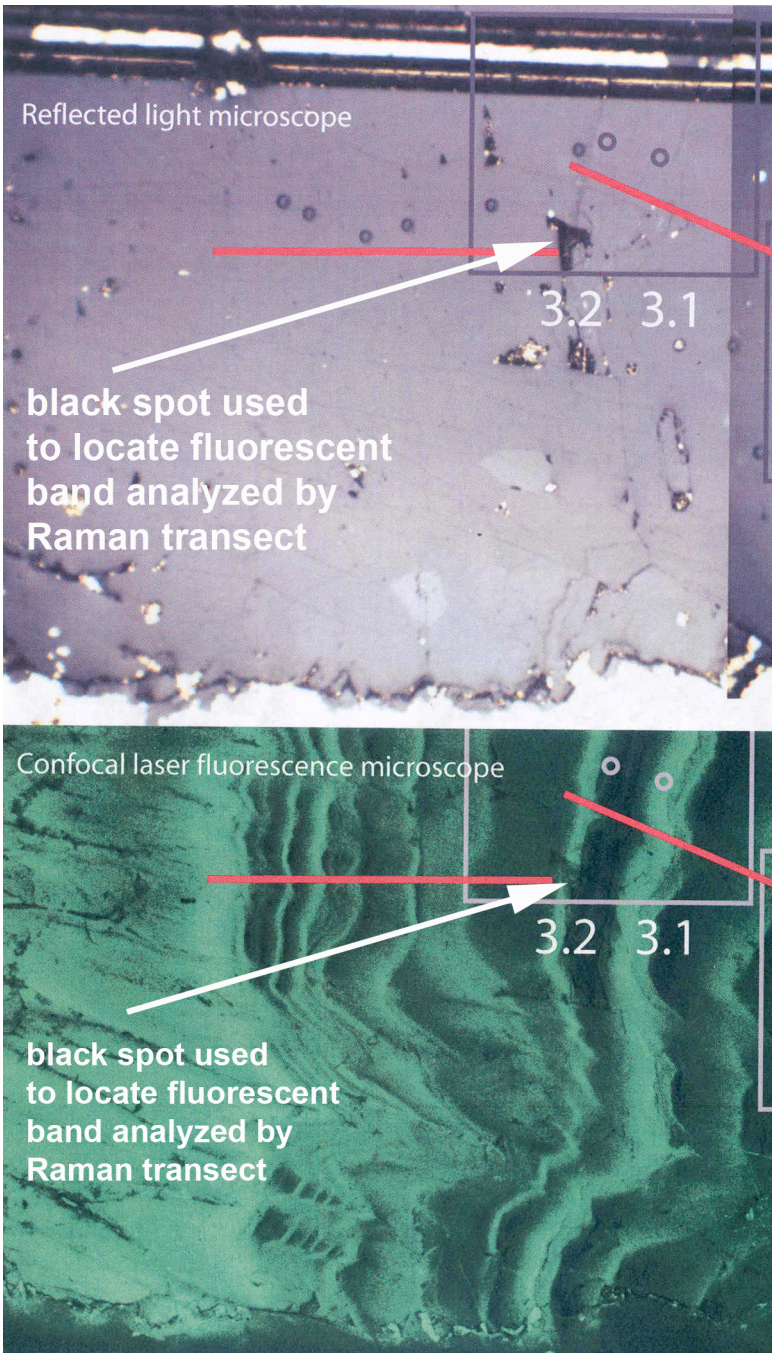

Figure C.2: The blue rectangle indicates the transect in sample 2N scanned by the 457.9 nm-wavelength laser for Raman analysis (field of view: 110 x 150 μm). Within the blue rectangle, bright blue areas are highly fluorescent material. The fluorescent area near the center of the image is part of the fluorescent band shown in Figure C.1 the crosses the "black spot." The black box that outlines the fluorescent material shows the area integrated to produce the Raman spectrum in Figure C.3. (Figure courtesy of J. W. Schopf, UCLA)

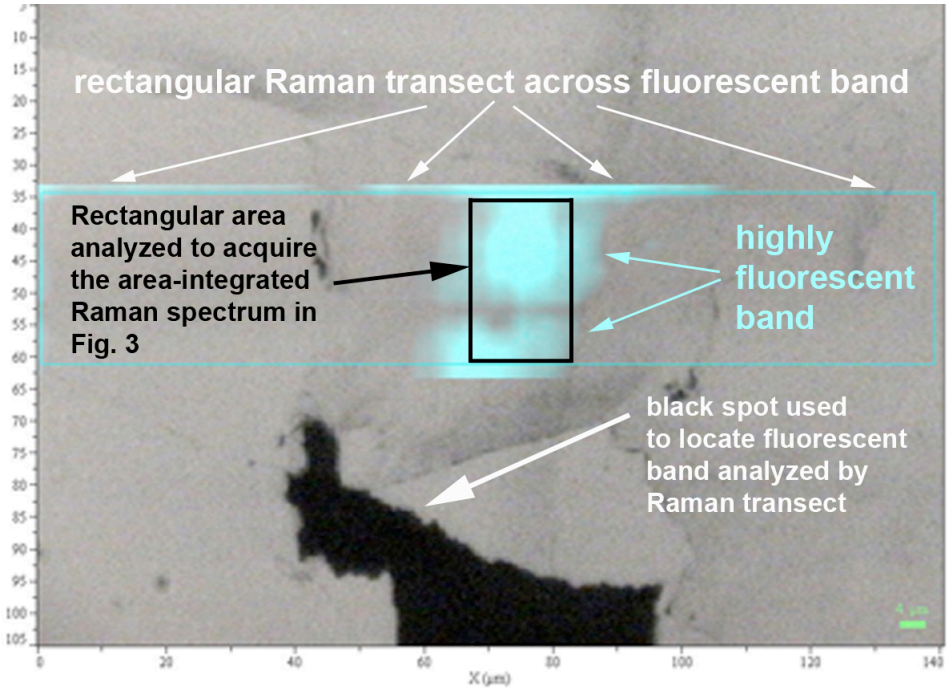

Figure C.3: Area-integrated Raman spectrum of the fluorescent band outlined (black box) in Figure C.2. The plot shows the intensity (counts per second) of light emitted across a range of wavelengths relative to the incident laser (termed the "Raman shift", cm^{-1}). Major and minor spectral bands for calcite are apparent. At Raman-shift wavelengths that are characteristic of carbonaceous matter (red bars), there are no obvious spectral peaks. It is possible that organic matter exists in the sample, but that fluorescence (indicated below) washes out the expected signal. There are some peaks in the fluorescence signal, but these are apparently noise. (Figure and interpretation courtesy of J. W. Schopf, UCLA)

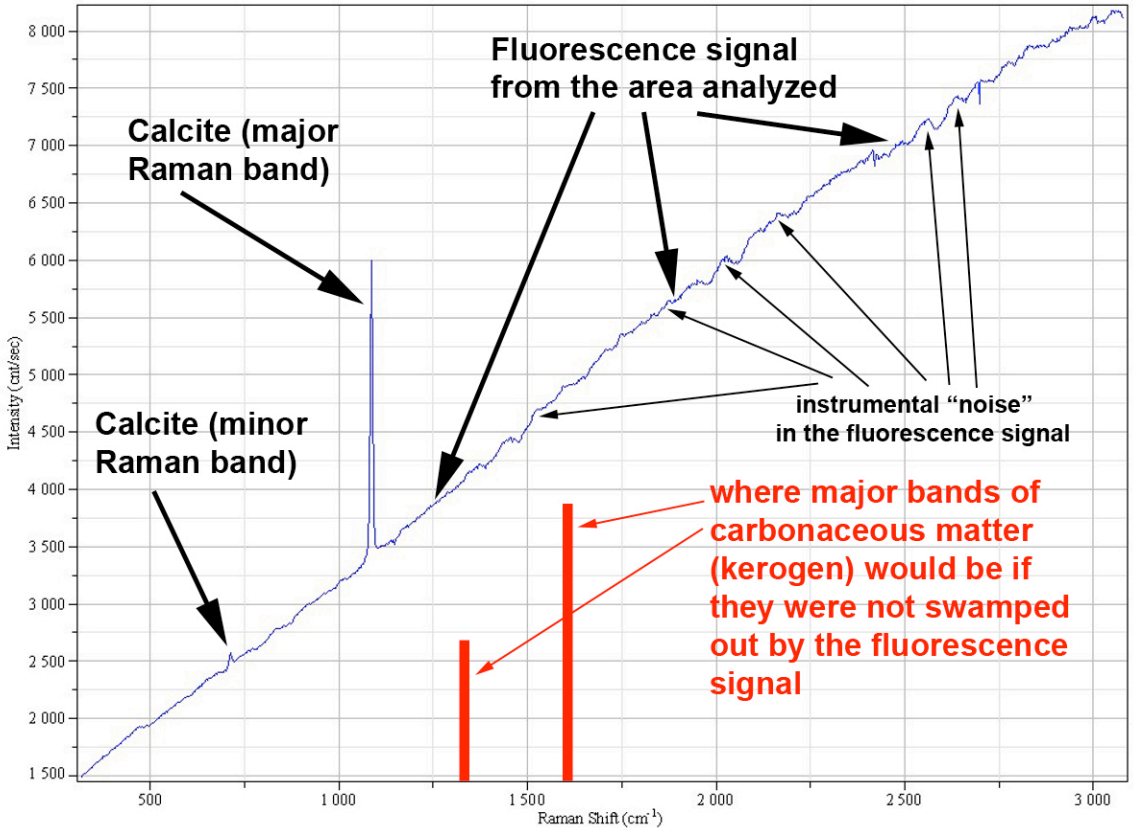

Supplement C References:

Baker A., Smith C. L., Jex C., Fairchild I. J., Genty D., and Fuller L. (2008) Annually laminated speleothems: a review. *Int. J. Spel.* **37**, 193-206.

Blyth A. J., Asrat A., Baker A., Gulliver P., Leng M. J., and Genty D. (2007) A new approach to detecting vegetation and lan-use change using high-resolution lipid biomarker records in stalagmites. *Quaternary Research* **68**, 314-324.

Borsato A., Frisia S., Fairchild I. J., Somogyi A. and Susini J. (2007) Trace element distribution in annual stalagmite laminae mapped by micropmeter-resolution X-ray fluorescence: Implications for incorporation of environmentally significant species. *Geochimica et Cosmochimica Acta* **71**, 1494-1512.

Fairchild I. J. and Treble P. C. (2009) Trace elements in speleothems as recorders of environmental change. *Quat. Sci. Rev.* **28**, 449-468.

Friedman I., and O'Neil J. R. (1977) Compilation of stable isotope fractionation factors of geochemical interest. In: Fleischer M. (Ed.), Data of Geochemistry Sixth Edition. U. S. Government Printing Office, Washington.

Jex C., Claridge E., Baker A., and Smith C. (2008) Hyperspectral imaging of speleothems. *Quaternary International* **187**, 5-14.

Lauritzen S. E., Ford D. C., and Schwarz H. P. (1986) Humic substances in a speleothem matrix. Proceedings of the 9th International Congress of Speleology, 77-79.

Orland I. J, Bar-Matthews M., Kita N. T., Ayalon A., Matthews A. and Valley J. W. (2009) Climate deterioration in the eastern Mediterranean as revealed by ion microprobe analysis of a speleothem that grew from 2.2 to 0.9 ka in Soreq Cave, Israel. *Quat. Res.* **71**, 27-35.

Perrette Y., Delannoy J.-J., Desmet M., Lignier V., and Destombes J.-L. (2005) Speleothem organic matter content imaging. The use of a Fluorescence Index to characterize the maximum emission wavelength. *Chem. Geol.* **214**, 193-208.

Rushdi A. I., Clark P. U., Mix A. C., Ersek V., Simoneit B. R. T., Cheng H. and Edwards R. L. (2011) Composition and sources of lipid compounds in speleothem calcite from southwestern Oregon and their paleoenvironmental implications. *Environ. Earth Sci.* **62**, 1245-1261.

Schopf J. W., Kudryavtsev A. B., Agresti D. G., Wdowiak T. J., and Czaja A. D. (2002) Laser-Raman imagery of Earth's earliest fossils. *Nature* **416**, 73-76.

Tan M., Baker A., Genty D., Smith C., Esper J., and Cai B. (2006) Applications of stalagmite laminae to paleoclimate reconstructions: Comparison with dendrochronology/ climatology. *Quat. Sci. Rev.* **25**, 2103-2117.

White W. B., and Brennan E. S. (1989) Luminescence of speleothems due to fulvic acid and other activators. Proceedings of the 10th International Congress of Speleology, 212-214.

Supplement D: Inter-lab comparison of $\delta^{18}O$ data from sample SVC-982, Spring Valley Caverns, MN, USA.

A collaborative project was initiated with Prof. R. L. Edwards at the University of Minnesota (UMinn) to analyze seasonal $\delta^{18}O$ variability in a calcite speleothem that records recent climate change. Stalagmite sample SVC-982 was collected by Prof. C. Alexander (UMinn) from Spring Valley Caverns in southeastern Minnesota. Fluorescent banding was identified by confocal laser fluorescent microscopy at UMinn by Dr. Sushmita Dasgupta and, in combination with U-series geochronology, interpreted as annual growth banding. U-series geochronology and band-counting indicate the sample grew from 546 ± 14 years BP (1950) to AD 1971.

WiscSIMS analysis of SVC-982 did not reveal a regular pattern of $\delta^{18}O$ variability across fluorescent bands dated between 1784 and 1971 (Orland, 2008; UW MS thesis). There was a discrepancy, however, between the ion microprobe $\delta^{18}O$ data reported in Orland (2008) and $\delta^{18}O$ values measured by conventional phosphoric acid-digestion techniques at UMinn (Dasgupta, 2008; UMinn PhD dissertation). As illustrated in Figure D.1, both analytical techniques measure a range of $\delta^{18}O$ values in sample SVC-982, but an offset is apparent. This section explains a series of tests that demonstrate congruence between the analytical techniques.

First, five conventional $\delta^{18}O$ analyses were made at UW across the same portion of the sample analyzed by ion microprobe (Figure D.2). Between 0.66 and 0.95 mg of calcite powder was removed by micro-mill from six growth bands (one was lost during sample preparation) and analyzed for $\delta^{18}O$ at the UW stable isotope lab using standard phosphoric acid techniques (Table D.4; analysis by Mike Spicuzza and Ian Orland). Results show a smaller offset than previously

measured, with a difference between the average ion microprobe and UW conventional values of 0.57‰ (Figure D.1A). Note that the sum of the average 2 s.d. for WiscSIMS and UW conventional analyses (0.50‰) is nearly as large as the observed offset. Furthermore, the UW conventional $\delta^{18}O$ measurements are relatively consistent across the sample – similar to WiscSIMS measurements – and do not reflect the range of $\delta^{18}O$ values reported from UMinn (Figure D.1B).

A second test was devised to see if the original ion microprobe data were biased by organic material in the sample. Similar to the process used to remove organic matter from biogenic carbonates, a slice of sample SVC-982 was roasted at 356°C for 3 hours in an evacuated quartz-tube. The 1x1x10 mm portions of sample SVC-982 used for roasting were cut from the original slab to match the two 1 cm-long chips already analyzed by ion microprobe (Figure D.3). Each roasted chip was cast in epoxy such that the analytical face matched that of the original ion microprobe mount. Figure D.1 shows the $\delta^{18}O$ values measured in the roasted portion by ion microprobe; roasting does not appear to significantly change the measured $\delta^{18}O$ value. In fact, the average $\delta^{18}O$ value measured in the roasted sample is only 0.14‰ lower than in the unroasted sample.

Although there is still a slight $\delta^{18}O$ offset between WiscSIMS and conventional results from UW, the above tests demonstrate compatibility of the two analytical techniques. Two issues remain, however: (1) the increase in UMinn conventional $\delta^{18}O$ values between 1000 and 2000 μm depth in SVC-982, and (2) the offset between UW and UMinn conventional values. With regard to the elevated $\delta^{18}O$ values, it is noted that a stalagmite growing only a few meters from SVC-982 in Spring Valley Cavern (named “SVC-983”) does not corroborate the $\delta^{18}O$ increase. SVC-983 data were acquired from Appendix 2.1 (p. 157) of Dasgupta (2008), and a simple linear

conversion was made between the reported age of each analysis to the corresponding depth in the annually-banded SVC-982. As for the offset between UW and UMinn conventional analyses, a test has been arranged to determine if inter-lab standard calibration is responsible for the consistent $\delta^{18}O$ offset.

Ion microprobe results from SVC-982 are tabulated by Orland (2008; see Appendix 7). Ion microprobe results from the roasting experiment as well as imaging of each analysis location are included in the data repository (DRSupp.1).

Figure D.1: Results of all conventional phosphoric-acid (filled squares) and ion microprobe (triangles) $\delta^{18}O$ analyses in sample SVC-982. Panel **A** shows that conventional analyses made at UW (blue squares) have a consistent, but reasonable, offset from ion microprobe results. Panel **B** shows that UMinn conventional analyses (filled red squares) are offset in the opposite direction from UW conventional measurements and increase below 10,000 μm depth. The open red squares show conventionally-measured $\delta^{18}O$ values from sample SVC-983 (adjacent to sample SVC-982 in Spring Valley Caverns) plotted versus depth in SVC-982 using annually-resolved ages (Dasgupta, 2008). The ion microprobe $\delta^{18}O$ results from the roasted portion of sample SVC-982 (brown triangles) have a small (0.14‰) offset from the unroasted analyses (orange triangles), suggesting that a roasting procedure to remove organic components is unnecessary for speleothem $\delta^{18}O$ measurements. In both panels, vertical error bars show 2 s.d. reproducibility; horizontal error bars on UW conventional measurements show width of drill trench (Figure D.2).

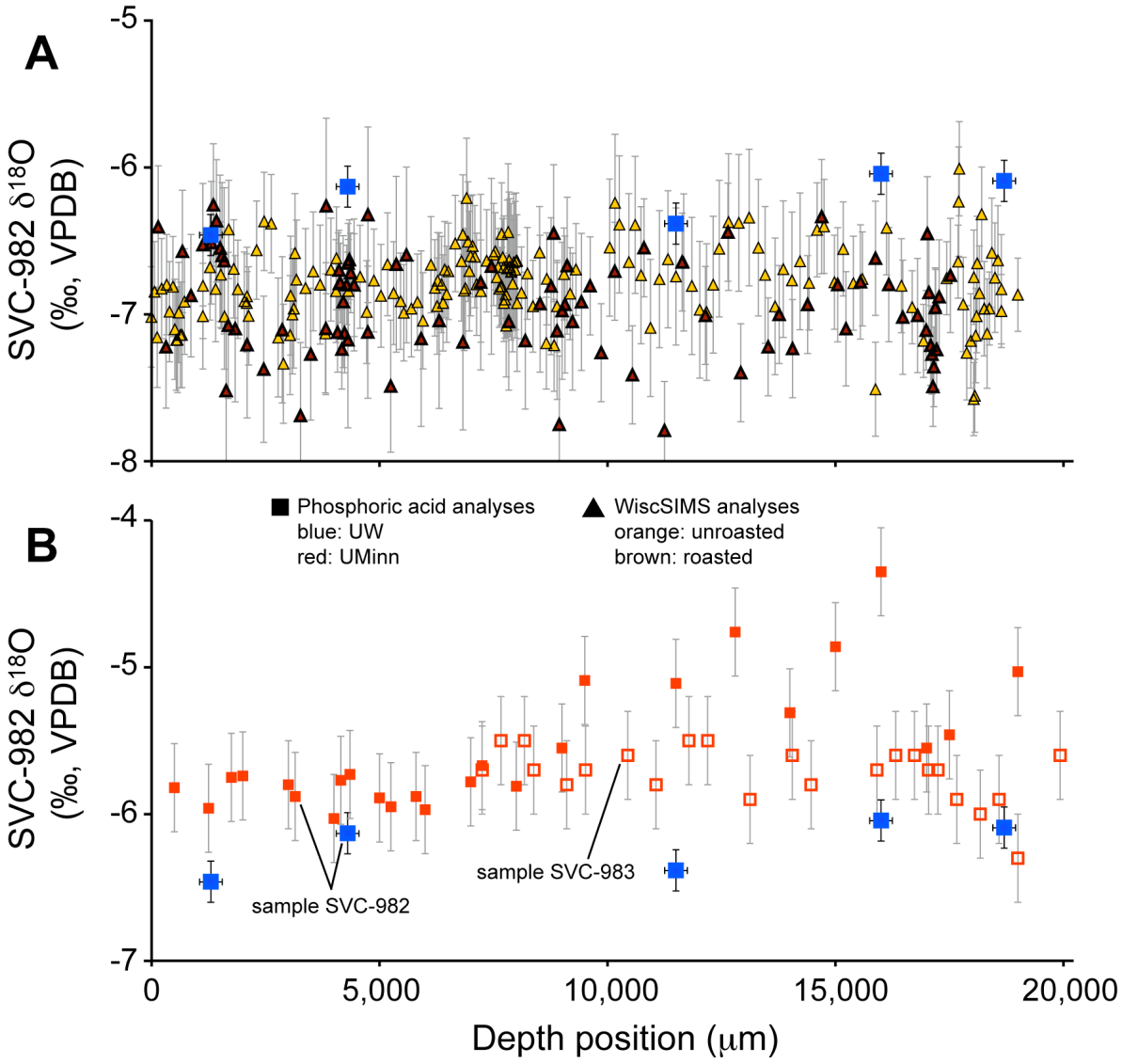

Figure D.2: The black ovals labeled 1.1-1.3 and 2.1-2.3 outline the micro-milled trenches in sample SVC-982 analyzed by conventional phosphoric-acid techniques at UW. The $\delta^{18}O$ values measured in each trench are listed in Table D.4. The 1-inch epoxy mount pictured here is the same mount used for ion microprobe analysis of $\delta^{18}O$ reported in Orland (2008). For reference, the top of the stalagmite is marked by the red dashed line and the growth direction is shown by the black arrows.

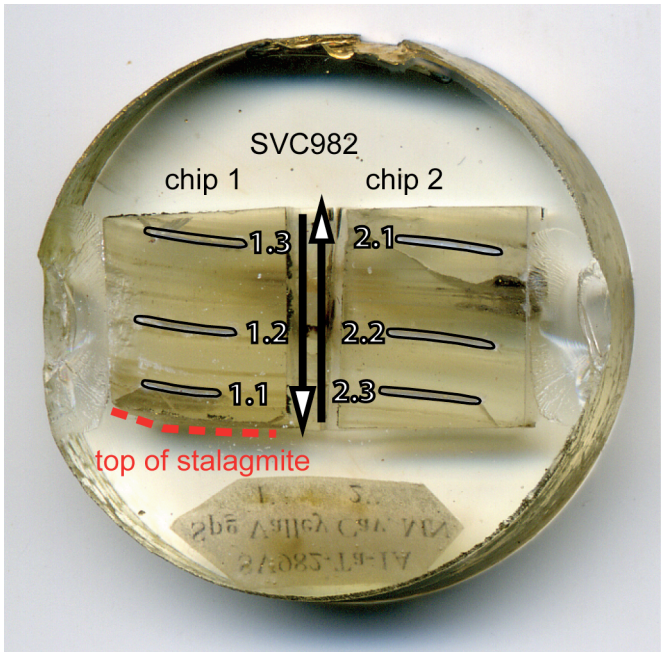

Figure D.3: Optical image showing the portions of sample SVC-982 (red dashed outline) removed for the roasting test. These two chips (~1x1x10 mm) were roasted in an evacuated quartz tube at 356 °C for 3 hours, then mounted along with three UWC-3 calcite standard grains in a 1 inch epoxy round for ion microprobe analysis.

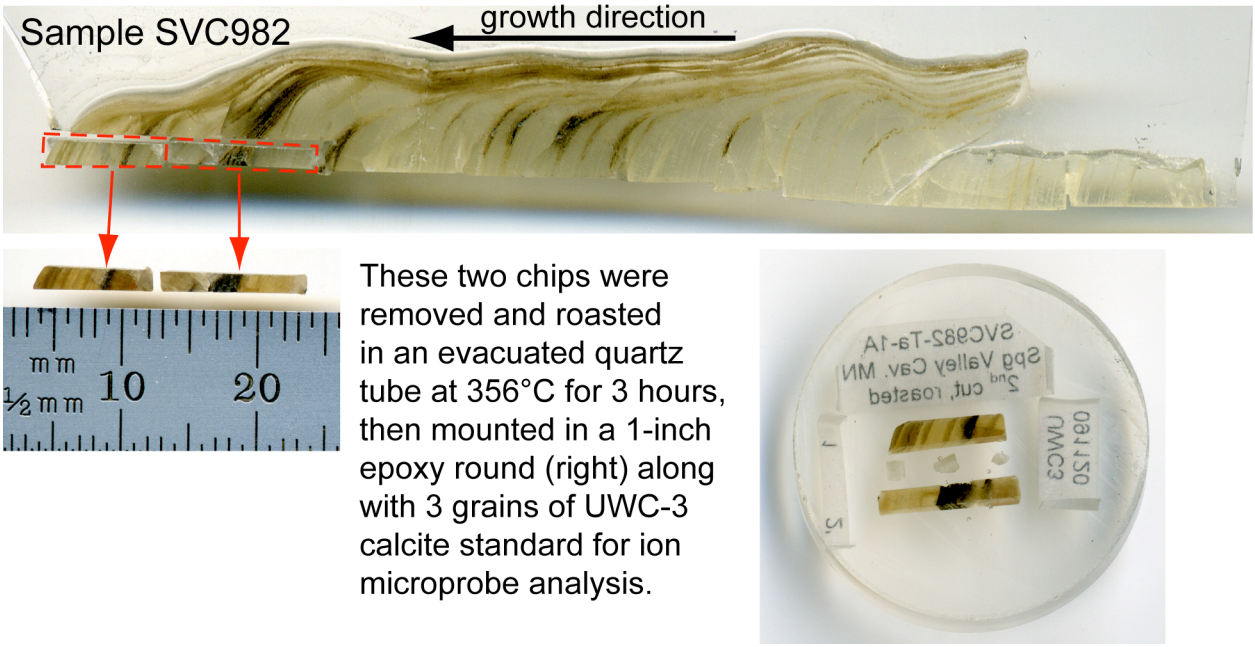

Table D.4: Conventional $\delta^{18}O$ analysis of five aliquots from calcite sample SVC-982 by phosphoric acid-digestion. Analysis by Mike Spicuzza and Ian Orland, 11/13/2009.

Book #	Sample #	mg powder	$\delta^{13}C$ (‰, VPDB)	$\delta^{18}O$ (‰, VSMOW)
C4-232-5	SVC982-1.1	0.68	**-9.56**	**24.25**
C4-232-6	SVC982-1.2	0.68	**-8.36**	**24.59**
C4-232-8	SVC982-2.1	0.95	**-9.26**	**24.33**
C4-232-9	SVC982-2.2	0.66	**-8.59**	**24.68**
C4-232-10	SVC982-2.3	0.80	**-7.97**	**24.63**
2 s.d. of 3 NBS-19 measurements:			**0.05**	**0.14**

Notes: Powder from sample SVC-982-1.3 (Figure D.2) was lost during preparation. Delta values are calculated using the CO_2(acid-calcite) fractionation factor (α-value) at 25°C of 1.01025 (Friedman and O'Neil, 1977), and corrected to the VPDB and VSMOW scales by using the average values of NBS-19 calcite standard (*n*=3) measured during this analytical session. The reproducibility of both $\delta^{13}C$ and $\delta^{18}O$ values is reported as two times the s.d. of the three NBS-19 analyses. All measurements were performed with high-density (1.94) phosphoric acid (McCrea, 1950; Sharma and Clayton, 1965), with accepted values of NBS-19 from Gonfiantini et al. (1995).

Supplement D References:

Dasgupta S. (2008) High-resolution speleothem record of Late Quaternary climate change from the upper Midwest, USA. University of Minnesota, PhD dissertation.

Friedman I., and O'Neil J. R. (1977) Compilation of stable isotope fractionation factors of geochemical interest. In: Fleischer M. (Ed.), Data of Geochemistry Sixth Edition. U. S. Government Printing Office, Washington.

Gonfiantini R., Stichler W., and Rozanski K. (1995) Standards and intercomparison materials distributed by the International Atomic Energy Agency for stable isotope measurements. Reference and Intercomparison Materials For Stable Isotopes Of Light Elements: International Energy Agency, Vienna, Austria. 13–29.

McCrea J. M. (1950) On the isotopic chemistry of carbonates and a paleotemperature scale. *J. Chem. Phys.* **18**, 849–857.

Orland I. J. (2008) Climate deterioration in the Eastern Mediterranean as revealed by ion microprobe analysis of a speleothem that grew from 2.2 to 0.9 ka in Soreq Cave, Israel. University of Wisconsin-Madison, MS thesis.

Sharma T. and Clayton R.N. (1965) Measurement of O^{18}/O^{16} ratios of total oxygen of carbonates. *Geochim. Cosmochim. Acta* **29**, 1347–1353.

Supplement D Data Repository:

Large data tables and figures for each chapter are included in the supplementary files available with the online version of this dissertation.

DRSupp.1: Ion microprobe raw and corrected oxygen isotope ratios from 89 analyses of a roasted portion of sample SVC-982 from Spring Valley Caverns, MN.

DRSupp.2: Reflected light and CLFM images from the roasted portion of sample SVC-982 (two chips) with ion microprobe analysis spots indicated.

Supplement E: Comparison of $\delta^{18}O$ data from ion microprobe and acid-digestion analysis of Soreq Cave sample 2N.

A portion of sample 2N that was analyzed for $\delta^{18}O$ by ion microprobe (chips C and D) was sent to the Geological Survey of Israel (GSI) for conventional acid-digestion analysis. A 0.5-mm-diameter drill bit was used to extract calcite powder from 14 spots in the same epoxy round used for ion microprobe analysis (Figure E.1). Table E.2 lists the $\delta^{18}O$ and $\delta^{13}C$ values (‰, VPDB) of the 14 conventional measurements.

In order to preserve the ion microprobe pits in chips C and D, the drilled spots were placed along the opposite edge of the analytical traverse delineated in Figure 2.1. High-resolution images of fluorescent banding in chips C and D (DR2.2) were compared with an optical image of the epoxy mount that was acquired with a flat-bed scanner (Figures E.3 and E.4, respectively). The locations of the drilled spots were then projected on the ion microprobe analytical traverse; Figure E.5 plots $\delta^{18}O$ values of ten drilled spots versus their projected position along the ion microprobe traverse. The remaining four drill spots are within bands that curve off the sample chips, and thus are not compared to ion microprobe analyses.

Figure E.5 shows that the average $\delta^{18}O$ value of all 184 ion microprobe analyses in chips C and D is 0.50‰ lower than the average $\delta^{18}O$ of the ten acid-digestion analyses. Table E.6 refines the value of the $\delta^{18}O$ offset by only comparing acid-digestion analyses to ion microprobe spots that they overlap. By this comparison, ion microprobe $\delta^{18}O$ analyses (n=85) are 0.45‰ lower than the corresponding acid-digestion measurements. The standard deviation of the offset for the 85 ion microprobe spots is 0.56‰, which highlights the significant amount of variability that is incorporated into each drill-spot measurement. Furthermore, we note that since each drill-

spot is placed within bands that are approximately parallel, more weight is given to the $\delta^{18}O$ value of a band running through the center of the spot than bands near the edge of the spot. Thus, a large population of ion microprobe pits is needed in order to obtain an accurate comparison of the two methods in a heterogeneous sample. Going forward, we will continue to compare the two analytical methods by preferentially mounting portions of samples for ion microprobe analysis that have already been drilled for acid-digestion.

Figure E.1: Scanned image of the 1-inch-diameter epoxy mount 2N-CD, with labeled drill-spots used for acid-digestion analysis of $\delta^{18}O$.

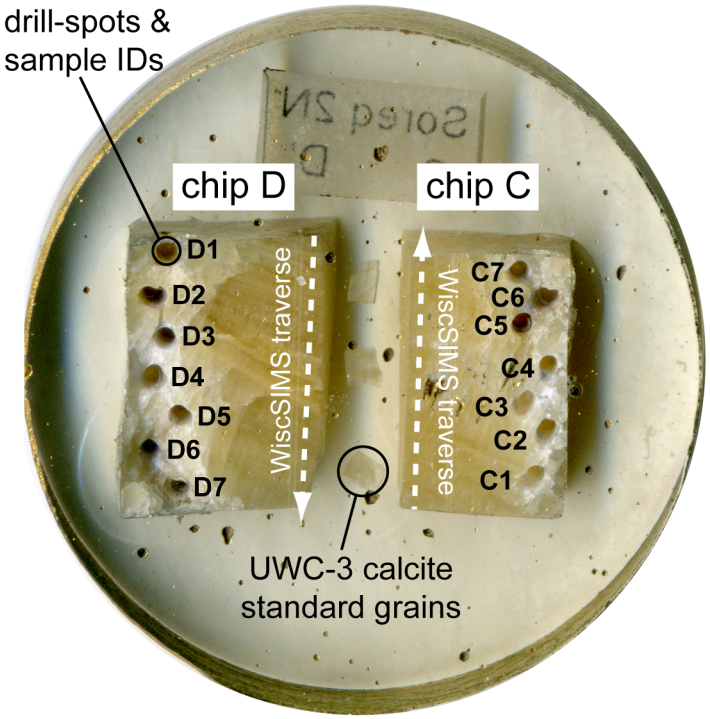

Table E.2: Values of $\delta^{18}O$ (‰, VPDB and VSMOW) and $\delta^{13}C$ (VPDB) measured by conventional acid-digestion at the Geological Survey of Israel. Analysis by Yuval Burstyn at the Geological Survey of Israel, 1/13/2012.

Sample ID	$\delta^{13}C$ (VPDB)	$\delta^{18}O$ (VPDB)	$\delta^{18}O$ (VSMOW)
2N-C1	-11.15	-5.51	25.23
2N-C2	-11.43	-5.58	25.15
2N-C3	-11.33	-5.64	25.10
2N-C4	-11.62	-5.39	25.36
2N-C5	-12.17	-6.11	24.61
2N-C6	-12.38	-5.90	24.83
2N-C7	-11.75	-5.48	25.27
2N-D1	-11.64	-6.22	24.50
2N-D2	-11.79	-5.99	24.74
2N-D3	-11.24	-5.49	25.25
2N-D4	-11.37	-5.47	25.27
2N-D5	-11.84	-6.28	24.44
2N-D6	-11.71	-5.89	24.84
2N-D7(6)	-11.65	-5.68	25.05

Figure E.3: Projection of the spots in chip 2N-C drilled for acid-digestion $\delta^{18}O$ analysis (red circles) onto the ion microprobe analytical traverse. The gray bars on the ion microprobe traverse (composite CLFM image) indicate the range of calcite sampled by each drill-spot. Table E.6 lists the ion microprobe analyses that each drill spot overlaps.

Figure E.4: Projection of the spots in chip 2N-D drilled for acid-digestion $\delta^{18}O$ analysis (red circles) onto the ion microprobe analytical traverse. The gray bars on the ion microprobe traverse (composite CLFM image) indicate the range of calcite sampled by each drill-spot. Table E.6 lists the ion microprobe analyses that each drill spot overlaps.

Figure E.5: Values of $\delta^{18}O$ in chips C and D of sample 2N measured by ion microprobe (blue crosses, green triangles, black squares) and acid-digestion (red circles). Brackets delineate the length of the analytical traverse in each ~1 cm chip. The color of each ion microprobe spot indicates its fluorescence classification (see legend). The position of each acid-digestion drill-spot is a projection onto the ion microprobe traverse (as in Figures E.3 and E.4); horizontal bars indicate the width of each drill-spot projected onto the ion microprobe traverse. Drill-spots that do not overlap completely with the ion microprobe traverse are excluded (analysis numbers 6 and 7 in each chip; Table E.2, Figures E.3 and E.4). The horizontal dashed lines illustrate the 0.50‰ offset between the average $\delta^{18}O$ values of all acid-digestion (red) and ion microprobe (gray) analyses along the analytical traverse of chips C and D. Table E.6 shows that the $\delta^{18}O$ offset is reduced (0.45‰) if the acid-digestion analyses are compared only to the ion microprobe spots that they overlap.

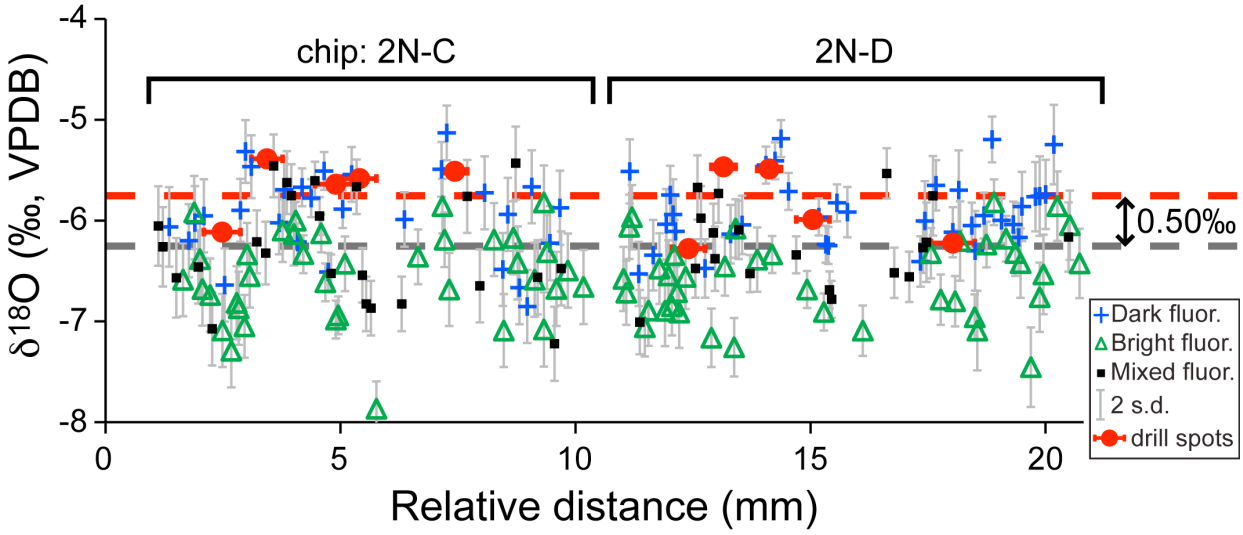

Table E.6: Comparison of 85 $\delta^{18}O$ values (‰, VPDB) measured by ion microprobe (10-μm-spots by WiscSIMS) and the corresponding $\delta^{18}O$ of 10 acid-digestion analyses (0.5-mm-spots) in chips C and D of sample 2N. The WiscSIMS sample names correspond to the analyses tabulated in Data Repository Table DR2.1.

Acid-digestion sample ID	$\delta^{18}O$ (VPDB)	WiscSIMS sample name	$\delta^{18}O$ (VSMOW)	$\delta^{18}O$ (VPDB)	$\delta^{18}O$ offset (SIMS-acid)
		2N-C-025	24.97	-5.76	-0.25
		2N-C-026	24.02	-6.68	-1.17
		2N-C-027	25.62	-5.13	0.38
		2N-C-028	24.53	-6.19	-0.68
		2N-C-029	25.25	-5.49	0.02
		2N-C-030	24.87	-5.86	-0.35
2N-C1	-5.51	**WiscSIMS average:**		-5.85	**-0.34**
		2N-C-034	22.80	-7.87	-2.28
		2N-C-035	23.83	-6.87	-1.29
		2N-C-036	23.87	-6.83	-1.24
		2N-C-037	24.17	-6.54	-0.96
		2N-C-038	25.07	-5.66	-0.08
		2N-C-039	25.20	-5.54	0.04
		2N-C-040	24.28	-6.43	-0.85
		2N-C-041	24.84	-5.89	-0.30
2N-C2	-5.58	**WiscSIMS average:**		-6.45	**-0.87**
		2N-C-038	25.07	-5.66	-0.03
		2N-C-039	25.20	-5.54	0.10
		2N-C-040	24.28	-6.43	-0.79
		2N-C-041	24.84	-5.89	-0.25
		2N-C-042	23.76	-6.94	-1.30
		2N-C-043	23.71	-6.98	-1.34
		2N-C-044	24.18	-6.52	-0.88
		2N-C-045	24.20	-6.51	-0.87
		2N-C-046	24.09	-6.61	-0.97
		2N-C-047	24.77	-5.96	-0.32
		2N-C-048	25.23	-5.51	0.13
		2N-C-049	24.59	-6.13	-0.49
		2N-C-050	25.13	-5.60	0.03
2N-C3	-5.64	**WiscSIMS average:**		-6.18	**-0.54**
		2N-C-060	24.62	-6.10	-0.71
		2N-C-061	24.70	-6.02	-0.63
		2N-C-062	25.28	-5.46	-0.07
		2N-C-063	24.39	-6.32	-0.93
		2N-C-064	24.51	-6.21	-0.82
		2N-C-065	25.28	-5.47	-0.08
2N-C4	-5.39	**WiscSIMS average:**		-5.93	**-0.54**
		2N-C-070	24.83	-5.90	0.22
		2N-C-071	23.83	-6.87	-0.76
		2N-C-072	23.39	-7.29	-1.18

Acid-digestion sample ID	$\delta^{18}O$ (VPDB)	WiscSIMS sample name	$\delta^{18}O$ (VSMOW)	$\delta^{18}O$ (VPDB)	$\delta^{18}O$ offset (SIMS-acid)
		2N-C-073	23.88	-6.82	-0.70
		2N-C-074	24.07	-6.64	-0.53
		2N-C-075	23.60	-7.09	-0.98
		2N-C-076	23.62	-7.07	-0.96
		2N-C-077	23.96	-6.74	-0.62
		2N-C-078	24.77	-5.95	0.16
2N-C5	-6.11	**WiscSIMS average:**		-6.71	**-0.59**
		2N-D-019	23.74	-6.96	-0.74
		2N-D-020	24.67	-6.05	0.17
		2N-D-021	23.90	-6.80	-0.58
		2N-D-022	24.61	-6.12	0.11
		2N-D-023	23.92	-6.78	-0.56
		2N-D-024	25.09	-5.65	0.57
		2N-D-025	24.39	-6.32	-0.10
		2N-D-089	23.60	-7.09	-0.87
		2N-D-090	24.42	-6.30	-0.08
		2N-D-091	24.52	-6.20	0.02
		2N-D-092	25.04	-5.70	0.52
		2N-D-093	24.98	-5.75	0.47
2N-D1	-6.22	**WiscSIMS average:**		-6.31	**-0.09**
		2N-D-035	24.02	-6.69	-0.70
		2N-D-036	24.47	-6.25	-0.26
		2N-D-037	24.48	-6.23	-0.25
		2N-D-038	23.79	-6.91	-0.92
		2N-D-039	24.76	-5.96	0.03
		2N-D-040	24.02	-6.68	-0.69
		2N-D-041	24.37	-6.34	-0.35
2N-D2	-5.99	**WiscSIMS average:**		-6.44	**-0.45**
		2N-D-043	25.56	-5.19	0.30
		2N-D-044	25.34	-5.41	0.08
		2N-D-045	24.38	-6.34	-0.85
		2N-D-046	25.29	-5.45	0.04
		2N-D-084	24.33	-6.39	-0.90
2N-D3	-5.49	**WiscSIMS average:**		-5.75	**-0.27**
		2N-D-050	24.64	-6.08	-0.61
		2N-D-051	23.43	-7.26	-1.79
		2N-D-052	24.59	-6.13	-0.67
		2N-D-053	24.26	-6.46	-0.99
		2N-D-054	25.00	-5.73	-0.26
		2N-D-055	24.60	-6.12	-0.66
		2N-D-056	23.53	-7.16	-1.70
		2N-D-083	24.33	-6.38	-0.91
2N-D4	-5.47	**WiscSIMS average:**		-6.41	**-0.95**
		2N-D-057	24.24	-6.47	-0.20

Acid-digestion sample ID	$\delta^{18}O$ (VPDB)	WiscSIMS sample name	$\delta^{18}O$ (VSMOW)	$\delta^{18}O$ (VPDB)	$\delta^{18}O$ offset (SIMS-acid)
		2N-D-058	24.24	-6.47	-0.20
		2N-D-059	23.99	-6.71	-0.43
		2N-D-060	23.85	-6.85	-0.57
		2N-D-063	23.78	-6.91	-0.64
		2N-D-064	24.61	-6.11	0.17
		2N-D-065	24.37	-6.34	-0.06
		2N-D-066	24.79	-5.94	0.34
		2N-D-080	24.15	-6.56	-0.28
		2N-D-081	24.75	-5.98	0.30
		2N-D-082	25.06	-5.67	0.61
2N-D5	-6.28		**WiscSIMS average:**	-6.37	**-0.09**
			Average offset of whole dataset (n=85):		**-0.45**

Sample Images and Descriptions

See Sample Index and UW Catalog Numbers (page x) for UW-Geology Museum catalog numbers.

Samples 2-6 and 12-1-54:

These images illustrate the scale and orientation of Soreq Cave (Israel) stalagmite samples 2-6 and 12-1-54. Sample 2-6 was collected from a broken stalagmite fragment lying on the floor of Soreq Cave. Sample 12-1-54, collected in 2003, grew on a man-made pathway within Soreq Cave that was built in 1973. In the images below, note that the arrows indicate growth direction (i.e. calcite is younger towards the head of the arrow). Chips A-E of sample 2-6 are cataloged as UW 1993/1.1-5. Sample 12-1-54 is catalogued as UW 1993/2 and described further in Orland (2008; UW-Madison MS thesis, Appendix 4).

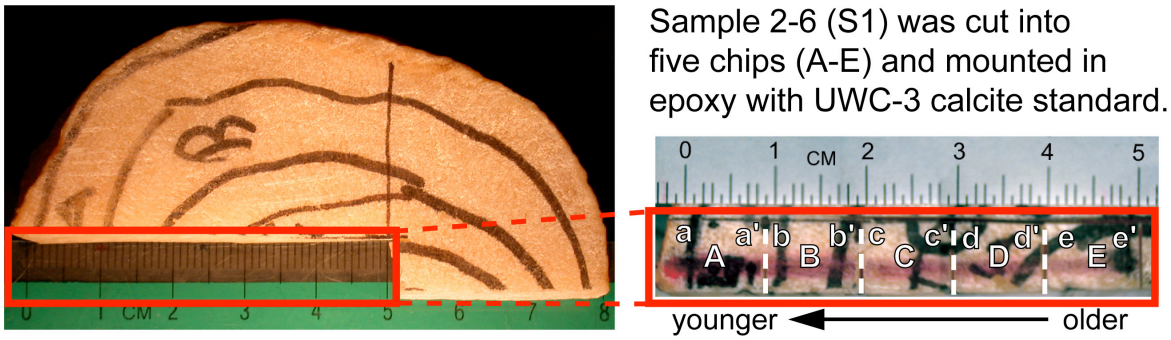

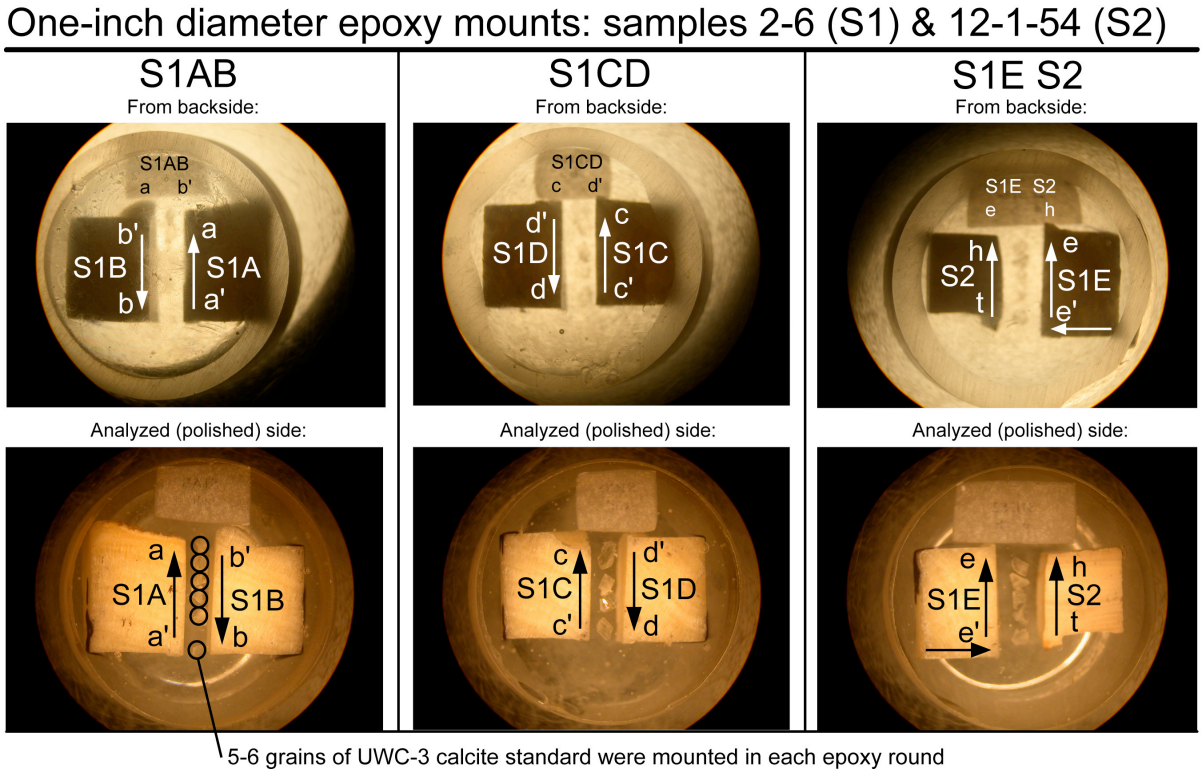

Sample 2N:

Sample 2N is a stalactite fragment collected from the floor of Soreq Cave, Israel. Pictured below are portions of the 1-cm-thick horizontal slab of sample 2N sent to UW-Madison that were not cut into 1 cm cubes. The two polished portions on the left are cataloged at UW-Madison as UW 1993/3 (large portion) and UW 1993/3.0 (smaller portion). The two portions on the right were returned to the Geological Survey of Israel. The vertical growth axis is marked with a large black spot; growth radiates outward from the vertical axis. The figure on the next page illustrates how sixteen cubes were cut along the planned analytical traverse of sample 2N (highlighted by a white dashed line) and cast in epoxy with UWC-3 calcite standard grains. Each epoxy mount is 1 inch in diameter and growth direction is indicated by arrows (i.e. calcite is younger towards the head of the arrow). Samples 2N-A through 2N-P are cataloged as UW 1993/3.1-16.

Sample 2N (ctd): Note that chips labeled AA-PP were returned to GSI.

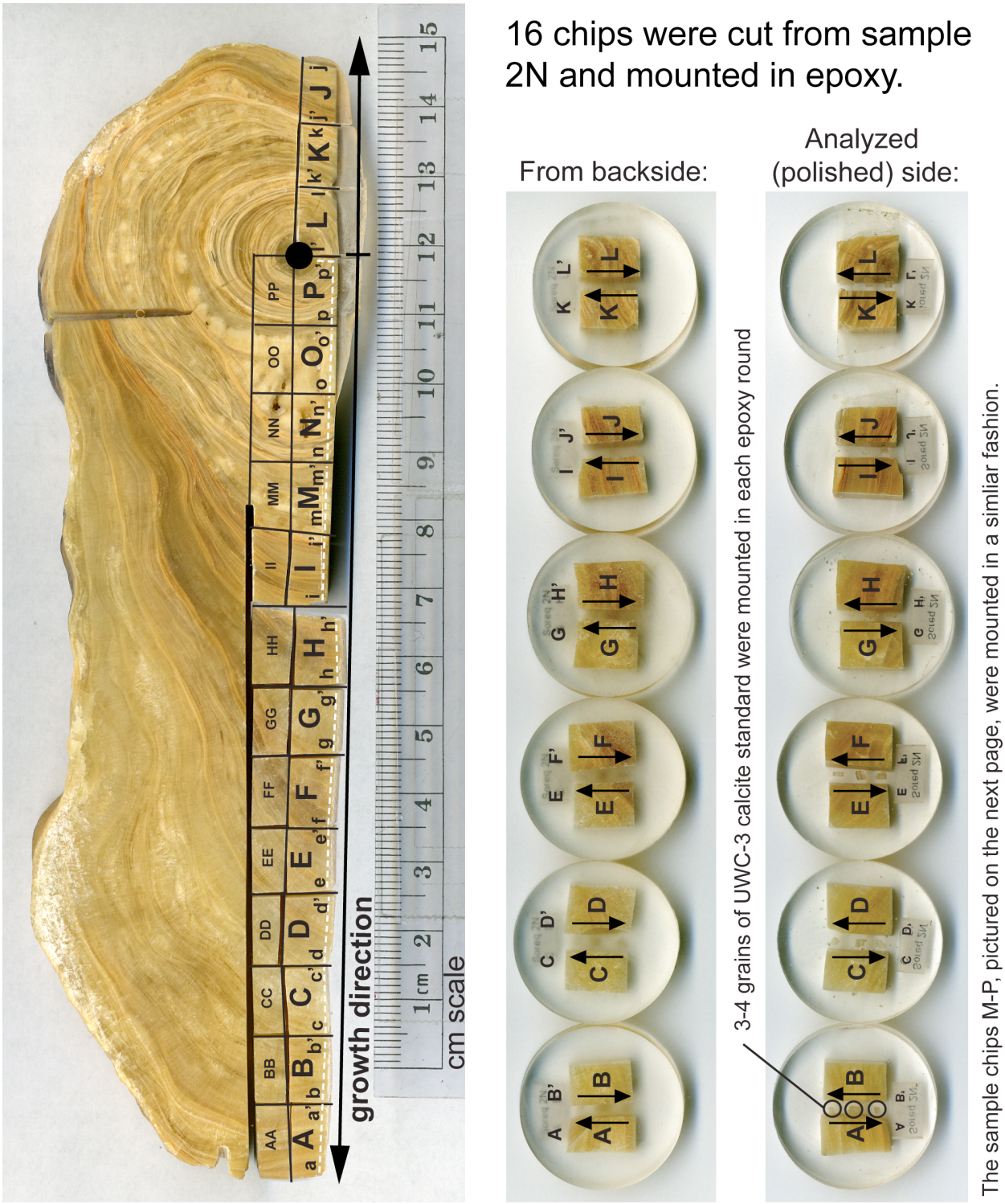

Sample 2N (ctd):

Sample 2N, chips M, N, O, P:

From backside:

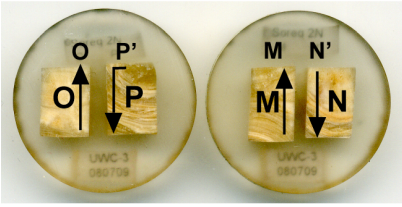

Analyzed (polished) side:

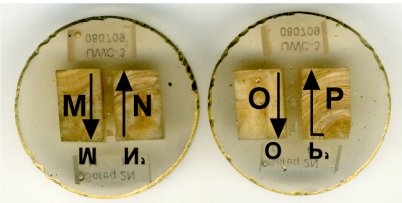

Plug backs:

The back of each plug was sawed off so that the mounts are each 5 mm thick. The removed potions each contain speleothem calcite. The eight resulting rounds were used to test polishing methods and could be used for pilot or replicate analyses. The back of each chip has the suffix "B" added to its catalog number: UW 1993/3.1B-16B

Analyzed (polished) side:

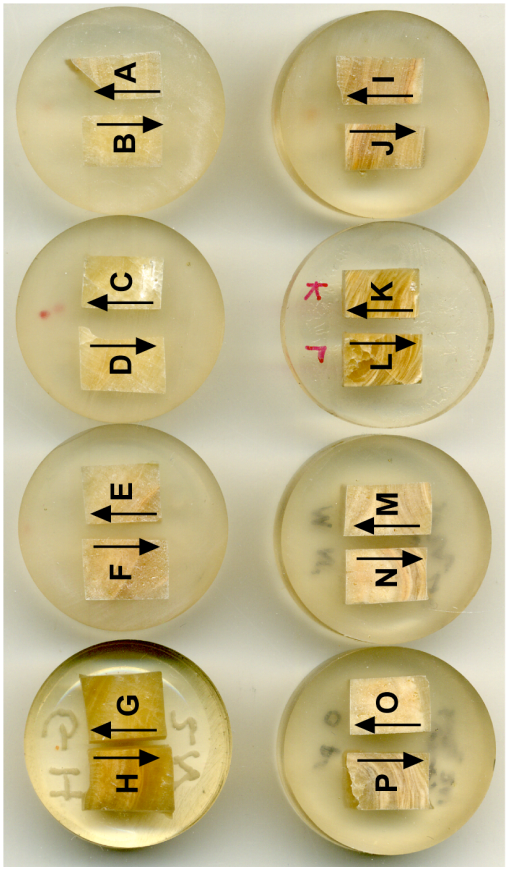

Sample SVC-982:
Stalagmite SVC-982 was collected in Spring Valley Caverns, Minnesota. Note that the arrows indicate growth direction (i.e. calcite is younger towards the head of the arrow). The scale bar refers to the image of the whole sample; each epoxy mount is 1 inch in diameter. The labels on each epoxy mount read "SV982-Ta-1A," a name given to the sample before it arrived at UW-Madison that refers to the sample face polished for ion microprobe analysis. Sample SVC-982 is cataloged as UW 1993/5. The lower panel shows chips removed for a roasting experiment.

8 chips (pre-cut outlines are seen to the left) were cut from sample SVC-982 and mounted in epoxy.

From backside:

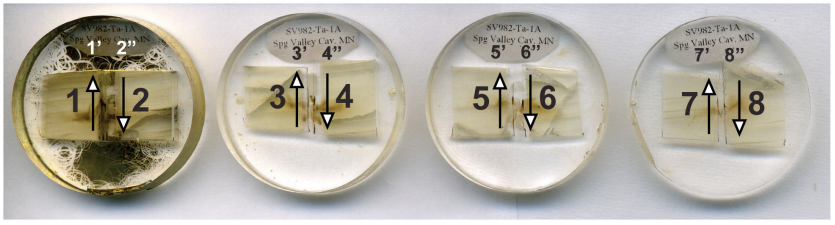

Analyzed (polished) side:

3-4 grains of UWC-3 calcite standard were mounted in each epoxy round

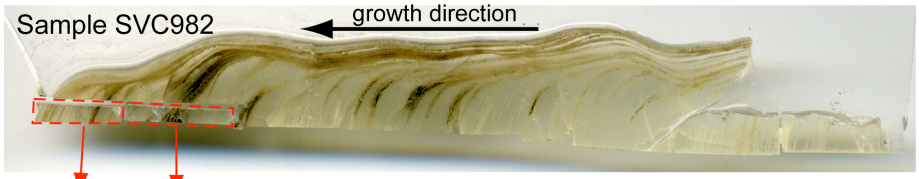

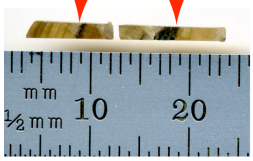

These two chips were removed and roasted in an evacuated quartz tube at 356°C for 3 hours, then mounted in a 1-inch epoxy round (right) along with 3 grains of UWC-3 calcite standard for ion microprobe analysis.

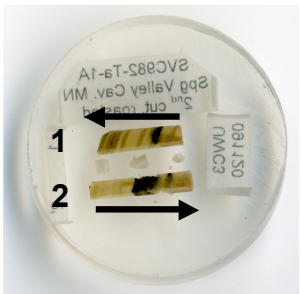

Sample 5-3b:

Sample 5-3b is a stalagmite collected from Soreq Cave (Israel) in 2008. It grew on the base of a drip-collecting stand placed in the cave in 1990. In each view of the sample, below, the dashed line shows the plane of the analytical surface and the arrow indicates growth direction (i.e. calcite is younger towards the head of the arrow). After casting the whole sample in a 1-inch-diamter epoxy round, a 1 mm-thick section was cut from the middle of the round that exposed the desired analytical surface. The 1 mm-thick section, which is shown in the image of the cut epoxy mount, was then trimmed of excess epoxy and mounted for analysis in a 1-inch-diameter epoxy round along with three grains of UWC-3 calcite standard. The resulting epoxy mount is catalogued as UW 2008/1. The remaining portions of the original stalagmite, embedded in epoxy, were returned to the Geological Survey of Israel.

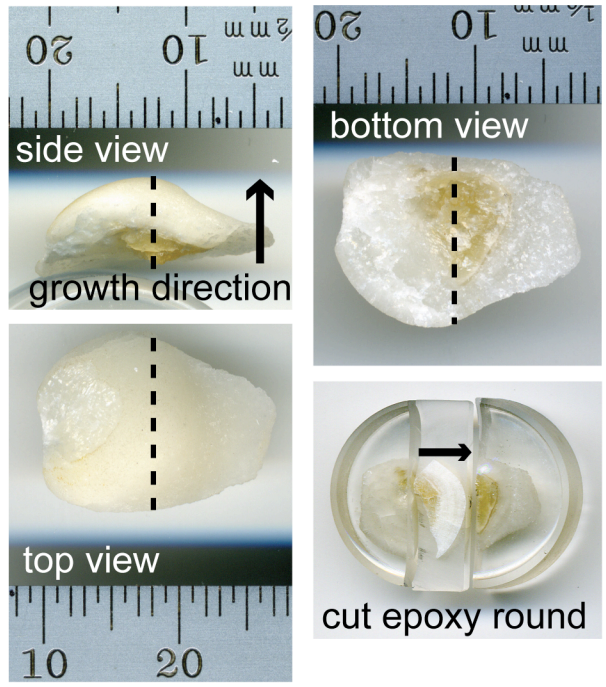

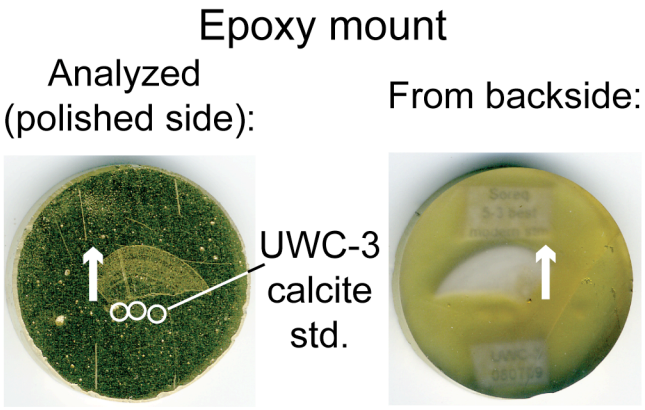

Sample 18-O specimen 1:

The sample "18-O specimen 1" is the right-hand otolith from a yellowfin sole. The left-hand otolith from the same fish (18-O specimen 2) was analyzed for $\delta^{18}O$ in Chapter 5 and returned to the Alaska Fisheries Science Center. Specimens 1 and 2 were prepared in the same way, illustrated below. The otoliths were first attached to a glass plate with clear nail polish, then cut in half with a thin-kerf (450 μm) jeweler's saw. The otolith pieces were then sequentially sonicated in acetone and distilled water to remove them from the glass plates. The half of each otolith that did not contain the central growth rings was roasted at 362°C for 3 hours in a 0.5 mTorr vacuum. The cut edges of the roasted and unroasted halves of each otolith were then mounted for ion microprobe analysis in two 1-inch-diameter epoxy rounds along with three grains of UWC-3 calcite standard. The unroasted and roasted halves of 18-O specimen 1 are catalogued as UW 2008/2.1 and 2.2, respectively.